

REPORT DOCUMENTATION PAGE			Form Approved OMB No. 0704-0188	
Public reporting burden for this collection of information is estimated to average 1 hour per response, including the time for reviewing instructions, searching existing data sources, gathering and maintaining the data needed, and completing and reviewing the collection of information. Send comments regarding this burden estimate or any other aspect of this collection of information, including suggestions for reducing this burden, to Washington Headquarters Services, Directorate for Information Operations and Reports, 1215 Jefferson Davis Highway, Suite 1204, Arlington, VA 22202-4302, and to the Office of Management and Budget, Paperwork Reduction Project (0704-0188), Washington, DC 20503.				
1. AGENCY USE ONLY (Leave blank)		2. REPORT DATE 8 Sep 97		3. REPORT TYPE AND DATES COVERED
4. TITLE AND SUBTITLE Automated Station-Keeping For Satellite Constellations			5. FUNDING NUMBERS	
6. AUTHOR(S) Naresh Harkishan Shah				
7. PERFORMING ORGANIZATION NAME(S) AND ADDRESS(ES) Massachusetts Institute Of Technology			8. PERFORMING ORGANIZATION REPORT NUMBER 97-119	
9. SPONSORING/MONITORING AGENCY NAME(S) AND ADDRESS(ES) THE DEPARTMENT OF THE AIR FORCE AFIT/CIA 2950 P STREET WPAFB OH 45433			10. SPONSORING/MONITORING AGENCY REPORT NUMBER	
11. SUPPLEMENTARY NOTES				
12a. DISTRIBUTION AVAILABILITY STATEMENT <div style="border: 1px solid black; padding: 5px; text-align: center;"> DISTRIBUTION STATEMENT A Approved for public release Distribution Unlimited </div>			12b. DISTRIBUTION CODE	
13. ABSTRACT (Maximum 200 words)				
14. SUBJECT TERMS			15. NUMBER OF PAGES 362	
			16. PRICE CODE	
17. SECURITY CLASSIFICATION OF REPORT	18. SECURITY CLASSIFICATION OF THIS PAGE	19. SECURITY CLASSIFICATION OF ABSTRACT	20. LIMITATION OF ABSTRACT	

Automated Station-Keeping For Satellite Constellations

by

Naresh Harkishan Shah

Submitted to the Department of Aeronautics and Astronautics
on May 23, 1997 in Partial Fulfillment of the
Requirements for the Degree of Master of Science in
Astronautical Engineering

ABSTRACT

The on-orbit control of future communications satellite constellations poses a challenge greater than the sum of the challenges of controlling each component satellite. New approaches are required which result in viable control systems that are flexible, reliable, and efficient. These approaches must also have the capability to derive control commands targeted at maintaining constellation-level metrics, and not just individual satellite positions and velocities. In addition, a certain level of autonomy is desired in order to minimize ground station communication and activity, and to allow for quick, responsive solutions to on-orbit failures. This work develops and tests a new methodology for the automated station-keeping of satellite constellations. Three conventional station-keeping strategies are proposed and studied, with the use of a constellation station-keeping simulation, for their ability to address the requirements of satellite constellations. In addition, three Lyapunov non-linear control strategies are developed mathematically. Finally, three sets of simulations are conducted to analyze the control and coverage characteristics of the Ellipso constellation. The Automated Station-Keeping Simulator (ASKS), created for this project, combines an optimal n-impulse rendezvous element to provide automated station-keeping for a constellation of satellites using realistic satellite dynamics calculations on a distributed network of workstations.

Thesis Supervisor: Dr. Ronald J. Proulx

Title: Technical Staff Engineer, The Charles Stark Draper Laboratory, Inc.

Thesis Supervisor: Dr. Paul J. Cefola

Title: Lecturer, Department of Aeronautics and Astronautics
Program Manager, The Charles Stark Draper Laboratory, Inc.

DTIC QUALITY INSPECTED 8

19970912 061

CSDL-T-1288

**AUTOMATED STATION-KEEPING
FOR SATELLITE CONSTELLATIONS**

by

Naresh Harkishan Shah

June 1997

**Master of Science Thesis
Massachusetts Institute of Technology**



The Charles Stark Draper Laboratory, Inc.
555 Technology Square, Cambridge, Massachusetts 02139-3563

Automated Station-Keeping For Satellite Constellations

by

Naresh Harkishan Shah

B.S. Astronautical Engineering
and Mathematical Sciences
United States Air Force Academy, 1995

SUBMITTED TO THE DEPARTMENT OF AERONAUTICS AND ASTRONAUTICS
IN PARTIAL FULFILLMENT OF THE REQUIREMENTS FOR THE DEGREE OF

MASTER OF SCIENCE IN ASTRONAUTICAL ENGINEERING
AT THE
MASSACHUSETTS INSTITUTE OF TECHNOLOGY

JUNE 1997

©Naresh H. Shah. All rights reserved.

The author hereby grants to MIT permission to reproduce and to distribute publicly
paper and electronic copies of this thesis document in whole or in part.

Signature of Author: Naresh Shah
Department of Aeronautics and Astronautics
May 23, 1997

Certified by: Ronald J. Proulx
Dr. Ronald J. Proulx
Thesis Supervisor, CSDL

Certified by: Paul J. Cefola
Dr. Paul J. Cefola
Thesis Supervisor, CSDL
Lecturer, Department of Aeronautics and Astronautics

Accepted by: Jaime Peraire
Professor Jaime Peraire
Chair, Graduate Office

[This page intentionally left blank.]

Automated Station-Keeping For Satellite Constellations

by

Naresh Harkishan Shah

Submitted to the Department of Aeronautics and Astronautics
on May 23, 1997 in Partial Fulfillment of the
Requirements for the Degree of Master of Science in
Astronautical Engineering

ABSTRACT

The on-orbit control of future communications satellite constellations poses a challenge greater than the sum of the challenges of controlling each component satellite. New approaches are required which result in viable control systems that are flexible, reliable, and efficient. These approaches must also have the capability to derive control commands targeted at maintaining constellation-level metrics, and not just individual satellite positions and velocities. In addition, a certain level of autonomy is desired in order to minimize ground station communication and activity, and to allow for quick, responsive solutions to on-orbit failures. This work develops and tests a new methodology for the automated station-keeping of satellite constellations. Three conventional station-keeping strategies are proposed and studied, with the use of a constellation station-keeping simulation, for their ability to address the requirements of satellite constellations. In addition, three Lyapunov non-linear control strategies are developed mathematically. Finally, three sets of simulations are conducted to analyze the control and coverage characteristics of the Ellipso constellation. The Automated Station-Keeping Simulator (ASKS), created for this project, combines an optimal n-impulse rendezvous element to provide automated station-keeping for a constellation of satellites using realistic satellite dynamics calculations on a distributed network of workstations.

Thesis Supervisor: Dr. Ronald J. Proulx

Title: Technical Staff Engineer, The Charles Stark Draper Laboratory, Inc.

Thesis Supervisor: Dr. Paul J. Cefola

Title: Lecturer, Department of Aeronautics and Astronautics

Program Manager, The Charles Stark Draper Laboratory, Inc.

[This page intentionally left blank.]

Acknowledgments

While this work carries my name, it is really a product of the invaluable advice, time, and effort donated by multiple persons.

First and foremost, I must thank my two thesis advisors, Dr. Ronald J. Proulx and Dr. Paul J. Cefola. Their guidance and expertise form the foundation of this thesis and of my appreciation of Astrodynamics in general. I could not have asked for a kinder, more knowledgeable pair of teachers.

Special thanks go to my parents, Harkishan and Hansa Shah, for showing me the value of hard work and perseverance; and to Dharmesh and Amy, my brother and sister-in-law, for always being ready with encouragement.

On the technical aspects of this thesis, thanks go to Brian Kantsiper for supplying the coverage software package, and for all the time spent discussing constellations and circles. To Scott Wallace for laying the ground work for parallel orbit propagation at Draper. To John Draim of MCHI for his frequent advice and assistance with the Ellipso constellation. To Pete Matthews, David Hoki, and Jack Atkins for patiently dealing with all of my panicked calls for assistance with the SPI computers. Thanks to David Carter and Wayne McClain for assistance on DSST and orbit dynamics problems.

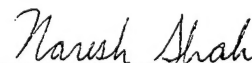
And to the score of Air Force graduate students and Draper Fellows I was privileged to meet in my two years here. Thanks to Jeff Barchers, Varun Puri, and Doug Wickert for being awesome housemates at 126 Oxford, and now lifelong friends. To Jack Fischer and Scott Carter for supplying advice, support, a well timed laugh, the occasional theorem, and help with this document. To Joe Neelon for being a ready friend. To Jon Jensen for keeping my taxes straight. And to Tony, Varun, Jeff, Raj, Jong, Chris, Ramses, Rudy, and Jack for two years of lunchtime non-sequiturs.

Finally, let me thank John Sweeney, Joan Chiffer, and Loretta Mitrano at the Draper Education Office, for opening up the possibility of the Draper Fellowship and providing help all along the way.

This thesis was prepared at The Charles Stark Draper Laboratory, Inc., with support from Draper Laboratory's DFY97 IR&D Task 837.

Publication of this thesis does not constitute approval by The Charles Stark Draper Laboratory, Inc., or the Massachusetts Institute of Technology of the findings or conclusions contained herein. It is published for the exchange and stimulation of ideas.

I hereby assign copyright of this thesis to The Charles Stark Draper Laboratory, Inc., Cambridge, Massachusetts.



Naresh Shah, 2Lt, USAF

Permission is hereby granted by The Charles Stark Draper Laboratory, Inc., to the Massachusetts Institute of Technology to reproduce any or all of this thesis.

[This page intentionally left blank.]

Contents

Chapter 1	Introduction.....	33
1.1	Statement of Objectives	33
1.2	The Station-Keeping Problem	34
1.2.1	Satellite Constellations	37
1.2.2	Ellipso Mobile Satellite System	39
1.2.3	The Automated Station-Keeping Approach	42
1.3	Thesis Overview	46
Chapter 2	Primer Vector Theory	49
2.1	The Optimal N-Impulse Rendezvous Problem	49
2.2	Development of Primer Vectors	51
2.2.1	The Primer Vector	52
2.2.2	Lawden's Necessary Conditions	56
2.2.3	Improving Transfers With Interior Impulses	60
2.2.4	Optimizing The Trajectory	68
2.3	Lambert's Problem	72
2.4	Near Optimal N-Impulse Rendezvous	77
Chapter 3	Orbit Propagation	87
3.1	Satellite Motion	88
3.1.1	Orbital Elements	88
3.1.2	Equations of Motion	93
3.1.3	Satellite Perturbations	96

3.1.3.1 Geopotential	99
3.1.3.2 Atmospheric Drag	103
3.1.3.3 Solar Radiation Pressure	105
3.1.3.4 Third Body Point Mass	106
3.2 Orbit Propagation Methods	108
3.2.1 Variation of Parameters	109
3.2.1.1 VOP Equations	109
3.2.1.2 Lagrange's Planetary Equations	111
3.2.1.3 Gauss' Form of the Variational Equations	114
3.2.2 Perturbation Theory	115
3.2.2.1 General Perturbations	116
3.2.2.2 Special Perturbations	117
3.2.2.3 Semi-Analytic Methods	120
3.2.3 Semi-Analytic Satellite Theory	122
3.2.3.1 The Method of Averaging	122
3.2.3.2 Averaged VOP Equations of Motion	123
3.3 DSST Orbit Propagator	131
3.3.1 Capabilities / Limitations	132
3.3.2 Software Interface	134
3.3.3 Mean Element Theory	135
3.3.4 Reference Frame Issues	135
Chapter 4 Lyapunov Control	141
4.1 History of Lyapunov Control Methods	141
4.2 Fundamentals of Lyapunov Control Theory	142

4.2.1	Equilibrium Points and Autonomy	143
4.2.2	Tracking Nominal Motion	145
4.2.3	Stability	147
4.2.4	Lyapunov Functions	148
4.2.5	Lyapunov Theorem For Stability	152
4.2.6	Artificial Potential Functions	153
4.2.7	Discrete Control Approaches	155
4.3	Lyapunov Control for Station-Keeping	158
4.3.1	Potential Function with Position Vector State	160
4.3.2	Potential Function with Full 6-Element State	163
4.3.3	Potential Function with Full State and State Rate	169
Chapter 5	Automated Station-Keeping Simulator	175
5.1	Capabilities	176
5.2	System Design	178
5.2.1	Ground Station Operation	179
5.2.2	Satellite Operation	181
5.2.3	Rendezvous Trajectory Planner	182
5.2.4	Orbit Propagator	184
5.3	Software Implementation	186
5.3.1	Constellation Level	187
5.3.2	Satellite Level	188
5.3.3	Optimal N-Impulse Transfer	189
5.3.4	DSST Software Interface	194
5.4	Input Deck	199

5.5	Network Environment	202
5.6	ASKS Source Code Location	204
5.7	Future Improvements	206
Chapter 6	Targeting Methods	207
6.1	Implementing Corrections	207
6.2	Element Targeting Criteria	209
6.3	Method 0	210
6.4	Method 1: Shooting the Nominal	210
6.5	Method 2: Overshooting the Nominal	212
6.6	Method 3: Directed Corrections	215
Chapter 7	Simulations	221
7.1	Ellipso Variations	222
7.2	Simulation 1: Validation of ASKS	227
7.3	Simulation 2: Absolute vs. Relative Mean Anomaly Control	233
7.4	Simulation 3: 81:10 Ellipso Coverage Analysis	239
Chapter 8	Conclusions and Future Work	243
8.1	Conclusions	245
8.2	Future Work	248
Appendix A	Mean of 1950 / True of Date Output Comparison	251
A.1	Run 1: Mean of 1950 Element Differences	252

A.2	Run 2: Instantaneous True of Date Element Differences	256
Appendix B	Simulation 1 Plots	261
B.1	Sim 1 / Run 1	261
B.1.1	Input Deck (Sim 1 / Run 1)	262
B.1.2	Method 2 (a,e,i) Borealis 8:1 Node at Dawn Orbital Element Difference Plots	265
B.1.3	Method 2 (a,e,i) Borealis 8:1 Node at Dusk Orbital Element Difference Plots	268
Appendix C	Simulation 2 Plots	271
C.1	Sim 2 / Run 1	271
C.1.1	Input Deck (Sim 2 / Run 1)	272
C.1.2	Coverage Plots (Sim 2 / Run 1)	276
C.1.3	Uncontrolled Concordia Orbital Element Difference Plots	278
C.1.4	Uncontrolled Borealis 8:1 Node at Noon Orbital Element Difference Plots	281
C.1.5	Uncontrolled Borealis 8:1 Node at Midnight Orbital Element Difference Plots	284
C.2	Sim 2 / Run 2	287
C.2.1	Input Deck (Sim 2 / Run 2)	288
C.2.2	Coverage Plots (Sim 2 / Run 2)	292
C.2.3	Method 3 Borealis 8:1 Node at Noon Orbital Element Difference Plots	294
C.2.4	Method 3 Borealis 8:1 Node at Midnight Orbital Element	

	Difference Plots	297
C.3	Sim 2 / Run 3	300
	C.3.1 Input Deck (Sim 2 / Run 3)	301
	C.3.2 Coverage Plots (Sim 2 / Run 3)	302
	C.2.3 Method 3 / Relative M Borealis 8:1 Node at Noon Element	
	Difference Plots	304
	C.2.4 Method 3 / Relative M Borealis 8:1 Node at Midnight	
	Element Difference Plots	307
Appendix D	Simulation 3 Plots	311
D.1	Sim 3 / Run 1	311
	D.1.1 Input Deck (Sim 3 / Run 1)	312
	D.1.2 Coverage Plots (Sim 3 / Run 1)	316
	D.1.3 Uncontrolled Concordia Orbital Element Difference Plots	318
	D.1.4 Uncontrolled Borealis 81:10 Node at Noon Element	
	Difference Plots	321
	D.1.5 Uncontrolled Borealis 81:10 Node at Midnight Element	
	Difference Plots	324
D.2	Sim 3 / Run 2	327
	D.2.1 Coverage Plots (Sim 3 / Run 2)	328
	D.2.2 Uncontrolled Borealis 4-4 81:10 Node at Noon Element	
	Difference Plots	330
	D.2.3 Uncontrolled Borealis 4-4 81:10 Node at Midnight Element	
	Difference Plots	333
D.3	Sim 3 / Run 3	336

D.3.1 Coverage Plots (Sim 3 / Run 3)	337
D.3.2 Uncontrolled Borealis 5-5 10 ω 81:10 Node at Noon Element Difference Plots	339
D.3.3 Uncontrolled Borealis 5-5 10 ω 81:10 Node at Midnight Element Difference Plots	342
D.4 Sim 3 / Run 4	345
D.4.1 Coverage Plots (Sim 3 / Run 4)	346
D.4.2 Uncontrolled Borealis 4-4 10 ω 81:10 Node at Noon Element Difference Plots	348
D.4.3 Uncontrolled Borealis 4-4 10 ω 81:10 Node at Midnight Element Difference Plots	351
References	355

[This page intentionally left blank.]

List of Figures

Figure 1.1	Ellipso Mobile Satellite System Orbits	40
Figure 1.2	Minimum Elevation Angles As Function of Latitude: 6 and 7 Satellite Concordia Arrays, and 4 and 5 Satellite Borealis Arrays	42
Figure 2.1	Optimal Two-Impulse Primer Vector Magnitude History	58
Figure 2.2	Non-Optimal Two-Impulse Primer Vector Magnitude History	58
Figure 2.3	Optimal Three-Impulse Primer Vector Magnitude History	59
Figure 2.4	Non-Optimal Three-Impulse Primer Vector Magnitude History	59
Figure 2.5	Two-Impulse Trajectory Perturbed at t_m	61
Figure 2.6	Non-Optimal Three-Impulse Trajectory with Cusp at t_m	68
Figure 2.7	Lambert Problem Illustration	73
Figure 2.8	Primer Vector Process Flowchart	79
Figure 2.9	Primer Vector Magnitude and Total Resulting Cost of Adding An Interior Impulse on Non-Optimal Two-Impulse Trajectory Discretized Time Grid	83
Figure 2.10	Primer Vector Magnitude and Primer Vector Rate Magnitude for Three-Impulse Trajectories	84
Figure 3.1	Keplerian Orbital Elements	90
Figure 3.2	Secular, Short Periodic and Long Periodic Variations	97
Figure 3.3	The Semi-Analytic Method	121
Figure 3.4	Precession and Nutation of the Equatorial Plane	136
Figure 4.1	Nominal and Perturbed Trajectories	146
Figure 4.2	Non-linear Mass Spring/Damper System	149
Figure 4.3	Positive Definite Function $V(\mathbf{x})$	151

Figure 4.4	Gradient of Potential Function and State Velocity Vector	156
Figure 5.1	Ground Station Process Flowchart	179
Figure 5.2	Satellite Process Flowchart	181
Figure 5.3	Rendezvous Trajectory Planner Flowchart	183
Figure 5.4	Orbit Propagator Operation Flowchart	185
Figure 5.5	Constellation Level Software Structure	187
Figure 5.6	Satellite Level Software Structure	188
Figure 5.7	Transfer Trajectory Planner Software Structure	190
Figure 5.8	4-Impulse Transfer Trajectory.....	190
Figure 5.9	DSST Interface Software Structure	194
Figure 5.10	Input Deck Format	199
Figure 5.11	Sample Control Parameter Block of Input Deck	200
Figure 5.12	Sample Plane Control Parameter Section of Input Deck	201
Figure 5.13	Sample Satellite Data Block of Input Deck	202
Figure 5.14	SPI Network Environment	203
Figure 5.15	ASKS Source Code Location	204
Figure 5.16	Location of Input Decks, Output Files, and Plot Files	206
Figure 6.1	Targeting Method 1	211
Figure 6.2	Targeting Method 2	214
Figure 6.3	Controlled SMA and Floating MA Differences from Nominal	216
Figure 6.4	Controlled ECC and INC, and Floating LAN Differences from Nominal	217
Figure 6.5	Controlled INC and Floating AP Differences from Nominal	218
Figure A-1	Semi-major Axis Differences in Mean of 1950 Frame	253
Figure A-2	Eccentricity Differences in Mean of 1950 Frame	253

Figure A-3	Inclination Differences in Mean of 1950 Frame	254
Figure A-4	Ascending Node Differences in Mean of 1950 Frame	254
Figure A-5	Argument of Perigee Differences in Mean of 1950 Frame	255
Figure A-6	Mean Anomaly Differences in Mean of 1950 Frame	255
Figure A-7	Semi-major Axis Differences in Instantaneous True of Date Frame ...	257
Figure A-8	Eccentricity Differences in Instantaneous True of Date Frame	257
Figure A-9	Inclination Differences in Instantaneous True of Date Frame	258
Figure A-10	Ascending Node Differences in Instantaneous True of Date Frame ...	258
Figure A-11	Ascending Node Differences in Instantaneous True of Date Frame ...	259
Figure A-12	Mean Anomaly Differences in Instantaneous True of Date Frame	259
Figure B-1	Semi-major Axis Difference From Nominal Trajectory (Method 2 (a,e,i) Borealis 8:1 Node at Dawn)	265
Figure B-2	Eccentricity Difference From Nominal Trajectory (Method 2 (a,e,i) Borealis 8:1 Node at Dawn)	265
Figure B-3	Inclination Difference From Nominal Trajectory (Method 2 (a,e,i) Borealis 8:1 Node at Dawn)	266
Figure B-4	Ascending Node Difference From Nominal Trajectory (Method 2 (a,e,i) Borealis 8:1 Node at Dawn)	266
Figure B-5	Argument of Perigee Difference From Nominal Trajectory (Method 2 (a,e,i) Borealis 8:1 Node at Dawn)	267
Figure B-6	Mean Anomaly Difference From Nominal Trajectory (Method 2 (a,e,i) Borealis 8:1 Node at Dawn)	267
Figure B-7	Semi-major Axis Difference From Nominal Trajectory (Method 2 (a,e,i) Borealis 8:1 Node at Dusk)	268

Figure B-8	Eccentricity Difference From Nominal Trajectory (Method 2 (a,e,i) Borealis 8:1 Node at Dusk)	268
Figure B-9	Inclination Difference From Nominal Trajectory (Method 2 (a,e,i) Borealis 8:1 Node at Dusk)	269
Figure B-10	Ascending Node Difference From Nominal Trajectory (Method 2 (a,e,i) Borealis 8:1 Node at Dusk)	269
Figure B-11	Argument of Perigee Difference From Nominal Trajectory (Method 2 (a,e,i) Borealis 8:1 Node at Dusk)	270
Figure B-12	Mean Anomaly Difference From Nominal Trajectory (Method 2 (a,e,i) Borealis 8:1 Node at Dusk)	270
Figure C-1	Ellipso One-Way Coverage (Uncontrolled Borealis 8:1 Node at Noon/Midnight and Concordia) ..	276
Figure C-2	Ellipso Two-Way Coverage (Uncontrolled Borealis 8:1 Node at Noon/Midnight and Concordia) ..	276
Figure C-3	Ellipso Three-Way Coverage (Uncontrolled Borealis 8:1 Node at Noon/Midnight and Concordia) ..	277
Figure C-4	Ellipso Four-Way Coverage (Uncontrolled Borealis 8:1 Node at Noon/Midnight and Concordia) ..	277
Figure C-5	Semi-major Axis Difference From Nominal Trajectory (Uncontrolled Concordia)	278
Figure C-6	Eccentricity Difference From Nominal Trajectory (Uncontrolled Concordia)	278
Figure C-7	Inclination Difference From Nominal Trajectory (Uncontrolled Concordia)	279

Figure C-8	Ascending Node Difference From Nominal Trajectory (Uncontrolled Concordia)	279
Figure C-9	Argument of Perigee Difference From Nominal Trajectory (Uncontrolled Concordia)	280
Figure C-10	Mean Anomaly Difference From Nominal Trajectory (Uncontrolled Concordia)	280
Figure C-11	Semi-major Axis Difference From Nominal Trajectory (Uncontrolled Borealis 8:1 Node at Noon)	281
Figure C-12	Eccentricity Difference From Nominal Trajectory (Uncontrolled Borealis 8:1 Node at Noon)	281
Figure C-13	Inclination Difference From Nominal Trajectory (Uncontrolled Borealis 8:1 Node at Noon)	282
Figure C-14	Ascending Node Difference From Nominal Trajectory (Uncontrolled Borealis 8:1 Node at Noon)	282
Figure C-15	Argument of Perigee Difference From Nominal Trajectory (Uncontrolled Borealis 8:1 Node at Noon)	283
Figure C-16	Mean Anomaly Difference From Nominal Trajectory (Uncontrolled Borealis 8:1 Node at Noon)	283
Figure C-17	Semi-major Axis Difference From Nominal Trajectory (Uncontrolled Borealis 8:1 Node at Midnight)	284
Figure C-18	Eccentricity Difference From Nominal Trajectory (Uncontrolled Borealis 8:1 Node at Midnight)	284
Figure C-19	Inclination Difference From Nominal Trajectory (Uncontrolled Borealis 8:1 Node at Midnight)	285

Figure C-20	Ascending Node Difference From Nominal Trajectory (Uncontrolled Borealis 8:1 Node at Midnight)	285
Figure C-21	Argument of Perigee Difference From Nominal Trajectory (Uncontrolled Borealis 8:1 Node at Midnight)	286
Figure C-22	Mean Anomaly Difference From Nominal Trajectory (Uncontrolled Borealis 8:1 Node at Midnight)	286
Figure C-23	Ellipso One-Way Coverage (Method 3 Borealis 8:1 Node at Noon/Midnight and Uncontrolled Concordia)	292
Figure C-24	Ellipso Two-Way Coverage (Method 3 Borealis 8:1 Node at Noon/Midnight and Uncontrolled Concordia)	292
Figure C-25	Ellipso Three-Way Coverage (Method 3 Borealis 8:1 Node at Noon/Midnight and Uncontrolled Concordia)	293
Figure C-26	Ellipso Four-Way Coverage (Method 3 Borealis 8:1 Node at Noon/Midnight and Uncontrolled Concordia)	293
Figure C-27	Semi-major Axis Difference From Nominal Trajectory (Method 3 Borealis 8:1 Node at Noon)	294
Figure C-28	Eccentricity Difference From Nominal Trajectory (Method 3 Borealis 8:1 Node at Noon)	294
Figure C-29	Inclination Difference From Nominal Trajectory (Method 3 Borealis 8:1 Node at Noon)	295

Figure C-30	Ascending Node Difference From Nominal Trajectory (Method 3 Borealis 8:1 Node at Noon)	295
Figure C-31	Argument of Perigee Difference From Nominal Trajectory (Method 3 Borealis 8:1 Node at Noon)	296
Figure C-32	Mean Anomaly Difference From Nominal Trajectory (Method 3 Borealis 8:1 Node at Noon)	296
Figure C-33	Semi-major Axis Difference From Nominal Trajectory (Method 3 Borealis 8:1 Node at Midnight)	297
Figure C-34	Eccentricity Difference From Nominal Trajectory (Method 3 Borealis 8:1 Node at Midnight)	297
Figure C-35	Inclination Difference From Nominal Trajectory (Method 3 Borealis 8:1 Node at Midnight)	298
Figure C-36	Ascending Node Difference From Nominal Trajectory (Method 3 Borealis 8:1 Node at Midnight)	298
Figure C-37	Argument of Perigee Difference From Nominal Trajectory (Method 3 Borealis 8:1 Node at Midnight)	299
Figure C-38	Mean Anomaly Difference From Nominal Trajectory (Method 3 Borealis 8:1 Node at Midnight)	299
Figure C-39	Ellipso One-Way Coverage (Method 3 / Relative M Borealis 8:1 Noon/Midnight and Uncontrolled Concordia)	302
Figure C-40	Ellipso Two-Way Coverage (Method 3 / Relative M Borealis 8:1 Noon/Midnight and Uncontrolled Concordia)	302

Figure C-41	Ellipso Three-Way Coverage (Method 3 / Relative M Borealis 8:1 Noon/Midnight and Uncontrolled Concordia)	303
Figure C-42	Ellipso Four-Way Coverage (Method 3 / Relative M Borealis 8:1 Noon/Midnight and Uncontrolled Concordia)	303
Figure C-43	Semi-major Axis Difference From Nominal Trajectory (Method 3 / Relative M Borealis 8:1 Node at Noon)	304
Figure C-44	Eccentricity Difference From Nominal Trajectory (Method 3 / Relative M Borealis 8:1 Node at Noon)	304
Figure C-45	Inclination Difference From Nominal Trajectory (Method 3 / Relative M Borealis 8:1 Node at Noon)	305
Figure C-46	Ascending Node Difference From Nominal Trajectory (Method 3 / Relative M Borealis 8:1 Node at Noon)	305
Figure C-47	Argument of Perigee Difference From Nominal Trajectory (Method 3 / Relative M Borealis 8:1 Node at Noon)	306
Figure C-48	Mean Anomaly Difference From Nominal Trajectory (Method 3 / Relative M Borealis 8:1 Node at Noon)	306
Figure C-49	Semi-major Axis Difference From Nominal Trajectory (Method 3 / Relative M Borealis 8:1 Node at Midnight)	307
Figure C-50	Eccentricity Difference From Nominal Trajectory (Method 3 / Relative M Borealis 8:1 Node at Midnight)	307
Figure C-51	Inclination Difference From Nominal Trajectory (Method 3 / Relative M Borealis 8:1 Node at Midnight)	308

Figure C-52	Ascending Node Difference From Nominal Trajectory (Method 3 / Relative M Borealis 8:1 Node at Midnight)	308
Figure C-53	Argument of Perigee Difference From Nominal Trajectory (Method 3 / Relative M Borealis 8:1 Node at Midnight)	309
Figure C-54	Mean Anomaly Difference From Nominal Trajectory (Method 3 / Relative M Borealis 8:1 Node at Midnight)	309
Figure D-1	5-5-7 Ellipso One-Way Coverage (Uncontrolled Borealis 81:10 Noon/Midnight and Concordia)	316
Figure D-2	5-5-7 Ellipso Two-Way Coverage (Uncontrolled Borealis 81:10 Noon/Midnight and Concordia)	316
Figure D-3	5-5-7 Ellipso Three-Way Coverage (Uncontrolled Borealis 81:10 Noon/Midnight and Concordia)	317
Figure D-4	5-5-7 Ellipso Four-Way Coverage (Uncontrolled Borealis 81:10 Noon/Midnight and Concordia)	317
Figure D-5	Semi-major Axis Difference From Nominal Trajectory (Uncontrolled 7 Concordia)	318
Figure D-6	Eccentricity Difference From Nominal Trajectory (Uncontrolled 7 Concordia)	318
Figure D-7	Inclination Difference From Nominal Trajectory (Uncontrolled 7 Concordia)	319
Figure D-8	Ascending Node Difference From Nominal Trajectory (Uncontrolled 7 Concordia)	319
Figure D-9	Argument of Perigee Difference From Nominal Trajectory (Uncontrolled 7 Concordia)	320

Figure D-10	Mean Anomaly Difference From Nominal Trajectory (Uncontrolled 7 Concordia)	320
Figure D-11	Semi-major Axis Difference From Nominal Trajectory (Uncontrolled Borealis 5-5 81:10 Node at Noon)	321
Figure D-12	Eccentricity Difference From Nominal Trajectory (Uncontrolled Borealis 5-5 81:10 Node at Noon)	321
Figure D-13	Inclination Difference From Nominal Trajectory (Uncontrolled Borealis 5-5 81:10 Node at Noon)	322
Figure D-14	Ascending Node Difference From Nominal Trajectory (Uncontrolled Borealis 5-5 81:10 Node at Noon)	322
Figure D-15	Argument of Perigee Difference From Nominal Trajectory (Uncontrolled Borealis 5-5 81:10 Node at Noon)	323
Figure D-16	Mean Anomaly Difference From Nominal Trajectory (Uncontrolled Borealis 5-5 81:10 Node at Noon)	323
Figure D-17	Semi-major Axis Difference From Nominal Trajectory (Uncontrolled Borealis 5-5 81:10 Node at Midnight)	324
Figure D-18	Eccentricity Difference From Nominal Trajectory (Uncontrolled Borealis 5-5 81:10 Node at Midnight)	324
Figure D-19	Inclination Difference From Nominal Trajectory (Uncontrolled Borealis 5-5 81:10 Node at Midnight)	325
Figure D-20	Ascending Node Difference From Nominal Trajectory (Uncontrolled Borealis 5-5 81:10 Node at Midnight)	325
Figure D-21	Argument of Perigee Difference From Nominal Trajectory (Uncontrolled Borealis 5-5 81:10 Node at Midnight)	326

Figure D-22	Mean Anomaly Difference From Nominal Trajectory (Uncontrolled Borealis 5-5 81:10 Node at Midnight)	326
Figure D-23	4-4-6 Ellipso One-Way Coverage (Uncontrolled Borealis 81:10 Noon/Midnight and Concordia)	328
Figure D-24	4-4-6 Ellipso Two-Way Coverage (Uncontrolled Borealis 81:10 Noon/Midnight and Concordia)	328
Figure D-25	4-4-6 Ellipso Three-Way Coverage (Uncontrolled Borealis 81:10 Noon/Midnight and Concordia)	329
Figure D-26	4-4-6 Ellipso Four-Way Coverage (Uncontrolled Borealis 81:10 Noon/Midnight and Concordia)	329
Figure D-27	Semi-major Axis Difference From Nominal Trajectory (Uncontrolled Borealis 4-4 81:10 Node at Noon)	330
Figure D-28	Eccentricity Difference From Nominal Trajectory (Uncontrolled Borealis 4-4 81:10 Node at Noon)	330
Figure D-29	Inclination Difference From Nominal Trajectory (Uncontrolled Borealis 4-4 81:10 Node at Noon)	331
Figure D-30	Ascending Node Difference From Nominal Trajectory (Uncontrolled Borealis 4-4 81:10 Node at Noon)	331
Figure D-31	Argument of Perigee Difference From Nominal Trajectory (Uncontrolled Borealis 4-4 81:10 Node at Noon)	332
Figure D-32	Mean Anomaly Difference From Nominal Trajectory (Uncontrolled Borealis 4-4 81:10 Node at Noon)	332
Figure D-33	Semi-major Axis Difference From Nominal Trajectory (Uncontrolled Borealis 4-4 81:10 Node at Midnight)	333

Figure D-34	Eccentricity Difference From Nominal Trajectory (Uncontrolled Borealis 4-4 81:10 Node at Midnight)	333
Figure D-35	Inclination Difference From Nominal Trajectory (Uncontrolled Borealis 4-4 81:10 Node at Midnight)	334
Figure D-36	Ascending Node Difference From Nominal Trajectory (Uncontrolled Borealis 4-4 81:10 Node at Midnight)	334
Figure D-37	Argument of Perigee Difference From Nominal Trajectory (Uncontrolled Borealis 4-4 81:10 Node at Midnight)	335
Figure D-38	Mean Anomaly Difference From Nominal Trajectory (Uncontrolled Borealis 4-4 81:10 Node at Midnight)	335
Figure D-39	5-5-7 10 ω Ellipso One-Way Coverage (Uncontrolled Borealis 81:10 Noon/Midnight and Concordia)	337
Figure D-40	5-5-7 10 ω Ellipso Two-Way Coverage (Uncontrolled Borealis 81:10 Noon/Midnight and Concordia)	337
Figure D-41	5-5-7 10 ω Ellipso Three-Way Coverage (Uncontrolled Borealis 81:10 Noon/Midnight and Concordia)	338
Figure D-42	5-5-7 10 ω Ellipso Four-Way Coverage (Uncontrolled Borealis 81:10 Noon/Midnight and Concordia)	338
Figure D-43	Semi-major Axis Difference From Nominal Trajectory (Uncontrolled Borealis 5-5 10 ω 81:10 Node at Noon)	339
Figure D-44	Eccentricity Difference From Nominal Trajectory (Uncontrolled Borealis 5-5 10 ω 81:10 Node at Noon)	339
Figure D-45	Inclination Difference From Nominal Trajectory (Uncontrolled Borealis 5-5 10 ω 81:10 Node at Noon)	340

Figure D-46	Ascending Node Difference From Nominal Trajectory (Uncontrolled Borealis 5-5 10 ω 81:10 Node at Noon)	340
Figure D-47	Argument of Perigee Difference From Nominal Trajectory (Uncontrolled Borealis 5-5 10 ω 81:10 Node at Noon)	341
Figure D-48	Mean Anomaly Difference From Nominal Trajectory (Uncontrolled Borealis 5-5 10 ω 81:10 Node at Noon)	341
Figure D-49	Semi-major Axis Difference From Nominal Trajectory (Uncontrolled Borealis 5-5 10 ω 81:10 Node at Midnight)	342
Figure D-50	Eccentricity Difference From Nominal Trajectory (Uncontrolled Borealis 5-5 10 ω 81:10 Node at Midnight)	342
Figure D-51	Inclination Difference From Nominal Trajectory (Uncontrolled Borealis 5-5 10 ω 81:10 Node at Midnight)	343
Figure D-52	Ascending Node Difference From Nominal Trajectory (Uncontrolled Borealis 5-5 10 ω 81:10 Node at Midnight)	343
Figure D-53	Argument of Perigee Difference From Nominal Trajectory (Uncontrolled Borealis 5-5 10 ω 81:10 Node at Midnight)	344
Figure D-54	Mean Anomaly Difference From Nominal Trajectory (Uncontrolled Borealis 5-5 10 ω 81:10 Node at Midnight)	344
Figure D-55	4-4-6 10 ω Ellipso One-Way Coverage (Uncontrolled Borealis 81:10 Noon/Midnight and Concordia)	346
Figure D-56	4-4-6 10 ω Ellipso Two-Way Coverage (Uncontrolled Borealis 81:10 Noon/Midnight and Concordia)	346
Figure D-57	4-4-6 10 ω Ellipso Three-Way Coverage (Uncontrolled Borealis 81:10 Noon/Midnight and Concordia)	347

Figure D-58	4-4-6 10 ω Ellipso Four-Way Coverage (Uncontrolled Borealis 81:10 Noon/Midnight and Concordia)	347
Figure D-59	Semi-major Axis Difference From Nominal Trajectory (Uncontrolled Borealis 4-4 10 ω 81:10 Node at Noon)	348
Figure D-60	Eccentricity Difference From Nominal Trajectory (Uncontrolled Borealis 4-4 10 ω 81:10 Node at Noon)	348
Figure D-61	Inclination Difference From Nominal Trajectory (Uncontrolled Borealis 4-4 10 ω 81:10 Node at Noon)	349
Figure D-62	Ascending Node Difference From Nominal Trajectory (Uncontrolled Borealis 4-4 10 ω 81:10 Node at Noon)	349
Figure D-63	Argument of Perigee Difference From Nominal Trajectory (Uncontrolled Borealis 4-4 10 ω 81:10 Node at Noon)	350
Figure D-64	Mean Anomaly Difference From Nominal Trajectory (Uncontrolled Borealis 4-4 10 ω 81:10 Node at Noon)	350
Figure D-65	Semi-major Axis Difference From Nominal Trajectory (Uncontrolled Borealis 4-4 10 ω 81:10 Node at Midnight)	351
Figure D-66	Eccentricity Difference From Nominal Trajectory (Uncontrolled Borealis 4-4 10 ω 81:10 Node at Midnight)	351
Figure D-67	Inclination Difference From Nominal Trajectory (Uncontrolled Borealis 4-4 10 ω 81:10 Node at Midnight)	352
Figure D-68	Ascending Node Difference From Nominal Trajectory (Uncontrolled Borealis 4-4 10 ω 81:10 Node at Midnight)	352
Figure D-69	Argument of Perigee Difference From Nominal Trajectory (Uncontrolled Borealis 4-4 10 ω 81:10 Node at Midnight)	353

Figure D-70 Mean Anomaly Difference From Nominal Trajectory

(Uncontrolled Borealis 4-4 10 ω 81:10 Node at Midnight) 354

[This page intentionally left blank.]

List of Tables

Table 1.1	Specialized Orbit Designs	35
Table 1.2	Constellation Orbit Design Factors	37
Table 1.3	Comparison of GPCS Systems	38
Table 1.4	Borealis Sub-Constellation Orbital Elements (81:10 RGT)	40
Table 1.5	Concordia Sub-Constellation Orbital Elements	41
Table 2.1	Inclination Test Case Initial and Target States	81
Table 2.2	Non-Optimal Two-Impulse Burnlist	82
Table 2.3	Optimal Three-Impulse Burnlist	85
Table 2.4	Inclination Test Case Initial and Target States	85
Table 3.1	Keplerian Element Set	89
Table 3.2	Accelerations Experienced by Spacecraft At Varying Altitudes	98
Table 3.3	Varying Types of Perturbation Effects	98
Table 3.4	Comparison of Mean of 1950 and True of Date Differences	139
Table 5.1	<i>coast_arc</i> Matrix	191
Table 5.2	<i>lamda_arc</i> Matrix	192
Table 5.3	<i>burnlist</i> Array	194
Table 5.4	<i>satopt_dbl</i> Array	195
Table 5.5	<i>satopt_int</i> Array	196
Table 5.6	<i>intervals</i> Array	197
Table 5.7	<i>satdata</i> Array	198
Table 6.1	Borealis Maximum Orbital Element Limits	208
Table 6.2	Concordia Maximum Orbital Element Limits	208
Table 7.1	Concordia Sub-Constellation Orbital Elements	222
Table 7.2	Borealis 8:1 Mean Element Sets for Node at Dawn/Dusk	223

Table 7.3	Borealis 8:1 Mean Element Sets for Node at Noon/Midnight	224
Table 7.4	Borealis 81:10 Mean Element Sets for Node at Noon/Midnight	225
Table 7.5	5 Year Predicted ΔV and Fuel Budget for Worst Case Borealis 8:1 Node at Dawn / Dusk Satellite	228
Table 7.6	2 $\frac{1}{2}$ Year ASKS / Sabol ΔV Comparison For Node At Dawn / Dusk Borealis Satellites	232
Table 7.7	2 Year ΔV Budgets For Node At Noon / Midnight Borealis Satellites Using Method 3 Controller With Absolute and Relative Mean Anomaly Station-Keeping	238
Table 8.1	Average and Maximum 2 $\frac{1}{2}$ Year ΔV Budgets for Borealis Node at Dawn / Dusk Satellites	246
Table 8.2	2 Year ΔV Budgets for Borealis Node at Noon / Midnight Satellites Using Absolute and Realtive Mean Anomaly Station- Keeping	247

Chapter 1

Introduction

1.1 Statement of Objectives

Satellite orbit maintenance can be broadly defined as the process of executing small corrections to the motion of a satellite to keep that satellite within parameters required to meet mission objectives. Since satellites today are manufactured to operate exclusively in their designed orbit, their performance may be severely degraded if that orbit cannot be achieved or maintained. This fact makes the science of keeping satellites “on-station” for their designed lifetime critically important to all applications that involve the use of space vehicles.

Station-keeping is important for other reasons as well. Constant improvement in many space technologies is redefining what determines the lifetime of a satellite system. Efficient solar panels, long life batteries, modern materials, state of the art communications equipment, and advanced computer processors have removed the traditional lifetime constraints. Increasingly, onboard fuel is becoming one of the defining factors for the lifetime of a modern satellite. This trend implies that for a given amount of fuel, the efficient operation of the station-keeping system directly affects the lifetime of the satellite.

The station-keeping challenges faced by the controller of a satellite are produced by the environment the satellite operates in. The space environment can vary based on many

factors and often is difficult to predict accurately. The job of a satellite station-keeping system is to reject disturbances which move a satellite away from a small range, in the orbital elements, of its nominal trajectory. It usually accomplishes this task with the use of impulsive thrusters. However, the limited amount of onboard fuel requires that orbit corrections be small, infrequent, and effective.

A recent trend in space based applications is the increased use of satellite constellations. A constellation is simply two or more satellites that operate together to accomplish a mission. Unfortunately, the complexity of a constellation does not increase linearly with the number of component satellites. For a constellation station-keeping system, not only is knowledge of each satellite's individual position important, but so is each satellite's relative position and velocity. Solving this problem is often compared to choreographing an intricate celestial dance involving hundreds of dancers.

The broad objective of this thesis is to study this special satellite choreography. In particular, the objective is to develop and test new approaches for a station-keeping system with the use of an adaptable, scaleable computer simulation, which automatically maintains the orbits of satellites in a constellation. The system is designed to support the future development of autonomous satellite operations. Real world satellite dynamics, which incorporate complicated perturbation models, are used in order to produce an accurate simulation to test the different strategies. In addition, the simulation has the capability of operating in parallel on a distributed network of processors.

1.2 The Station-Keeping Problem

The design of any satellite's orbit is driven primarily by its mission requirements. An orbit designer is able to tailor the five slowly varying orbital elements to create an orbit

which has characteristics suitable to the tasks assigned to the satellite. Since satellite missions range widely, the scope of the orbits that can be designed to meet the requirements is also wide. Table 1.1 lists general orbit types and characteristics that are useful for some common satellite applications.

Table 1.1: Specialized Orbit Designs [37]

Orbit	Characteristic	Application
Geosynchronous	maintains nearly fixed position over equator	communications, weather
Sun synchronous	orbit plane rotates to maintain constant orientation with respect to Sun	Earth resources, weather
Molniya	biases coverage to northern latitudes	high latitude communications
Frozen orbit	minimizes changes in orbit parameters	any orbit requiring stable conditions
Repeat ground track	subsattellite trace repeats	any orbit requiring constant viewing angles of ground locations

Satellite orbits are designed with the expectation that their orbital elements will be maintained for the duration of the mission. However, several factors related to the space environment can affect a satellite over time and have a detrimental affect on the favorable characteristics of its orbit. These factors, called perturbations, include non-spherical Earth geopotential, atmospheric drag, solar radiation pressure, third body point mass disturbances, and several other smaller scale effects. The task of maintaining the orbit of a satellite in the presence of perturbations is assigned to the station-keeping system.

A station-keeping system for a satellite does not necessarily aim to maintain a 2 body orbit - the orbit that excludes the affects of all perturbations. In several cases, the motion of the orbit due to a perturbation is essential to its design. An example of this is the Sun synchronous orbit listed in table 1.1. The rate of change of the ascending node of a Sun synchronous orbit is caused by the oblateness of the Earth, which is modeled as the J_2

zonal harmonic of the geopotential. It is an essential component of the orbit design and should not be counteracted. Therefore, a station-keeping system attempts to track a nominal orbit, or the orbit that includes all favorable perturbations, and not necessarily the 2 body orbit.

The station-keeping problem does not scale easily from a single satellite to a satellite constellation. Because all the satellites in a constellation must work together to accomplish the constellation mission, their orbits must also be maintained relative to one another. One simple way to accomplish this is to treat each satellite in the constellation individually and maintain it within a very strictly defined set of six orbital elements at all times. This approach, while only requiring a linear scale up in the control resources, does not take advantage of the distributed nature of the new problem. Since each satellite has two neighbors in its plane, and since each plane has neighboring planes, a common drifting in some of the orbital elements can be allowed if it does not degrade the ability of the constellation to address its mission. This approach of addressing relative orbital parameters has the potential for significant savings in fuel expenditure. Of course, its drawback is its increased complexity.

It is important to note that while this thesis only addresses the station-keeping problem, there are actually several flight dynamics processes that must be considered for satellites and constellations. They include

- transfer from launch conditions to mission orbit,
- orbit determination,
- attitude determination and control,
- telemetry uplink / downlink,
- satellite collision avoidance,
- maneuver planning / repositioning, and
- end-of-life deorbit.

1.2.1 Satellite Constellations

The most important reason to treat several satellites as one unit, or a constellation, is their functionality. Certain missions are best addressed with the use of multiple satellites working together. The most notable example of this is the Global Positioning System (GPS). It is an integrated system of 24 identical satellites which beam signals down to the Earth for the purpose of precise position determination. Since the method of determining position relies on signals originating from multiple dispersed sources, a single satellite cannot accomplish the task alone. Another example is the Molniya communications constellation. Three satellites in inclined, highly elliptical orbits are used with appropriate phasing to insure that at least one satellite is always visible from the high latitudes of the former Soviet Union.

The design of a constellation differs from the design of a single satellite orbit. Several important design factors, their effects, and the way they are resolved are listed in table 1.2.

Table 1.2: Constellation Orbit Design Factors [37]

Factor	Effect	Selection Criteria
Number of Satellites	principle cost and coverage driver	minimize number to meet coverage and performance plateau requirements
Altitude	coverage; launch & transfer cost	typically system-level trade of cost vs. performance
Number of Orbit Planes	flexibility; coverage plateaus, growth and degradation	minimize number of planes consistent with coverage
Inclination	determines latitude distribution of coverage	latitude coverage vs. launch cost
Phasing Between Planes	determines uniform coverage	select best coverage among discrete set of phasing options
Eccentricity	mission complexity, achievable altitude, and coverage vs. cost	normally zero unless driven to another value by mission needs

One of the most exciting applications of satellite constellations in recent times is the global personal communications system (GPCS). Several companies are racing to establish a system that will open up direct satellite based communications to virtually the entire planet. While these systems differ in their scope and specific applications, they are similar in that they each propose to launch and operate a multiple satellite system to provide communications on demand to a global market. Despite having similar goals, all the systems proposed to date have selected significantly different constellation designs. Table 1.3 lists several characteristics of some of the most prominent GPCS systems. Note that the orbital element values provided in table 1.3 are only approximations to be used for a coarse level comparison. Precise orbital designs are often considered proprietary information.

Table 1.3: Comparison of GPCS Systems* [31]

	Ellipso Borealis/Concordia	Globalstar	Iridium	Odyssey	Teledesic**
Orbit Type	SSFLA	LEO	LEO	MEO	LEO
Altitude (km)	520-7846 / 8063	1401	785	10354	695 to 705
Eccentricity	0.35 / 0.0	0.0	0.0013	0.0	0.00118
Inclination (deg)	116.6 / 0.0	52.0	86.4	55.0	98.2
Period (hr)	3.0 / 4.67	1.9	1.68	5.98	1.66
Number of Sats	10 / 7	48	66	12	840
Number of Planes	2 / 1	8	6	3	21
Number of Sats Per Plane	5 / 7	6	11	4	40
Coverage Claim	90°N to 55°S	global	global	global	global
Min Elev Angle Claim (deg)	25 / 10	10	8.2	22	unk

*This table contains values that are more up to date than those available in the original reference.

**This is the original Teledesic constellation design. It has since changed to a 288 satellite design.

The constellation chosen for analysis in this thesis is the Ellipso Mobile Satellite System. It was chosen over the others because of its combination of size, orbit design, and coverage pattern. A constellation of smaller size is favorable because of the fixed computing capability available for this project. An execution of the station-keeping simulator on the 840 satellite Teledesic constellation, while possible, would require significantly more processors than available to the author to complete in the same time as a simulator execution on a smaller constellation. The unique orbits of Ellipso are particularly important. They allow the simulation to demonstrate that it is applicable to more than just circular orbits. The more complex coverage claim for Ellipso also allows the simulator to demonstrate that its coverage utility is able to adapt to different requirements.

1.2.2 Ellipso Mobile Satellite System

The Ellipso constellation, proposed by Mobile Communications Holdings Inc., intends to achieve near global coverage using two low/medium altitude sub-constellations in tandem. The first consists of two critically-inclined, eccentric orbit planes. It is complemented by a circular, equatorial sub-constellation. This concept, developed and patented by Castiel, Draim, and Brosius [11], is supported by a study that shows that medium altitude elliptical orbits are more efficient than traditional low Earth orbit (LEO) or geostationary Earth orbit (GEO) systems in balancing the dual demands of global coverage and transmission power [20]. The Ellipso constellation is displayed in figure 1.1.

The two critically inclined orbit planes are known as the Ellipso Borealis sub-constellation. The Borealis orbit planes are aligned 180° apart in ascending node and

operate in a manner similar to Molniya orbits. They provide 24 hour coverage of the northern hemisphere with four spacecraft and one spare in each orbit. The orbits themselves are Sun synchronous with a frozen line of apsides (SSFLA).

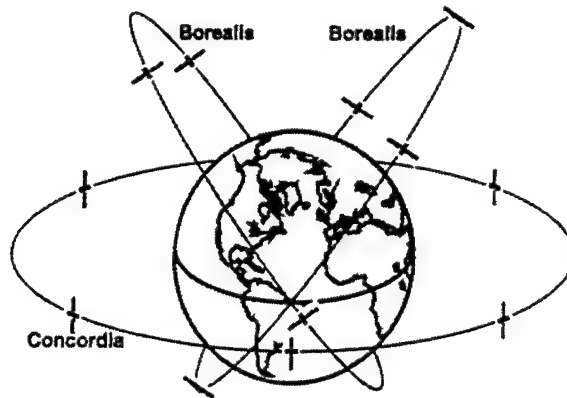


Figure 1.1: Ellipso Mobile Satellite System Orbits [10]

This implies that the ascending nodes of the planes will remain at noon and midnight throughout their lifetime. An orbit analysis of the Borealis sub-constellation is available in Sabol's master's thesis [51] and in a paper by Sabol, Draim, and Cefola [52]. The precise orbital elements for the 5 satellites of each the two Borealis planes at 1 January, 1997 are listed in table 1.4.

Table 1.4: Borealis Sub-Constellation Orbital Elements (81:10 RGT) [52]

Element	Node at Noon Plane	Node at Midnight Plane
a	10472.201 km	10472.200 km
e	0.32652	0.32662
i	116.583°	116.582°
ω	270°	270°
Ω	280°	100°
M	0°, 72°, 144°, 216°, and 288°	0°, 72°, 144°, 216°, and 288°
Epoch	Midnight, Jan 1 1997	Midnight, Jan 1 1997

The elements listed in table 1.4 represent the most refined state of the Borealis orbits to date, and are for an 81:10 repeat ground track. Sabol, Draim, and Cefola demonstrated that this configuration results in significantly reduced station-keeping fuel costs while maintaining essentially the same coverage compared to the original 8:1 repeat ground track configuration [52].

The medium altitude circular equatorial orbit is the Ellipso Concordia sub-constellation. Concordia consists of 6 satellites with one on-orbit spare. It provides coverage around the tropical and southern latitudes. The apogee radius of the Borealis and Concordia orbits are approximately the same to insure that the same communications equipment can be used for every satellite in the constellation. The orbital elements for the 7 satellites of the Concordia plane are listed in table 1.5.

Table 1.5: Concordia Sub-Constellation Orbital Elements [53]

Element	Concordia Plane
a	14440.137 km
e	0.0
i	0.0°
ω	90°
Ω	0.0°
M	0°, 51.43°, 102.86°, 154.29°, 205.71°, 257.14°, and 308.57°

The two sub-constellations of Ellipso give it unique flexibility in how it covers the globe. The design is based on the distribution of land and population by latitude [12]. The two

Borealis planes cover the northern hemisphere, where much of the customer base for the mobile communications system is projected, with the use of elliptic orbits. The Concordia complements the Borealis planes by providing coverage to the population and land masses in the equatorial and southern hemispheric zones. Since all relevant land masses lie above the southern 55th parallel, no requirement for satellite coverage is stated below this line. Figure 1.2 illustrates the minimum elevation angles achievable by the Concordia and Borealis planes.

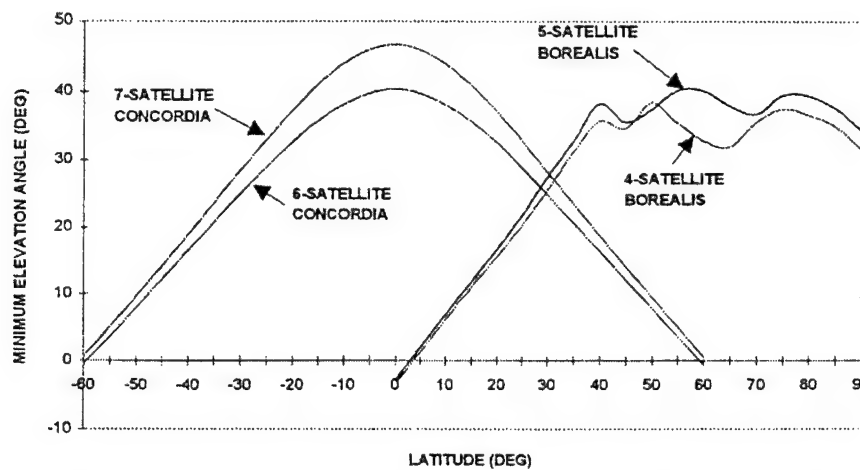


Figure 1.2: Minimum Elevation Angles As Function of Latitude: 6 and 7 Satellite Concordia Arrays, and 4 and 5 Satellite Borealis Arrays [21]

The current plan is to use 5 satellites in each Borealis plane, and 7 satellites in the Concordia plane. This allows Ellipso to meet its coverage requirements with a 10° minimum elevation angle in the southern hemisphere and a 25° min elevation angle in the northern hemisphere.

1.2.3 The Automated Station-Keeping Approach

The on-orbit control of a satellite constellation poses challenges that do not exist in the control of individual satellites. Control methodologies which address these challenges

must be able to derive control commands based upon constellation level metrics and not just individual satellite positions and velocities. A certain level of autonomy is also desired to minimize ground station activity and to allow for quick, responsive solutions to on-orbit failures. In addition, the control methodologies must be flexible, reliable, and efficient. This thesis will study three different control methods with the use of a constellation wide station-keeping simulation.

The Automated Station-Keeping Simulator (ASKS), created for this project, considers the station-keeping status of every satellite in a constellation simultaneously. It implements this approach on a distributed process architecture using the Message Passing Interface (MPI) [27,56] on a network of UNIX workstations. Every satellite operates as its own process on the network and communicates with other satellites in the constellation through a master process known as the “ground station”. Using this architecture, the entire constellation progresses through time as an integrated unit, which shares information and maintains its constellation level mission, while still allowing satellites to individually accomplish the station-keeping task.

Each satellite process looks upon the station-keeping task as a trajectory tracking problem. The *nominal trajectory* is defined as the flight path, in state space, that is associated with totally achieving the mission’s orbital requirements. For a communications constellation, having every satellite perfectly on its respective nominal trajectory implies achieving the optimum coverage and minimum elevation angle design specifications. The six element state space “point” along the nominal trajectory at a specified time is the *nominal state* at that time. The *actual trajectory* is the state space flight path followed by a satellite that also experiences disturbing accelerations not incorporated into the orbit design. The “point” along the actual trajectory at a specified time is the *actual state* at that time. The tracking problem, then, is to maintain the actual

trajectory within a small region of the nominal trajectory. This is analogous to keeping the actual state within the specified state space limits of the nominal state at every time in a time iterated loop. If the time step of the loop is kept small, it is reasonable to assume that the limits will not be violated between successive iteration times. The maximum allowable state deviation from the nominal state is the amount beyond which mission capability is degraded. The deviation in each of the elements is usually determined by the constellation designer.

There are two ways to consider the trajectory tracking problem in the context of a constellation of satellites. The first is simply to treat all the satellites individually. For a constellation, however, the angular spacing requirements between neighboring satellites in a plane, and nodal spacing requirements between orbit planes, cannot be ignored. To assure that these spacing requirements are not violated, the orbital element limits for each satellite must be very strictly defined, particularly in the mean anomaly and ascending node. This method of separately maintaining each satellite within a tight limit of its nominal state is often referred to as absolute station-keeping, or the “box” method. It is similar to the approach used by the GPS constellation and is the method proposed for the Iridium constellation [26].

The second method is to address the relative spacing of the mean anomaly and ascending node, rather than their actual values. This method requires communication across the satellites in a plane and across the planes in a constellation at each time step in the iterated loop. While this may be tedious, it allows all the satellites in the plane to drift in mean anomaly at the same rate and all the planes in the constellation to drift in ascending node at the same rate. With this method, often called relative station-keeping or “formation flying”, there is a potential for significant savings in station-keeping fuel with

no accompanying loss in mission capability. ASKS offers the user a choice of which station-keeping method to use.

Another critical part of the station-keeping problem is what to do when the actual state lies outside the orbital element boundary limits of the nominal state. The approach taken by ASKS is to 1) determine a target state for the next iteration time step, and 2) execute an orbit transfer from the current actual state to the future target state over the intervening time step. The calculation of the target state is determined by the control law being used. Three different control laws are currently incorporated into ASKS. To minimize the amount of station-keeping fuel used for the orbital transfer, an optimal n -impulse transfer is calculated using the principles of Primer Vector theory [32]. In addition to being optimal, the timed series of impulses, called the burnlist, is also accurate enough to insure that the target state will always be achieved.

One of the most important components of ASKS is its orbit propagator. The Draper Semi-Analytic Satellite Theory (DSST) standalone orbit propagator was chosen for this role. This efficient tool has been applied previously to real world flight dynamics applications such as the mission support system of the Canadian Space Agency Radarsat system [15]. DSST is capable of incorporating burnlists, modeling realistic satellite dynamics, including complex perturbations, and producing state rate information. The nominal state is propagated at every iteration time using central body gravitation and only those perturbations that are incorporated into the orbit design. The actual satellite is propagated using all perturbations, and with a burnlist when a transfer trajectory to a target state is required.

The constellation used for all simulation executions is the Ellipso Mobile Satellite System. The simulation test plan for Ellipso was designed to address three goals:

- demonstrate that ASKS produces reasonable lifetime station-keeping estimates
- investigate the advantage of using the “formation flying” approach rather than the “box” approach to constellation station-keeping
- demonstrate that ASKS can be used to analyze constellation orbit designs

A fully functional station-keeping simulation such as ASKS provides an excellent method for accurately estimating lifetime fuel requirements for a constellation of satellites. It can also be used by constellation designers as a tool to determine optimal constellation orbit parameters. The ASKS approach is unique in that it combines an optimal n -impulse rendezvous element to provide automated station-keeping for a constellation of satellites using realistic satellite dynamics calculations on a distributed network of workstations.

1.3 Thesis Overview

The intent of this chapter was to provide an introduction to the constellation station-keeping problem and an explanation of how it will be addressed in this thesis. The remainder of the document includes a description of background theories, proposed ideas, implementation, and analysis involved in developing and executing the station-keeping strategies and simulation.

Chapter 2 is primarily an overview of Primer Vector theory and its application to optimal orbital transfers. It also includes a description of how some parts of the preexisting theory had to be modified to suit the station-keeping transfer problem. Chapter 3 includes a review of the fundamentals of orbit propagation, the development of semi-analytic satellite theory, and a discussion of the specific orbit propagator used in the

simulation. Chapter 4 includes an overview of Lyapunov non-linear control theory. While control laws based upon this theory are not incorporated into the current version of ASKS, several Lyapunov control based strategies are proposed and developed. Chapter 5 provides a description of the software and hardware implementation of the Automated Station-Keeping Simulator (ASKS). Chapter 6 contains a description of the three control methods developed in this project. Chapter 7 includes a description of the simulation executions on the Ellipso constellation and an analysis of the results. And finally, Chapter 8 gives the final conclusions of the project and some ideas for future work related to this topic.

[This page intentionally left blank.]

Chapter 2

Primer Vector Theory

2.1 The Optimal N-Impulse Rendezvous Problem

The time fixed, two point boundary value problem has received much attention in both classical and modern times. Originally, its solution was required to determine the orbital trajectories of planets and comets from observational data. According to Battin [3], Leonhard Euler was the first to address this problem for parabolic orbits. However, he did not pursue the study for elliptical or hyperbolic orbits. Johann Heinrich Lambert is generally accredited with having addressed the problem for general orbits. It was henceforth known as Lambert's problem.

In modern times, a solution to Lambert's problem is essential to calculating rendezvous trajectories for satellite and missile applications. The orbit connecting two position vectors for a fixed time of travel is the solution to Lambert's problem. If the position vectors reside on separate trajectories then the Lambert orbit connecting them is also the two-burn fixed time of rendezvous solution. For modern applications, however, successful rendezvous is not the only criterion. A solution which uses less fuel by allowing the transfer trajectory to contain multiple burns is desired. The problem is that of finding an optimal n-impulse rendezvous trajectory to a target state at a given future time. Other constraints, such as the maximum individual burn magnitude, are also important factors to consider.

An optimal n-impulse rendezvous to a target state is precisely what is required for the Automated Station-Keeping System. The determination of target states and times depends on the method being used. For the simplest method, the future target state will be the nominal state at the next iteration time. More complicated methods will generate target states depending on state rate information, strategies which consider the coupled nature of the orbital elements, and the states of neighboring satellites. Each of the methods, however, requires that the targeted state be achieved to a high degree of precision if continuous control of a satellite is to be maintained.

A broad survey of rendezvous trajectory planning was conducted in 1991 by Jezewski, Brazzel, Prust, Brown, Mulder, and Wissinger [33]. They divide the various approaches into three general categories: primer vector, finite thrust, and cooperative rendezvous. In the current work, the primer vector theory is used to calculate a solution to the optimal n-impulse rendezvous problem. This theory was chosen because it deals with impulsive burns and because it is adaptable to non-linear cases. Its theoretical basis was first laid down by Lawden in the 1950's [38]. While no past use of primer vector theory for station-keeping or orbital repositioning was found, the principles behind it apply to this problem just as well.

A short overview of the basic concepts of primer vector theory is provided next. It is recommended that the reader desiring intimate knowledge of the following derivations consult some of the items listed as references. Following the theory, a short overview of solving Lambert's problem is also provided. Finally, the author's approach to utilizing primer vectors in the calculation of near optimal transfer trajectories is outlined.

2.2 Development of Primer Vectors

The development of primer vector theory can be attributed to many people. Its theoretical basis was first stated by Lawden in the form of necessary conditions which, if met, assure that an impulsive trajectory is optimal [38]. In 1968, Lion and Handelsman developed a method by which one can determine if the addition of an interior impulse to a given impulsive trajectory will decrease the total fuel expenditure [40]. Soon after, Jezewski and Rozendaal [34] developed an efficient method of calculating optimal two-body n -impulse trajectories by applying the Lion and Handelsman work in the framework of a computational search scheme. The result was the development of the Optimal Multi-Impulse Rendezvous (OMIR) software package [32]. Further work on the subject was accomplished by Prussing [47] and a series of his students. They applied primer vector theory for orbital transfers involving path constraints [57], circular orbits [48], cooperative transfers [49], and direct ascent rendezvous [28]. Carter and Brient further improved on primer vector theory by applying it to non-circular Keplerian orbits [9].

Each refinement and addition was significant to primer vector theory, but they all were formed on the basis of two basic assumptions - impulsive burns, and linear or linearized equations of motion. The impulsive burn assumption states that the corrective burns provided by the satellite thrusters can be modeled as near zero duration, high impulse burns. Essentially this allows an instantaneous change in velocity while maintaining continuity in position. This assumption is very good for burns of small magnitude. For actual satellite corrections, it is possible to accurately translate an impulsive burn at a given time into the short duration continuous thrust that would actually occur. Linearized equations of motion result from calculating the dynamics about a known reference trajectory. This assumption is generally good for small deviations from the reference, but can be problematic elsewhere.

For the purposes of this study, a software package similar to the OMIR program was developed for the determination of optimal n-impulse rendezvous solutions as applied to station-keeping. While the impulsive burn assumption is maintained, the requirement for accurately modeling true satellite dynamics means linearization can not be used. The non-linear nature of the problem is dealt with by using the DSST orbit propagator for all dynamics calculations. This inherent non-linearity, and other alterations to the method made to suit the station-keeping problem, mean that the software package created for this application can only claim to provide near optimal solutions. The optimality of the solutions produced by the primer vector code is addressed further in section 2.4.

2.2.1 The Primer Vector

The equations and general flow of the explanation to follow are a summary of primer vector theory as explained in references 32, 34, and 40. However, departures occur from the traditional application of primer vector theory at several points for the purposes of addressing the station-keeping problem in particular. All changes will be noted.

The equations of motion for a satellite are described by

$$\begin{aligned}\dot{\mathbf{R}} &= \mathbf{V} \\ \dot{\mathbf{V}} &= \frac{\beta c}{m} \boldsymbol{\ell} + \mathbf{G} \\ \dot{m} &= -\beta\end{aligned}\tag{2.1a,b,c}$$

where \mathbf{R} is the position vector, \mathbf{V} is the velocity vector, \mathbf{G} is the gravity vector, $\boldsymbol{\ell}$ is the direction cosine vector of the thrust, β is the mass flow rate, c is the characteristic velocity, and m is the mass of the satellite. The constraints on the direction cosine vector and mass flow rate are

$$\begin{aligned}\ell^T \ell &= 1 \\ \beta(\beta_{\max} - \beta) &= \alpha^2 \geq 0\end{aligned}\tag{2.2}$$

where α is a slack variable. A slack variable of $\alpha=0$ implies that the mass flow rate will be zero or maximum. This is the equivalent of a bang-bang controller.

It is desirable to minimize a cost function J using the control variables $\ell(t)$, $\alpha(t)$, and $\beta(t)$ subject to the algebraic (equation 2.2) and differential (equation 2.1) constraints. The Hamiltonian function for this problem is

$$H = \lambda^T \left(\frac{\beta c}{m} \ell + G \right) + \phi^T V - \eta \beta - \mu_1 (\ell^T \ell - 1) - \mu_2 [\beta(\beta_{\max} - \beta) - \alpha^2].\tag{2.3}$$

The vectors λ and ϕ and the scalars μ_1 , μ_2 , and η are time varying Lagrange multipliers. Variational calculus states that the necessary conditions for the trajectory which optimizes the cost function J are

$$\dot{\lambda}^T = -\frac{\partial H}{\partial V} = -\phi^T\tag{2.4a}$$

$$\dot{\phi}^T = -\frac{\partial H}{\partial R} = -\lambda^T \frac{\partial G}{\partial R}\tag{2.4b}$$

$$\dot{\eta} = -\frac{\partial H}{\partial m} = \frac{\beta c}{m^2} \lambda^T \ell\tag{2.4c}$$

$$0 = -\frac{\partial H}{\partial \ell} = -\frac{\beta c}{m} \lambda^T + 2\mu_1 \ell^T\tag{2.4d}$$

$$0 = -\frac{\partial H}{\partial \beta} = -\frac{c}{m} \lambda^T \ell + \eta + \mu_2 (\beta_{\max} - 2\beta)\tag{2.4e}$$

$$0 = -\frac{\partial H}{\partial \alpha} = -2\mu_2 \alpha\tag{2.4f}$$

A good introduction to the use of Hamiltonian functions, variational calculus, and optimal control theory is available in reference 36 by Kirk.

The term primer vector was introduced by Lawden to describe the vector λ . It is the vector whose components are the three Lagrange multipliers related to the velocity vector. It is also a costate vector in the costate equations (equations 2.4a, 2.4b, and 2.4c) for the optimization problem. One of the important properties of the primer vector is evident in equation 2.4d. If there is a burn ($\beta \neq 0$) and it has a distinct direction ($\mu_1 \neq 0$), then the primer vector is parallel with the direction cosine vector of the burn. Furthermore, application of the Weierstrass condition yields

$$\ell = \frac{\lambda}{|\lambda|},$$

or that an optimal burn occurs only when it is aligned with the primer vector. Note that if β is allowed to go to infinity and the duration of the burn is assumed to be zero, then the solution to problem described above is an impulsive burn trajectory.

For another interpretation of the primer vector, consider the case of a coasting arc - a trajectory where there are no intervening burns. Since β is zero for this trajectory, the equations of motion become

$$\begin{aligned}\dot{R} &= V \\ \dot{V} &= G = \nabla U(R, t)\end{aligned}\tag{2.1d,e}$$

where ∇ is the gradient operator and U is the potential in a central force field. If differences are taken about a reference trajectory such that δR represents the difference between the perturbed position R' and the reference position R , then the linearized equations of motion about the reference trajectory are

$$\begin{bmatrix} \delta \dot{R} \\ \delta \dot{V} \end{bmatrix} = F \begin{bmatrix} \delta R \\ \delta V \end{bmatrix} \quad (2.5)$$

where

$$F = \begin{bmatrix} 0 & I \\ \frac{\partial G}{\partial R} & 0 \end{bmatrix}.$$

Here, $\partial G/\partial R$ is the gravity gradient matrix and I is the matrix identity. The system of equations adjoint to equation 2.5 is

$$\begin{bmatrix} \dot{\varphi} \\ \dot{\lambda} \end{bmatrix} = -F^T \begin{bmatrix} \varphi \\ \lambda \end{bmatrix} = \begin{bmatrix} 0 & -\left(\frac{\partial G}{\partial R}\right)^T \\ -I & 0 \end{bmatrix} \begin{bmatrix} \varphi \\ \lambda \end{bmatrix} \quad (2.6)$$

where φ and λ are the vectors adjoint to δR and δV , respectively. Therefore, the primer vector is also the vector adjoint to the velocity difference vector. Note that adjoint equations of motion of equation 2.6 are identical to the costate equations of motion for a coasting arc given by equations 2.4a and 2.4b.

Given that the gravity gradient matrix is symmetric in a central force field, equations 2.5 and 2.6 written in second order form become

$$\begin{aligned} \delta \ddot{R} &= \frac{\partial G}{\partial R} \delta R \\ \ddot{\lambda} &= \left(\frac{\partial G}{\partial R}\right)^T \lambda = \frac{\partial G}{\partial R} \lambda \end{aligned} \quad (2.7)$$

Equation 2.7 states that the primer vector and its derivative are propagated in time using the same equations of motion as are δR and δV . This implies that the state transition matrix, Φ , defined by

$$\begin{bmatrix} \delta R(t) \\ \delta V(t) \end{bmatrix} = \Phi(t, t_o) \begin{bmatrix} \delta R(t_o) \\ \delta V(t_o) \end{bmatrix} \quad (2.8)$$

applies in the same manner to λ and $\dot{\lambda} = -\dot{\phi}$ so that

$$\begin{bmatrix} \lambda(t) \\ \dot{\lambda}(t) \end{bmatrix} = \Phi(t, t_o) \begin{bmatrix} \lambda(t_o) \\ \dot{\lambda}(t_o) \end{bmatrix}. \quad (2.9)$$

Equation 2.9 is important, because the state transition matrix will be the manner by which the primer vector and primer vector rate histories along a coasting arc (non thrusting trajectory) are determined. Another important relation is the adjoint equation.

$$\lambda^T \delta V - \dot{\lambda}^T \delta R = \text{const} \quad (2.10)$$

Since equation 2.10 has the same value along any given coasting arc, it can be used to relate the boundary conditions of that arc. The boundaries of a coasting arc are occasions where impulsive burns occur. If t_o and t_f are the beginning and end times of a coasting arc such that ΔV_o and ΔV_f are the respective impulsive burns at those times, then by definition,

$$\begin{aligned} \lambda(t_o) &= \lambda_o = \frac{\Delta V_o}{|\Delta V_o|} \\ \lambda(t_f) &= \lambda_f = \frac{\Delta V_f}{|\Delta V_f|} \end{aligned} \quad (2.11)$$

2.2.2 Lawden's Necessary Conditions

In 1963, Lawden applied variational calculus to the problem of impulsive rendezvous to derive four conditions which must be met for the rendezvous solution to be optimal [38].

His cost function was the characteristic velocity, or the sum of all the impulses in the solution. These conditions, known today as Lawden's conditions, are

- 1) *The primer vector and its first derivative are continuous everywhere.*
- 2) *Whenever an impulse occurs, the primer vector is aligned with the impulse and has unit magnitude.*
- 3) *The primer vector magnitude must never exceed unity on a coasting arc.*
- 4) *The time derivative of the primer vector magnitude must be zero at all interior junction points separating coasting arcs.*

If t_0 is the initial time, t_f is the final time, and t_i are the times of all interior impulses, then the necessary conditions can be expressed as

$$\begin{aligned}
 \lambda(t^-) &= \lambda(t^+) \quad \text{and} \quad \dot{\lambda}(t^-) = \dot{\lambda}(t^+) \quad , t_0 \leq t \leq t_f \\
 \lambda(t_i) &= \frac{\Delta V_i}{|\Delta V_i|} \quad , \forall t_i \\
 |\lambda(t)| &\leq 1 \quad , t_0 \leq t \leq t_f \\
 |\dot{\lambda}(t_i)| &= 0 \quad , \forall t_i
 \end{aligned} \tag{2.12a-d}$$

where \forall denotes 'for all'. A typical two impulse optimal primer vector magnitude history is displayed in figure 2.1.

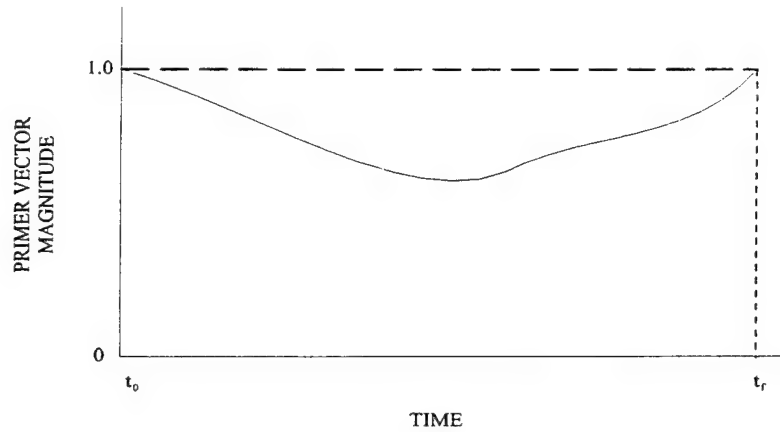


Figure 2.1: Optimal Two-Impulse Primer Vector Magnitude History [34]

If the two impulse trajectory were a non-optimal transfer, then the primer vector history would resemble figure 2.2.

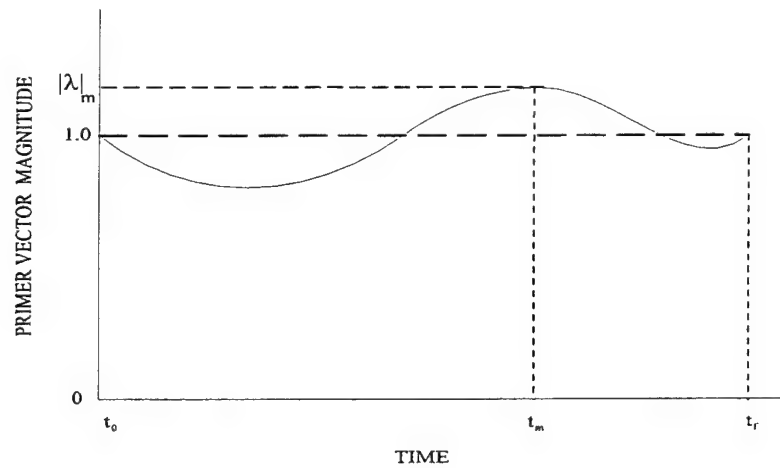


Figure 2.2: Non-Optimal Two-Impulse Primer Vector Magnitude History [34]

Note that the primer vector magnitude exceeds unity along some portion of the arc. It will be shown later that the addition of an impulse of appropriate magnitude at any time at which the primer vector magnitude exceeds unity along a coasting arc will result in a three impulse transfer trajectory with a lower characteristic velocity. The addition of an impulse at time t_m in figure 2.2 could result in the primer vector magnitude history shown

in figure 2.3 if the optimal number of burns for this transfer were three and t_m was the optimal time for the interior impulse.

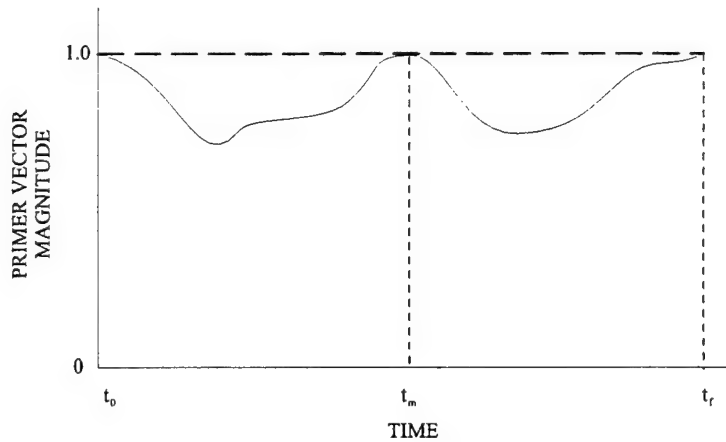


Figure 2.3: Optimal Three-Impulse Primer Vector Magnitude History [34]

Note that if t_m was not the optimal time to add an interior impulse, the resulting characteristic velocity would still be reduced, but not to its minimum value for a three impulse solution. If t_m was not the optimal time to add a third impulse, or if this transfer required more than three burns to be optimal, then the addition of an impulse at t_m could change the primer vector history from that displayed in figure 2.2 to that displayed in figure 2.4.

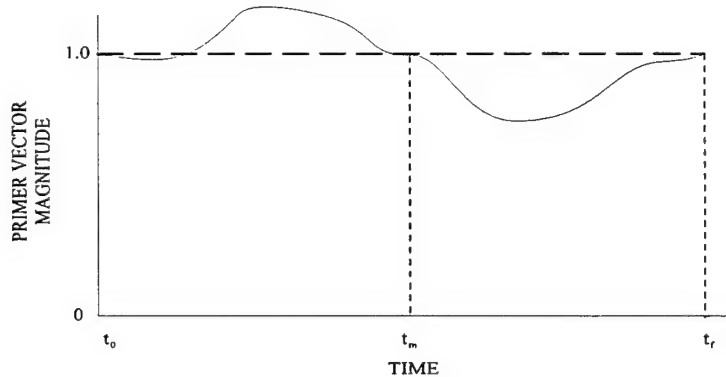


Figure 2.4: Non-Optimal Three-Impulse Primer Vector Magnitude History

The first recourse at this point would be to change the time of the t_m burn until the lowest resulting characteristic velocity is achieved. This would be the optimal three impulse solution, but not the optimal n -impulse solution. If figure 2.4 represented the optimal three impulse solution, then reducing the characteristic velocity further would require another interior impulse. Note that no additional fourth impulse between t_m and t_f can improve this three impulse solution. The fourth impulse should be applied in the region between t_o and t_m where the primer vector magnitude exceeds unity.

Two important procedures dictate the success of the primer vector process. The first is choosing the correct time of an interior impulse. The best choice is the one that results in the maximum decrease in characteristic velocity. The second choice is the magnitude of the interior impulse. It turns out that the two choices are intimately tied to one another.

2.2.3 Improving Transfers With Interior Impulses

To appreciate the addition of an interior impulse to a transfer trajectory between two orbits, consider the following problem. Let $[R_o, V_o]$ and $[R_f, V_f]$ represent the initial and final states of the transfer from initial time t_o to final time t_f . Finding the orbit which connects these two states over the time interval $\Delta t = t_f - t_o$ is the solution to Lambert's problem. If the velocity of the Lambert transfer orbit is V_1 at time t_o and V_2 at time t_f , then the two impulse transfer is defined by figure 2.5.

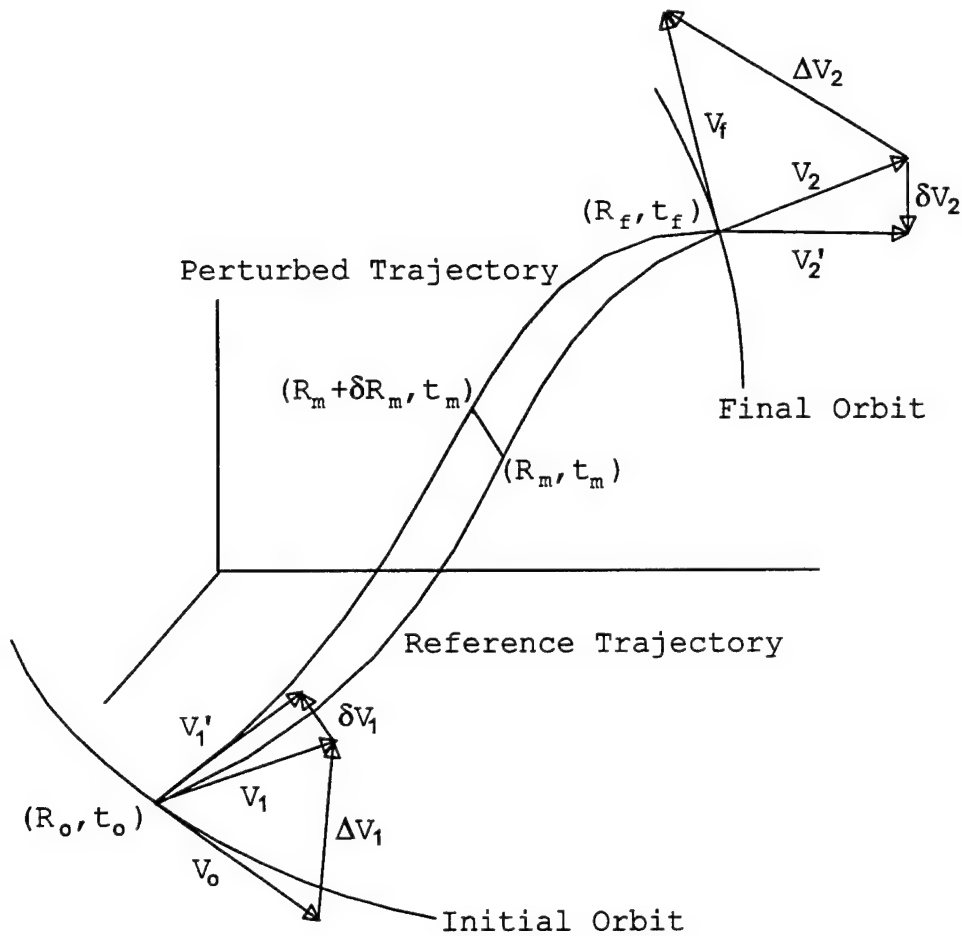


Figure 2.5: Two-Impulse Trajectory Perturbed at t_m [32]

Consider the two impulse Lambert transfer orbit to be the reference trajectory. To improve upon this trajectory with an interior impulse, we must find a perturbed trajectory such that at time t_m , the position vector on the reference trajectory, R_m , is perturbed by an amount δR_m . The existence of an impulse at $R_m + \delta R_m$ implies that there are now two coasting arc trajectories. If Lambert transfer orbits are calculated between the following position vectors on the perturbed trajectory

- 1) $[R_o, t_o] \rightarrow [R_m + \delta R_m, t_m]$
- 2) $[R_m + \delta R_m, t_m] \rightarrow [R_f, t_f]$

then the velocity vectors on the perturbed trajectory differ from those on the reference trajectory by the following amounts:

δV_o at time t_o

δV_m^- at time t_m^-

δV_m^+ at time t_m^+

δV_f at time t_f

First, we attempt to show that the addition of an interior impulse at a time where the magnitude of the primer vector is greater than unity results in a transfer from t_o to t_f with a reduced characteristic velocity. The cost of the reference and perturbed trajectory, respectively, are

$$J = |\Delta V_o| + |\Delta V_f| \quad (2.13)$$

$$J' = |\Delta V_o + \delta V_o| + |\delta V_m^+ - \delta V_m^-| + |\Delta V_f - \delta V_f|. \quad (2.14)$$

The cost increment of adding an interior impulse is

$$dJ = J' - J \quad (2.15)$$

At this point, Jezewski subtracts equation 2.13 from 2.14 and expands the result into an infinite series. If we assume that

$$\begin{aligned} |\delta V_o| &<< |\Delta V_o| \quad \text{and} \\ |\delta V_f| &<< |\Delta V_f| \end{aligned} \quad (2.16a,b)$$

then we can ignore higher order terms and show that to first order

$$dJ = \frac{\Delta V_o^T \delta V_o}{|\Delta V_o|} + |\delta V_m^+ - \delta V_m^-| - \frac{\Delta V_f^T \delta V_f}{|\Delta V_f|} \quad (2.17)$$

or

$$dJ = \lambda_o^T \delta V_o + |\delta V_m^+ - \delta V_m^-| - \lambda_f^T \delta V_f \quad (2.18)$$

Recall the adjoint equation (equation 2.10). If it is applied over the two coasting arcs of the perturbed trajectory, we have

$$\begin{aligned} \lambda_o^T \delta V_o - \dot{\lambda}_o^T \delta R_o &= (\lambda_m^-)^T \delta V_m^- - (\dot{\lambda}_m^-)^T \delta R_m^- \\ (\lambda_m^+)^T \delta V_m^+ - (\dot{\lambda}_m^+)^T \delta R_m^+ &= \lambda_f^T \delta V_f - \dot{\lambda}_f^T \delta R_f \end{aligned} \quad (2.19a,b)$$

Recognizing that since λ and $\dot{\lambda}$ are evaluated on the reference trajectory yields

$$\begin{aligned} \lambda_m^+ &= \lambda_m^- = \lambda_m \quad \text{and} \\ \dot{\lambda}_m^+ &= \dot{\lambda}_m^- = \dot{\lambda}_m \end{aligned} \quad (2.20)$$

Requiring continuity in position,

$$\begin{aligned} \delta R_o &= 0 \\ \delta R_f &= 0 \\ \delta R_m^+ &= \delta R_m^- \end{aligned} \quad (2.21)$$

and substituting equations 2.19a and 2.19b into equation 2.18, we obtain

$$dJ = |\delta V_m^+ - \delta V_m^-| - \lambda_m^T (\delta V_m^+ - \delta V_m^-) \quad (2.22)$$

If c and the unit vector i_c are defined as

$$c = |\delta V_m^+ - \delta V_m^-| \quad \text{and} \quad (2.23a,b)$$

$$i_c = \frac{\delta V_m^+ - \delta V_m^-}{c}$$

they can be interpreted as the magnitude and direction of an impulse at time t_m . Substituting into equation 2.22, the cost increment becomes

$$dJ = c (1 - \lambda_m^T i_c) \quad (2.24)$$

Equation 2.24 shows that to first order, if the magnitude of the primer vector at time t_m is greater than one, then the cost increment can be made negative with the addition of an interior impulse. This in turn implies that the resulting three burn trajectory will have a lower characteristic velocity while still achieving the terminal state in the same amount of time. In addition, we can also state that to first order, the best improvement in cost is achieved by applying the interior impulse in the direction of λ_m , at the time where $|\lambda_m|$ is a maximum.

Having obtained a good approximation for the time of an additional impulse, the next step is to determine what the magnitude of that impulse should be. At first glance, equation 2.24 suggests that if i_c is parallel to λ_m , then a larger value for c decreases cost the most. Large values for c , however, invalidate the first order assumption made in obtaining equation 2.17. We must determine c using another method. In pursuit of this goal, we begin by first developing a relation between the interior impulse magnitude, c , and the difference in position from the reference trajectory at the time of the impulse, δR_m .

Applying the state transition matrix relation first seen in equation 2.8 across the two arcs of the perturbed trajectory, we obtain

$$\begin{aligned} \begin{bmatrix} \delta R_m^- \\ \delta V_m^- \end{bmatrix} &= \Phi(t_m, t_o) \begin{bmatrix} \delta R_o \\ \delta V_o \end{bmatrix} \\ \begin{bmatrix} \delta R_m^+ \\ \delta V_m^+ \end{bmatrix} &= \Phi(t_m, t_f) \begin{bmatrix} \delta R_f \\ \delta V_f \end{bmatrix} \end{aligned} \quad (2.25a,b)$$

Note that these state transition matrices can be partitioned into four constituent matrices such that

$$\Phi(t, \tau) = \begin{bmatrix} \varphi_{11}(t, \tau) & \varphi_{12}(t, \tau) \\ \varphi_{21}(t, \tau) & \varphi_{22}(t, \tau) \end{bmatrix} \quad (2.26)$$

Applying equation 2.26 to equations 2.25a and 2.25b and using the continuity relations in equation 2.21, it can be shown that if $\varphi_{12}^{-1}(t_m, t_o)$ and $\varphi_{12}^{-1}(t_m, t_f)$ exist, then

$$\begin{aligned} \delta V_m^- &= \varphi_{22}(t_m, t_o) \varphi_{12}^{-1}(t_m, t_o) \delta R_m \quad \text{and} \\ \delta V_m^+ &= \varphi_{22}(t_m, t_f) \varphi_{12}^{-1}(t_m, t_f) \delta R_m \end{aligned} \quad (2.27a,b)$$

Subtracting equation 2.27a from 2.27b and applying the definitions of c and i_c from equation 2.23, we have that

$$c \cdot i_c = \delta V_m^+ - \delta V_m^- = A \delta R_m \quad (2.28)$$

where

$$A = \varphi_{22}(t_m, t_f) \varphi_{12}^{-1}(t_m, t_f) - \varphi_{22}(t_m, t_o) \varphi_{12}^{-1}(t_m, t_o) \quad (2.29)$$

If the interior impulse is applied in the direction of λ_m then

$$\delta R_m = c A^{-1} i_c = c A^{-1} \frac{\lambda_m}{|\lambda_m|} \quad (2.30)$$

Having resolved a relation between c and δR_m , we now consider the cost increment directly to determine a good value for c . From our previous discussion of costs, we have that the cost increment is defined by

$$dJ = |\Delta V_o + \delta V_o| - |\Delta V_o| + |\Delta V_f - \delta V_f| - |\Delta V_f| + c \quad (2.31)$$

To help determine c , Jezewski uses the same expansion for equation 2.31 as was used to obtain equation 2.17, except that this time second order terms are retained as well. However, this method still relies on the assumptions in equation 2.16a and 2.16b. These assumptions are good for most cases, particularly for large orbital transfers, but they do not suffice for some basic station-keeping cases. For example, if the only difference between the initial and final states is a small change in inclination, then the addition of an interior impulse at a nodal crossing can entirely negate the initial and final burns. In this case, δV_o and ΔV_o will be of equal magnitude and opposite direction. An alternate form of the cost increment, which does not rely on assumptions 2.16a and 2.16b, was developed for the station-keeping transfer calculation. It is

$$dJ = |\Delta V_o| \sqrt{1 + 2 \frac{\delta V_o^T \Delta V_o}{|\Delta V_o|^2} + \frac{\delta V_o^T \delta V_o}{|\Delta V_o|^2}} + |\Delta V_f| \sqrt{1 + 2 \frac{\delta V_f^T \Delta V_f}{|\Delta V_f|^2} + \frac{\delta V_f^T \delta V_f}{|\Delta V_f|^2}} + c - |\Delta V_o| - |\Delta V_f| \quad (2.32)$$

Note that equation 2.30 and equations 2.25a and 2.25b yield

$$\begin{aligned} \delta V_o &= \varphi_{12}^{-1}(t_m, t_o) \delta R_m = c \alpha \quad \text{and} \\ \delta V_f &= \varphi_{12}^{-1}(t_m, t_f) \delta R_m = c \beta \end{aligned} \quad (2.33a,b)$$

where

$$\begin{aligned}\alpha &= \varphi_{12}^{-1}(t_m, t_o) A^{-1} \frac{\lambda_m}{|\lambda_m|} \quad \text{and} \\ \beta &= \varphi_{12}^{-1}(t_m, t_f) A^{-1} \frac{\lambda_m}{|\lambda_m|}\end{aligned}\tag{2.34a,b}$$

Substituting for δV_o and δV_f , equation 2.32 becomes

$$dJ = |\Delta V_o| \sqrt{1 + 2c \frac{\alpha^T \Delta V_o}{|\Delta V_o|^2} + c^2 \frac{\alpha^T \alpha}{|\Delta V_o|^2}} + |\Delta V_f| \sqrt{1 + 2c \frac{\beta^T \Delta V_f}{|\Delta V_f|^2} + c^2 \frac{\beta^T \beta}{|\Delta V_f|^2}} + c - |\Delta V_o| - |\Delta V_f|\tag{2.35}$$

The best improvement in cost occurs for the value of c at which

$$\frac{\partial dJ}{\partial c} = \frac{(2c q_f + p_f) r_f}{2\sqrt{c^2 q_f + c p_f + 1}} + \frac{(2c q_o + p_o) r_o}{2\sqrt{c^2 q_o + c p_o + 1}} + 1 = 0\tag{2.36}$$

where

$$\begin{aligned}p_o &= 2 \frac{\alpha^T \Delta V_o}{|\Delta V_o|^2} \\ p_f &= -2 \frac{\beta^T \Delta V_f}{|\Delta V_f|^2} \\ q_o &= \frac{\alpha^T \alpha}{|\Delta V_o|^2} \\ q_f &= \frac{\beta^T \beta}{|\Delta V_f|^2} \\ r_o &= |\Delta V_o| \\ r_f &= |\Delta V_f|\end{aligned}\tag{2.37}$$

Note that the appropriate c can be determined from the Jezewski's 2nd order equivalent of equation 2.36 analytically. Evaluating equation 2.36, however, requires a numerical search scheme. The function itself is rather complicated with quick rises followed by long plateaus. However, the authors experience using this method is that the solution for c exists and is unique when $|\lambda_m| > 1$.

2.2.4 Optimizing The Trajectory

In the preceding sections good estimates for the time, magnitude, and direction of an interior impulse were determined. A three impulse trajectory resulting from the addition of such an impulse will have a continuous primer vector magnitude trajectory where the magnitude is unity at the times of the impulses and less than one elsewhere. However, this does not necessarily imply that this three impulse solution is optimal. Note that all of Lawden's conditions have to be met to insure optimality. In particular, at this point, the continuity and value of the primer vector rate at burn times may not meet Lawden's conditions. Such a situation would result in the primer vector magnitude history having a cusp at the interior impulse point. This is illustrated in figure 2.6

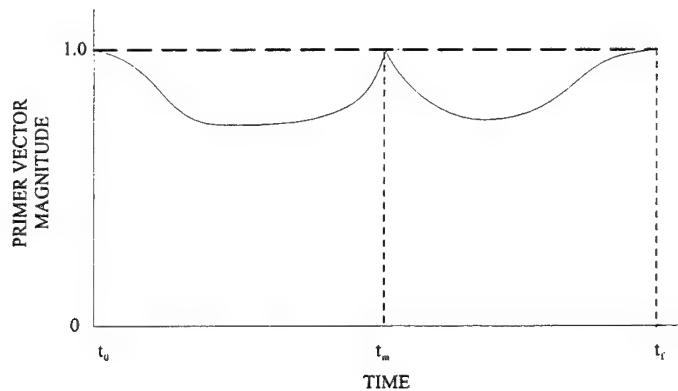


Figure 2.6: Non-Optimal Three-Impulse Trajectory with Cusp at t_m [32]

To resolve this problem, Jezewski defines the non-optimal three impulse trajectory as the reference and attempts to find a variation of it that meets Lawden's conditions. The independent variables in the variation are t_m and δR_m [32]. Jezewski uses a first order determination of the cost increment to create a gradient vector on the cost function. Using gradient vector information, a numerical search scheme quickly determines the optimal combination of t_m and δR_m .

The use of a first order cost increment to determine the gradient does not work for the station-keeping problem. Analysis of cost functions from test cases show that they do not resemble near quadratic functions. Gradient search methods work best for quadratic functions because they can search for only local minima. The station-keeping functions are very sensitive to any changes in the components of δR_m . Even very small deviations in the components of δR_m results in large increases in the cost function. This sensitivity results in cost "walls" around good solutions, thus preventing improvement of the initial guess with the use of a gradient. Since the global minimum is isolated, a gradient search scheme using Jezewski's gradient determination does not alter the non-optimal because it can not direct the search away from the local minimum.

A multivariable search over a large search space for a function with isolated minima where no gradient information is available requires a search scheme such as a genetic algorithm. However, implementation of a genetic algorithm also requires more computing capability and computing time than is feasible for this project. The author decided to adopt another approach which results in near-optimal solutions determined over reasonable time periods.

The solution is to reduce the search from four variables for every interior impulse to one. The time of the interior impulse remains the only independent variable in the search. The

cost function on only the time variable proves to be smooth and near quadratic. However, the possibility for a handful of minima still exists. To deal with this situation, a better method of choosing the initial guess for the search is also developed. This approach allows the use of a conventional non-gradient search scheme. The author choose to use the classical Powell's Method [45].

To reduce the number of search variables from the original four to only the time of the interior impulse, a method for determining the unique, best solution for the perturbed position, given the interior time, is required. To try to maintain near-optimality, as many assumptions as possible need to be removed in the determination of the interior impulse itself.

We begin by developing a better method for determining an initial estimate for the interior impulse time. Equation 2.24, restated as equation 2.38, shows that, to first order, adding an interior impulse at the time associated with the maximum value of $|\lambda_m|$ results in the greatest decrease in the cost.

$$dJ = c \left(1 - \lambda_m^T i_c \right) \quad (2.38)$$

It is desirable to remove this first order dependence. This is done by creating a discretized time grid between the initial and final times, and then evaluating what the cost increment of adding an interior impulse at each of these times is. Instead of letting t_m be the time of $|\lambda|_{\max}$ occurrence, we assign t_m as the time of $|J+dJ|_{\min}$ occurrence. In a situation where there are multiple cost wells, this approach tends to find the correct one to pursue optimization on if the time period is discretized sufficiently.

Equation 2.24 also states that to first order, an interior impulse should be added in the direction of λ_m . Jezewski relies on the multivariable optimization process to correct this

initial choice of direction to the optimal direction. For our problem, however, analysis shows that the accurate determination of c , the magnitude of the interior impulse, is more important once a good estimate of the direction is known. Because of this, no change is made and the direction of the interior impulse is left to be the direction of λ_m .

This leaves the determination of an accurate value of c . Recall that Jezewski uses a second order approximation of the cost increment to calculate an initial estimate for c . Once again, he relies on the multivariable search scheme to converge to the optimal value of c . For our determination of c we use equations 2.35, 2.36, and 2.37. No truncation of higher order terms are required because no series expansion takes place. Therefore, Jezewski's assumptions are no longer applicable. Note that we are calculating the optimal magnitude of the interior impulse for a given time and direction.

All that remains is to determine δR_m , the perturbed position at time t_m . For this we recall equation 2.30. It is restated as equation 2.39 below.

$$\delta R_m = c A^{-1} i_c = c A^{-1} \frac{\lambda_m}{|\lambda_m|} \quad (2.39)$$

Having already accepted i_c to be in the direction of λ_m , we now have a method of calculating a unique δR_m for a given t_m . This link leaves us free to execute a non-gradient search on only time for the minimum cost of a three impulse trajectory.

The major difference which removes us from true optimality is the use of the first order assumption in accepting the direction of the interior impulse to be the direction of the primer vector on the reference trajectory at the time of the interior impulse. However, this assumption, made only once in this approach, allows the use of a much simpler search scheme which can compute a near-optimal trajectory much quicker than a full

fledged general multivariable search. One future area of research is to obtain a more complicated form of equation 2.24/2.38 which results from the cost increment displayed in equation 2.32, where no first order truncation is made, rather than Jezewski's first order cost increment of equation 2.17.

The other contributor to near-optimality is the non-linear nature of the application. One of the project goals is to incorporate accurate satellite dynamics. The Draper SST, the orbit propagator used for prediction, gives us this capability, but it also preserves the non-linearity of the dynamics. Therefore, primer vector theory can provide optimal solutions only as well as its linearized equations model the non-linear nature of the dynamics. Since the accuracy of the linearized equations is reduced in the presence of satellite perturbations, so is the ability of primer vector theory to produce true optimal solutions.

One of the consequences of near-optimality is that more than the optimal number of interior impulses are required to bring the entire primer vector magnitude to a value less than or equal to one. While the burnlist generated from this approach may not be ideal for actual satellites to execute, it does provide total burn magnitudes which are surprisingly close to the optimal solutions. Section 2.4 contains examples which demonstrate how close the computed solutions are to the theoretical optimal.

2.3 Lambert's Problem

The problem of finding the time fixed transfer orbit connecting two positions in space is known as Lambert's problem. In his book, *An Introduction to the Mathematics and Methods of Astrodynamics*, Battin devotes an entire chapter to the development of different solutions to Lambert's problem [3]. The following section borrows heavily

from Battin's discussion. In fact, the method chosen by the author to solve Lambert's problem is Gauss' Method modified by Battin to assure rapid convergence and eliminate singularities.

Lambert recognized that the transfer orbit was dependent on only one orbital element. His findings are summarized in the well known Lambert's Theorem:

The orbital transfer time depends only upon the semi-major axis, the sum of the distances of the initial and final points of the arc from the center of force, and the length of the chord joining these points.

In formula notation, Lambert's theorem is equivalent to equation 2.40

$$\sqrt{\mu}(t_2 - t_1) = F(a, r_1 + r_2, c) \quad (2.40)$$

where a is the semi-major axis, r_1 and r_2 are the respective distances of the body from the central force, and c is the chord. The transfer problem is displayed in figure 2.7.

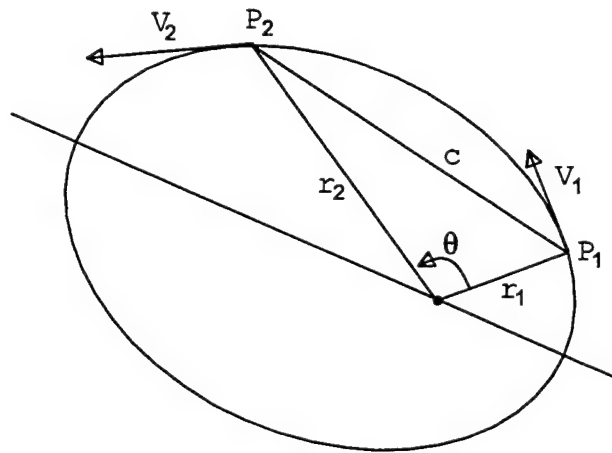


Figure 2.7: Lambert Problem Illustration

The quantity θ is the transfer angle between the two radii. If we let s be the semiperimeter of the r_1, r_2, c triangle and a_m be the semi-major axis of the minimum energy orbit connecting r_1 and r_2 then

$$s = \frac{1}{2}a_m = r_1 + r_2 + c \quad (2.41)$$

Lagrange's form of the time transfer equation is

$$\sqrt{\mu}(t_2 - t_1) = a^{\frac{3}{2}}[(\alpha - \sin \alpha) - (\beta - \sin \beta)] \quad (2.42)$$

where

$$\begin{aligned} \alpha &= \phi + \psi & \beta &= \phi - \psi \\ \psi &= \frac{1}{2}(E_2 - E_1) \\ \cos \phi &= e \cos \frac{1}{2}(E_2 + E_1) \end{aligned} \quad (2.43)$$

E_1 and E_2 are the eccentric anomalies at t_1 and t_2 , respectively.

The biggest drawbacks of equation 2.42 are: 1) the transfer time is a double valued function of the semi-major axis, and 2) there is a singularity at $\theta=180^\circ$. The double valued nature of the function can result in two solutions for Lambert problem, only one of which is correct for our application. Jezewski faces this problem in his solutions of Lambert's problem [34]. He conducts decisions on which one of the two solutions to pursue at each step. Battin solves this problem by substituting for a , a new variable x such that

$$x = \cos \frac{1}{2}\alpha \quad \text{and} \quad x^2 = 1 - \frac{a_m}{a} \quad (2.44)$$

Note that the range of x for elliptic orbits is $-1 < x < 1$. x is negative valued when the transfer time is greater than half the period of the transfer orbit, and positive valued elsewhere.

Battin continues his analysis of Lambert's problem by discussing Gauss' Method. The transfer time equation for Gauss' Method is

$$\sqrt{\mu}(t_2 - t_1) = a^{\frac{3}{2}}(2\psi - \sin 2\psi) + 2\lambda s a^{\frac{1}{2}} \sin \psi \quad (2.45)$$

where

$$\lambda s = \sqrt{r_1 r_2} \cos \frac{1}{2} \theta \quad (2.46)$$

It can be applied simply in an iterative convergence scheme to calculate an orbital solution. However, Gauss' Method also suffers from a singularity at $\theta = 180^\circ$ and is slow to converge to a solution.

To produce a method which is rapidly convergent and immune to any singularities, Battin combines aspects of Gauss' and Lagrange's approaches to develop a third, better method. It is based on the invariance of the mean point and the introduction of a free parameter in Kepler's equation. The result is the Improved Gauss Method. This method is outlined in section 7.5 of reference 3. It rapidly produces the semi-major axis and eccentricity of the transfer orbit given two radial vectors and the transfer time between them.

The last step in the solution of Lambert's problem as related to trajectories is to calculate the velocity vectors at the two endpoints. Once again, Battin has a clean and compact formulation.

$$\begin{aligned}
V_1 &= \sqrt{\frac{\mu}{a_m}} \left[-x(i_1 \cdot i_{r1})i_1 + y\sqrt{\frac{r_2}{r_1}}(i_2 \cdot i_{r2})j_1 \right] \\
V_2 &= \sqrt{\frac{\mu}{a_m}} \left[x(i_2 \cdot i_{r2})i_2 + y\sqrt{\frac{r_1}{r_2}}(i_1 \cdot i_{r1})j_2 \right]
\end{aligned} \tag{2.47}$$

where j_1 and j_2 are the directions of the minimum energy orbit velocity vectors at the initial and final points, and i_1 and i_2 are unit vectors which form the coordinate pairs i_1, j_1 and i_2, j_2 . Finally, y is a positive valued quantity defined by

$$y = \sqrt{1 - \left(\frac{s-c}{s} \right)^2 (1-x^2)} \tag{2.48}$$

Since the velocity vectors defined by equation 2.47 are formed from a geometric interpretation, they face a problem in the small neighborhood around $\theta=180^\circ$. Since the two input position vectors are nearly parallel at that point, determination of the transfer orbit plane becomes problematic. This can be solved by adapting the plane of the either the input or exit state to be the transfer orbit plane.

The solutions to Lambert's problem discussed so far are all effective, but they are also all two-body solutions. A two burn solution to the two-body Lambert problem will significantly miss the target state if the satellite is propagated incorporating perturbations such as non-spherical gravity, drag, solar radiation pressure and lunar/solar point masses. To obtain a Lambert solution in the presence of perturbations, Battin describes a method of iteratively correcting the two-body solution to fit a full perturbation model. The solution is guaranteed to hit the target state of the transfer to the same precision of the tolerance in the convergence algorithm.

One of the important drawbacks of the Lambert methods described above is that they are limited to solutions where the transfer trajectory cannot be greater than one orbital period.

A method exists for multiple revolution transfer orbits, but unfortunately the number of solutions increases with the number of revolutions allowed. To avoid the confusion of having to choose from multiple Lambert trajectories, multiple revolution transfers are not considered in this application. The limitation caused by this decision is that the iteration time step of the control loop cannot be greater than one orbital period of the satellite. Note that this decision does not constrain the time step of the integrator in the orbit propagator in any way.

The Improved Gauss Method of solving Lambert's problem, and the iterative convergence algorithm to correct for errors induced by perturbations, were both coded for this project. The combined utility proved to be quick, reliable, and quite useful for applications other than its originally intended use.

2.4 Near Optimal N-Impulse Rendezvous

This section outlines the use of primer vectors in the context of the software package created to calculate near-optimal n-impulse trajectories for the purpose of station-keeping. The goal of the primer vector software is to calculate an n-impulse burnlist that will transfer the initial state to a targeted final state in the defined transfer time. The maximum number of impulses allowed for each transfer is an input parameter. A burnlist is a time history, from the initial to the final time, of the magnitude and direction of all burns needed for the transfer.

For the software to be useful, it has to meet two targeting criteria. These criteria were developed after a preliminary round of test runs of the nascent code failed to hit the intended target altogether. The criteria set a standard which helped focus the effort to

improve the methods and code. All elements of the project documented in this thesis represent the furthest refinement to date. The first criterion is that the final state must be achieved to a level of precision at least two orders of magnitude better than the orbital parameter limits of the satellite. For example, if the satellite limit on semi-major axis deviation from the nominal trajectory is 1 km, then the software must assure that the actual semi-major axis achieved after applying the indicated burnlist is at most only 10 m off of the target state semi-major axis. The second criterion is that the cost of the burns in the calculated burnlist must be within 25% of the idealized optimal burnlist. The first requirement is checked by simply differencing the actual achieved final state from the targeted final state. The second requirement, however, is difficult to gauge because the idealized optimal transfer cost is not always calculable, particularly when more than one orbital element is targeted in the presence of multiple perturbations.

A flowchart which illustrates the process of calculating the burnlist is shown in figure 2.8. The process begins with the two impulse trajectory determined by solving for the Lambert orbit from the initial to the target position vector. Since the two burn times are specified and fixed, this solution is likely to be a very expensive transfer in terms of characteristic velocity. This is because the location of the burn in the orbit has a significant impact on the magnitude of the burn required to achieve the transfer. For example, an inclination correction is usually executed at a nodal crossing while semi-major axis and eccentricity are usually corrected with burns at apogee and perigee. Inclination, semi-major axis and eccentricity corrections can be accomplished with burns elsewhere in the orbit, but at the expense of valuable on board station-keeping fuel.

To improve on the two impulse solution, the addition of an interior burn is considered. First the primer vector magnitude history from the initial to the final time is determined. Interior burns will only result in an improvement in the total cost if the primer vector

magnitude ($|\lambda|$) is greater than unity at the time of the interior burn. To determine the best time for the addition of the interior burn, a cost analysis is made at each of the time grid points eligible for an additional burn, instead of simply

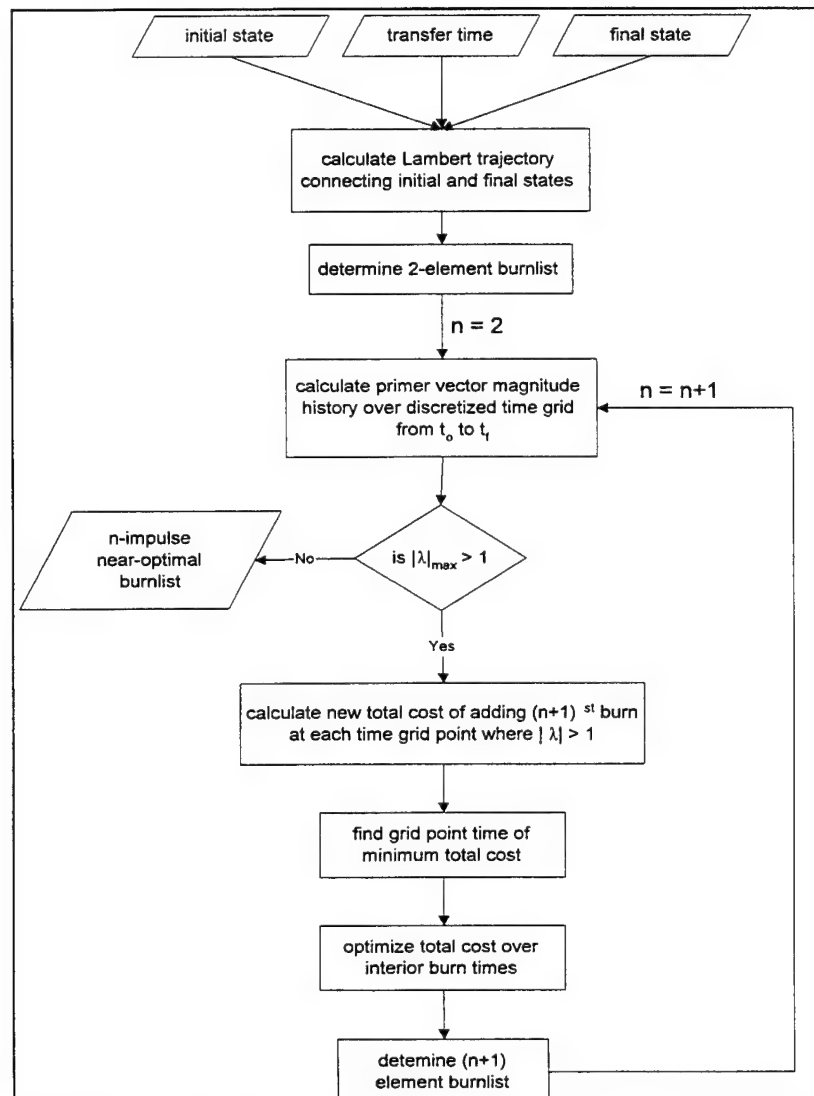


Figure 2.8: Primer Vector Process Flowchart

choosing the time at which $|\lambda|$ has its largest value greater than one. A test point is eligible for a burn only if $|\lambda| > 1$ at that time grid point. At each test point the software calculates an estimate of the new characteristic velocity of a three impulse trajectory such

that the interior burn is at that test point. The test point which results in the minimum new total characteristic velocity is chosen as the initial time estimate for addition of the interior impulsive burn.

Since the initial time estimate comes from a discretized grid, and because there is the possibility of cusps in the new primer vector magnitude history, an optimization algorithm must be run to find the optimal time for adding the interior impulse. The optimization algorithm is really a function minimization algorithm since “optimality” is determined purely by minimizing the characteristic velocity on time and not by meeting Lawden’s conditions. For this reason, only near-optimality can be achieved. The function minimization algorithm used is Powell’s method.

After calculating the optimal time for addition of the interior impulse, the primer vector history over the new three impulse trajectory is calculated. If $|\lambda|$ is less than unity across the entire time span of the transfer trajectory, then no additional interior impulses will reduce the characteristic velocity further, and the process is complete. If $|\lambda| > 1$ for any section of the trajectory, then further reduction in cost is possible and the process is repeated with the addition of a second interior impulse. Note that Powell’s method will find the minimum characteristic velocity by varying all interior burn times. Therefore, it is a multivariable search if more than one interior impulse is required.

Repetition of this loop in figure 2.8 results in a near-optimal n-impulse burnlist.

Several controlled test cases were executed to determine how well the primer vector code operates. Only one of the cases is described in detail below, but some general discussion about the others is provided.

For station-keeping, and orbital re-positioning in general, some of the most expensive burns are those which correct inclination. Therefore, it is important for the primer vector code to work in a case that involves a pure inclination change. Special consideration must be taken in setting up a test case because of the existence of perturbations such as zonal harmonics, tesseral harmonics, atmospheric drag, lunar/solar effects, and solar radiation pressure. We begin with an element set which describes an elliptic orbit inclined 5.00° with the satellite at the ascending node. This element set is propagated back in time for 15% of its orbital period to produce the initial state. Then the same element set, except this time with an inclination of 5.01° degrees, is propagated forward in time 35% of the orbital period to produce the target state. Therefore we have a station-keeping problem which requires that the inclination of an orbit be changed by 0.01° within the span of 50% of the orbital period. The initial state and target state are listed in table 2.1.

Table 2.1: Inclination Test Case Initial and Target States

	Initial State	Target State
SMA	10000.000 km	10000.000 km
ECC	0.200000	0.200000
INC	5.00017°	5.00960°
LAN	0.03849°	359.91018°
AP	269.92332°	270.17892°
MA	35.96255°	216.08737°

The transfer time for the problem is 4976.002 seconds, or half of the period. Note that the element sets are not idealized because of the effects of perturbations. Since the case is run with realistic perturbations turned on, idealized element sets cause the primer vector

software to actual simulate the effects of the perturbations with burns, thus skewing the total characteristic velocity.

The ascending node crossing occurs 1492.801 seconds into the orbit. This is about the time we expect an interior burn to occur. If this were a 2-body case with no perturbations, then a ΔV of 0.0011469 km/sec accomplishes a 0.01° degree plane change at the ascending node of this orbit. However, the initial and final inclinations expressed in table 2.1 suggest a plane change of only 0.009434° . This translates into an ideal ΔV of 0.0010819 km/sec for a 2-body orbit. As stated before, it is difficult to pin down exactly what the “optimal” transfer for trajectories in the presence of significant perturbations. The difference between the two versions of “ideal” is fairly significant. Therefore, we expect a ΔV solution from the primer vector code which is roughly within 25% of approximately 0.001100 km/sec.

The first step is to calculate the two-impulse transfer determined from the orbit connecting the initial and final positions. The burnlist for this clearly non-optimal two-impulse transfer is listed in table 2.2.

Table 2.2: Non-Optimal Two-Impulse Burnlist

Burn	Time (sec)	ΔV_x (km/sec)	ΔV_y (km/sec)	ΔV_z (km/sec)	$ \Delta V $ (km/sec)
1	0.000	-0.000001	-0.000217	0.002476	0.002485
2	4976.002	-0.000000	-0.000107	0.001216	0.001220
Total					0.003705

Analysis of the primer vector and cost of adding an additional burn is done next. Figure 2.9 contains plots summarizing this analysis. The first plot is of the primer vector magnitude on the discretized time grid of the trajectory. By definition, $|\lambda|$ is equal to one

at the terminal points, where burns occur. The maximum value of $|\lambda|$ on the coasting arc is 4.7302 and occurs at $t = 2261.819$ seconds. The second plot is of the cost, or characteristic velocity, resulting from the addition of the interior impulse at the respective time grid point. The minimum cost is 0.0011321 km/sec and occurs when an interior impulse is added at $t = 904.738$ seconds. This clearly demonstrates that the first order relation (equation 2.24/2.38) stating that the largest reduction in cost occurs by adding the interior burn at the time of $|\lambda|_{\max}$ is not accurate.

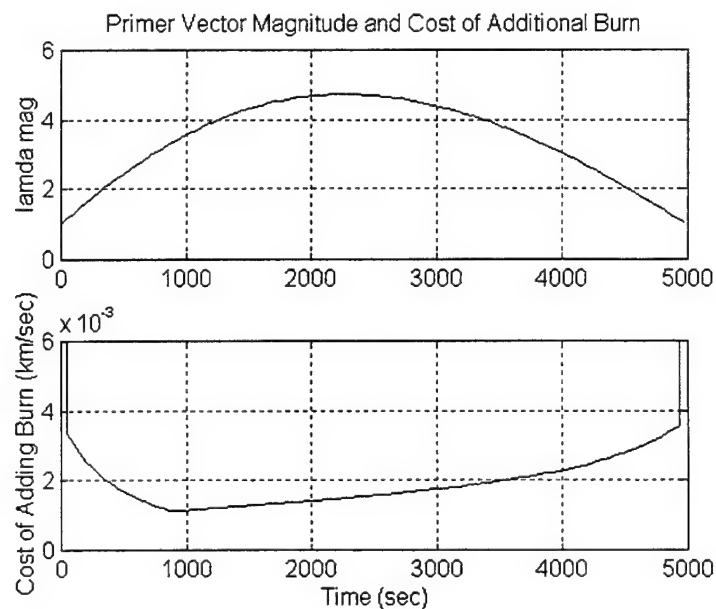


Figure 2.9: Primer Vector Magnitude and Total Resulting Cost of Adding An Interior Impulse on Non-Optimal Two-Impulse Trajectory Discretized Time Grid

The three-impulse trajectory resulting from adding an interior impulse at 904.738 seconds is not optimal. This is because the time was determined from a time grid rather than allowing for any time on the time line. To make the interior burn time optimal, Powell's method is applied with the characteristic velocity as the function and the interior burn time as the variable. Figure 2.10 contains the plots for the non-optimal and optimal primer vector magnitude and primer vector rate magnitude.

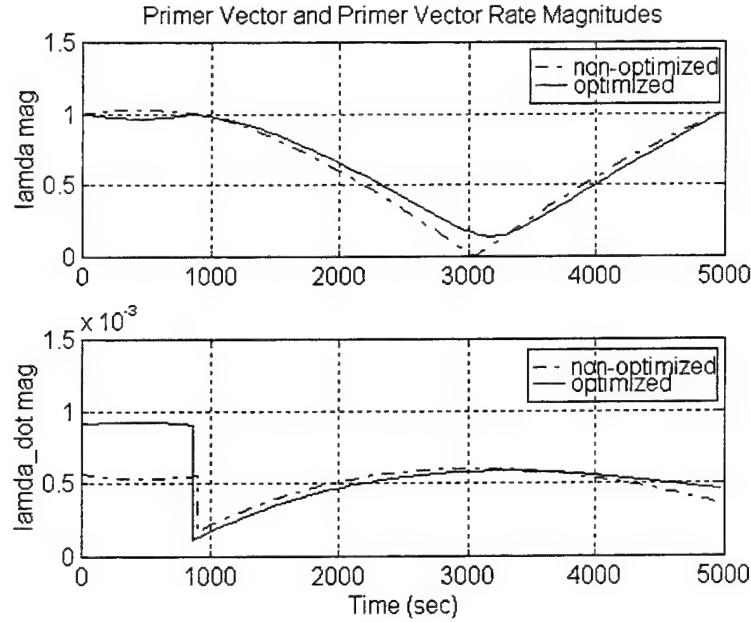


Figure 2.10: Primer Vector Magnitude and Primer Vector Rate Magnitude for Three-Impulse Trajectories

The interior impulse time for the optimal trajectory is $t = 865.790$ seconds. Note that the non-optimal $|\lambda|$ history has a section which is greater than one. However, optimization results in $|\lambda|$ history which does not have any value greater than one. Note also that the $|\dot{\lambda}|$ history for the “optimal” trajectory has a discontinuity. While the optimal time to add an interior impulse has been found, not all of Lawden’s conditions have been met. Since no more interior impulses can be added and since any change in the interior burn time will increase the total characteristic velocity, we are forced to accept this “near-optimal” solution. The burnlist for the “optimal” three-impulse trajectory is listed in table 2.3.

The burns at the initial and final times have both become zero as expected. However, the interior burn does not occur at the ascending node ($t_{AN} = 1492.801$ sec), as expected for a 2-body only orbit. The orbital element variations caused by perturbations account for this effect. As stated previously, the ideal 0.01° inclination correction for a 2-body only

situation is approximately 0.0011 km/sec. The 0.001125 km/sec transfer trajectory calculated by the primer vector code is only 2.27% greater than the ideal.

Table 2.3: Optimal Three-Impulse Burnlist

Burn	Time (sec)	ΔV_x (km/sec)	ΔV_y (km/sec)	ΔV_z (km/sec)	$ \Delta V $ (km/sec)
1	0.000	0.000000	0.000001	0.000001	0.000001
2	865.790	-0.000001	-0.000099	0.001119	0.001124
3	4976.002	0.000000	0.000000	0.000000	0.000000

Total	0.001125
--------------	-----------------

The only remaining concern is to compare the actual final state, or the state produced by propagating the initial state with the calculated burnlist, to the target state. Table 2.3 tabulates the actual final state, the target state, and their difference. The differences indicate that using the two order of magnitude requirement stated previously, semi-major axis can be maintained for a limit as small as 20 meters and for virtually any eccentricity or angular element limit. The magnitude of the differences is directly related to the tolerance condition for convergence to the target position in the Lambert algorithm. This test indicates that that tolerance does not need to be tightened up.

Table 2.4: Inclination Test Case Initial and Target States

	Actual Final State	Target State	Difference
SMA	10000.000250 km	10000.000087 km	0.000163 km
ECC	0.200000	0.200000	0.000000
INC	5.009603°	5.009603°	0.000000°
LAN	359.910177°	359.910178°	0.000001°
AP	270.178940°	270.178922°	0.000018°
MA	216.087352°	216.087375°	0.000023°

Similar test cases were conducted for a variety of targeting scenarios that resemble station-keeping situations. The characteristic velocities for burnlists to correct semi-major axis and eccentricity tended to be within 10% of their ideal 2-body solutions. The transfer trajectories for the remaining elements could not be analyzed quite as accurately for two reasons. The first is the aforementioned difficulty of calculating the true optimal transfers for these elements in the presence of perturbations. The second reason is the requirement to conduct the transfer to the targeted state within the span of one orbital period. For example, corrections to mean anomaly are generally accomplished by slightly adjusting the semi-major axis for the span of multiple orbits. Mean anomaly is never adjusted directly within the span of one orbit. Requiring this results in burns which are technically correct, but much larger than what can be achieved through other means. The solution to this problem is to place some additional intelligence in the targeting strategies so that, for example, they direct a correction to the semi-major axis when the mean anomaly variation from the nominal trajectory approaches its limit.

As a whole, the primer vector code produces solutions which are entirely acceptable for making station-keeping strategy decisions for a satellite.

Chapter 3

Orbit Propagation

Orbit propagation can be defined as the problem of predicting the future position and velocity of an object in space given its current position and velocity. The same principles applied centuries ago to predict the motion of heavenly bodies, are used today by modern space systems to carry out critical operational functions. For example, ballistic missile control systems rely on knowledge of their predicted trajectory to hit their targets, while satellite systems need trajectory information to carry out virtually any function, from communication with a ground station to overflight of specific target locations on the Earth to rendezvous with other spacecraft.

This chapter begins with a review of the motion of artificial satellites. The general two body equations of motion are developed and followed by a study of significant orbital perturbations. This is followed by a summary of different approaches taken to solve the orbit propagation problem. A closer analysis is provided for semi-analytical theory, the approach used in this project. Finally, the specific software implementation of the orbit propagator chosen for this project is discussed. New capabilities, modifications, and limitations are identified.

3.1 Satellite Motion

Detailed derivations for the equations of motion and accompanying perturbations needed to accurately describe satellite motion are included in numerous texts. The following explanation is a compilation of material from Roy's *Orbital Motion* [50], Battin's *An Introduction to the Mathematics and Methods of Astrodynamics* [3], Chobotov's *Orbital Mechanics* [16], and Bate, Mueller, and White's *Fundamentals of Astrodynamics* [2]. To maintain commonality, Battin's notation is used whenever possible.

3.1.1 Orbital Elements

The first requirement for describing the location and motion of a spacecraft in orbit is a convenient inertial reference frame. This type of frame provides fixed axes upon which to form a coordinate system and define variables which change over time. For orbits about the sun, the heliocentric-ecliptic frame is chosen. The fundamental plane of this sun-centered system is the plane defined by the orbit of the Earth about the sun, or the ecliptic plane. For satellite motion about the Earth, however, the geocentric-equatorial system is the appropriate choice. The fundamental plane of this system is the Earth's equator, while the origin is the geocenter. The principal direction for both systems is the vernal equinox, or the direction of the line of intersection of the ecliptic and equatorial planes at the time the sun appears to cross from the southern to the northern hemisphere. The x-axis of the geocentric-equatorial coordinate system is in the principal direction. The z-axis is in the direction of the north pole. The y-axis completes the right-handed xyz orthogonal triplet.

Six independent quantities are required to uniquely define the position of a satellite in a specific orbit with respect to the coordinate system. A minimum of two of these values is required to describe the size and shape of the orbit. Only one quantity is required to place the satellite in the orbit. Finally, a minimum of three values are needed to orient the orbit with respect the reference frame.

The classical set of six orbital elements, known as the Keplerian element set, is listed in table 3.1. The semi-major axis and eccentricity define the size and shape, respectively, of the orbit. The longitude of the ascending node, inclination, and argument of perigee are the three Euler angles which uniquely orient the orbit with respect to the inertial coordinate system. If the periapsis direction is defined as the direction from the occupied focus to the position in the orbit of the lowest altitude, then the true anomaly is the angle between the periapsis direction and the position vector of the satellite at any given time.

Table 3.1: Keplerian Element Set

Element Symbol	Element Name
a	semi-major axis
e	eccentricity
i	inclination
ω	argument of perigee
Ω	longitude of the ascending node
v	true anomaly

Figure 3.1 illustrates the angular Keplerian elements. In the figure, \mathbf{i}_x , \mathbf{i}_y , and \mathbf{i}_z are the unit vectors along the axes which define the geocentric-equatorial coordinate system, \mathbf{r} is the position vector of the satellite, \mathbf{i}_e is the unit vector in the periapsis direction, \mathbf{i}_n is the

unit vector in the direction of the line of nodes, or the line defined by the intersection of the equatorial and orbital planes, and \mathbf{i}_h is the unit vector normal to the orbital plane

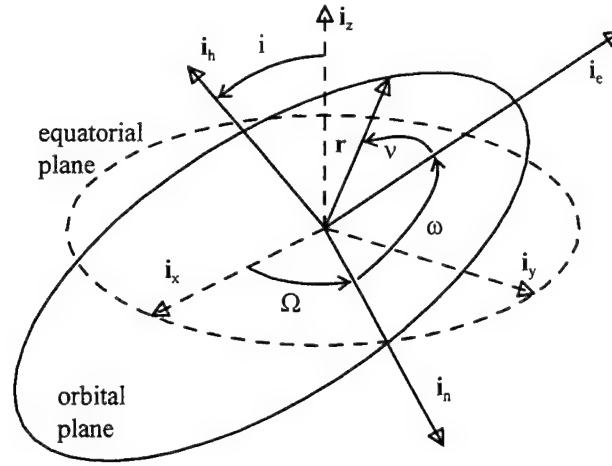


Figure 3.1: Keplerian Orbital Elements

It is often more convenient to describe the location of the satellite in its orbit as a function of the time since periapsis passage. To accomplish this, a replacement element for v , called the mean anomaly M , is defined.

$$M = \sqrt{\frac{\mu}{a^3}} (t - \tau) = n \Delta t \quad (3.1)$$

In equation 3.1, n , called the mean motion, is the average angular rate of the motion of the satellite about the focal point, μ is the gravitational constant of the Earth, and τ is the time of perigee passage. If t is the current time, then $\Delta t = t - \tau$ is the time since perigee passage. Therefore, the mean anomaly M is an angular expression of the average angular motion of the satellite in its orbit. Note that it has no geometrical interpretation, and thus cannot be viewed in the picture of an orbit.

The Keplerian element set of table 3.1 experiences two significant singularities. The first is caused by circular orbits, or orbits of zero eccentricity. Since the radial distance from

the geocenter is constant for these orbits, the periapsis direction becomes undefined and removes the reference for the mean anomaly and the argument of perigee. The second singularity is caused by equatorial orbits, or orbits of zero inclination. In this case, the line of nodes is undefined.

More importantly, the method of the variation of parameters (to be discussed in section 3.2.1) cannot be applied for these singular orbit cases. Because of this, orbits with small initial inclination and eccentricity can be very troublesome for an orbit propagator using Keplerian elements. Since perturbations cause the elements to vary with time, special checks are required in these propagators to guard against straying into a region of singularity. To avoid this problem, we consider the equinoctial elements, an element set originally developed by Lagrange which does not experience these singularities. The equinoctial element set also resolves the special case of 90° inclination. Defined in terms of the Keplerian elements, the equinoctial elements are

$$\begin{aligned}
 a &= a \\
 h &= e \sin(\omega + I\Omega) \\
 k &= e \cos(\omega + I\Omega) \\
 p &= \tan^{-1}\left(\frac{i}{2}\right) \sin \Omega \\
 q &= \tan^{-1}\left(\frac{i}{2}\right) \cos \Omega \\
 \lambda &= M + \omega + \Omega
 \end{aligned} \tag{3.2a-f}$$

where I is the retrograde factor which assumes the following values

$$I = \begin{cases} 1, & \text{for } 0 \leq i < \pi \\ -1, & \text{for } 0 < i \leq \pi \end{cases}$$

If $I = 1$, the resulting element set is known as the direct equinoctial elements. If $I = -1$, then the element set is known as the retrograde equinoctial elements. This formulation was introduced because the direct elements experience a singularity at $i = \pi$ and the retrograde elements experience a singularity at $i = 0$. When equinoctial elements are needed in this project, only the direct equinoctial elements are used. This is because none of the constellation orbits to be studied have an inclination near π .

In the 1970's Broucke and Cefola [4] derived the partial derivatives of the position and velocity vectors with respect to the elements, the state transition matrix, and the Lagrange bracket matrix corresponding to the equinoctial elements. Together, Broucke, Cefola, and later the Russians Lidov and Yurasov[59], derived the analytic equations required to build a propagator entirely in the non-singular equinoctial element set. This made the element set useful for application to both special and general perturbation methods.

Both the Keplerian and equinoctial element sets are used in this project. The Keplerian elements are more convenient for visualizing the variations caused by perturbations in propagated orbits. For this reason, and the fact that all satellite orbital information is published in Keplerian elements, the top level code, as well as all the input and output, is structured for Keplerian elements. Equinoctial elements, though, are more convenient for the DSST orbit propagator. Therefore, any interface with the propagator is conducted in equinoctial elements. The simulation's users are never exposed to the conversion between elements.

3.1.2 Equations of Motion

Newton's Law of Gravitation states that any two masses experience an equal and opposite attractive force, along the line connecting their centers, proportional to the product of their masses and inversely proportional to the distance between them. Thus the total force \mathbf{f}_i affecting the i^{th} mass in an n -mass system is

$$\mathbf{f}_i = m_i \frac{d^2 \mathbf{r}_i}{dt^2} = \sum_{\substack{j=1 \\ j \neq i}}^n G \frac{m_i m_j}{r_{ij}^3} (\mathbf{r}_j - \mathbf{r}_i) \quad (3.3)$$

where G is the universal gravitational constant, \mathbf{r}_i and \mathbf{r}_j are the position vectors, in an inertial coordinate system, to the i^{th} and j^{th} masses, respectively, and r_{ij} is the distance between the i^{th} and j^{th} masses.

For systems with only two relevant masses, the equations describing the forces affecting the masses are

$$\begin{aligned} m_1 \frac{d^2 \mathbf{r}_1}{dt^2} &= G \frac{m_1 m_2}{r_{12}^3} (\mathbf{r}_2 - \mathbf{r}_1) \\ m_2 \frac{d^2 \mathbf{r}_2}{dt^2} &= G \frac{m_1 m_2}{r_{12}^3} (\mathbf{r}_1 - \mathbf{r}_2) \end{aligned} \quad (3.4a,b)$$

Since we are interested in the motion of one mass with respect to the other, differencing the equations 3.4a and 3.4b yields

$$\frac{d^2 \mathbf{r}}{dt^2} + \frac{\mu}{r^3} \mathbf{r} = \mathbf{0} \quad (3.5)$$

where

$$\mathbf{r} = \mathbf{r}_2 - \mathbf{r}_1 \quad (3.6)$$

is the position vector of the second mass with respect to the first, r is its magnitude, and $\mu = G(m_1 + m_2)$. Equation 3.5 is often referred to as the two body equation of motion because it discounts the effects of any other masses and accelerations due to other causes. If we define the velocity vector as

$$\mathbf{v} = \frac{d\mathbf{r}}{dt} \quad (3.7)$$

then equation 3.5 can be restated as the following system of equations

$$\begin{bmatrix} \dot{\mathbf{r}} \\ \dot{\mathbf{v}} \end{bmatrix} = \begin{bmatrix} \mathbf{0} & \mathbf{I} \\ -\frac{\mu}{r^3} & \mathbf{0} \end{bmatrix} \begin{bmatrix} \mathbf{r} \\ \mathbf{v} \end{bmatrix} \quad (3.8)$$

Since the two body equations of motion are non-linear, solving equation 3.8 explicitly is extremely difficult. No closed form solution exists for $\mathbf{r}(t)$ and $\mathbf{v}(t)$ for general 2 body orbits.

Another important relation is the gravitational potential of a mass. For a mass m_i in an n -mass system, the gravitational potential is defined as

$$V_i = G \sum_{\substack{j=1 \\ j \neq i}}^n \frac{m_j}{r_{ij}} \quad (3.9)$$

For the 2 body case, the gravitational potential of a satellite in the Earth-satellite system is

$$V_{2body} = G \frac{m_e}{r} \approx G \frac{m_e + m_{sat}}{r} = \frac{\mu}{r} \quad (3.10)$$

where m_e is the mass of the Earth and m_{sat} is the mass of the satellite, μ is the universal gravitational constant times the sum of the masses, and r is the distance from the geocenter to the satellite. Note that since $m_e \gg m_{sat}$, μ is often approximated as $\mu = Gm_e$.

One of the important properties of the gravitational potential is that the gradient of V_i is the acceleration experienced by mass m_i due to the other masses in the system. Thus we have

$$\mathbf{f}_i^T = m_i \left[\frac{d^2 \mathbf{r}_i}{dt^2} \right]^T = m_i \frac{\partial V_i}{\partial \mathbf{r}_i} \quad (3.11)$$

To relate the motion of the n-mass system in energy terms, we introduce a new function U , called the force function.

$$U = \frac{1}{2} \sum_{i=1}^n m_i V_i \quad (3.12)$$

U is equivalent to the total work required to bring the n-mass system from a relative distance of infinity to the current configuration. Therefore, $-U$ is known as the potential energy of the system. The force function U is related to the force vector \mathbf{f}_i by

$$\mathbf{f}_i^T = \frac{\partial U}{\partial \mathbf{r}_i} \quad (3.13)$$

Using the definitions above, the force function for the two body system is

$$U_{2body} = G \frac{m_e m_{sat}}{r} \quad (3.14)$$

3.1.3 Satellite Perturbations

The two body approximation used to derive equation 3.5 is sufficient to gain a general appreciation of the motion of artificial satellites about the Earth, but is not accurate enough for orbit propagation over any significant period of time. Accelerations which are not apparent in the 2 body model, but which are present for actual satellites, are known as perturbing accelerations. In general they are small and are significant only over longer periods of time. The primary exception to this general rule is the J_2 zonal harmonic, which results in significant deviations within one orbital period. The time spans of the orbit analyses done for this project are based on the projected lifetimes of the constellation systems. Since these lifetimes range from 5 to 12 years, orbital perturbations cannot be ignored.

Orbital perturbations will generally cause three types of variations in the orbital elements: secular, short period, and long period. Figure 3.2 illustrates the differences between the three. Secular variations result in monotonically increasing or decreasing changes in the orbital elements. Short periodic variations generally cause smaller amplitude, high frequency changes. If the acceptable limits on the variations of the orbital elements entirely encompass the short period variations, then they can generally be ignored in the context of station-keeping. Finally, long period variations result in lower frequency changes of the elements. In general, variations with longer periods tend to be of greater magnitude as well [13]. Note from figure 3.2 that the frequency dividing line between short and long periodic variations is a relative matter. Generally, the orbital period of the satellite, or some multiple thereof, is used to determine the border between the two.

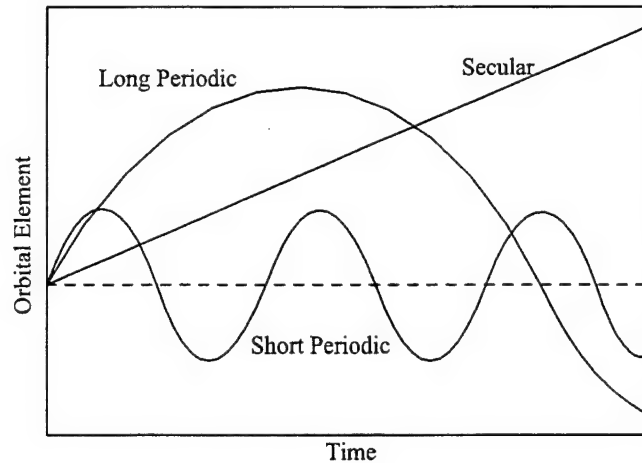


Figure 3.2: Secular, Short Periodic and Long Periodic Variations

The Earth's geopotential, atmospheric drag, solar radiation pressure and third body accelerations are regarded as the four most significant perturbations. Of the four, geopotential and third body effects result in conservative perturbing forces. Conservative forces are those that do not change the energy of the orbit. The remaining two, solar radiation pressure and atmospheric drag are non-conservative forces, which change the energy of an orbit. It is possible to model solar radiation pressure as a conservative force if the satellite is always sunlit [16]. Examples of perturbations of lesser magnitude than the four listed above are solid Earth tides and albedo pressure.

The relative effect of each of these perturbations is dependent on the orbit and the physical characteristics of the spacecraft. For example, orbits of low altitude or high eccentricity will spend more time within the Earth's atmosphere, and thus face greater drag effects, while satellites with large solar panels provide a greater surface area for the effects of solar radiation pressure. Table 3.2 compares, at different altitudes, the accelerations caused by the four major perturbations and the central gravity acceleration of the Earth for a satellite with an area to mass ratio of $0.0212 \text{ m}^2/\text{kg}$ [58,51].

Table 3.2: Accelerations Experienced by Spacecraft At Varying Altitudes [58,51]

(m/sec ²)	150 km Altitude	750 km Altitude	1500 km Altitude	Geosynchronous
Central Gravity	9.35	7.85	6.42	0.22
<u>Geopotential</u>				
<u>Zonals</u>				
J ₂	30 x 10 ⁻³	20 x 10 ⁻³	14 x 10 ⁻³	16 x 10 ⁻⁶
J ₃	.09 x 10 ⁻³	.06 x 10 ⁻³	.04 x 10 ⁻³	8 x 10 ⁻⁹
J ₄	.07 x 10 ⁻³	.04 x 10 ⁻³	.02 x 10 ⁻³	1 x 10 ⁻⁹
<u>Tesserals</u>				
J _{2,2}	.09 x 10 ⁻³	.07 x 10 ⁻³	.04 x 10 ⁻³	0.05 x 10 ⁻⁶
Atmospheric Drag	3 x 10 ⁻³	0.1 x 10 ⁻⁶	negligible	negligible
Solar/Lunar Third Body	1 x 10 ⁻⁶	1 x 10 ⁻⁶	1 x 10 ⁻⁶	7 x 10 ⁻⁶
Solar Radiation Pressure	0.1 x 10 ⁻⁶	0.1 x 10 ⁻⁶	0.1 x 10 ⁻⁶	0.1 x 10 ⁻⁶

Perturbations can have varying affects on different orbital elements. Table 3.3 describes the type of variations caused by the four primary perturbations on each of the orbital elements [58,51].

Table 3.3: Varying Types of Perturbation Effects [58,51]

	Semi-major Axis	Eccentricity	Inclination	Ascending Node	Argument of Perigee	Mean Anomaly
<u>Geopotential</u>						
Even Zonals	periodic	periodic	periodic	secular	secular	secular / per
All Zonals	periodic	periodic	periodic	periodic	periodic	periodic
Tesserals	periodic	periodic	periodic	periodic	periodic	periodic
Atmospheric Drag	secular decrease	secular decrease	periodic	periodic	periodic	periodic
Solar/Lunar Third Body	periodic	periodic	periodic	secular / periodic	secular / periodic	periodic
Solar Radiation Pressure	secular / periodic	secular / periodic	secular / periodic	secular / periodic	secular / periodic	secular / periodic

It is important to note that not all perturbations from the 2 body orbit are unwanted. Sun synchronous satellites maintain an inclination which causes a 1°/day secular drift in the ascending node due to the J_2 geopotential perturbation. This allows the orbit plane to rotate about the Earth at the same rate that the Earth revolves around the Sun. The result is that the orbit plane maintains a constant orientation with respect to the Sun - a very valuable feature for solar panels.

3.1.3.1 Geopotential

Geopotential perturbations are caused by the fact that the Earth is not a perfect sphere with a constant density. These two assumptions were required to treat the Earth as a point mass for the two body equations. The consequence of a non-spherical non-constant density Earth is reflected in the potential function for the satellite in the Earth-satellite system. For a complex geopotential model, this function can be represented by

$$V = V_{2body} + R \quad (3.15a)$$

where V_{2body} is the gravitational potential function described in equation 3.10, and R is the disturbing function representing the change from the 2 body model. This form is useful because it readily leads to the equations of motion of the disturbed satellite. Applying the property of the gravitational potential function displayed in equation 3.11, the acceleration of the satellite about an Earth with a complex geopotential is

$$\frac{d\ddot{\mathbf{r}}^T}{dt} = \frac{\partial V}{\partial \mathbf{r}} = \frac{\partial V_{2body}}{\partial \mathbf{r}} + \frac{\partial R}{\partial \mathbf{r}} = -\frac{\mu}{r^3} \mathbf{r}^T + \ddot{\mathbf{r}}_{dist}^T \quad (3.15b)$$

where \mathbf{r} is the vector from the geocenter to the satellite, r is its magnitude, and

$$\ddot{\mathbf{r}}_{dist} = \left[\frac{\partial R}{\partial \mathbf{r}} \right]^T \quad (3.15c)$$

is the disturbing acceleration caused by geopotential variations from a spherical, constant density Earth.

To calculate R , consider the Earth to be composed of $n-1$ masses of the same order of magnitude as the mass of the satellite, the n^{th} mass. Then by equations 3.9 and 3.11, the acceleration experienced by the satellite can be expressed as

$$\frac{d^2 \mathbf{r}^T}{dt^2} = \frac{\partial}{\partial \mathbf{r}} \sum_{j=1}^{n-1} G \frac{m_j}{r_{jn}} \quad (3.16)$$

Since the $n-1$ mass objects of the Earth are clustered extremely close together, and n is large, the summation in equation 3.16 can be expressed as a volume integral over the planet.

$$\frac{d^2 \mathbf{r}^T}{dt^2} = \frac{\partial}{\partial \mathbf{r}} \iiint \frac{G dm}{\sqrt{r^2 + \rho^2 + 2r\rho \cos \gamma}} \quad (3.17)$$

In equation 3.17, ρ is the radial distance from the geocenter to the mass element dm , and γ is the angle between the vector from the geocenter to the satellite and the vector from the geocenter to the mass element. From equation 3.10 we see that the integral of equation 3.17 is the gravitational potential for the satellite.

$$V = \iiint \frac{G dm}{\sqrt{r^2 + \rho^2 + 2r\rho \cos \gamma}} \quad (3.18)$$

The form of equation 3.18 lends itself to a special substitution. The generating function for a Legendre polynomial is

$$\sqrt{1-2vx+x^2} = \sum_{k=0}^{\infty} P_k(v) x^k \quad (3.19)$$

where $P_k(v)$ is the k^{th} order Legendre polynomial. Incorporating Legendre polynomials into equation 3.17 yields

$$V = \frac{G}{r} \iiint \left(\frac{\rho}{r} \right)^k P_k(\cos \gamma) dm \quad (3.20)$$

If axial symmetry of the mass of the Earth is assumed, then the solution to equation 3.20 is

$$V = \frac{Gm_e}{r} \left[1 - \sum_{k=2}^{\infty} J_k \left(\frac{R_e}{r} \right)^k P_k(\cos \phi) \right] \quad (3.21)$$

where ϕ is the satellite latitude, R_e is the radius of the Earth, and J_k are constants that are determined through accurate measurements of perturbed satellite trajectories. Equation 3.21 describes the potential function of the 2 body system corrected by disturbances caused by zonal (constant across longitude) harmonics. Some of the initial J_k constants are [3]

$$\begin{aligned} J_2 &= 0.00108263 \\ J_3 &= -0.00000254 \\ J_4 &= -0.00000161 \end{aligned}$$

From the value of these constants, we see that the term corresponding to the J_2 correction is the dominant source of disturbance. This is confirmed by the comparison in table 3.2.

A general solution of equation 3.20, which does not rely on axial symmetry, is obtained by treating the geopotential as a boundary value problem and using Laplace's equation [51]. If the geocenter is used as the origin of the coordinate system, this method results in an expression for the geopotential of the form [51,25,6]

$$V = \frac{\mu}{r} \left[1 + \sum_{n=2}^{\infty} \sum_{m=0}^n \left(\frac{R_e}{r} \right)^n P_n^m(\sin \phi) (C_n^m \cos m\lambda + S_n^m \sin m\lambda) \right] \quad (3.22)$$

where λ is the satellite longitude, and P_n^m is the Legendre function of the first kind of degree n and order m such that

$$P_n^m(v) = (1-v^2)^{\frac{1}{2}m} \frac{d^m}{dv^m} P_n(v) \quad (3.23)$$

In equation 3.22, C_n^m and S_n^m , are known as the spherical harmonic coefficients. They have been determined through high values of n and m with the use of satellite measurements. When $m = 0$, equation 3.22 reduces to equation 3.21 so that it represents only the zonal harmonics with $J_n = -C_n^0$. Tesseral harmonics are defined when $n \geq m$ and $m \neq 0$. While zonal harmonics tend to be the most dominant of the spherical harmonics, tesseral harmonics become important for cases when satellites have repeat ground tracks. Since the satellite trajectory repeatedly brings it over the same region of the Earth on a fixed schedule, the effects of the tesserals build up in a manner similar to resonance. In these situations, the resulting perturbation is called tesseral resonance.

By changing equation 3.22 to the form of equation 3.15, we find that the general disturbing function R due to the Earth's geopotential is

$$R = \frac{\mu}{r} \left[\sum_{n=2}^{\infty} \sum_{m=0}^n \left(\frac{R_e}{r} \right)^n P_n^m(\sin \phi) (C_n^m \cos m\lambda + S_n^m \sin m\lambda) \right] \quad (3.24)$$

3.1.3.2 Atmospheric Drag

For satellite orbits whose perigee altitude is below 1000 km, a significant perturbation which cannot be ignored appears - atmospheric drag. The particles of the Earth's atmosphere collide with the cross sectional area of the satellite exposed to the direction of motion. The net effect of this interaction is a reduction in the energy of the orbit. For this reason, drag is considered a non-conservative perturbing force. The primary affect on the orbital elements is a secular decrease in the semi-major axis and eccentricity. Since satellites in elliptical orbits experience the largest drag forces at perigee passage, the tendency for these orbits is to circularize over time. If allowed to go unchecked, atmospheric drag will eventually cause the satellite to reenter the lower atmosphere.

The rate of decay of the orbit depends on three primary factors: atmospheric density, orbital velocity, and satellite ballistic coefficient. The atmospheric density decreases rapidly with increased altitude, but its precise value varies with time and geographic position and can only be estimated with the use of atmospheric models. The ballistic coefficient is equal to the sea level weight W of the spacecraft divided by the product of the cross sectional area A exposed to the atmospheric particles and the coefficient of drag C_D [16]. The coefficient of drag is a dimensionless value which depends on the shape of the vehicle, its attitude with respect to the velocity vector, and whether it is spinning, tumbling, or is stabilized. Above 200 km, the drag coefficient varies from 2.2 for a sphere to 3.0 for a cylinder [16]. However, it can take on values as high as 11.0 depending on the satellite [13]. The drag force exerted on the spacecraft is linearly proportional to the atmospheric density, inversely proportional to the ballistic coefficient, and proportional to the square of the orbital velocity. The equation for the drag force is

$$F_{drag} = -\frac{1}{2} \rho g_o V^2 \frac{C_D A}{W} \quad (3.25)$$

where ρ is the atmospheric density, g_o is the Earth's gravitational acceleration at sea level and V is the velocity of the satellite. The disturbing acceleration on the spacecraft due to drag is

$$\ddot{\mathbf{r}}_{drag} = -\frac{1}{2} \rho \frac{C_D A}{m} |\dot{\mathbf{r}}_{sc/atm}| \dot{\mathbf{r}}_{sc/atm} \quad (3.26)$$

where m is the spacecraft mass and $\dot{\mathbf{r}}_{sc/atm}$ is velocity vector of the spacecraft with respect to the moving atmosphere.

The most difficult part of equation 3.25 to determine is the atmospheric density. The precise density at a point is function of the altitude, exospheric temperature, and geographic location. Since the temperature of the atmosphere is affected by the 11 year solar flux cycle, the atmospheric density is also an implicit function of time. Due to the complex nature of the density function, estimates of the atmospheric density are generally obtained from atmospheric density models. The density model used for this project is the Jacchia-Roberts model. It uses an empirical temperature profile to solve the diffusive equilibrium equations and determine the atmospheric density at a given altitude [6]. A study of different semi-empirical models conducted by Cox, Feiertag, Oza, and Doll suggests that while newer models outperform the Jacchia-Roberts model for special orbits, it is still the best model for general orbits over short arcs [51,18]. In the absence of a comparable study for long arc predictions, Jacchia-Roberts is still retained.

3.1.3.3 Solar Radiation Pressure

The third significant perturbation, solar radiation pressure, is caused by the interaction of the satellite with charged particles ejected from the Sun. The force exerted by the resulting transfer of momentum is in the direction of the vector from the Sun to the satellite, \mathbf{r}_{vs} . The magnitude of the force is proportional to the effective surface area A of the satellite normal to the sun vector, the surface reflectivity η , and the luminosity L_D of the sun, and is inversely proportional to speed of light c and the square of the distance r_{vs} to the sun [6].

$$F_{sp} = \frac{L_s (1 + \eta) A}{4\pi r_{vs}^2 c} \quad (3.27)$$

If the coefficient of reflectivity is defined as

$$C_R = 1 + \eta$$

then the disturbing acceleration due to solar radiation pressure is

$$\ddot{\mathbf{r}}_{sp} = \nu \frac{S}{c} \frac{C_R A}{m} \frac{\mathbf{r}_{vs}}{r_{vs}} \quad (3.28)$$

where

$$S = \frac{L_s}{4\pi r_{vs}^2}$$

is the mean solar flux at one astronomical unit, and ν is the eclipse factor. The eclipse factor scales the magnitude of the solar radiation pressure induced acceleration based upon the shadow status of the satellite. It is defined as

$v = 0$:	satellite in umbra (full shadow of Earth)
$v = 1$:	satellite in sunlight
$0 < v < 1$:	satellite is in penumbra (partial shadow of Earth)

While solar radiation pressure affects all the elements, the typical effect on satellite orbits is a long periodic variation in eccentricity. Since the force defined in equation 3.28 results in a change in the energy of the orbit, solar radiation pressure is a non-conservative perturbation. In contrast to atmospheric drag, however, the energy of the orbit is not always reduced. The Borealis orbit planes of the Ellipso constellation demonstrate that solar radiation pressure can occasionally boost the energy of an orbit [52]. The satellites of one of the Borealis planes actually increase their semi-major axis over time due to solar radiation pressure! While this behavior is not common, it demonstrates that the effects of solar radiation pressure are significant and quite dependent of the orbit and satellite being studied.

3.1.3.4 Third Body Point Mass

Third body perturbations are caused by the gravitational influence of distant celestial bodies, modeled as point masses, on the motion of spacecraft in the vicinity of Earth. As the altitude of an orbit increases, the variation caused by this external influences increase in such a manner that it cannot be ignored for orbit predictions over long time intervals. The two masses with the most significant affect on satellite motion about the Earth are the moon and the sun.

To determine how distant bodies can affect satellite motion, recall from section 3.1.2 that the total force \mathbf{f}_i affecting the i^{th} mass in an n -mass system is

$$\mathbf{f}_i = m_i \frac{d^2 \mathbf{r}_i}{dt^2} = \sum_{\substack{j=1 \\ j \neq i}}^n G \frac{m_i m_j}{r_{ij}^3} (\mathbf{r}_j - \mathbf{r}_i) \quad (3.3)$$

If m_e is the mass of the Earth, m_s is the mass of the satellite, and m_t is the mass of the third body, then the equations of motion for the Earth and satellite are

$$\begin{aligned} m_e \frac{d^2 \mathbf{r}_e}{dt^2} &= G \frac{m_e m_s}{r_{se}^3} (\mathbf{r}_s - \mathbf{r}_e) + G \frac{m_e m_t}{r_{et}^3} (\mathbf{r}_t - \mathbf{r}_e) \\ m_s \frac{d^2 \mathbf{r}_s}{dt^2} &= G \frac{m_s m_e}{r_{se}^3} (\mathbf{r}_e - \mathbf{r}_s) + G \frac{m_s m_t}{r_{st}^3} (\mathbf{r}_t - \mathbf{r}_s) \end{aligned} \quad (3.29a,b)$$

where \mathbf{r}_s , \mathbf{r}_e , and \mathbf{r}_t are the vectors from the origin of an inertial reference frame to the satellite, Earth, and third body, respectively and r_{ab} represents the distance from mass a to mass b. Since the motion of the satellite with respect to the Earth is of primary interest, differencing equations 3.29a and 3.29b yields

$$\frac{d^2 \mathbf{r}}{dt^2} = -\frac{G(m_e + m_s)}{r^3} \mathbf{r} + \frac{Gm_t}{r_{st}^3} (\mathbf{r}_t - \mathbf{r}_s) - \frac{Gm_t}{r_{et}^3} (\mathbf{r}_t - \mathbf{r}_e) \quad (3.30)$$

where $\mathbf{r} = \mathbf{r}_s - \mathbf{r}_e$ is the vector from the geocenter to the satellite and $r = r_{se}$ is its magnitude. Equation 3.30 indicates that the disturbing acceleration due to the gravitational influence of the mass of a third body is

$$\ddot{\mathbf{r}}_t = Gm_t \left[\frac{\mathbf{r}_t - \mathbf{r}_s}{r_{st}^3} - \frac{\mathbf{r}_t - \mathbf{r}_e}{r_{et}^3} \right] \quad (3.31)$$

Since the third body perturbations are conservative, equation 3.31 has a related disturbing function. It is

$$R_t = Gm_t \left(\frac{1}{r_{st}} - \frac{1}{r_{et}} \right) \quad (3.32)$$

The combined effects of lunar and solar third body perturbations typically cause long period and/or secular variations in orbit eccentricity, inclination, ascending node, and argument of perigee. For example, geosynchronous satellites experience a long period variation in inclination that causes roughly a 1°/year increase for about 10 years until a maximum variation of 15° is reached at 27 years [16]. The period of the total inclination motion for geosynchronous satellites is approximately 53 years.

3.2 Orbit Propagation Methods

The non-linear nature of the 2 body equations of motion implies that no general closed form analytical solution exists for $\mathbf{r}(t)$ and $\mathbf{v}(t)$ in terms of elementary functions. This, however, does not preclude analyzing the resulting motion. Recognizing that the orbits which result from equation 3.5 must be conic sections reveals enough to fully characterize the motion of a 2 body system. If the Keplerian elements are used, we see that five of the six elements, a , e , i , ω , and Ω , are fixed over time while the sixth element, the mean anomaly M , varies at a constant rate which is a function of only the fixed semi-major axis. So while the equations are not solvable, the resulting motions can still be studied.

Unfortunately, the 2 body equations are not adequate to describe artificial satellite motion in the presence of real world perturbations. As early as the 1700's, astronomers attempted to develop mathematical methods for orbit prediction which included perturbations. One the most successful of these methods was the Variation of

Parameters. In recent history, several newer approaches have been implemented to address perturbed dynamics. Put together, they form an area of study called perturbation theory.

3.2.1 Variation of Parameters

The Variation of Parameters (VOP) is a method originally developed by John Bernoulli to solve linear differential equations. In the late 18th century, it was adapted by Euler and Lagrange for the problem of disturbed orbital motion. It is used to develop analytical expressions which describe the variations in the orbital elements due to disturbing potential functions. The following is summary of the VOP equations, Lagrange planetary equations and Gauss' form of the variational equations as presented by Battin [3].

3.2.1.1 VOP Equations

Applying equations 3.11 and 3.15a, the equations of motion of a body in the presence of a conservative and non-conservative perturbations are

$$\frac{d^2 \mathbf{r}}{dt^2} + \frac{\mu}{r^3} \mathbf{r} = \mathbf{a}_{nc} + \left[\frac{\partial R}{\partial \mathbf{r}} \right]^T \quad (3.33)$$

where R is the disturbing potential function for all conservative perturbations, $\partial R / \partial \mathbf{r}$ is the acceleration due to R , and \mathbf{a}_{nc} is the acceleration due to all non-conservative perturbing forces. Expressed in terms of position and velocity, the equations are

$$\frac{d\mathbf{r}}{dt} = \mathbf{v} \quad \text{and} \quad \frac{d\mathbf{v}}{dt} + \frac{\mu}{r^3} \mathbf{r} = \mathbf{a}_{nc} + \left[\frac{\partial R}{\partial \mathbf{r}} \right]^T \quad (3.34)$$

The solutions to the undisturbed 2 body equations can be expressed as $\mathbf{r}(t, \mathbf{e})$ and $\mathbf{v}(t, \mathbf{e})$ where \mathbf{e} is a six element set of integration constants. The vector \mathbf{e} can also be interpreted as the set of orbital elements. Note that \mathbf{e} in this context is not to be confused with the eccentricity vector. As with the method of variation of parameters for linear differential equations, the ‘constants’ of \mathbf{e} are allowed to vary in order to obtain a solution for the non-homogenous system of equations 3.34. The solutions $\mathbf{e}(t)$ to the new differential equations have the property that they are only affected by the perturbing accelerations and not the central gravitational acceleration.

Since $\mathbf{e}(t)$ is constant for undisturbed motion, the partial derivatives of \mathbf{r} and \mathbf{v} with respect to time are the solutions to the homogenous 2 body system. Therefore

$$\frac{\partial \mathbf{r}}{\partial t} = \mathbf{v} \quad \text{and} \quad \frac{\partial \mathbf{v}}{\partial t} + \frac{\mu}{r^3} \mathbf{r} = \mathbf{0} \quad (3.35)$$

This is equivalent to saying that the velocity vectors for the disturbed and undisturbed motion are the same at any given time, or that

$$\frac{d\mathbf{r}}{dt} = \frac{\partial \mathbf{r}}{\partial t} \quad (3.36)$$

By the definition of a derivative, we have that

$$\frac{d\mathbf{r}}{dt} = \frac{\partial \mathbf{r}}{\partial t} + \frac{\partial \mathbf{r}}{\partial \mathbf{e}} \frac{d\mathbf{e}}{dt} \quad (3.37)$$

Substituting equation 3.36 into 3.37 yields

$$\frac{\partial \mathbf{r}}{\partial \mathbf{e}} \frac{d\mathbf{e}}{dt} = \mathbf{0} \quad (3.38)$$

Applying the definition of a derivative to velocity, we have that

$$\frac{d\mathbf{v}}{dt} = \frac{\partial \mathbf{v}}{\partial t} + \frac{\partial \mathbf{v}}{\partial \mathbf{e}} \frac{d\mathbf{e}}{dt} \quad (3.39)$$

Applying equations 3.34 and 3.35, we find that

$$\frac{\partial \mathbf{v}}{\partial \mathbf{e}} \frac{d\mathbf{e}}{dt} = \mathbf{a}_{nc} + \left[\frac{\partial R}{\partial \mathbf{r}} \right]^T \quad (3.40)$$

Equations 3.38 and 3.40 represent the 6 differential equations which must be solved to obtain a solution for the orbital elements $\mathbf{e}(t)$.

3.2.1.2 Lagrange's Planetary Equations

In 1782, Lagrange developed a series of equations to describe the motion of comets in elliptical orbits. These equations are the solutions to the differential equations

$$\frac{\partial \mathbf{r}}{\partial \mathbf{e}} \frac{d\mathbf{e}}{dt} = \mathbf{0} \quad (3.38)$$

$$\frac{\partial \mathbf{v}}{\partial \mathbf{e}} \frac{d\mathbf{e}}{dt} = \left[\frac{\partial R}{\partial \mathbf{r}} \right]^T \quad (3.41)$$

Notice that equation 3.41 is different from equation 3.40 in that it does not include the acceleration due to non-conservative forces. Lagrange's only requirement was to consider the third body effects of the planets on comet trajectories. Gauss' formulation,

discussed in the following section, does not distinguish between the origins of the perturbing accelerations.

If equation 3.38 is multiplied by $[\partial \mathbf{v} / \partial \mathbf{e}]^T$ and equation 3.41 is multiplied by $[\partial \mathbf{r} / \partial \mathbf{e}]^T$ then their difference can be expressed as

$$\frac{d\mathbf{e}}{dt} = \mathbf{L}^{-1} \left[\frac{\partial R}{\partial \mathbf{r}} \right]^T \quad (3.42)$$

where the 6 x 6 skew-symmetric matrix

$$\mathbf{L} = \left[\frac{\partial \mathbf{r}}{\partial \mathbf{e}} \right]^T \frac{\partial \mathbf{v}}{\partial \mathbf{e}} - \left[\frac{\partial \mathbf{v}}{\partial \mathbf{e}} \right]^T \frac{\partial \mathbf{r}}{\partial \mathbf{e}} \quad (3.43)$$

is the Lagrange matrix. The i,j element of the Lagrange matrix, $[e_i, e_j]$, is equal to

$$[e_i, e_j] = \frac{\partial \mathbf{v}^T}{\partial e_j} \frac{\partial \mathbf{r}}{\partial e_i} - \frac{\partial \mathbf{v}^T}{\partial e_i} \frac{\partial \mathbf{r}}{\partial e_j} \quad (3.44)$$

and is called a Lagrange bracket. It has the following properties

$$\begin{aligned} [e_i, e_i] &= 0 \\ [e_i, e_j] &= -[e_j, e_i] \\ \frac{\partial}{\partial t} [e_i, e_j] &= 0 \end{aligned}$$

An alternate form of equation 3.42 can be obtained which avoids an inverted matrix.

Define a state vector \mathbf{s} such that

$$\mathbf{s} = \begin{bmatrix} \mathbf{r} \\ \mathbf{v} \end{bmatrix} \quad (3.45)$$

Then the Lagrange matrix can be expressed as

$$\mathbf{L} = \left[\frac{\partial \mathbf{s}}{\partial \mathbf{e}} \right]^T \mathbf{J} \frac{\partial \mathbf{s}}{\partial \mathbf{e}} \quad (3.46)$$

where the matrix \mathbf{J} is defined as

$$\mathbf{J} = \begin{bmatrix} \mathbf{0} & \mathbf{I} \\ -\mathbf{I} & \mathbf{0} \end{bmatrix} \quad (3.47)$$

The matrix $\partial \mathbf{s} / \partial \mathbf{e}$ is known as the Jacobian matrix of the transformation from element space to state space. The inverse of the Jacobian matrix, $\partial \mathbf{e} / \partial \mathbf{s}$, is known as the matrizant of the 2 body problem [3]. Since $\mathbf{J}^2 = -\mathbf{I}$, if we define the matrix \mathbf{P} as

$$\mathbf{L} = \frac{\partial \mathbf{e}}{\partial \mathbf{s}} \mathbf{J} \left[\frac{\partial \mathbf{e}}{\partial \mathbf{s}} \right]^T \quad (3.48)$$

then we see that

$$\mathbf{P} \mathbf{L} = -\mathbf{I} \quad \text{and} \quad \mathbf{P} = -\mathbf{L}^{-1}$$

The matrix \mathbf{P} is called the Poisson matrix. Its elements, known as the Poisson brackets, have the same properties as that of the Lagrange brackets. Since the \mathbf{L} is skew symmetric, the relation between the Lagrange and Poisson matrices can also be expressed as

$$\mathbf{P}^T = \mathbf{L}^{-1} \quad (3.49)$$

Using this relation, equation 3.42 can be rewritten as

$$\frac{d\mathbf{e}}{dt} = \mathbf{P}^T \left[\frac{\partial R}{\partial \mathbf{r}} \right]^T \quad (3.50)$$

To determine the Poisson brackets, an element set must be chosen. If the Keplerian elements are considered, then \mathbf{P}^T is singular for an eccentricity of zero and one, or for an inclination of zero. Equation 3.50 cannot be solved for an orbit which exhibits any of these singularities. For equinoctial elements, \mathbf{P}^T is singular when the inclination is π for the direct elements or when the inclination is zero for the retrograde elements [3]. Therefore, when using the variation of parameters, a more general solution for the motion of the orbital elements is available when equinoctial elements are used. Lagrange's planetary equations in equinoctial elements are available in reference 4 by Broucke and Cefola.

3.2.1.3 Gauss' Form of the Variational Equations

The process Lagrange used to obtain Lagrange's planetary equations (equation 3.42/3.50) is valid when considering any type of accelerations. If we define the disturbing acceleration

$$\mathbf{a}_d = \mathbf{a}_{nc} + \left[\frac{\partial R}{\partial \mathbf{r}} \right]^T \quad (3.51)$$

to be the sum of all the conservative and non-conservative perturbing accelerations, then the equations of motion for the orbital elements are

$$\frac{\partial \mathbf{r}}{\partial \mathbf{e}} \frac{d\mathbf{e}}{dt} = \mathbf{0} \quad (3.38)$$

$$\frac{\partial \mathbf{v}}{\partial \mathbf{e}} \frac{d\mathbf{e}}{dt} = \mathbf{a}_d \quad (3.52)$$

As in the previous section, multiply equation 3.38 by $[\partial \mathbf{v} / \partial \mathbf{e}]^T$ and equation 3.52 by $[\partial \mathbf{r} / \partial \mathbf{e}]^T$ to obtain

$$\frac{d\mathbf{e}}{dt} = \mathbf{L}^{-1} \left[\frac{\partial \mathbf{r}}{\partial \mathbf{e}} \right]^T \mathbf{a}_d \quad (3.53)$$

Substituting for the Lagrange matrix yields

$$\frac{d\mathbf{e}}{dt} = \mathbf{P}^T \left[\frac{\partial \mathbf{r}}{\partial \mathbf{e}} \right]^T \mathbf{a}_d \quad (3.54)$$

Solving for each element of the vector $[\partial \mathbf{r} / \partial \mathbf{e}]^T \mathbf{a}_d$ yields Gauss' form of the variational equations. They are analytic expressions which describe the rates of change of each of the orbital elements in terms of the components of the disturbing accelerations. Equation 3.54 can also be represented as

$$\frac{d\mathbf{e}}{dt} = \frac{\partial \mathbf{e}}{\partial \mathbf{v}} \mathbf{a}_d \quad (3.55)$$

which is the classical form of the Gaussian Variation of Parameters equations.

3.2.2 Perturbation Theory

Perturbation theory traditionally was divided into two parts. The first included all the procedures that use the method of general perturbations. These procedures attempted to obtain analytical expressions to describe the variation of the elements from their 2 body

solutions. The second part included the procedures that use the method of special perturbations. These procedures attempted to numerically integrate equations of motion which included specific terms for the perturbations. There are distinct advantages and disadvantages to the both of these methods. More recently, a third approach has formed. Called semi-analytic theory, it attempts to do a mixture of analytical and numerical work in order to capitalize on the advantages of both.

3.2.2.1 General Perturbations

The method of general perturbations is based on the concept that a gravitational potential function for a satellite in a complex system can be described by

$$V = V_{2body} + R \quad (3.15a)$$

where V_{2body} is the potential function due to the Earth treated as a point mass, and R is a disturbing potential function due to other massive bodies, or irregularities of the Earth from its point mass representation. The effect of R must be an order of magnitude smaller than V_{2body} for general perturbations to be valid [50]. This is because the theories rely on an assumption that the motion caused by V_{2body} will only change slowly due to R . General perturbation theories use the conic section solution of the 2 body problem and determine the variations in the orbital elements caused by perturbations. An orbit history which includes the short period, long period, and secular variations caused by perturbations is called the osculating orbit.

One of the important steps in the process is obtaining analytic expressions for R which accurately represent the effect of perturbations. From the previous sections, though, we saw that disturbing functions exist only for conservative forces. This is one of the

limitations of using general perturbations. Note, however, that some general perturbation theories do incorporate the effects of non-conservative forces [5]. For example, the HANDE satellite theory, developed by Felix Hoots, incorporates atmospheric drag effects with a dynamic atmospheric model that uses Jacchia 1970 atmospheric tables [51,29]. When analytic expressions for conservative disturbing functions are determined, they are often expressed as infinite series in powers of a small parameter. While some accuracy is lost, these series must be truncated at low orders to reduce calculation time.

The principal advantage to general perturbations is in the small computation time required to carry out the orbit propagation calculations. Because analytic expressions are used throughout the process, the time of calculation is independent of the propagation time. Accuracy can be maintained if the expansions of the analytic equations are not truncated at low orders. However, retaining higher order terms can significantly increase the computation time. In practice, series truncation and the assumptions made to incorporate non-conservative perturbations reduce the accuracy of the results for large prediction times and practical physical cases [13].

3.2.2.2 Special Perturbations

The class of orbit propagators that directly integrate the equations of motion form the method of special perturbations. Given a spacecraft's current position and velocity, and equations of motion which express the influence of central body gravitation as well as all relevant perturbations, the effect of all the resulting forces can be computed over a short time period so that a new position and velocity at a future time are obtained. When this process is repeated to produce an orbit trajectory, each repetition is called a step and the time period between successive steps is the step size.

There are two primary types of error in applying special perturbations: round off and truncation error. Round off error occurs because only a finite number of significant digits are carried through the calculation. This limit forces the computer to round off the results of every calculation at the end of the significant digits. Round off error accumulates with the number of calculations performed. The net result of repeated steps of the orbit propagator can be an error in the last few significant digits of a calculated value [50]. One method of reducing round off error is increasing the number of significant digits. Another is reallocating more bits in the memory storage of a number to the mantissa from the exponent [13]. A more reasonable solution is to simply increase the step size of the propagation so that fewer calculations take place.

The maximum value of the step size, however, is limited by the truncation error. Consider the solution to the future position of a satellite expressed in terms of a Taylor series expansion

$$\mathbf{r}(t) = \mathbf{r}_o + (t - t_o) \left. \frac{d\mathbf{r}}{dt} \right|_o + \frac{(t - t_o)^2}{2!} \left. \frac{d^2\mathbf{r}}{dt^2} \right|_o + \frac{(t - t_o)^3}{3!} \left. \frac{d^3\mathbf{r}}{dt^3} \right|_o + \dots \quad (3.56)$$

where \mathbf{r}_o is the position of the satellite at initial time t_o . Truncation error is caused by limiting the number of terms of the Taylor expansion used in the numerical integration. The order of the method used describes how many terms of the Taylor expansion are maintained. For example, a 4th order Runge-Kutta integrator carries terms up to and including $(t - t_o)^4$. Because an increase in the step size $t - t_o$ causes the value of the higher order terms to increase, truncation error limits the maximum value of the step size in order to maintain a given accuracy requirement.

In 1973, Merson identified five major factors in special perturbation problems [50]. They are 1) the type of orbit, 2) the operational requirements, 3) the formulation of the

equations of motion, 4) the numerical integration method, and 5) the available computing facilities. The type of orbit is important because it directly affects the modeling of the perturbations. A orbit propagator which works well for circular orbits may not produce accurate trajectories for highly elliptical orbits. The operational requirements are usually the desired accuracy in the elements and the amount of time available for computation. The formulation of the equation of motions deals with the order of the equations being used. For example, the Lagrange planetary equations are a first-order set. The numerical integration method usually concerns whether the integrator uses previously computed values as inputs into the current value. If previous values are used, the method is considered multistep. The fifth factor, available computing facilities, have seen dramatic improvements in recent years. It has allowed numerical integration to become an option to every type of user. One additional factor, not mentioned by Merson, that must also be considered is the articulation of the physical models. These models attempt to quantify variables associated with physical systems such as the Earth's atmosphere, or the activity of the Sun. The accuracy and complexity of these models have a significant impact on the operation and function of orbit propagators.

One of the most widely applied special perturbation theories is Cowell's Method. Originally developed by Cowell and Crommelin in 1908 to investigate the motion of Jupiter's eighth satellite moon [50], this method makes no distinction between the central and disturbing functions and uses differential equations of motion expressed in rectangular coordinates. The Fixed Cowell approach is applied to low eccentricity orbits with a fixed time step of approximately 100 to 200 steps per revolution [13]. The Time Regularized Cowell approach is used for medium and high eccentricity orbits where the step size is tied to evenly spaced true anomaly values [13].

Numerical integration enjoys the advantage of being extremely accurate. In fact, the process can be tuned to the accuracy requirements of the problem at hand. The most stringent implementation of special perturbations to date has been for the Ocean Topography Experiment (TOPEX) spacecraft. The TOPEX spacecraft required 3 cm radial accuracy to support the processing of laser ranging altimeter data for ocean circulation models [8,13]. Unfortunately, the price for accuracy is large amounts of computation time. The choice between the use of special or general perturbation theory for orbit propagation usually takes many factors into account. Computing resources, orbit type, and accuracy requirements are only some of these factors.

3.2.2.3 Semi-Analytic Methods

Semi-analytic methods were devised in order to combine the accuracy of special perturbations with the elegance and quick computation time of general perturbations.

Semi-analytic methods accomplish this task by applying the Generalized Method of Averaging (GMA) to the Variation of Parameters equations of motion. This allows the orbit propagator to decompose the osculating satellite equations of motion into a part which contains the secular and long periodic effects, and a part which contains only the short periodic effects [22]. Figure 3.3 illustrates the process used by most semi-analytic methods.

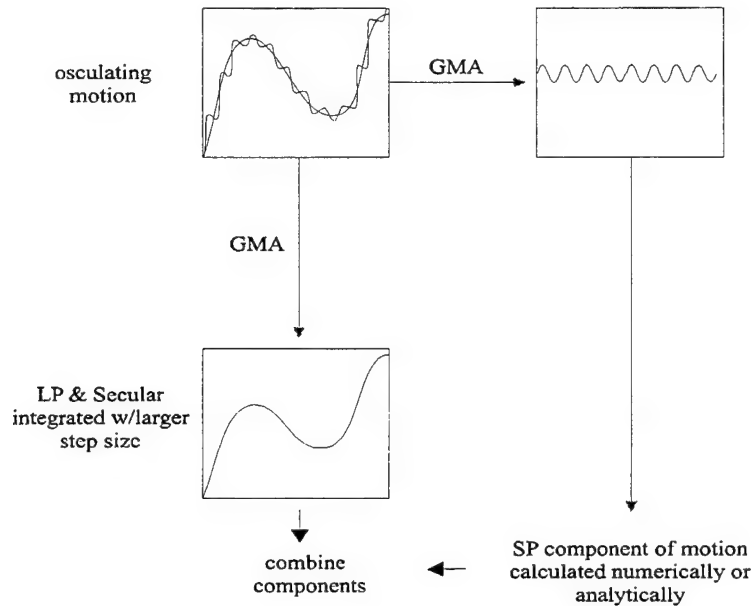


Figure 3.3: The Semi-Analytic Method [24]

The secular and long period components form the mean element equations of motion. Since all high frequency terms have been removed, the step size for the mean equations is constrained by the period of the shortest long period effect. In practice, this step size is several orders of magnitude larger than that required for the osculating equations. In fact, the step sizes can often be so large that interpolation is required to determine mean element sets at request times that fall between interval times. The short periodic equations are usually represented as a Fourier series in the satellite's "fast" variable. To achieve closed form expressions, multiple orbital longitudes are employed as the fast variable. The fast variable can be the eccentric longitude, Greenwich hour angle, mean longitude, or true longitude depending on the short periodic equation being considered. The coefficients of the Fourier series are slowly varying functions of the slowly varying elements, and thus can also be evaluated with interpolation. The short periodic variations are solved numerically or analytically and added to the mean elements at the request times to produce an osculating element history.

3.2.3 Semi-Analytic Satellite Theory

The following section provides an overview of the concepts of semi-analytic theory as it is presented in McClain's *A Semianalytic Artificial Satellite Theory* [44]. A more complete analysis is available in this reference and in a technical report completed at the Naval Postgraduate School, *Semianalytic Satellite Theory (SST): Mathematical Algorithms* [19].

3.2.3.1 The Method of Averaging

Semi-analytic orbit propagation techniques are based on the application of the Method of Averaging (MOA) to the variation of parameters equations of motion. This is done in an effort to increase the step size of the numerical integration of the equations of motion. In general, the maximum step size for the numerical integration of a set of differential equations is constrained by period of the highest frequency term in the equations. The MOA removes these high frequency (short periodic) terms. The resulting equations, called the mean element equations of motion, describe only the secular and long period motions. The orbital elements corresponding to the mean element equations are called the mean elements. The short periodic equations of motion describe only the high frequency short periodic effects.

The Method of Averaging can be applied in two ways, numerically and analytically. The analytical approach, developed first, only applies when conservative perturbing forces are considered. This is because it relies on Lagrange's formulation of the equations of motion. The numerical averaging approach applies for any type of perturbing force. It removes the high frequency terms with the use of a quadrature around an appropriate

formulation of the osculating equations of motion [44]. Numerical averaging has been successfully applied and shown to be significantly more efficient than high-precision orbit generators. Its largest drawback is that the force models must be evaluated at each step of the quadrature rather than once per time step as with analytical averaging. The computation of mean element rates is also more precise with analytical averaging [44]. The Draper Semi-analytic Satellite Theory (DSST) orbit propagator uses analytic averaging for conservative perturbations and numerical averaging for non-conservative perturbations.

3.2.3.2 Averaged VOP Equations of Motion

In the remainder of this section, the osculating equations of motion will be separated into the mean equations and the short periodic equations. We start with a formulation of the osculating equations which is readily related to both Lagrange's planetary equations of equation 3.50 and Gauss' form of the variational equations of equation 3.54.

$$\frac{da_i}{dt} = \varepsilon F_i(\mathbf{a}, l) \quad \text{for } i = 1, 2, \dots, 5 \quad (3.57a)$$

$$\frac{dl}{dt} = n(a_1) + \varepsilon F_6(\mathbf{a}, l) \quad (3.57b)$$

In equation 3.57, l is the fast variable orbital element, the vector \mathbf{a} consists of the remaining five slow varying elements, ε is a small parameter, n is the mean motion, and $F_i(\mathbf{a}, l)$ are perturbing functions which we assume to be 2π periodic in l . For conservative perturbations, the perturbing functions are constructed by the relation

$$\varepsilon F_i(\mathbf{a}, l) = - \sum_{j=1}^6 (a_i, a_j) \frac{\partial R}{\partial a_j} \quad (3.58)$$

where (a_i, a_j) is the ij Poisson bracket and R is a disturbing potential function such as that obtained for the spherical harmonic perturbations in equation 3.24. Examples of the small parameters, then, are J_2 and J_3 for zonal harmonics and C_D , the coefficient of drag, for atmospheric drag.

The fast variable l is separated from the remaining elements because it is a linear combination of the time with an element such that

$$l = nt + a_6 \quad (3.59)$$

This modification is required in order to avoid mixed secular terms [3,44].

We now assume that the osculating elements and osculating element rates can be expressed as asymptotic expansions of the mean elements and element rates, respectively, plus higher order terms.

If the mean elements are denoted with bars, then the near identity transformation from (\mathbf{a}, l) to $(\bar{\mathbf{a}}, \bar{l})$ is assumed to be

$$a_i = \bar{a}_i + \sum_{j=1}^N \varepsilon^j \eta_{i,j}(\bar{\mathbf{a}}, \bar{l}) + O(\varepsilon^{N+1}) \quad i = 1, 2, \dots, 5 \quad (3.60a)$$

$$l = \bar{l} + \sum_{j=1}^N \varepsilon^j \eta_{6,j}(\bar{\mathbf{a}}, \bar{l}) + O(\varepsilon^{N+1}) \quad (3.60b)$$

where the functions η_{ij} are 2π periodic in \bar{l} . The presence of the small parameter ε is important to the Method of Averaging because it forms the basis of later series expansions that need to be truncated.

One of the goals of the Method of Averaging is to describe the mean equations of motion in terms of only the slowly varying elements. Thus the mean equations are assumed to take the form

$$\frac{d\bar{a}_i}{dt} = \sum_{j=1}^N \varepsilon^j A_{i,j}(\bar{\mathbf{a}}) + O(\varepsilon^{N+1}) \quad (3.61a)$$

$$\frac{d\bar{l}}{dt} = n(\bar{a}_i) + \sum_{j=1}^N \varepsilon^j A_{6,j}(\bar{\mathbf{a}}) + O(\varepsilon^{N+1}) \quad (3.61b)$$

Equation 3.61 is complete with expressions for the functions $A_{i,j}$. These functions are obtained by resolving both sides of equation 3.57 and then eliminating the fast variable dependence.

Left Hand Side

We can resolve the left hand side of equation 3.57 by first taking the time derivative of equation 3.60. The resulting expressions relate the osculating element rates to the mean element rates.

$$\frac{da_i}{dt} = \frac{d\bar{a}_i}{dt} + \sum_{j=1}^N \varepsilon^j \sum_{k=1}^6 \frac{\partial \eta_{i,j}}{\partial \bar{a}_k} \frac{d\bar{a}_k}{dt} + O(\varepsilon^{N+1}) \quad (3.62a)$$

$$\frac{dl}{dt} = \frac{d\bar{l}}{dt} + \sum_{j=1}^N \varepsilon^j \sum_{k=1}^6 \frac{\partial \eta_{6,j}}{\partial \bar{a}_k} \frac{d\bar{a}_k}{dt} + O(\varepsilon^{N+1}) \quad (3.62b)$$

where a_6 means \bar{l} for the summation in equation 3.62b.

Substituting equation 3.52 into equation 3.53 and rearranging the summations yields

$$\frac{da_i}{dt} = \sum_{j=1}^N \varepsilon^j \left[A_{i,j}(\bar{\mathbf{a}}) + n(\bar{a}_1) \frac{\partial \eta_{i,j}}{\partial \bar{\ell}} + \sum_{k=1}^6 \sum_{p=1}^{j-1} A_{k,p}(\bar{\mathbf{a}}) \frac{\partial \eta_{i,j-p}}{\partial \bar{a}_k} \right] + O(\varepsilon^{N+1}) \quad (3.63a)$$

$$\frac{dl}{dt} = n(\bar{a}_1) + \sum_{j=1}^N \varepsilon^j \left[A_{6,j}(\bar{\mathbf{a}}) + n(\bar{a}_1) \frac{\partial \eta_{6,j}}{\partial \bar{\ell}} + \sum_{k=1}^6 \sum_{p=1}^{j-1} A_{k,p}(\bar{\mathbf{a}}) \frac{\partial \eta_{6,j-p}}{\partial \bar{a}_k} \right] + O(\varepsilon^{N+1}) \quad (3.63b)$$

In equation 3.63b, the summation over p is not performed for $j = 1$. Note that both the A_{ij} and η_{ij} functions are unknown at this point. To obtain expressions for them, we now address the right hand side of equation 3.57.

Right Hand Side

A related expression for the right hand side of equation 3.57 is obtained by first expanding the perturbing functions in a Taylor series about the mean elements and then rearranging the series components as a power series in the small parameter ε . This process yields the following representation of the perturbing function

$$F_i(\mathbf{a}, l) = \sum_{j=0}^N \varepsilon^j f_{i,j}(\bar{\mathbf{a}}, \bar{l}) + O(\varepsilon^{N+1}) \quad (3.64)$$

where

$$\begin{aligned} f_{i,0} &= F_i(\bar{\mathbf{a}}, \bar{l}) \\ f_{i,1} &= \sum_{k=1}^6 \eta_{k,1} \frac{\partial F_i}{\partial \bar{a}_k} \\ f_{i,2} &= \sum_{k=1}^6 \left(\eta_{k,2} \frac{\partial F_i}{\partial \bar{a}_k} + \frac{1}{2} \sum_{m=1}^6 \eta_{k,1} \eta_{m,1} \frac{\partial^2 F_i}{\partial \bar{a}_k \partial \bar{a}_m} \right) \end{aligned} \quad (3.65)$$

and so forth.

The mean motion in equation 3.57b can also be expanded in a Taylor series about the mean element \bar{a}_1 and rearranged in a power series in the small parameter ϵ . The resulting expression for the mean motion is

$$n(a_1) = \sum_{j=0}^N \epsilon^j N_j(\bar{\mathbf{a}}, \bar{l}) \quad (3.66)$$

where

$$\begin{aligned} N_0 &= n(\bar{a}_1) = \bar{n} \\ N_1 &= -\frac{3\bar{n}}{2\bar{a}_1} \eta_{1,1} \\ N_2 &= -\frac{3\bar{n}}{2\bar{a}_1} \eta_{1,2} + \frac{15\bar{n}}{8\bar{a}_1^2} \eta_{1,1}^2 \\ N_3 &= -\frac{3\bar{n}}{2\bar{a}_1} \eta_{1,3} + \frac{15\bar{n}}{4\bar{a}_1^2} \eta_{1,1} \eta_{1,2} - \frac{35\bar{n}}{16\bar{a}_1^3} \eta_{1,1}^3 \end{aligned} \quad (3.67)$$

and so forth.

Substituting equations 3.63, 3.64 and 3.66 into equation 3.57 allows us to equate like powers of ϵ to determine the j^{th} order contribution to the osculating element rates.

$$A_{i,j}(\bar{\mathbf{a}}) + n(\bar{a}_1) \frac{\partial \eta_{i,j}}{\partial \bar{l}} + \sum_{k=1}^6 \sum_{p=1}^{j-1} A_{k,p}(\bar{\mathbf{a}}) \frac{\partial \eta_{i,j-p}}{\partial a_k} = f_{i,j-1}(\bar{\mathbf{a}}, \bar{l}) \quad (3.68a)$$

$$A_{6,j}(\bar{\mathbf{a}}) + \bar{n} \frac{\partial \eta_{6,j}}{\partial \bar{l}} + \sum_{k=1}^6 \sum_{p=1}^{j-1} A_{k,p}(\bar{\mathbf{a}}) \frac{\partial \eta_{6,j-p}}{\partial a_k} = N_j(\bar{\mathbf{a}}, \bar{l}) + f_{6,j-1}(\bar{\mathbf{a}}, \bar{l}) \quad (3.68b)$$

Removing Fast Variable Dependence

Note that equation 3.68 remains a function of the fast variable l because the functions $\eta_{i,j}$ are 2π periodic in \bar{l} . To obtain expressions for the functions $A_{i,j}$ in equation 3.61, the fast variable dependence must be removed. This is accomplished by integrating both sides of equation 3.68 over the fast variable \bar{l} on the interval $[0, 2\pi]$. This process, called the averaging operation, is defined as

$$\langle H(\bar{\mathbf{a}}, \bar{l}) \rangle_{\bar{l}} = \frac{1}{2\pi} \int_0^{2\pi} H(\bar{\mathbf{a}}, \bar{l}) d\bar{l} \quad (3.69)$$

Since the functions $\eta_{i,j}$ are 2π periodic in \bar{l} ,

$$\left\langle \frac{\partial \eta_{i,j}}{\partial \bar{l}} \right\rangle_{\bar{l}} = 0 \quad (3.70)$$

Note that applying the averaging operator to equation 3.62 yields

$$\left\langle \frac{da_i}{dt} \right\rangle_{\bar{l}} = \frac{d\bar{a}_i}{dt} \quad \left\langle \frac{d\bar{l}}{dt} \right\rangle_{\bar{l}} = \frac{d\bar{l}}{dt} \quad (3.71)$$

and

$$\left\langle \frac{\partial \eta_{i,j}}{\partial \bar{a}_k} \right\rangle_{\bar{l}} = 0 \quad (3.72)$$

These constraints result in the following expressions for the j^{th} order contribution to the mean element rates

$$A_{i,j}(\bar{\mathbf{a}}) = \left\langle f_{i,j-1}(\bar{\mathbf{a}}, \bar{l}) \right\rangle_{\bar{l}} \quad (3.73a)$$

$$A_{6,j}(\bar{\mathbf{a}}) = \left\langle N_j(\bar{\mathbf{a}}, \bar{l}) \right\rangle_{\bar{l}} + \left\langle f_{6,j-1}(\bar{\mathbf{a}}, \bar{l}) \right\rangle_{\bar{l}} \quad (3.73b)$$

Substituting equation 3.71 into equation 3.61 yields the averaged equations of motion expressed in terms of the perturbing function and the mean mean motion.

$$\frac{d\bar{a}_i}{dt} = \sum_{j=1}^N \varepsilon^j \left\langle f_{i,j-1}(\bar{\mathbf{a}}, \bar{l}) \right\rangle_{\bar{l}} + O(\varepsilon^{N+1}) \quad (3.74a)$$

$$\frac{d\bar{l}}{dt} = n(\bar{a}_1) + \sum_{j=1}^N \varepsilon^j \left\langle f_{6,j-1}(\bar{\mathbf{a}}, \bar{l}) + N_j \right\rangle_{\bar{l}} + O(\varepsilon^{N+1}) \quad (3.74b)$$

Short Periodics

The short periodic contributions to equation 3.60 are determined by solving for the functions $\eta_{i,j}$. Subtracting equation 3.73 from 3.68 yields

$$\bar{n} \frac{\partial \eta_{i,j}}{\partial \bar{l}} = f^s_{i,j-1} - \sum_{p=1}^{j-1} \sum_{k=1}^6 A_{k,p} \frac{\partial \eta^s_{i,j-p}}{\partial \bar{a}_k} \quad (3.75a)$$

$$\bar{n} \frac{\partial \eta_{6,j}}{\partial \bar{l}} = f^s_{6,j-1} + N_j^s - \sum_{p=1}^{j-1} \sum_{k=1}^6 A_{k,p} \frac{\partial \eta^s_{6,j-p}}{\partial \bar{a}_k} \quad (3.75b)$$

where the superscript ^s is used to indicate the short periodic part of a function such that

$$f^s_{i,j-1} = f_{i,j-1} - \left\langle f_{i,j-1} \right\rangle_{\bar{l}} \quad (3.76)$$

Substituting equation 3.75 into equation 3.60 completely specifies the near identity transformation.

$$a_i = \bar{a}_i + \frac{1}{\bar{n}} \sum_{j=1}^N \varepsilon^j \int \left[f_{i,j-1}^s(\bar{\mathbf{a}}, \bar{l}) - \sum_{k=1}^6 \sum_{p=1}^{j-1} A_{k,p} \frac{\partial \eta_{i,j-p}^s}{\partial \bar{a}_k} \right] d\bar{l} + O(\varepsilon^{N+1}) \quad (3.77a)$$

$$l = \bar{l} + \frac{1}{\bar{n}} \sum_{j=1}^N \varepsilon^j \int \left[\{f_{6,j-1}^s(\bar{\mathbf{a}}, \bar{l}) + N_j^s\} - \sum_{k=1}^6 \sum_{p=1}^{j-1} A_{k,p} \frac{\partial \eta_{6,j-p}^s}{\partial \bar{a}_k} \right] d\bar{l} + O(\varepsilon^{N+1}) \quad (3.77b)$$

Practical Application

Equation 3.74, represents the j^{th} order contribution to the mean element rates. Admitting up to only second order contributions, equation 3.74 becomes

$$\frac{d\bar{a}_i}{dt} = \varepsilon \langle f_{i,0}(\bar{\mathbf{a}}, \bar{l}) \rangle_{\bar{l}} + \varepsilon^2 \langle f_{i,1}(\bar{\mathbf{a}}, \bar{l}) \rangle_{\bar{l}} + O(\varepsilon^3) \quad (3.78a)$$

$$\frac{d\bar{l}}{dt} = \bar{n} + \varepsilon \langle f_{6,0}(\bar{\mathbf{a}}, \bar{l}) + N_1 \rangle_{\bar{l}} + \varepsilon^2 \langle f_{6,1}(\bar{\mathbf{a}}, \bar{l}) + N_2 \rangle_{\bar{l}} + O(\varepsilon^3) \quad (3.78b)$$

Further simplification yields

$$\frac{d\bar{a}_i}{dt} = \varepsilon \langle F_i(\bar{\mathbf{a}}, \bar{l}) \rangle_{\bar{l}} + \varepsilon^2 \left\langle \sum_{k=1}^6 \eta_{k,1}(\bar{\mathbf{a}}, \bar{l}) \frac{\partial F_i(\bar{\mathbf{a}}, \bar{l})}{\partial \bar{a}_k} \right\rangle_{\bar{l}} + O(\varepsilon^3) \quad (3.79a)$$

$$\frac{d\bar{l}}{dt} = \bar{n} + \varepsilon \langle F_6(\bar{\mathbf{a}}, \bar{l}) \rangle_{\bar{l}} + \varepsilon^2 \left\langle \sum_{k=1}^6 \eta_{k,1}(\bar{\mathbf{a}}, \bar{l}) \frac{\partial F_6(\bar{\mathbf{a}}, \bar{l})}{\partial \bar{a}_k} + \frac{15}{8} \frac{\bar{n}}{\bar{a}_1^2} \eta_{1,1}^2(\bar{\mathbf{a}}, \bar{l}) \right\rangle_{\bar{l}} + O(\varepsilon^3) \quad (3.79b)$$

Note that the second order contribution to the mean element rates requires knowledge of the first order functions $\eta_{i,1}$. This implies that the computation must be done on an order by order basis.

In addition, the effects of multiple perturbing functions must be considered for practical applications. The equations developed to this point only consider one perturbation

source. To first order in the small parameters, the equations of motion for the case of two perturbing functions is

$$\frac{da_i}{dt} = \varepsilon F_i(\mathbf{a}, l) + \nu G_i(\mathbf{a}, l) \quad \text{for } i = 1, 2, \dots, 5 \quad (3.80a)$$

$$\frac{dl}{dt} = n + \varepsilon F_6(\mathbf{a}, l) + \nu G_6(\mathbf{a}, l) \quad (3.80b)$$

Equation 3.80 only represents the first order superposition. Mixed terms in the small parameters appear when considering higher order combinations.

3.3 DSST Orbit Propagator

In 1979, the Draper Laboratory initiated development of a general semi-analytical satellite theory [14]. The products of this venture were incorporated into a large software utility called the Research and Development Goddard Trajectory Determination System (R&D GTDS). Today GTDS is a package which provides a litany of orbit utilities and contains subprograms which execute general perturbation, special perturbation, and semi-analytic theories. In 1984, the semi-analytic theory was transplanted from GTDS to a medium sized standalone propagator called the Draper Semi-analytic Satellite Theory Orbit Propagator (DSST).

A 1995 study conducted by Barker, Casali, and Wallner [1] of the Kaman Sciences Corporation compared the accuracy and run times of DSST and several other semi-analytic and general perturbation theories. Orbit propagation by a full model special perturbation theory was used as a baseline. The study concluded that of all the propagators considered, DSST contained the most complete perturbation models, and

thus performed best in terms of accuracy for all four different types of orbits studied. In addition, for orbits where drag was not a major factor, DSST gave accuracy results comparable to the special perturbation baseline while only requiring 50 to 100 percent more CPU time than the strictly general perturbation theories.

The remainder of this section discusses the specific implementation of DSST used for this project. First, the capabilities and limitations of the standalone propagator are outlined. Then the software interface that was modified/developed for use with the constellation station-keeping code is reviewed. This is followed by a short explanation of why only the mean equations of motion are used. Finally, one of the limitations of DSST, which is important in the context of this project, is explored in greater detail.

3.3.1 Capabilities / Limitations

The standalone DSST propagator includes the following perturbations in the mean equations of motion [22]

- Central body gravitational spherical harmonics of arbitrary degree and order
- J_2^2 second order effect. An explicit analytical expression, truncated to the first power of the satellite eccentricity, is used for the mean element rates of change
- Third body point mass effects.
- Atmospheric drag on a spherical satellite. Both Jacchia-Roberts and Harris-Priester atmospheric density models are available.
- Solar radiation pressure on a spherical satellite with eclipsing.

The following perturbations are included in the short-periodic variations [22]

- Central body gravitational zonal harmonics of arbitrary degree.
- Central body gravitational m-daily sectoral and tesseral harmonics of arbitrary degree and order.

Lunar/solar perturbations to the short periodic variations have been added in a new version of DSST standalone[13].

All of the perturbation models listed above can be turned on or off by the user. The user must also define the epoch time, epoch state, output request times, and physical properties of the spacecraft. At each request time, the orbit generator calculates the following values

- mean equinoctial elements
- osculating equinoctial elements
- position and velocity vectors
- mean equinoctial element rates
- J_2 mean element state transition matrix

The coordinate system for the input epoch state must be either the Mean of 1950 reference frame or the true of date reference frame. The choice of integration reference frame is limited to the Mean of 1950 frame and the true of reference frame. Since no special output frame option exists, the output frame is the same as the integration frame. Note that true of date output is not available in the current version. This limitation is discussed in section 3.3.4.

3.3.2 Software Interface

Developing a versatile software interface to interact with the existing DSST orbit generator routines was a critical element of this effort. The interface had to meet several specific requirements of the parallel processing environment and the primer vector code. Rather than starting from scratch, an interface developed earlier by Scott Wallace at Draper Laboratory [58] was adopted. This old interface, called *sat_prop*, had the following capabilities functioning

- Keplerian and equinoctial element input/output
- use of a time interval with step size for definition of output request times
- orbit propagation forward in time

While Wallace's interface was developed with parallel propagation in mind, it did not enable all the functionality that existed in the DSST orbit generator. Subroutine *sat_prop* was modified in order to meet the requirements of this project. The modifications were incorporated into a new subroutine called *sat_prop_mod*, which retains essentially the same structure as *sat_prop*, but also includes the following capabilities

- position and velocity vector input
- orbit propagation backward in time
- option of including a burnlist of time specified velocity vectors
- output of J_2 based state transition matrix in position and velocity
- output of Keplerian or equinoctial element rates

3.3.3 Mean Element Theory

While the DSST orbit propagator is capable of calculating the short periodic variation of the elements, this option is not utilized in this project. Eliminating the short periodic variations implies that the mean elements, and not the osculating elements, are used by the station-keeping control laws to determine when and how much to correct the trajectory. It also indicates that only the mean equations of motion are integrated in the orbit propagator. This procedure of using only the mean elements is not unusual for station-keeping applications. In fact station-keeping planning done on real satellites also avoids including the short periodic motions [46]. This is because the mean elements reveal the long term trends in the motion of the elements better than the osculating elements. For example, consider the case of targeting nodal crossing. Because of short periodic motion, the osculating element set varies for the nodal crossing at each revolution [46]. Therefore, a mean element set must be used to target the nodal crossing. When station-keeping requirements which involve precise positioning over the ground are not considered, the mean element trajectories provide a good basis for determining the total number and size of station-keeping corrections.

3.3.4 Reference Frame Issues

In section 3.1.1, we defined the geocentric-equatorial coordinate system as an inertial reference frame, i.e. it remains fixed in space over time. In reality, however, this is not the case. Since the coordinate system is based on the Earth's equatorial plane, it undergoes a slow change with time due to the gravitational influence of the Sun, Moon, and planets. This change is primarily composed of two parts, precession and nutation. Precession is a steady rotation of the coordinate axes about the vector perpendicular to the

Earth's orbital plane. This rotation has a 26,000 year period, but the angle between the z-axis of the frame and the vector perpendicular to Earth's orbital plane, also known as the obliquity of the ecliptic ϵ , remains approximately constant at 23.5° [55]. Nutation is a periodic variation from the precession which is caused by the "nodding" of the z-axis of the geocentric-equatorial frame [55]. The period of nutation is approximately 18.6 years. Figure 3.4 illustrates the effects of precession and nutation.

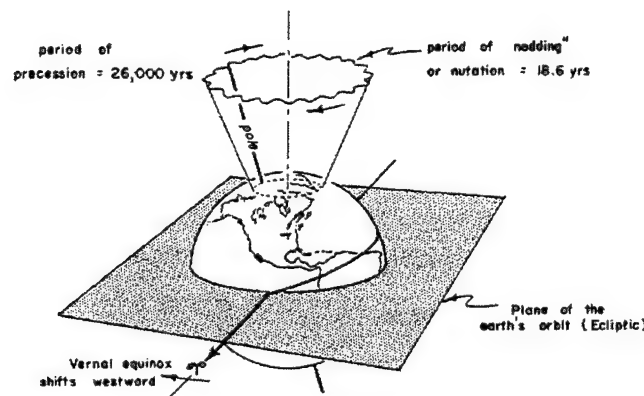


Figure 3.4: Precession and Nutation of the Equatorial Plane [2]

Because of the motion of the geocentric-equatorial coordinate system, every satellite state defined in that frame must be tagged with a specific time. At each time, there are two geocentric-equatorial coordinate systems available. The first, called the true-of-date frame, is influenced by both the nutation and precession effects on the equatorial plane, and thus represents the true location of the plane in time. The second, called the mean-of-date frame, is moved only by precession effects. In a sense, it 'averages' out the nutation effect. Common practice for Earth centered orbit determination is to use one inertial reference frame for the integration of the equations of motion. The mean-of-date frame that occurred at 1950.0 is chosen as the standard. This frame is more often referred to as the Mean of 1950 reference frame.

However, if satellite trajectories that involve some association with the ground (such as communication with Earth-based receivers) are needed, then the output of the orbit generator must be in the true-of-date frame of the time of interest. To meet this requirement, the output of the integrator must be transformed from the Mean of 1950 frame to the true of date frame at each request time. This transformation consists of two parts. The first transforms the position vector of the satellite in Mean of 1950 coordinates to the position vector in the mean-of-date coordinates at the request time with the use of the rotation matrix **A** such that

$$\mathbf{r}_{\text{mean-of-date}} = \mathbf{A} \mathbf{r}_{\text{Mean-of-1950}} \quad (3.81)$$

The second rotation matrix **N** transforms the mean-of-date position vector to the true-of-date position vector.

$$\mathbf{r}_{\text{true-of-date}} = \mathbf{N} \mathbf{r}_{\text{mean-of-date}} \quad (3.82)$$

If the two rotation matrices are multiplied such that **C** = **NA**, then the full transformation in one step is

$$\mathbf{r}_{\text{true-of-date}} = \mathbf{C} \mathbf{r}_{\text{Mean-of-1950}} \quad (3.83)$$

The transformation of the velocity vector is determined from the derivative of equation 3.83.

$$\mathbf{v}_{\text{true-of-date}} = \mathbf{C} \mathbf{v}_{\text{Mean-of-1950}} + \frac{d\mathbf{C}}{dt} \mathbf{r}_{\text{Mean-of-1950}} \quad (3.84)$$

In practice, the time derivative of **C** is often ignored. The maximum error that results from this is only 0.005 cm/sec at one Earth radius [55].

We noted in section 3.3.1 that the version of DSST used for this project does not have the capability of outputting orbital elements in the true-of-date reference frame. This would be a severe limitation if the ephemerides produced by the orbit generator were required for interaction with specific locations on the Earth. Fortunately, this does not occur anywhere in the project. In fact the ephemerides themselves are only used in the calculations of global coverage. Aside from that, only the differences in the ephemerides are used. Since the percent coverage of the Earth is not affected by the rotation transformations described in equations 3.83 and 3.84, the Mean of 1950 ephemerides are acceptable for this application.

The station-keeping controllers utilize the differences of the actual satellite states (propagated in the presence of perturbations) from nominal satellite states. Since the nominal trajectories themselves are propagated and output in Mean of 1950 coordinates, our only concern is to ensure that the differences between the actual and nominal trajectory in the Mean of 1950 coordinates are the same as the differences between the actual and nominal trajectory in true-of-date coordinates. This condition is verified by executing a test run on the version of SST available in the GTDS software package. GTDS/SST is able to output elements in the instantaneous true-of-date frame.

The test case involves one satellite of the Ellipso Borealis constellation plane. Two executions of the GTDS code are required. The first calculates the difference between the actual and nominal satellite states in the Mean of 1950 frame. The second calculates the difference between the two trajectories in the true-of-date frames of the corresponding comparison times. The nominal trajectory includes only the zonal geopotential field model to 21st degree. The actual satellite trajectory includes a full 21x21 geopotential field, tesseral resonance, solar radiation pressure, atmospheric drag, and solar/lunar third body effects. The GTDS input decks for both of these runs and difference plots in

Keplerian elements are located in Appendix A. A summary of the radial, cross track and along track differences are tabulated in table 3.4.

Table 3.4: Comparison of Mean of 1950 and True of Date Differences

Date	Radial Difference (km)			Cross-Track Difference (km)			Along-Track Differences (km)		
	Mean of 1950	True of Date	Delta	Mean of 1950	True of Date	Delta	Mean of 1950	True of Date	Delta
1-Jan-98	4.61634E+03	4.61634E+03	0.00000E+00	-3.53598E+00	-3.53598E+00	0.00000E+00	1.24410E+04	1.24410E+04	0.00000E+00
1-Jan-99	7.33585E+03	7.33585E+03	0.00000E+00	6.79117E+00	6.79117E+00	0.00000E+00	6.99304E+03	6.99304E+03	0.00000E+00
1-Jan-00	5.49901E+01	5.49901E+01	0.00000E+00	8.61351E+00	8.61351E+00	0.00000E+00	-4.88708E+03	-4.88708E+03	0.00000E+00
1-Jan-01	1.77929E+05	1.77929E+05	0.00000E+00	2.88769E+02	2.88769E+02	0.00000E+00	3.61889E+03	3.61889E+03	0.00000E+00
1-Jan-02	1.34257E+03	1.34257E+03	0.00000E+00	-3.94606E+02	-3.94606E+02	0.00000E+00	8.41482E+03	8.41482E+03	0.00000E+00

The orbital element difference plots for the Mean of 1950 output and true of date output are identical in all respects. The data in table 3.1 agrees with the plots. It shows that the differences are identical down to at least 10 m in the radial direction, 1 m in the cross-track direction, and 1 m in the along track direction. The differences produced in the two different reference frames were so close that this case was rerun to guard against any errors. The conclusion is that the difference of the actual and nominal trajectory in the Mean of 1950 reference frame is the same as the difference in the true of date frame, for at least 5 years. Therefore, using Mean of 1950 state differences as the basis for determining control commands is acceptable.

[This page intentionally left blank.]

Chapter 4

Lyapunov Control

4.1 History of Lyapunov Control Methods

In the late 19th century, the Russian mathematician Alexandr Mikhailovich Lyapunov developed general approaches for studying non-linear motion. Lyapunov's work, published in 1892, contains two methods which are still considered to be the most useful approaches for the stability analysis of non-linear systems [54]. The first, called the linearization method, develops conclusions about the local stability of a non-linear system from the stability properties of its linear approximation. The second, called the direct method, determines the stability of a non-linear system by analyzing an energy-type function developed from the system variables. Lyapunov's work went largely ignored outside of Russia until the 1960's. According to Slotine and Li [54], however, the linearization method has since become the justification for linear control and the direct method is now considered to be the most important tool for non-linear system analysis and design.

Since satellite motion is by its nature non-linear, consideration of Lyapunov control theory for the problem of station-keeping was inevitable. This chapter explains the design for several Lyapunov controllers designed for satellite station-keeping. First, it begins with a summary of the important definitions and theorems which form the basis of Lyapunov control theory. An approach for developing discrete controllers is also reviewed. Finally three different controllers, each corresponding to a different

formulation of an artificial potential function, are proposed. The following chapter details the ideas and approaches taken; implementation is left to be pursued at a later date.

4.2 Fundamentals of Lyapunov Control Theory

The following summary of the fundamental concepts of Lyapunov control theory is composed of two parts. The first part, covering sections 4.2.1 to 4.2.5, is the mathematical basis for Lyapunov control. The overview of this material borrows heavily from Slotine and Li's *Applied Non-Linear Control* [54]. This reference provides an excellent introduction to general non-linear control theory. The second part, sections 4.2.6 and 4.2.7, introduces artificial potential functions and outlines how they are used to apply the theorems and definitions covered in the first part.

The first of Lyapunov's methods, linearization, is based upon the idea that a non-linear system will behave like a linear system in the local region about a point when small motions are considered. While this method is valid for many systems, it has limitations. The first is that it can only provide information about the local stability of the system. Finding the point at which the linearization assumption is no longer valid can be difficult. For satellite motion which incorporates the effects of multiple significant disturbing perturbations, the linearization assumption can be tenuous. For these reasons, the approach taken with this project is to delay having to linearize the equations of motion until absolutely necessary for developing a control solution. Therefore, only Lyapunov's second, direct method is pursued further.

4.2.1 Equilibrium Points and Autonomy

A general n^{th} order non-linear system of equations can be expressed by the vector relation

$$\dot{\mathbf{x}} = \mathbf{f}(\mathbf{x}, t) \quad (4.1)$$

where \mathbf{x} is an $n \times 1$ vector containing the state variable of the system, t is time, and \mathbf{f} is a non-linear vector function describing the motion of the state variables x_1, x_2, \dots, x_n . While the vector \mathbf{x} describes n values, it is still considered a 'point' in state space. The solution to equation 4.1 is the curve in state space described by the vector function $\mathbf{x}(t)$. The solution over time is often called the state trajectory. For non-linear systems of equations, determining $\mathbf{x}(t)$ explicitly as a closed form solution in terms of elementary functions is not always possible. When $\mathbf{x}(t)$ is not available directly, an analysis of the stability of the system described by equation 4.1 can be conducted to determine the motion about the system equilibrium points.

If equation 4.1 describes the dynamics of a system which includes a closed-loop feedback controller, then it can also be written as

$$\dot{\mathbf{x}} = \mathbf{f}(\mathbf{x}, \mathbf{u}, t) \quad (4.2)$$

where the control law is some function of the state and time.

$$\mathbf{u} = \mathbf{g}(\mathbf{x}, t) \quad (4.3)$$

The stability properties of a closed-loop feedback system tell us how well the control law addresses the goals of the control problem.

If the system dynamics are linear, equation 4.1 can also be expressed as

$$\dot{\mathbf{x}} = \mathbf{A}(t) \mathbf{x} \quad (4.4)$$

where \mathbf{A} is an $n \times n$ matrix.

Linear systems are divided into two categories, time-varying and time-invariant. If all the components of the matrix \mathbf{A} in equation 4.4 were constant, then the associated system would be time-invariant. The non-linear analogs to time-varying and time-invariant are non-autonomous and autonomous. Slotine and Li define a non-linear system to be autonomous if the vector function \mathbf{f} does not depend explicitly on time. An autonomous system can be described by

$$\dot{\mathbf{x}} = \mathbf{f}(\mathbf{x}). \quad (4.5)$$

All systems with time dependent vector functions are non-autonomous. For a system which describes closed loop dynamics to be autonomous, both the vector function and the control law must be explicitly independent of time. Therefore,

$$\dot{\mathbf{x}} = \mathbf{f}(\mathbf{x}, \mathbf{u}) \quad (4.6)$$

is autonomous only if \mathbf{u} is explicitly independent of time, or

$$\mathbf{u} = \mathbf{g}(\mathbf{x}). \quad (4.7)$$

The motion of satellites without orbital perturbations is dependent only on the orbital elements, and thus is autonomous. However, when perturbations which depend on the location of other bodies, such as solar/lunar third body affects and solar radiation pressure, or perturbations which depend on the intensity of the sun, such as atmospheric drag, are included, the system of equations becomes time dependent and thus non-autonomous. But, if we assume that the equations describing satellite motion vary slowly with time, or

$$\frac{\partial \mathbf{f}}{\partial t} \approx 0 \quad (4.8)$$

then the system can once again be considered to be autonomous. Slotine and Li point out that all real physical systems are technically non-autonomous since none of the dynamic characteristics can be time invariant. In practice, though, if system properties change slowly change with time, the time variation can often be neglected with little meaningful error.

An examination of the stability of non-linear systems is done around special points called equilibrium points. An equilibrium point, \mathbf{x}^* , is defined as a point in state space where

$$\mathbf{f}(\mathbf{x}^*, t) = \mathbf{0} \quad \forall t > t_o.$$

This is equivalent to saying that once the system reaches an equilibrium point, it will always remain there unless disturbed.

4.2.2 Tracking Nominal Motion

Not all dynamic control problems can be defined as trying to maintain a state space equilibrium point. In some cases, the desire is to maintain the motion of the system. Maintaining the trajectory of an airplane in the presence of wind gusts is an example of this type of problem. The stability of such systems is concerned with how well the motion of a trajectory modified by small perturbations will track the original motion trajectory.

Slotine and Li show how this class of problem can be transformed into an equilibrium point stability problem. The system resulting from the transformation, however, is always

non-autonomous regardless of whether the original system was autonomous or non-autonomous. To illustrate this process, consider the autonomous system described by equation 4.5. Let $\mathbf{x}^*(t)$ be the solution to equation 4.5 corresponding to the initial condition $\mathbf{x}^*(0) = \mathbf{x}_0$. Call the trajectory defined by $\mathbf{x}^*(t)$ the nominal motion trajectory. Then, if equation 4.5 is solved for a slightly perturbed initial condition such that

$$\mathbf{x}(0) = \mathbf{x}_0 + \delta \mathbf{x}_0,$$

the resulting perturbed trajectory, $\mathbf{x}(t)$, will not follow the original nominal trajectory. Define the difference between the two trajectories at any time $t > t_0$ as the motion error

$$\mathbf{e}(t) = \mathbf{x}(t) - \mathbf{x}^*(t) \quad (4.9)$$

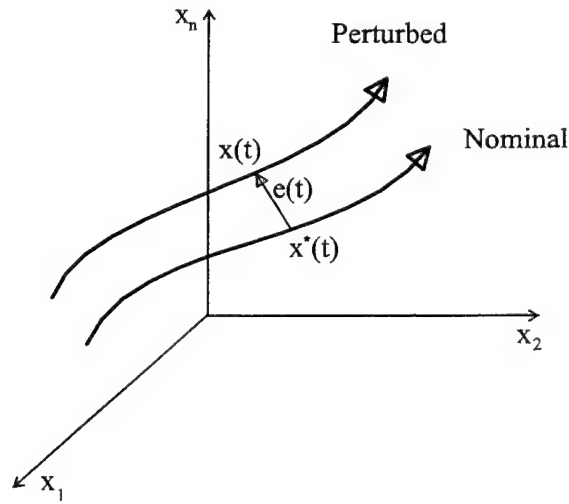


Figure 4.1: Nominal and Perturbed Trajectories [54]

Since both trajectories satisfy the system of equations,

$$\begin{aligned} \dot{\mathbf{x}}^* &= \mathbf{f}(\mathbf{x}^*), & \mathbf{x}(0) &= \mathbf{x}_0 \\ \dot{\mathbf{x}} &= \mathbf{f}(\mathbf{x}), & \mathbf{x}(0) &= \mathbf{x}_0 + \delta \mathbf{x}_0 \end{aligned} \quad (4.10a,b)$$

Then $\mathbf{e}(t)$ satisfies the following non-autonomous differential equation.

$$\dot{\mathbf{e}} = \mathbf{f}(\mathbf{x}^* + \mathbf{e}) - \mathbf{f}(\mathbf{x}^*) = \mathbf{h}(\mathbf{e}, t) \quad (4.11)$$

with initial condition $\mathbf{e}(0) = \delta \mathbf{x}_0$. Since $\mathbf{e}(t_i) = \mathbf{0}$ for a time $t_i > t_0$ implies $\mathbf{e}(t) = \mathbf{0}$ and $\mathbf{h}(\mathbf{e}(t), t) = \mathbf{0}$ for all $t > t_i$, the new dynamic system with \mathbf{e} as the state and \mathbf{h} as the non-linear, non-autonomous vector function has an equilibrium point at the origin of the new state space. Therefore, a controller which can drive \mathbf{e} directly to or near its equilibrium point over a time period in the presence of disturbances will also control a perturbed trajectory so that it converges to the nominal trajectory in the same manner. Note that the controller can only affect the error from the nominal trajectory by adjusting the perturbed trajectory. The stability characteristics of a satellite system, which includes a controller and disturbances, about its equilibrium point define how well the controller performs its function.

4.2.3 Stability

To study the stability characteristics of non-linear systems, we must first define the concepts of stability. When some system is said to be stable, the statement being made is that the system trajectory will remain within a certain bound of its equilibrium point if the trajectory's initial point is sufficiently close to that equilibrium point. Stated mathematically, the equilibrium state $\mathbf{x} = \mathbf{0}$ is stable at t_0 if, for any $R > 0$, there exists an $r(R, t_0) > 0$, such that $|\mathbf{x}(0)| < r$ implies $|\mathbf{x}(t)| < R$ for all $t \geq t_0$. The equilibrium point is locally uniformly stable at t_0 if r can be chosen independently of the initial time t_0 . Since autonomous systems are time-invariant, stability and uniform stability for these systems are synonymous.

An equilibrium point is said to be asymptotically stable if it is stable and the trajectory will eventually move closer to the equilibrium point as time continues given that the initial point of the system trajectory is sufficiently close to the equilibrium point. Stated mathematically, an equilibrium point $\mathbf{0}$ is asymptotically stable at t_0 if it is stable and if there exists an $r(t_0) > 0$ such that $|\mathbf{x}(0)| < r$ implies that $\mathbf{x} \rightarrow \mathbf{0}$ as $t \rightarrow \infty$. As before, the equilibrium point is locally uniformly asymptotically stable if r can be chosen independently of t_0 .

In the context of satellite station-keeping, asymptotic stability implies that not only will a satellite perturbed from its nominal trajectory remain in the vicinity of the nominal trajectory, but that the control input and natural motion of the satellite will combine to drive the satellite back to the nominal trajectory. This is the stability characteristic which is the goal for any Lyapunov controlled system of equations.

4.2.4 Lyapunov Functions

Lyapunov's direct method is based on the idea that if the energy is continually dissipated from a system, then it must eventually reach an equilibrium point. Thus, the stability characteristics of a system can be determined by examining the behavior of a scalar function which describes the 'energy' of that system.

Slotine and Li illustrate this energy relationship with the autonomous mass spring/damper system shown in Figure 4.2. The equation of motion which describes this system is

$$m\ddot{x} + b\dot{x} + k_0x + k_1x^3 = 0 \quad (4.12)$$

where $b\dot{x}|\dot{x}|$ is the non-linear dissipation, or damping, and $(k_o x + k_1 x^3)$ is the non-linear spring term. The closed form solution to equation 4.12, $x(t)$, cannot be determined in terms of elementary functions. However, examining the behavior of the system energy does reveal information about the motion of the system. Equation 4.13 represents the total mechanical energy of the system.

$$V(x) = \frac{1}{2}m\dot{x}^2 + \int_0^x (k_o x + k_1 x^3) dx = \frac{1}{2}m\dot{x}^2 + \frac{1}{2}k_o x^2 + \frac{1}{4}k_1 x^4 \quad (4.13)$$

The following conclusions can be drawn:

1. Zero energy corresponds to the equilibrium point ($x = 0, \dot{x} = 0$)
2. Asymptotic stability implies the convergence of mechanical energy to zero.
3. Instability is related to the growth of mechanical energy.

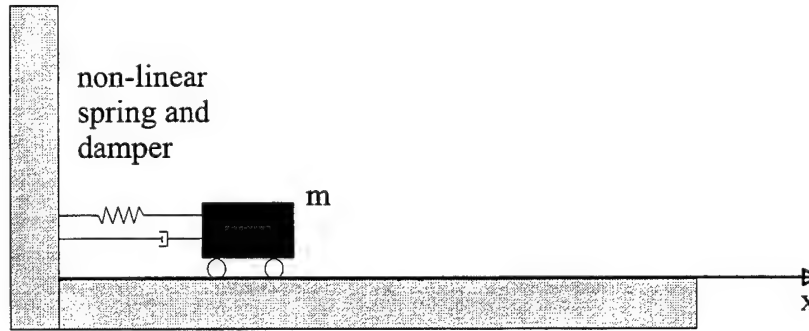


Figure 4.2: Non-linear Mass Spring/Damper System [54]

Therefore, we see that the value of the mechanical energy is directly related to the state of the system at any time. The rate of change of energy for this is

$$\dot{V}(x) = m\dot{x}\ddot{x} + (k_o x + k_1 x^3)\dot{x} = \dot{x}(-b\dot{x}|\dot{x}|) = -b|\dot{x}|^3 \quad (4.14)$$

Equation 4.14 suggests that the energy of the system is continuously dissipated until the mass settles to its equilibrium state. Therefore, by examining the form of the energy of

the non-linear system of figure 4.2, we can make conclusions about its stability characteristics even though we cannot explicitly solve the system equations of motion.

One of the important properties of energy functions is that they must be positive definite. A time-invariant scalar function $V(\mathbf{x})$ is said to be locally positive definite if $V(\mathbf{0}) = 0$ and in a ball \mathbf{B}_{R_0} , $\mathbf{x} \neq \mathbf{0}$ implies $V(\mathbf{x}) > 0$. The notation \mathbf{B}_{R_0} denotes the spherical region, or ball, defined by $|\mathbf{x}| < R_0$ and centered at the equilibrium point $\mathbf{x} = \mathbf{0}$ in state space. If the positive definiteness holds over the entire state space, then the function is globally positive definite. If $V(\mathbf{0}) = 0$ and $V(\mathbf{x}) \geq 0$ for all $\mathbf{x} \neq \mathbf{0}$, then the scalar function $V(\mathbf{x})$ is said to be positive semi-definite.

A time-varying scalar function $V(\mathbf{x},t)$ is said to be locally positive definite if $V(\mathbf{0},t) = 0$ and there exists a time-invariant positive definite function $V_0(\mathbf{x})$ such that $V(\mathbf{x},t) \geq V_0(\mathbf{x})$ for all $t > t_0$. This last requirement is the same as saying $V(\mathbf{x},t)$ dominates $V_0(\mathbf{x})$. A time-varying scalar function $V(\mathbf{x},t)$ is decrescent if $V(\mathbf{0},t) = 0$, and if there exists a time-invariant positive definite function $V_1(\mathbf{x})$ which dominates it.

Any scalar function $V(\mathbf{x})$ [$V(\mathbf{x},t)$] is negative definite if $-V(\mathbf{x})$ [$-V(\mathbf{x},t)$] is positive definite.

The typical shape of a time-invariant positive definite function is shown in figure 4.3.

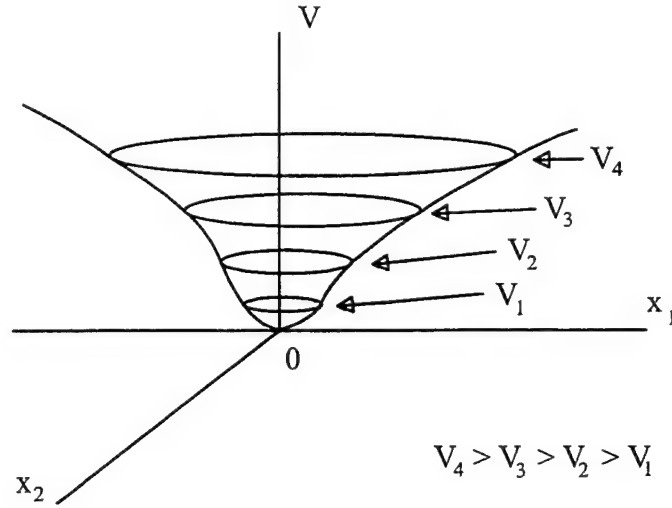


Figure 4.3: Positive Definite Function $V(\mathbf{x})$

One of the critical elements involved in the analysis of the mass spring/damper system of figure 4.2 is the rate of change of the scalar energy function. The energy function is an implicit function of time, and assuming that it is differentiable, it can generally be determined by the chain rule, or

$$\dot{V} = \frac{dV(\mathbf{x},t)}{dt} = \frac{\partial V}{\partial t} + \frac{\partial V}{\partial \mathbf{x}} \dot{\mathbf{x}} = \frac{\partial V}{\partial t} + [\nabla V(\mathbf{x})]^T \mathbf{f}(\mathbf{x}) \quad (4.15a)$$

where $\nabla V(\mathbf{x})$ is the gradient of the energy function. If the scalar function V is time-invariant, then

$$\frac{\partial V}{\partial t} = 0 \quad \text{and} \quad \dot{V} = [\nabla V(\mathbf{x})]^T \mathbf{f}(\mathbf{x}) \quad (4.15b)$$

Energy-like functions whose derivatives display the behavior demonstrated in the mass spring/damper example form the basis of Lyapunov's direct method, and are given the name Lyapunov functions. Any scalar function $V(\mathbf{x},t)$ with continuous partial derivatives is a Lyapunov function if it meets the following criteria:

- 1) V is positive definite.
- 2) \dot{V} exists and is negative semi-definite.

4.2.5 Lyapunov Theorem For Stability

The core of Lyapunov's direct method lies in how Lyapunov functions reveal the stability of non-linear systems. This relationship is stated in Lyapunov's Theorem for Local Stability.

For autonomous systems, the theorem is as follows. If, in a ball \mathbf{B}_{R_0} , there exists a scalar function $V(\mathbf{x})$ with continuous first partial derivatives such that

- V is positive definite (locally in \mathbf{B}_{R_0})
- \dot{V} is negative semi-definite (locally in \mathbf{B}_{R_0})

then the equilibrium point $\mathbf{0}$ is locally stable. If \dot{V} is locally negative definite, then the system is asymptotically stable at the equilibrium point.

For non-autonomous systems, the theorem is the same except that the scalar function can be of the form $V(\mathbf{x}, t)$. Furthermore, if V is decrescent, then the system is uniformly asymptotically stable at the equilibrium point.

Note that there is no requirement that the Lyapunov function for a non-autonomous system be time-varying. Since a time-invariant scalar function $V(\mathbf{x})$ is constant with respect to time, it is dominated by itself. Therefore, if this scalar function is positive definite, it is also decrescent. This means that when a time-invariant Lyapunov function is used for a non-autonomous system, if the system meets the conditions for being asymptotically stable, it also meets the conditions for being uniformly asymptotically stable.

The two critical steps in the procedure to determine the stability of a non-linear system using Lyapunov's direct method are to choose a positive definite scalar function and to determine if that scalar function meets the conditions which qualify it to be a Lyapunov function. The second step is generally accomplished by analyzing the time derivative of the scalar function.

Note that many Lyapunov functions can exist for the same system. Slotine and Li demonstrate that if V is a Lyapunov function for a given system, then so is

$$V_1 = \rho V^\alpha \quad (4.16)$$

where ρ is any strictly positive constant and α is any scalar greater than 1. Multiple Lyapunov functions for the same system are not limited to the relationship shown in equation 4.16. They can be of different forms altogether. While different choices of Lyapunov functions will not produce contradictory stability conclusions, some choices may reveal more about the system than others.

4.2.6 Artificial Potential Functions

Lyapunov functions for simpler non-linear systems can be obtained from a purely mathematical approach. As long as the conditions for a Lyapunov function are met, Lyapunov's theorem still applies. Purely mathematical approaches for determining Lyapunov functions for complex non-linear systems, however, become extremely complicated. Instead, physical insight into the dynamics of the system can be used to generate functions which not only work, but reveal the nature of the stability in an elegant fashion.

The example of a robot arm control is used by Slotine and Li to demonstrate this point. A robot arm is composed of a series of joints connected by links. The control inputs are the motor torques applied at each of the joints. The dynamics of an n -joint robot arm can be expressed as

$$\mathbf{H}(\mathbf{q})\ddot{\mathbf{q}} + \mathbf{b}(\mathbf{q}, \dot{\mathbf{q}}) + \mathbf{g}(\mathbf{q}) = \boldsymbol{\tau} \quad (4.17)$$

where \mathbf{q} is an n -dimensional vector describing joint positions, $\boldsymbol{\tau}$ is the vector of input torques, \mathbf{g} is the vector of gravitational torques, \mathbf{b} represents the Coriolis and centripetal forces caused by motion of the links, and \mathbf{H} is the $n \times n$ inertia matrix of the robot arm. Note that the “state” for this system is the $2n$ element vector containing the components of \mathbf{q} and $\dot{\mathbf{q}}$. The traditional control law used for robot arms is to use proportional and derivative feedbacks with a gravity compensation element, as shown in equation 4.18.

$$\boldsymbol{\tau} = -\mathbf{K}_D \dot{\mathbf{q}} - \mathbf{K}_P \mathbf{q} + \mathbf{g}(\mathbf{q}) \quad (4.18)$$

Here \mathbf{K}_P and \mathbf{K}_D are positive definite $n \times n$ matrices.

If a 5-link or 6-link robot arm is considered, equation 4.17 suddenly contains hundreds of terms. A trial and error approach for finding a Lyapunov function for such a system will not work. Instead, an appreciation for the physical nature of the problem is used. Since \mathbf{H} must be positive definite for any vector \mathbf{q} , the following scalar function is proposed

$$V(\mathbf{q}, \dot{\mathbf{q}}) = \frac{1}{2} [\dot{\mathbf{q}}^T \mathbf{H} \dot{\mathbf{q}} + \mathbf{q}^T \mathbf{K}_P \mathbf{q}] \quad (4.19)$$

The first term represents the kinetic energy of the manipulator and the second term represents an ‘artificial potential energy’ since the elements of \mathbf{K}_P can be interpreted as mimicking a combination of springs and dampers.

The energy theorem in mechanics states that the rate of change of kinetic energy is equal to the power provided by the external forces. Using this understanding, the derivative of the proposed scalar function becomes

$$\dot{V} = \dot{\mathbf{q}}^T (\boldsymbol{\tau} - \mathbf{g}) + \dot{\mathbf{q}}^T \mathbf{K}_p \mathbf{q} \quad (4.20)$$

Substituting equation 4.18 into equation 4.20, we have

$$\dot{V} = -\dot{\mathbf{q}}^T \mathbf{K}_D \dot{\mathbf{q}} \quad (4.21)$$

Since \mathbf{K}_D is positive definite and $\dot{\mathbf{q}}$ cannot be zero at any point other than $\mathbf{q} = \mathbf{0}$, equation 4.21 is always negative definite.

Therefore, we have demonstrated that the control law from equation 4.18 causes the robot arm to be asymptotically stable about its equilibrium point with the use of a Lyapunov function obtained only from appreciating the physical properties of the problem. When terms which simulate an energy-like property of the problem, like $\mathbf{q}^T \mathbf{K}_p \mathbf{q}$ in equation 4.19, are used, the resulting Lyapunov functions are often called potential functions or artificial potential functions. As shown, they can work remarkably well for complex systems.

4.2.7 Discrete Control Approaches

In all of the examples and equations considered so far, the control input into the system of equations has always been a continuous function of the state (equation 4.7), or a continuous function of the state and time (equation 4.3). For the station-keeping system, however, the planned control inputs are impulsive burns. To address this problem we

turn to an approach developed by McInnes which allows the use of discrete controllers with Lyapunov control theory [41,42,43].

If a time-invariant positive definite scalar function is used as a candidate for the Lyapunov function of a system, then the time derivative of that function is of the form

$$\dot{V} = [\nabla V(\mathbf{x})]^T \dot{\mathbf{x}}. \quad (4.22)$$

According to Lyapunov's theorem for stability, equation 4.22 must be negative definite for the equilibrium point to be asymptotically stable. We can insure that \dot{V} will be negative by defining switching times for the application of a discrete control, such as

$$\begin{aligned} \dot{V}(t) < 0 &\Rightarrow u(t) = 0 \\ \dot{V}(t) \geq 0 &\Rightarrow u(t) = 1 \end{aligned} \quad (4.23)$$

In equation 4.23, $u(t) = 1$ indicates that the controller is activated. The next question is what instantaneous change must the control event produce? Consider figure 4.4.

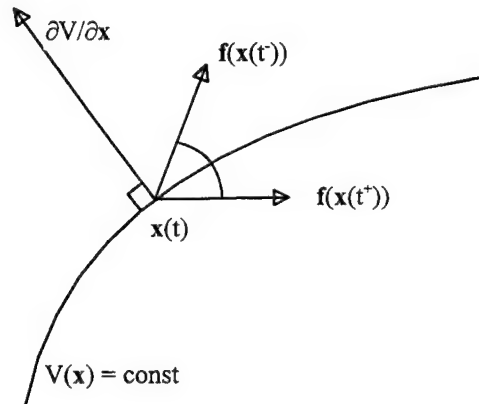


Figure 4.4: Gradient of Potential Function and State Velocity Vector [39]

In this figure, t^- and t^+ are defined as the times immediately before and after an instantaneous control event, respectively. $\mathbf{f}(\mathbf{x}(t^-))$ is the state velocity vector before the

control event, or $\mathbf{x}(t)$. Note that equation 4.22 is positive only when the state space 'angle' between $\mathbf{f}(\mathbf{x}(t))$ and the gradient of the potential function, $\partial V/\partial \mathbf{x}$, is less than 90° . \dot{V} will be negative after the control event if the angle separating the state velocity vector and the gradient vector is greater than 90° . In fact, the largest reduction in the value of the potential function after the control event occurs if the state velocity vector after the control event, $\mathbf{f}(\mathbf{x}(t^+))$ or $\dot{\mathbf{x}}(t^+)$, is in the direction opposite to the gradient vector. This is defined as the steepest approach method of determining the control event. Therefore, we wish to execute an instantaneous control event $\Delta \dot{\mathbf{x}}$ such that

$$\dot{\mathbf{x}}(t^+) = \dot{\mathbf{x}}(t^-) + \Delta \dot{\mathbf{x}} = -K(\mathbf{x}, \dot{\mathbf{x}}(t^-)) \frac{\nabla V}{|\nabla V|} \quad (4.24)$$

where K is a positive scalar function of the state and state rate before the control event. If $\dot{\mathbf{x}}(t^+)$ can be achieved as defined in equation 4.24, then the rate of change of the scalar function immediately after the control event is

$$\dot{V}(t^+) = -K(\mathbf{x}, \dot{\mathbf{x}}(t^-)) |\nabla V| \quad (4.25)$$

Equations 4.23 and 4.25 together insure that the rate of change of the proposed scalar potential function will always be negative definite. Then by Lyapunov's stability theorem, we can conclude that the system with the controller defined by equation 4.24 is asymptotically stable at the equilibrium point.

One of the implicit assumptions made in using the discrete controller above is that continuity in state is maintained across the discrete control events. Mathematically, this implies that

$$\mathbf{x}(t^+) = \mathbf{x}(t^-) = \mathbf{x}(t). \quad (4.26)$$

Continuity of the state also insures continuity of the gradient of the potential function across the control event. If equation 4.26 is not enforced, then an interesting situation may develop where the discrete control events implemented to insure that $\dot{V}(t^+)$ remains negative also moves the state away from the equilibrium point in discrete steps. If this occurs, the system may not be asymptotically stable.

Another assumption is that the controller has control authority to change the elements defined in equation 4.24. For example, a satellite using impulsive burns only has control authority to implement instantaneous changes in its velocity vector. Instantaneous changes in position and acceleration vectors, are not possible. But, it may be possible to simulate instantaneous changes in elements over which the controller has no authority by executing a series of control events over a finite time. The time must be finite, and preferably small, for the system to be asymptotically stable.

The effort to simulate changes in elements for which the controller has no instantaneous authority, by applying multiple control events over finite periods of time, was developed for this project. Since its implementation is dependent on the particular artificial potential function being used, it will be explained in more detail in the following section. It is important to note, however, that since the following methods were not coded or tested in this project, a validation of this procedure does not exist at this time.

4.3 Lyapunov Control for Station-Keeping

In the following section, three different approaches for implementing Lyapunov control in the context of satellite station-keeping are proposed. Each of the approaches is defined

by a unique artificial potential function which is used to derive the control law. All three approaches are designed to control the station-keeping of only one satellite.

Each of the three approaches is designed to be used in the context of a control scheme which checks the station-keeping status of the satellite at evenly spaced times during the satellites trajectory. The time between checks on the satellite state is the iteration step size for the governing control loop. All the methods also assume the capability of achieving a calculated target state at the next iteration time step. This orbital transfer problem was solved in chapter 2 using primer vector theory. Recall from chapter 2 that the calculation of an n -impulse near-optimal transfer trajectory required the transfer time to be shorter than one orbital period. Because of this limitation, the iteration step size of the governing control loop must also be shorter than one orbital period.

The first artificial potential function contains only the position difference from the nominal orbit as the state. This is done to conform to constraints imposed by lack of control authority. The second and third potential functions attempt to circumvent this constraint by applying multiple burns over the following iteration time interval. The second potential function contains all 6 elements required to uniquely define a satellite's orbital state. It is implemented with the orbital elements rather than position and velocity vectors. The third potential function attempts to expand upon the second by including the state rates in the potential function as well. To accomplish this, however, some assumptions need to be made. The control goal of all three functions is to track the nominal reference trajectory.

Some new vector comparison operators are introduced for use in the sections to follow.

If \mathbf{a} and \mathbf{b} are n element vectors, then

$$\begin{aligned}
\mathbf{a} \hat{>} \mathbf{b} &: \text{if } a_i > b_i \quad \forall i \in (1, \dots, n) \\
\mathbf{a} \succ \mathbf{b} &: \text{if } \exists i \in (1, \dots, n) \quad \ni a_i > b_i
\end{aligned} \tag{4.27}$$

4.3.1 Potential Function with Position Vector State

The following notation is used in this section,:

\mathbf{x}_p	:	actual position vector
\mathbf{r}_p	:	nominal position vector
\mathbf{x}_v	:	actual velocity vector
\mathbf{r}_v	:	nominal velocity vector
$\delta \mathbf{r}_{\max, p}$:	maximum parameter limits on position
$\delta \mathbf{r}_{\text{db}, p}$:	deadband parameter limits on position
$\delta \mathbf{r}_{\max, v}$:	maximum parameter limits on velocity
$\delta \mathbf{r}_{\text{db}, v}$:	deadband parameter limits on velocity
\mathbf{M}	:	positive definite shaping matrix (3 x 3)

The elements of $\delta \mathbf{r}_{\max, p}$ and $\delta \mathbf{r}_{\max, v}$ are the maximum deviations of the respective vector beyond which mission capability is degraded. The minimum goal of the control system, then, is to insure that the position and velocity vectors of the actual satellite never violate the following requirements

$$\begin{aligned}
\left(r_p^i - \delta r_{\max, p}^i \right) &\leq x_p^i \leq \left(r_p^i + \delta r_{\max, p}^i \right) & \text{and} \\
\left(r_v^i - \delta r_{\max, v}^i \right) &\leq x_v^i \leq \left(r_v^i + \delta r_{\max, v}^i \right) & \text{for } i = 1, 2, 3
\end{aligned} \tag{4.28}$$

The real goal, of course, is to drive the difference of the actual and nominal position and velocity vectors to nearly zero, or in other words, to have the actual trajectory track the nominal trajectory. For this purpose, we define the differences as

$$\begin{aligned} \mathbf{z}_p(t) &= \mathbf{x}_p(t) - \mathbf{r}_p(t) \quad \text{and} \\ \mathbf{z}_v(t) &= \mathbf{x}_v(t) - \mathbf{r}_v(t) \end{aligned} \quad (4.29a,b)$$

Attempting to maintain absolute zero difference in \mathbf{z}_p and \mathbf{z}_v would require an impulsive burn at every time step. This is possible, but is not worth the fuel expenditure when small errors from the nominal are acceptable. For this reason, deadband limits are introduced. If the elements of \mathbf{z}_p and \mathbf{z}_v lie within the deadband regions defined by $\delta \mathbf{r}_{db, p}$ and $\delta \mathbf{r}_{db, v}$ then there is no reason to execute a correction to the actual state of the satellite.

Now define the artificial potential function as

$$V = \frac{1}{2} \mathbf{z}_p^T \mathbf{M} \mathbf{z}_p \quad (4.30)$$

Since \mathbf{M} is a positive definite matrix, equation 4.29 is a positive definite function. Note that we are defining the 'state' in this example to include only the position. The limitations of taking this step are discussed below.

The gradient of the potential function is

$$\nabla V = \frac{\partial V}{\partial \mathbf{z}_p} = \mathbf{M} \mathbf{z}_p \quad (4.31)$$

The time derivative of the potential function is

$$\dot{V} = \frac{dV}{dt} = [\nabla V]^T \dot{\mathbf{z}}_p = \mathbf{z}_p^T \mathbf{M} \dot{\mathbf{z}}_p = \mathbf{z}_p^T \mathbf{M} \mathbf{z}_v \quad (4.32)$$

By Lyapunov's stability theorem, the system will be asymptotically stable about the equilibrium point at the origin if \dot{V} is always negative definite. To insure that this is true along the state trajectory, we define the following impulsive thruster firing function

$$u(t) = \begin{cases} 1, & \dot{V}(t) > 0, \text{ and } \left[\left(\mathbf{z}_p(t) \succ \delta \mathbf{r}_{db,p} \right) \text{ or } \left(\mathbf{z}_v(t) \succ \delta \mathbf{r}_{db,v} \right) \right] \\ 0, & \text{elsewhere} \end{cases} \quad (4.33)$$

where the deadband limits discussed previously have been incorporated. The introduction of the deadbands allows the possibility that \dot{V} may be zero or positive for times when the actual satellite is within the deadband region of the nominal trajectory. But if the equilibrium 'point' is redefined to mean the entire region in state space within the deadband limits, then we can still claim that the resulting system is asymptotically stable about the deadband region. Within the deadband region, we are not concerned about the value of the state.

Using the method of steepest descent (explained in section 4.2.7) the control input when $u(t) = 1$ is

$$\Delta \mathbf{v} = \Delta \mathbf{z}_v(t) = \mathbf{z}_v(t^+) - \mathbf{z}_v(t^-) = -K \nabla V - \mathbf{z}_v(t^-) = -K \mathbf{M} \mathbf{z}_p - \mathbf{z}_v(t^-) \quad (4.34)$$

Note from equation 4.34 that the control input for this potential function is an instantaneous change in velocity only. An impulsive thruster is capable of performing this control. Since impulsive burns do not affect the position vector, state continuity and gradient continuity are maintained across the burn, or

$$\begin{aligned} \mathbf{z}_p(t^+) &= \mathbf{z}_p(t^-) = \mathbf{z}_p(t) \\ \nabla V(t^+) &= \nabla V(t^-) = \nabla V(t) \end{aligned}$$

The time derivative of the potential function immediately following the impulsive burn is

$$\dot{V}(t^+) = -K |\nabla V|^2 \quad (4.35)$$

Since K is a positive valued function, equation is assured to be negative definite.

For the control law defined by equation 4.34 there is state (position) feedback and state rate (velocity) feedback to the system dynamics. This implies that oscillations in difference of the actual and nominal position trajectories will be damped. However, such a conclusion cannot be made about the relative velocity trajectories. The possibility that the controller will enforce convergence of the position trajectories by radical maneuvers that leave a large difference in velocity between the actual and nominal trajectory exists. One way to correct for this is to reduce the magnitude of the corrections as the position error, \mathbf{z}_p , approaches the origin. To do this, we introduce a new scalar function L into the control law so that now

$$\Delta \mathbf{v} = \mathbf{z}_v(t^+) - \mathbf{z}_v(t^-) = -K(\mathbf{z}_p, \mathbf{z}_v^-) \mathbf{M} \mathbf{z}_p - L(\mathbf{z}_p) \mathbf{z}_v^- \quad (4.36)$$

Recall that K is a positive scalar function of the state and state rate prior to the control input. In a similar manner, let L be a positive scalar function of the state such that

$$L(\mathbf{z}_p) = \ell \|\mathbf{z}_p\|^m \quad (4.37)$$

The values of ℓ and m are left as parameters to be optimized. While the introduction of the function L may help reduce large corrections when the position error is small, it is not a complete fix. Since the potential function ignores errors in velocity, the possibility of large velocity oscillations still exists. One solution to this problem is to expand the potential function to include velocity elements.

4.3.2 Potential Function with Full 6-Element State

The following notation is used in this section:

\mathbf{x}	:	actual satellite vector (orbital elements)
\mathbf{r}	:	nominal trajectory vector (orbital elements)
$\delta \mathbf{r}_{\max}$:	maximum orbital element parameter limits
$\delta \mathbf{r}_{\text{db}}$:	deadband orbital element parameter limits
\mathbf{M}	:	positive definite shaping matrix (6 x 6)

Since a minimum of six parameters are needed to uniquely define the orbital state of a satellite, the state vector for the potential function in this section contains 6 elements. Orbital elements are used instead of the position and velocity vectors to take advantage of the versatility of the shaping matrix \mathbf{M} . The use of \mathbf{M} is explained shortly.

First, define the state of the system as the difference between the actual orbital elements of a satellite and the orbital elements of the nominal trajectory

$$\mathbf{z}(t) = \mathbf{x}(t) - \mathbf{r}(t) \quad (4.38)$$

The motion of the state is described by

$$\dot{\mathbf{z}}(t) = \dot{\mathbf{x}}(t) - \dot{\mathbf{r}}(t) \quad (4.39)$$

Now define a potential function V as

$$V = \frac{1}{2} \mathbf{z}^T \mathbf{M} \mathbf{z} \quad (4.40)$$

Since \mathbf{M} is a positive definite matrix, equation 4.40 is assured to be a positive definite function. Note that the eigenvectors of the shaping matrix \mathbf{M} determine what the 7-dimensional plot of the potential function is. The shape is particularly important when using the method of steepest descent to determine control inputs. This method causes the state trajectory to converge to the origin using a path that depends on the 'shape' of the function V . If \mathbf{M} is a diagonal matrix, then increasing the i^{th} component of the diagonal, whose values have already been scaled to balance the units of the different elements,

causes a 6-dimensional ‘valley’ to form in the direction of the i^{th} component. Valleys in the potential function can be created to make the controlled system reduce the error in certain orbital elements before addressing others. Adjusting the components of \mathbf{M} is left as a direction to explore once a Lyapunov controller is fully implemented.

The gradient and time derivative of the potential function are

$$\nabla V = \frac{\partial V}{\partial \mathbf{z}} = \mathbf{M} \mathbf{z} \quad (4.41)$$

$$\dot{V} = \frac{dV}{dt} = [\nabla V]^T \dot{\mathbf{z}} = \mathbf{z}^T \mathbf{M} \dot{\mathbf{z}} \quad (4.42)$$

respectively. To insure that \dot{V} is negative definite, the following discrete control function is introduced

$$u(t) = \begin{cases} 1, & \dot{V}(t) > 0, \text{ and } \mathbf{z}(t) \succ \delta \mathbf{r}_{db} \\ 0, & \text{elsewhere} \end{cases} \quad (4.43)$$

Using the steepest descent method, the instantaneous control input must be

$$\Delta \dot{\mathbf{z}} = \dot{\mathbf{z}}(t^+) - \dot{\mathbf{z}}(t^-) = -K \nabla V - \dot{\mathbf{z}}(t^-) = -K \mathbf{M} \mathbf{z} - \dot{\mathbf{z}}(t^-) \quad (4.44)$$

If this control input can be executed, the time derivative of the potential function immediately after the control input becomes

$$\dot{V}(t^+) = -K |\nabla V|^2 \quad (4.45)$$

which is clearly negative definite. The conditions for Lyapunov asymptotic stability have been theoretically obtained. The next step is to ascertain whether the control input is feasible.

Equation 4.44 suggests that the control input must cause an instantaneous change in the difference of the orbital element rates while maintaining continuity in the difference of the orbital elements. Since the reference trajectory is unaffected by disturbances or control inputs,

$$\dot{\mathbf{r}}(t^+) = \dot{\mathbf{r}}(t^-) = \dot{\mathbf{r}}(t) \quad \text{or} \quad \Delta \dot{\mathbf{r}} = \mathbf{0} \quad . \quad (4.46)$$

Applying equation 4.39, the control input becomes

$$\Delta \dot{\mathbf{z}} = \Delta \dot{\mathbf{x}} = -\mathbf{K} \mathbf{M} \mathbf{z} - \dot{\mathbf{z}}(t^-) \quad (4.47)$$

which correctly implies that only the actual satellite executes the control. The required control input, then, is an instantaneous change in the orbital element rates of the satellite with no accompanying change in the orbital elements themselves. Clearly, this can not be accomplished with a single impulsive burn. Therefore, the system does not have enough control authority to execute this maneuver as an instantaneous change.

The application of the potential function of equation 4.40 can be salvaged by taking advantage of the manner in which the control system is implemented. As explained in the introduction of section 4.3, the state of the satellite with respect to the nominal trajectory is sampled only at iteration time steps. Control inputs are also only contemplated at these times. Let t_0 be the time of the current iteration time step and $t_0 + \Delta t$ the time of the next iteration time step. If the satellite had enough control authority to execute the required maneuver, no further maneuvers could be contemplated until the next time step anyway. Therefore, if we can apply a series of impulsive burns, over the time span from t_0 to $t_0 + \Delta t$, that cause the satellite to attain the state that it would have attained by implementing the original instantaneous maneuver, then we will have

successfully simulated that instantaneous maneuver. The following paragraphs explain how this simulation is accomplished.

First, propagate the nominal state and actual satellite state to the next iteration time assuming no control input at the current time. Note that the propagation of the nominal trajectory does not include unwanted perturbations that are treated as disturbances. The state difference at $t_o + \Delta t$ is

$$\mathbf{z}_{prop}(t_o + \Delta t) = \mathbf{x}_{prop}(t_o + \Delta t) - \mathbf{r}_{prop}(t_o + \Delta t) \quad (4.48)$$

where the subscript 'prop' refers to element sets determined through orbit propagation of the original state and state rate at time t_o . For a small Δt , we can assume that

$$\mathbf{z}_{prop}(t_o + \Delta t) \approx \mathbf{z}(t_o) + [\dot{\mathbf{z}}(t_o)]\Delta t \quad (4.49)$$

This formulation neglects second order effects on the orbital elements. Since Δt must be less than one orbital period, equation 4.49 is a valid estimate.

Now, if an instantaneous $\Delta \dot{\mathbf{z}}$ had been applied at time t_o such that there was no accompanying $\Delta \mathbf{z}$, then to first order, the perturbed state difference at time $t_o + \Delta t$ would be

$$\mathbf{z}_{pert}(t_o + \Delta t) = \mathbf{z}(t_o) + [\dot{\mathbf{z}}(t_o) + \Delta \dot{\mathbf{z}}]\Delta t \quad (4.50)$$

where the subscript 'pert' refers to element sets determined through orbit propagation of the original state and perturbed state rate at time t_o . Substituting equation 4.49 into 4.50 results in

$$\mathbf{z}_{pert}(t_o + \Delta t) \approx \mathbf{z}_{prop}(t_o) + [\Delta \dot{\mathbf{z}}]\Delta t \quad (4.51)$$

Since no control measures affect the nominal trajectory,

$$\mathbf{r}_{pert}(t_0 + \Delta t) = \mathbf{r}_{prop}(t_0 + \Delta t) \quad (4.52)$$

Using equation 4.52, equation 4.51 can be restated as

$$\mathbf{x}_{pert}(t_0 + \Delta t) \approx \mathbf{x}_{prop}(t_0) + [\Delta \dot{\mathbf{z}}] \Delta t \quad (4.53)$$

If $\mathbf{x}(t_0)$ is considered the initial state and $\mathbf{x}_{pert}(t_0 + \Delta t)$ is considered the target state, then primer vector theory can be applied to calculate a near-optimal n-impulse transfer trajectory. Allowing the actual satellite to follow this transfer trajectory brings it to the same state as would have been obtained if an instantaneous change $\Delta \dot{\mathbf{x}}$ had been possible at time t_0 . It is important to note that this process simulates the effects of an instantaneous change in state rate ($\Delta \dot{\mathbf{x}}$) on the state, but not on the state rate itself. If second order information is available, then a similar procedure can be constructed to estimate the effects on the state rates as well.

The use of this procedure, which simulates an instantaneous $\Delta \dot{\mathbf{x}}$ control input over the following iteration time interval, retains the stability properties defined by meeting Lyapunov's conditions for stability. There is still some important information which remains unused, however. The DSST orbit propagator generates satellite orbital elements and orbital element rates. The use of these rates in the potential function may improve the performance of a Lyapunov controller.

4.3.3 Potential Function with Full State and State Rate

The variable notation for this section is the same as for the previous section with a few exceptions. \mathbf{M} is now the 6 x 6 positive definite shaping matrix for \mathbf{z} , and a new 6 x 6 positive definite matrix, \mathbf{N} , is the shaping matrix for $\dot{\mathbf{z}}$.

To incorporate state rate information into the control process, define a new potential function

$$V = \frac{1}{2} \mathbf{z}^T \mathbf{M} \mathbf{z} + \frac{1}{2} \dot{\mathbf{z}}^T \mathbf{N} \dot{\mathbf{z}} \quad (4.54)$$

Note that this potential function does not reach a value of zero when the nominal and actual trajectories are the same. This is because $\dot{\mathbf{z}}(t) \neq \mathbf{0}$ when $\mathbf{z}(t) = \mathbf{0}$. In fact, because disturbing perturbations are always present, $\dot{\mathbf{z}}(t)$ does not equal $\mathbf{0}$ for any time t . However, this potential function may qualify as a Lyapunov function for an equilibrium point described by

$$\mathbf{z}^T \mathbf{M} \mathbf{z} = -\dot{\mathbf{z}}^T \mathbf{N} \dot{\mathbf{z}} \quad (4.55)$$

To be sure, we need to show that the gradient of V at the equilibrium point of equation 4.55 is zero.

Begin by first calculating the partial derivatives of the potential function. The partial derivative of V with respect to the state difference, \mathbf{z} , is

$$\frac{\partial V}{\partial \mathbf{z}} = \mathbf{M} \mathbf{z} + \left[\frac{\partial \dot{\mathbf{z}}}{\partial \mathbf{z}} \right]^T \mathbf{N} \dot{\mathbf{z}} \quad (4.56)$$

The partial derivative of $\dot{\mathbf{z}}$ with respect to \mathbf{z} is essentially the matrix of partial derivatives which defines the dynamics of \mathbf{z} . Sometimes it is also referred to as the force matrix. If

$$\mathbf{A}_z = \frac{\partial \dot{\mathbf{z}}}{\partial \mathbf{z}} \quad (4.57)$$

then

$$\frac{d \Phi_z(t, \tau)}{dt} = \mathbf{A}_z \Phi_z(t, \tau) \quad (4.58)$$

where $\Phi(t, \tau)$ is the state transition matrix for \mathbf{z} such that

$$\mathbf{z}(t) = \Phi(t, \tau) \mathbf{z}(\tau) \quad (4.59)$$

To find the components of \mathbf{A}_z , take the partial derivative of the two sides of equation 4.39. This results in

$$\frac{\partial \dot{\mathbf{z}}}{\partial \mathbf{z}} = \frac{\partial \dot{\mathbf{x}}}{\partial \mathbf{x}} \frac{\partial \mathbf{x}}{\partial \mathbf{z}} - \frac{\partial \dot{\mathbf{r}}}{\partial \mathbf{r}} \frac{\partial \mathbf{r}}{\partial \mathbf{z}} \quad (4.60)$$

Taking the partial derivative of equation 4.38 with respect to \mathbf{x} and \mathbf{r} , results in the following equations.

$$\frac{\partial \mathbf{z}}{\partial \mathbf{x}} = \mathbf{I} - \frac{\partial \mathbf{r}}{\partial \mathbf{x}} \quad (4.61)$$

$$\frac{\partial \mathbf{z}}{\partial \mathbf{r}} = \frac{\partial \mathbf{x}}{\partial \mathbf{r}} - \mathbf{I} \quad (4.62)$$

Since the motion of \mathbf{x} and \mathbf{r} are independent of each other

$$\frac{\partial \mathbf{x}}{\partial \mathbf{r}} = \mathbf{0} \quad \text{and} \quad \frac{\partial \mathbf{r}}{\partial \mathbf{x}} = \mathbf{0} \quad (4.63a,b)$$

Substituting equations 4.61, 4.62, 4.63a, and 4.63b into equation 4.60 yields

$$\mathbf{A}_z = \frac{\partial \dot{\mathbf{z}}}{\partial \mathbf{z}} = \frac{\partial \dot{\mathbf{x}}}{\partial \mathbf{x}} - \frac{\partial \dot{\mathbf{r}}}{\partial \mathbf{r}} \quad (4.64)$$

which is equivalent to

$$\mathbf{A}_z = \mathbf{A}_x - \mathbf{A}_r \quad (4.65)$$

The formulation of \mathbf{A}_z in equation 4.65 is convenient because the DSST orbit propagator analytically calculates the \mathbf{A}_x and \mathbf{A}_r matrices for 2-body + J_2 geopotential dynamics in the process of propagating the \mathbf{x} and \mathbf{r} states, respectively. Since the perturbation caused by the J_2 geopotential is three orders of magnitude greater than the effect of the next largest geopotential term, and the time interval between iteration time steps is less than one orbital period, using the \mathbf{A} matrices provided by the propagator is an acceptable approximation.

Having solved for $\partial \dot{\mathbf{z}} / \partial \mathbf{z}$, equation 4.56 becomes

$$\frac{\partial V}{\partial \mathbf{z}} = \mathbf{M} \mathbf{z} + \mathbf{A}_z^T \mathbf{N} \dot{\mathbf{z}} \quad (4.66)$$

The partial derivative of V with respect to the state difference rate, $\dot{\mathbf{z}}$, is

$$\frac{\partial V}{\partial \dot{\mathbf{z}}} = \mathbf{N} \dot{\mathbf{z}} + \left[\frac{\partial \mathbf{z}}{\partial \dot{\mathbf{z}}} \right]^T \mathbf{M} \mathbf{z} = \mathbf{N} \dot{\mathbf{z}} + \mathbf{A}_z^{-T} \mathbf{M} \mathbf{z} \quad (4.67)$$

Since \mathbf{A}_z is the result of subtracting two matrices which describe very similar motions, it is likely to be singular or near-singular. Trying to find its inverse could be a very

difficult task if it is possible at all. Instead, consider what $\partial \mathbf{z} / \partial \dot{\mathbf{z}}$ means. It represents the affect on the state of changing the state rates. This analogous to second order terms such as $\ddot{\mathbf{z}}$. If we assume that $\dot{\mathbf{z}}$ varies very slowly through the course of an orbit, then we can ignore all second order terms and $\partial \mathbf{z} / \partial \dot{\mathbf{z}}$. This assumption may not be valid for highly eccentric orbits or those orbits heavily affected by atmospheric drag. If such an assumption is made, though, equation 4.67 becomes

$$\frac{\partial V}{\partial \dot{\mathbf{z}}} = \mathbf{N} \dot{\mathbf{z}} \quad (4.68)$$

Having expressions for the partial derivatives, the gradient of the potential function is

$$\nabla V = \begin{bmatrix} \frac{\partial V}{\partial \mathbf{z}} \\ \frac{\partial V}{\partial \dot{\mathbf{z}}} \end{bmatrix} = \begin{bmatrix} \mathbf{M} \mathbf{z} + \mathbf{A}_z^T \mathbf{N} \dot{\mathbf{z}} \\ \mathbf{N} \dot{\mathbf{z}} \end{bmatrix} \quad (4.69)$$

The control input needed to follow the steepest descent method results in the following motion

$$\begin{bmatrix} \dot{\mathbf{z}}(t^+) \\ \ddot{\mathbf{z}}(t^+) \end{bmatrix} = -K [\nabla V(t^+)] = -K \begin{bmatrix} \mathbf{M} \mathbf{z}(t^+) + \mathbf{A}_z(t^+)^T \mathbf{N} \dot{\mathbf{z}}(t^+) \\ \mathbf{N} \dot{\mathbf{z}}(t^+) \end{bmatrix} \quad (4.70)$$

As with the previous potential functions, the satellite orbital element state \mathbf{x} must be constrained so that it is continuous across the control input. Since the trajectory is unaffected by the controls, the state difference, \mathbf{z} , and its associated force matrix, \mathbf{A}_z , must also be continuous across the control event.

$$\begin{aligned} \mathbf{z}(t^+) &= \mathbf{z}(t^-) = \mathbf{z}(t) & \text{and} \\ \mathbf{A}_z(t^+) &= \mathbf{A}_z(t^-) = \mathbf{A}_z(t) \end{aligned} \quad (4.71a,b)$$

Ignoring the second order requirements and incorporating the continuities defined by equations 4.71a and 4.71b, equation 4.70 becomes

$$\dot{\mathbf{z}}(t^+) = -K[\mathbf{M}\mathbf{z} + \mathbf{A}_z^T \mathbf{N}\dot{\mathbf{z}}(t^+)] \quad (4.72)$$

Solving for $\dot{\mathbf{z}}(t^+)$ yields

$$\dot{\mathbf{z}}(t^+) = -K[\mathbf{I} + K\mathbf{A}_z^T \mathbf{N}]^{-1} \mathbf{M}\mathbf{z} \quad (4.73)$$

Since \mathbf{z} is continuous and second order terms with $\ddot{\mathbf{z}}$ are ignored, the control input must be

$$\Delta\dot{\mathbf{z}} = \dot{\mathbf{z}}(t^+) - \dot{\mathbf{z}}(t^-) = -\dot{\mathbf{z}}(t^-) - K[\mathbf{I} + K\mathbf{A}_z^T \mathbf{N}]^{-1} \mathbf{M}\mathbf{z} \quad (4.74)$$

A impulsive thruster cannot achieve the change in state difference rates required by 4.74. Therefore, the method of simulating an instantaneous change in state difference rates through with the use of a series of impulsive burns over the following iteration time interval, described in section 4.3.2, must be used. The resulting control system incorporates orbital elements and orbital element rate information to track a nominal trajectory. Note that the existence of the first order assumption needed to go from equation 4.70 to equation 4.72 may restrict the type of orbits this controller is good for.

To appreciate how state difference rate information changes the control law, recall the control law obtained from the previous potential function which did not include the state difference rate. This control law is restated as equation 4.75.

$$\Delta\dot{\mathbf{z}} = -\dot{\mathbf{z}}(t^-) - K\mathbf{M}\mathbf{z} \quad (4.75)$$

The state rate contribution is introduced with the $K\mathbf{A}_z\mathbf{N}$ term of equation 4.74. Since \mathbf{A}_z is a sparse matrix, the instantaneous control inputs defined by equations 4.74 and 4.75 are nearly parallel. The effectiveness of each of the control laws can be determined by implementing them on a simulation like the one developed for this project.

Chapter 5

Automated Station-Keeping Simulator

The Automated Station-Keeping Simulator is a technology demonstration software product which combines an accurate satellite orbit propagator and an optimal impulsive rendezvous planner to test different control methodologies for the constellation station-keeping problem in a parallel computing environment. This unique combination of functions has been assembled as a tool for the orbit designer as well as the orbit maintainer. For the designer, it provides a detailed and accurate analysis of the performance of a constellation's orbit over long time spans. And for the maintainer, it provides a method for easily testing different station-keeping controllers and measuring their comparative performance.

This chapter begins with a summary of the capabilities of the simulator. Section 5.2 contains an overview of the operations and data flow at all levels of the software. Section 5.3 outlines some of the important data structures in the code and the software features of many of the routines. Section 5.4 contains a description of an input file. Section 5.5 describes the networking environment used for this thesis project. Section 5.6 lists the current location of the ASKS source code and output of the simulation runs conducted for this project. And finally, several areas for future improvements are discussed in section 5.7.

5.1 Capabilities

The Automated Station-Keeping Simulator (ASKS) was designed to be an accurate, useful tool that can be applied to virtually any type of satellite constellation. Special care was taken throughout the development process to avoid making assumptions about the constellations to be considered, thus making it as generally applicable as possible. ASKS is also a work in progress. It is expected that more functionality will be added in the near future. The capabilities of the current version of ASKS are summarized below.

ASKS can operate on constellations of any size. The number of satellites in the constellation defines the number of processes that will execute simultaneously to solve the problem. Therefore, given a fixed amount of computing capability, it takes longer to run for a larger constellation. But since ASKS operates in a parallel processing environment, computing capability can be added by simply adding more workstations to the parallel network, and distributing the workload. When using the Message Passing Interface (MPI), this is as easy as adding the names of the additional workstations onto a list. This capability allows for the use of several standard workstations rather than requiring one more powerful machine when dealing with larger constellations.

ASKS is capable of studying satellite orbits of virtually any type: LEO, MEO, HEO, GEO, etc. There is also no requirement for the orbits to be circular or near-circular. The DSST orbit propagator has demonstrated accuracy with medium and highly eccentric orbits [1,23]. Since equinoctial elements are used in the propagation, the singularities traditionally faced with circular and equatorial orbits don't exist. However, ASKS is not capable of dealing with parabolic or hyperbolic trajectories. None of the generated impulsive burns will transfer the satellite out of elliptical orbit.

In addition to accepting general orbits, the simulation includes accurate perturbation modeling. The user has the option of switching on the following perturbing effects in both the nominal and actual satellite trajectories:

- spherical harmonics to arbitrary degree and order
- solar radiation pressure
- atmospheric drag, and
- solar/lunar third body point mass disturbances

A Jacchia-Roberts atmospheric density model, which incorporates monthly solar flux and geomagnetic indices provided by Schatten [7], is used in the determination of the drag effects. All perturbation models are implemented within the DSST orbit propagator. In comparison tests with other general perturbation and semi-analytic propagators, DSST proved to be an excellent compromise between computational efficiency and prediction accuracy [1].

One of the most adaptable aspects of ASKS is the way it deals with station-keeping controllers. In its current version, there are four controllers available. Each of these is discussed in greater detail in the following chapter. For any of the controllers, however, the user is able to define the orbital element limits of the satellites, as well as the way and amount in which each of the elements are to be corrected. Note that the orbital element limits must apply to every satellite in the constellation. Adding more control methodologies only requires modification of one subroutine, *target*.

During a run, ASKS stores the nominal state, nominal state rate, actual state, actual state rate, and their respective differences at each iteration time step. In addition, it calculates and stores the magnitude, direction, and time history of the sequence of optimal n -impulse transfers required to stay within the user defined orbital element limits. The

simulation also provides the coverage of the satellite constellation at each time step. N-way coverage information is available for different latitude bands across the Earth. This option is included for communication constellations that have coverage requirements over only populated areas.

5.2 System Design

The operating architecture of the ASKS design includes two functional categories: ground station and satellite. This architecture was chosen to emulate the operation of a real constellation. All communication between the functional elements is analogous to communication between two satellites or between satellite and ground station. All the duties of the ground station are executed by one process while each satellite in the constellation executes on its own process. Therefore, for an n satellite system, there are $n+1$ simultaneous processes executed for a run. These processes communicate information to each other using the Message Passing Interface (MPI) [27,56]. MPI is a list of communication protocols common across a distributed network of workstations. Actual constellations will include a capability called crosslink. This means that neighboring satellites in the constellation can communicate with each other independent of the ground station. While MPI allows independent communication between subordinate processes, the current version of ASKS requires all communication to go through the ground station first. Note that in the following sections, the terms 'ground station' and 'satellite' are often used to designate the computer processes that simulate their actions.

5.2.1 Ground Station Operation

The ground station process duties include obtaining the constellation profile from the input file, transmitting the appropriate satellite state and nominal state to each satellite process at startup, updating the nominal mean anomalies and ascending nodes of each satellite at each time step, calculating coverage at each time step, and storing all the constellation data at each time step in an output file. Figure 5.1 illustrates the process in flowchart form. All boxes with bars at the sides symbolize actions that involve communication with multiple satellite processes.

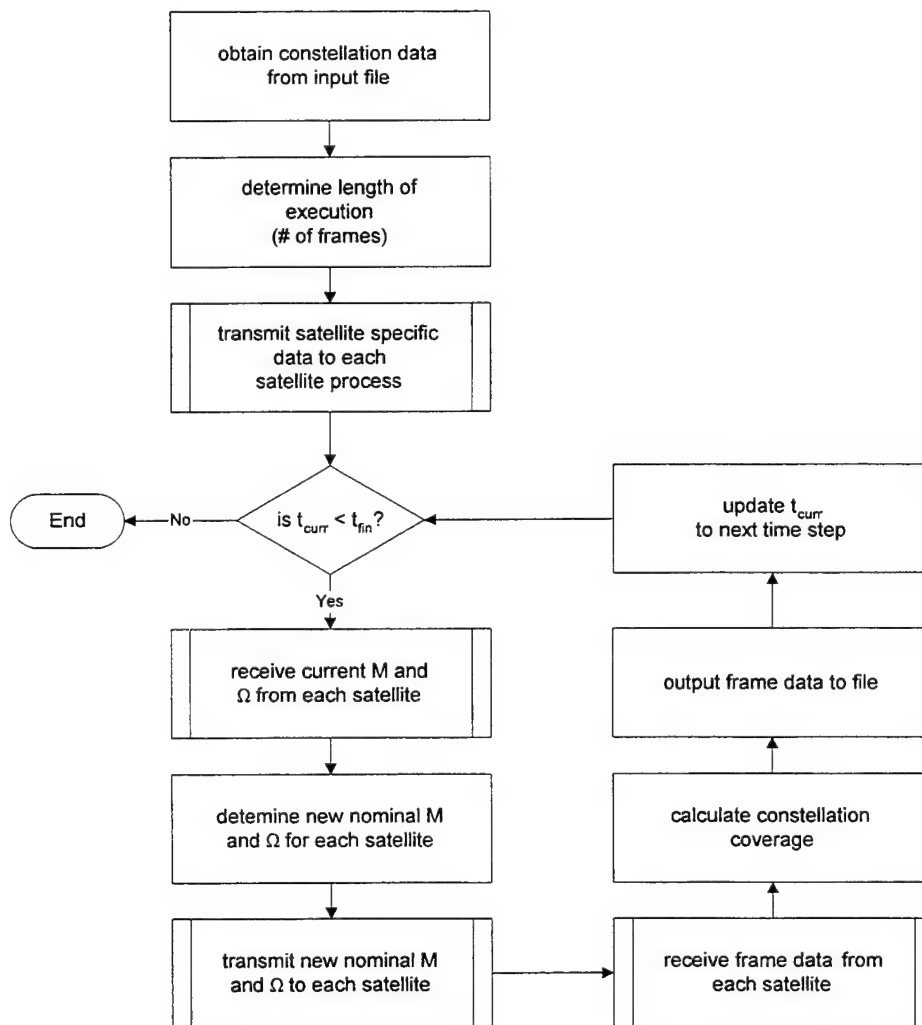


Figure 5.1: Ground Station Process Flowchart

The term used to define all the operations in one time step is the *frame*. The frame number is important for synchronizing communications with the subordinate satellite processes. For example, when collecting the mean anomaly and ascending node from each of the satellites at a time step, it is important to use only information from that time step alone. This is done by tagging the transmitted information with the frame number of the time step. Therefore, when collecting information from the multiple satellite processes, the ground station will only access communication packets that are tagged with the frame number of interest.

The mean anomaly M and the ascending node Ω for the nominal trajectories of the satellites are recalculated at each time step to take advantage of the M and Ω motions of the actual satellites, which are common across the planes and constellation. For example, there is no need to correct the mean anomaly disturbance of a satellite from its nominal value if the remaining satellites in the same plane experience the same disturbance. Since relative mean anomaly spacing is the factor of interest, the nominal mean anomaly values for each satellite in a plane are updated at each time step so that the sum of the square of the difference between the actual and nominal M values are minimized. This method requires the least amount of correction for the entire constellation. A similar procedure is applied for the relative spacing of the ascending nodes of the planes in the constellation.

Global coverage is calculated using a software package developed by Brian Kantsiper [35]. This package analytically calculates the n -way coverage of a constellation, averaged over one orbital period, using the inclusion-exclusion principle. It allows for the use of elliptical orbits and has the capability of applying latitude restrictors so that coverage at particular latitude bands can be analyzed. This coverage utility was chosen because calculating coverage analytically is significantly more efficient than using numerical techniques for constellations of less than approximately 50 satellites [35].

5.2.2 Satellite Operation

Each satellite process is responsible for continuously propagating the nominal and actual states of the satellite assigned to it by the ground station. A satellite process operates on the same satellite throughout the run.

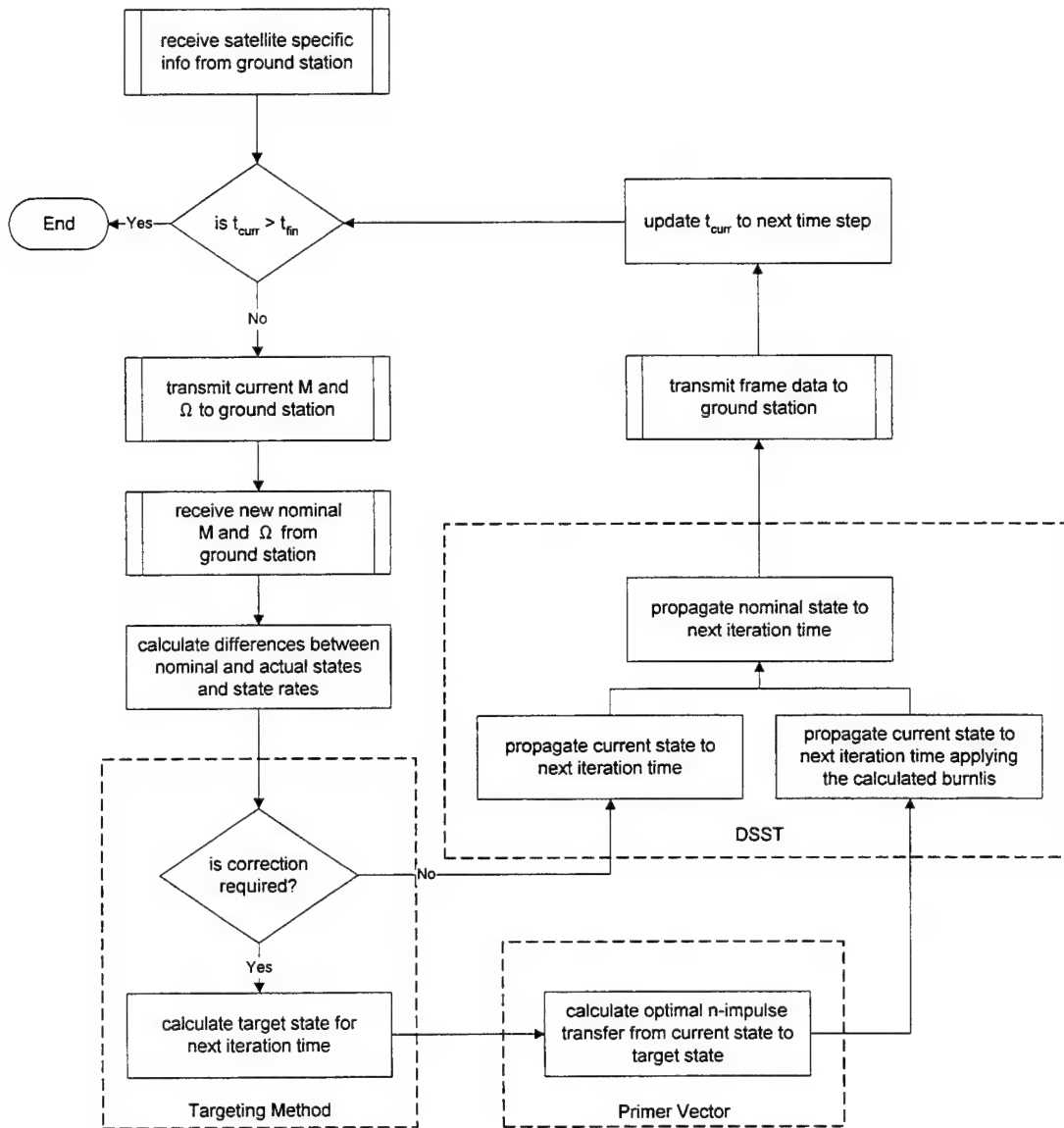


Figure 5.2: Satellite Process Flowchart

Figure 5.2 below illustrates all the major functions involved. As in figure 5.1, boxes with bands at the sides indicate functions which involve communication with the ground station.

The operations involved in each time step are divided into three major functions. The first, defined by the targeting method, compares the difference between the actual state and the nominal state to the orbital element limits of the satellite in order to determine if a correction needs be made in this time step. Note that this comparison is made using a nominal state whose mean anomaly and ascending node has already been modified by the ground station based on the states of the other satellites in the constellation. If a correction is required, the appropriate target state for the actual satellite at the next iteration time step is calculated based on the control law. The second function, which applies Primer Vector theory, calculates the near-optimal n-impulse transfer trajectory to the future target state. The transfer trajectory is defined by the impulsive burns that form the burnlist. The third function, orbit propagation, is executed by the DSST interface. If a controlled transfer trajectory is required, then the current actual state is propagated with the burnlist included. If no correction is required, then the actual state is propagated freely. The nominal state is always propagated freely.

The calculation of the transfer, or rendezvous, trajectory and the operation of the DSST orbit propagator interface are outlined in the following two subsections.

5.2.3 Rendezvous Trajectory Planner

The rendezvous trajectory planner is responsible for calculating a near-optimal n-impulse transfer between a given initial and final state over the defined transfer time. It

accomplishes this task by implementing the principles of Primer Vector theory described in Chapter 2. The entire operation of the trajectory planner, outlined in figure 5.3 below, falls into the “Primer Vector” box of figure 5.2.

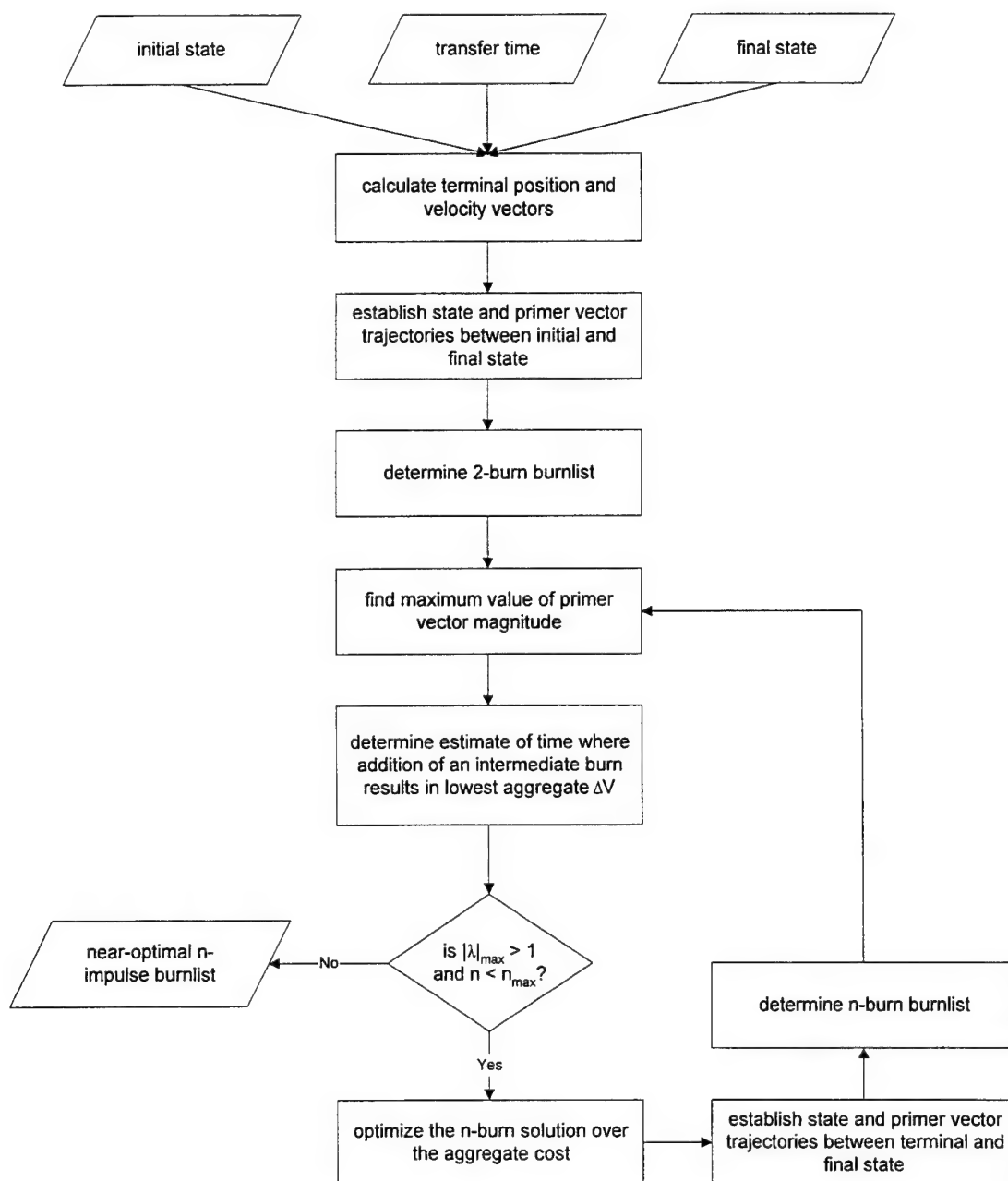


Figure 5.3: Rendezvous Trajectory Planner Flowchart

The optimization algorithm used is Powell's method [45]. This is a direction-set algorithm which finds the minimum of a multidimensional function without using derivatives. It operates by minimizing the function along a series of multidimensional directions until global minimization occurs. The function value in this application is the characteristic velocity, or total ΔV . The independent variables are the intermediate burn times.

The maximum number of impulses allowed in each transfer, n_{\max} , and the discretization size of the time grid between the initial and final state times are both defined by the user in the constellation input file. The minimum allowable value for n_{\max} is 2. Increasing n_{\max} will result in a lower total delta-V expenditure. However, since optimization and recalculation of the primer vector and state trajectories are computationally expensive, the minimum value of n_{\max} that yields acceptable burn magnitudes should be used. In practice, increasing n_{\max} past 4 or 5 results in only marginal improvement in the characteristic velocity. Note that the flowchart in figure 5.3 identifies $n < n_{\max}$ and $|\lambda|_{\max} > 1$ as the only conditions for exiting the control loop. In actuality, if the improvement in the cost with the addition of the $(n+1)^{\text{st}}$ burn is not greater than a specific tolerance value, then the extra burn is not included and the loop is terminated.

The output of the trajectory planner algorithm is an n -element burnlist containing the impulsive velocity vectors to apply and the times to apply them.

5.2.4 Orbit Propagator

The orbit propagator is used for many different purposes in this project. Figure 5.4 illustrates the flow of the DSST software interface algorithm.

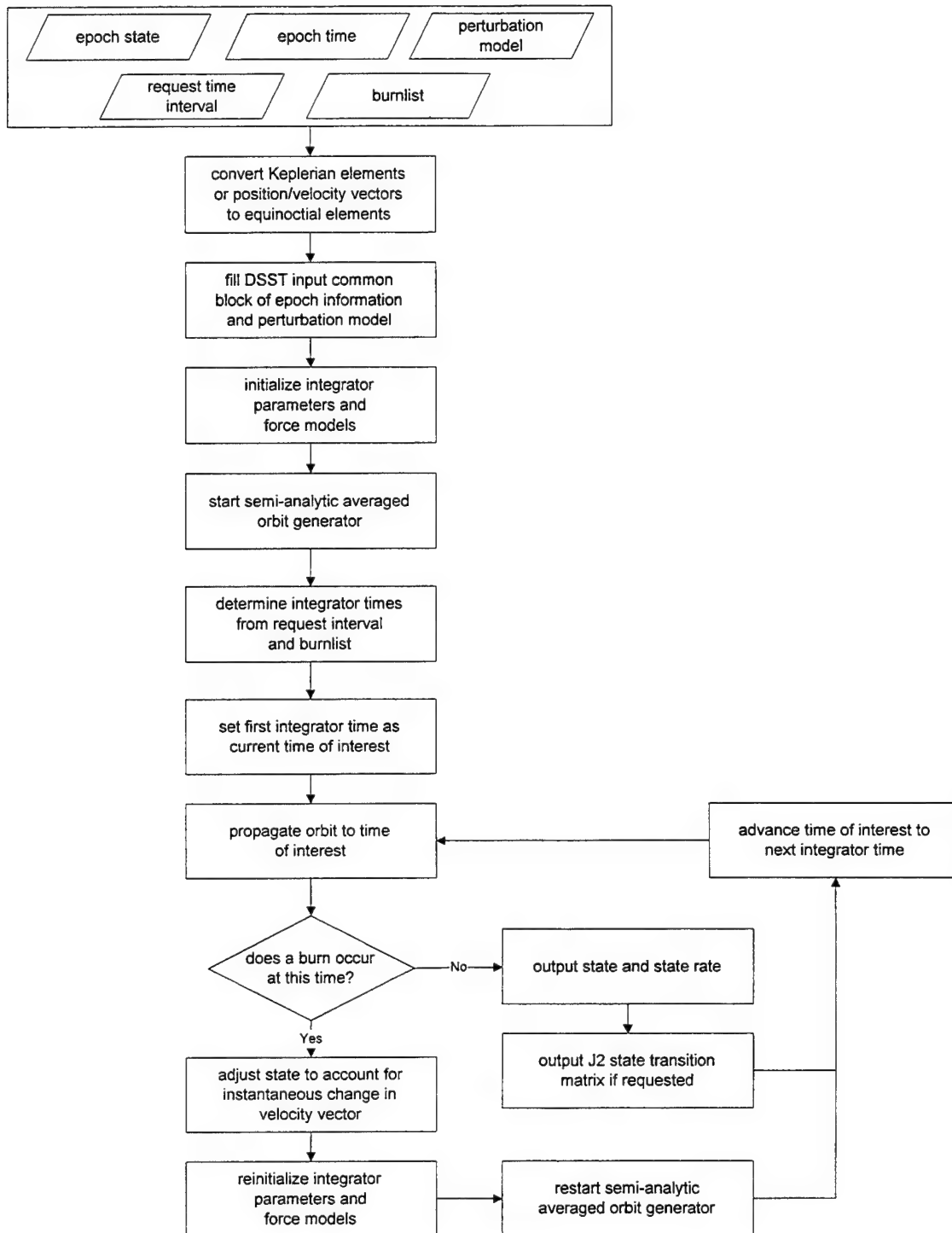


Figure 5.4: Orbit Propagator Operation Flowchart

The interface is capable of extracting the state and state rate at all request times, and the state transition matrix from the epoch time to all request times. It can output the state and

state rate in equinoctial or Keplerian element set notation. The state transition matrix contains the partial derivatives of the Cartesian position and velocity at the request time with respect to position and velocity at the epoch time and includes only the central body gravitation and J_2 zonal harmonic.

For input, the interface can accept the epoch state in equinoctial elements, Keplerian elements, or even inertial position and velocity vectors. The request times are defined by an initial request time, final request time, and a time step size. The burnlist must include the time of each burn, in seconds since the epoch time, and the impulsive velocity vector in inertial coordinates. Other inputs which must be specified are the direction of the propagation (forward / backward), the number of burns in the burnlist, and the perturbation models to use.

Note that the averaged orbit integrator reinitializes the integrator parameters and force models every time there is an impulsive burn. Therefore, the propagation time is significantly lengthened when there is a burnlist involved. The run time also increases with the addition of perturbations, particularly drag.

5.3 Software Implementation

The following section outlines the structure of the ASKS code. Because of the complexity and layers of operation, the outline is broken up into four distinct functional groups: constellation level, satellite level, optimal n-impulse transfer, and DSST interface. These groups roughly correspond to the flowcharts in the four subsections of section 5.2.

5.3.1 Constellation Level

The constellation level is the top level execution of the ASKS. $n+1$ copies of program *const_keep* are begun with the UNIX MPI executable command:

```
mpirun -np XX const_keep
```

where *XX* is the number of processes specified by the user. This number must be one more than the total number of satellites specified in the input file. The extra process is for the operation of the ground station function. The $n+1$ copies of *const_keep* are each assigned a task id number, ranging from 0 to n , by MPI. Process 0 assumes the role of the ground station. Processes 1 to n assume the role of satellites 1 through n , whose numbers are defined in the input file. If a process recognizes itself as the ground station, it ignores the satellite portion of the code and executes only the ground station functions.

The constellation level software structure is illustrated in figure 5.5. The box *grnd_stat* has a dotted line because it does not exist as its own routine. Instead, it is embedded in the *const_keep* routine. If a process recognizes itself as a satellite, it will ignore the ground station portion of *const_keep* and initiate the call to routine *sat_keep*, which includes all satellite operations. This level of the code is discussed in the next subsection.

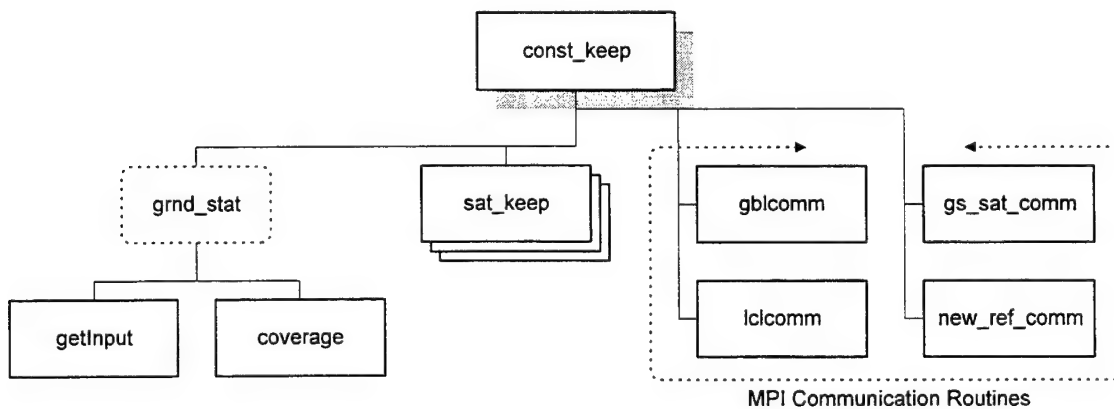


Figure 5.5: Constellation Level Software Structure

The four MPI communication routines are called upon by each of the different copies of *const_keep* to communicate with each other. Routine *gblcomm* allows the ground station to broadcast data that is relevant to all the satellites as a global communications packet. Routine *lclcomm* is used when the ground station must communicate satellite specific data to a particular satellite. Routine *gs_sat_comm* is used by the individual satellites to transmit frame data to the ground station at each iteration time. And routine *new_ref_comm* is used in the process of updating the nominal mean anomaly and ascending node of each satellite at each iteration time. Since these last two routines are needed at each time step, they are also called within the satellite process.

5.3.2 Satellite Level

The satellite level is entered from *const_keep* by each of the satellite processes when the satellite number, epoch nominal state, epoch actual state, run time, and orbital element limit information is known. All communication with the ground station is executed through routines *new_ref_comm* and *gs_sat_comm*.

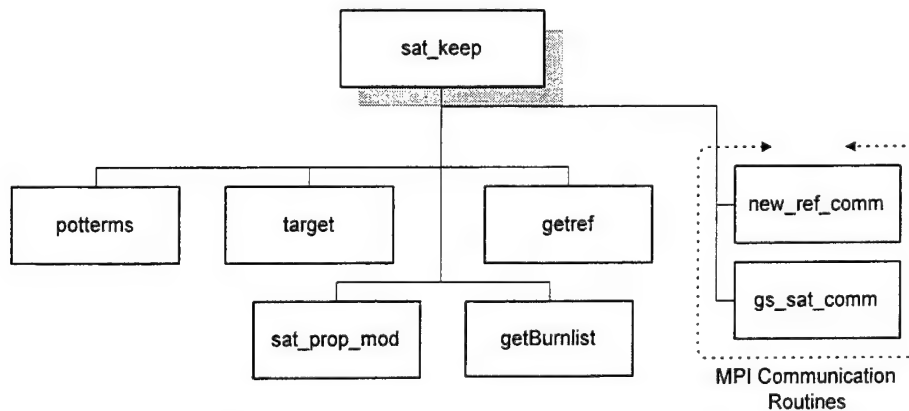


Figure 5.6: Satellite Level Software Structure

The software structure, shown in figure 5.6, is closely linked with the satellite operations flow shown in figure 5.2. The calculation of the state and state rate differences is conducted in routine *potterms*. The name for this subroutine is a concatenation of the phrase 'potential function terms'. When a Lyapunov based controller is installed, this routine will be expanded to include the calculation of the artificial potential function. The calculation of the target state for the next iteration time is conducted in routine *target*. Currently, there are four targeting options. Additional targeting options, including Lyapunov based control laws are to be added to this subroutine.

The calculation of the optimal n-impulse trajectory is conducted in routine *getBurnlist*. A more detailed explanation of its structure is provided in the following subsection. Routine *sat_prop_mod* is used to propagate the actual state of the satellite, with or without an attached burnlist. It is explained further in subsection 5.3.4. The nominal state is propagated to the next iteration time by routine *getref*. This is done differently to allow multiple ways to define the nominal trajectory. For example, *getref* currently contains an option to propagate the nominal state using fixed element rates defined in the input file. This method bypasses the orbit propagator. Note, however, that this fixed rates method is not valid if the actual state output is in the Mean of 1950 frame. This capability will become useful only after the orbit propagator has been modified to output in the current true of date frame.

5.3.3 Optimal N-Impulse Transfer

Routine *getBurnlist* contains all the programming required to calculate a near optimal n-impulse orbital rendezvous to a target state in a defined time. This routine, and all of its dependencies, can readily be extracted from the *const_keep* program and used elsewhere

for the same function. Because it involves the iterated use of an optimization scheme, it is also the most computationally demanding part of the overall program. If the user limits the number of burns for the transfer to two, then the solution defined by the Lambert trajectory connecting the initial and final state is quickly output. Any number greater than two requires the execution of the Primer Vector theory code. Figure 5.7 contains the structure of the *getBurnlist* routine.

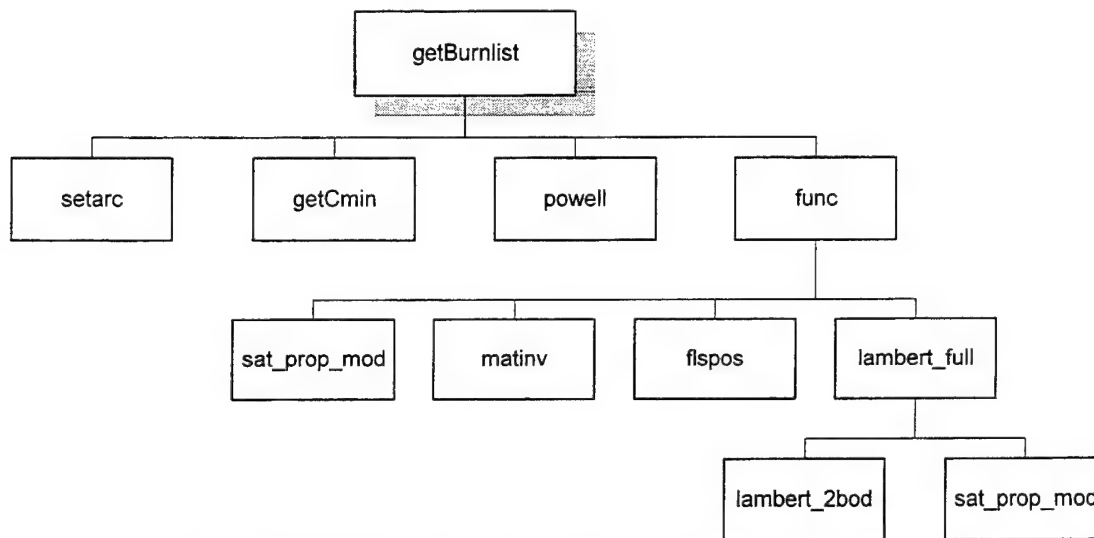


Figure 5.7: Transfer Trajectory Planner Software Structure

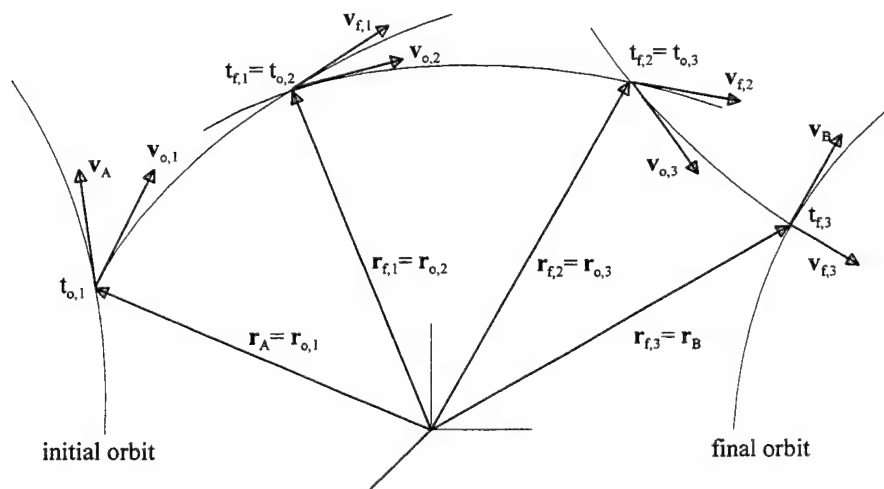


Figure 5.8: 4-Impulse Transfer Trajectory

One of the first tasks addressed by *getBurnlist* is establishing data structures that make the analysis of the transfer trajectory and the primer vector trajectory connecting the terminal states easier. Consider the n -impulse transfer trajectory connecting the initial and final state to consist of $(n-1)$ coasting arcs, or periods where there are no burns.

An example of a 4-impulse transfer is shown in figure 5.8. $(\mathbf{r}_A, \mathbf{v}_A)$ and $(\mathbf{r}_B, \mathbf{v}_B)$ are the initial and final position/velocity vectors, respectively, corresponding to the initial and final state. Each of the three coasting arcs is defined by the position, velocity, and time of its start and the position, velocity, and time of its end. If there are j coasting arcs connecting the initial and final state, then a $j \times 18$ element matrix, with components as defined in table 5.1, completely describes the transfer trajectory. This matrix variable is called *coast_arc*. For the 2 burn solution, it has only one row. Every additional intermediate burn adds one more row while, but the total time span (ie the transfer time defined by $t_B - t_A$) remains the same.

Table 5.1: *coast_arc* Matrix

Element	Data Item	Description
(j,1)	$t_{o,j,date}$	date of beginning of coasting arc j (YYYYMMDD.0)
(j,2)	$t_{o,j,time}$	time of beginning of coasting arc j (HHMMSS.SSSS)
(j,3)	$\Delta t_{(o,j)-epoch}$	time since beginning of first coasting arc (sec)
(j,4-6)	$\mathbf{r}_{o,j}$	position vector at beginning of coasting arc j (km)
(j,7-9)	$\mathbf{v}_{o,j}$	velocity vector at beginning of coasting arc j (km/sec)
(j,10)	$t_{f,j,date}$	date of end of coasting arc j (YYYYMMDD.0)
(j,11)	$t_{f,j,time}$	time of end of coasting arc j (HHMMSS.SSSS)
(j,12)	$\Delta t_{(f,j)-epoch}$	time since beginning of first coasting arc (sec)
(j,13-15)	$\mathbf{r}_{f,j}$	position vector at end of coasting arc j (km)
(j,16-18)	$\mathbf{v}_{f,j}$	velocity vector at end of coasting arc j (km/sec)

For every coasting arc in the state trajectory, there is a corresponding arc in the primer vector trajectory. In Chapter 2, we demonstrated that the state transition matrix operates on the primer vector and its derivative as it does on the position and velocity deviations from a reference trajectory. To calculate the primer vector history between burn times, then, the primer vector and its rate must be known at the terminal times of each of the corresponding coasting arc. To store this data, a data structure similar to *coast_arc*, called *lamda_arc*, was developed. It is described in table 5.2.

Table 5.2: *lamda_arc* Matrix

Element	Data Item	Description
(j,1)	$t_{o,j,date}$	date of beginning of coasting arc j (YYYYMMDD.0)
(j,2)	$t_{o,j,time}$	time of beginning of coasting arc j (HHMMSS.SSSS)
(j,3)	$\Delta t_{(o,j)-epoch}$	time since beginning of first coasting arc (sec)
(j,4-6)	$\lambda_{o,j}$	primer vector at beginning of coasting arc j
(j,7-9)	$[d\lambda/dt]_{o,j}$	primer vector rate at beginning of coasting arc j
(j,10)	$t_{f,j,date}$	date of end of coasting arc j (YYYYMMDD.0)
(j,11)	$t_{f,j,time}$	time of end of coasting arc j (HHMMSS.SSSS)
(j,12)	$\Delta t_{(f,j)-epoch}$	time since beginning of first coasting arc (sec)
(j,13-15)	$\lambda_{f,j}$	primer vector at end of coasting arc j
(j,16-18)	$[d\lambda/dt]_{f,j}$	primer vector rate at end of coasting arc j

Routine *setarc* establishes the *coast_arc* and *lamda_arc* matrices and fills them with the 2-burn transfer trajectories. These matrices are expanded each time an interior burn is added within the loop in figure 5.7.

Routine *getCmin* conducts the coarse grain search for the time to add an interior burn. It begins by calculating the primer vector trajectory on a discretized time grid over all the coasting arcs. If the primer vector magnitude, $|\lambda|$, is greater than one on any of these

trajectories, then an additional interior burn is required. For every grid point where $|\lambda|$ is greater than one, *getCmin* calculates the characteristic velocity of the transfer that results from adding an interior burn at that grid point time. The minimum characteristic velocity at all of these points is C_{min} . The grid point time associated with C_{min} is a coarse approximation of the best time to add another interior burn.

Since the time on the discretized grid is not entirely accurate, an optimized time is determined by routine *powell*, which implements Powell's function minimization. The function to be minimized is the total characteristic velocity of the impulsive transfer. Note that *powell* varies all the interior impulse times to find the minimum, not only the newly added impulse time.

For a given set of interior burn times, routine *func* calculates the resulting characteristic velocity. *matinv*, a preexisting routine, is used to calculate the inverse of the A matrix described in equations 2.29 and 2.30. It executes the Moore-Penrose generalized inverse algorithm. Routine *flspos* is also a preexisting routine. It executes a binary search for the roots of a given equation. In this context, it is used to find the optimal magnitude of an interior impulse given its firing time. It finds the root of equation 2.36, which defines the impulse magnitude that causes the biggest improvement in the cost function.

Routine *lambert_full* is used to calculate precise Lambert trajectories connecting any two states. It incorporates non-2 body motion with the use of a targeting correction algorithm. The targeting error of a 2 body Lambert trajectory is repeatedly fed back to correct the target state until convergence to the original target is achieved. This procedure is similar to a sharp shooter purposely aiming a rifle off target to account for wind along the path. The 2 body Lambert trajectory is calculated by *lambert_2bod*. The targeting error is determined with the use of the orbit propagator, which is accessed

through the *sat_prop_mod* interface. The difference of the final transfer orbit state obtained through a full perturbation model propagation and the 2 body transfer orbit final state is the error. The correction process is repeated until the required accuracy is obtained. This process is explained further in reference 3.

The final result of routine *getBurnlist* is an n-element burnlist which describes the time, magnitude and direction of all the burns. The array which holds all the burn information is called *burnlist* and is described in table 5.3. Note that the j^{th} and $(j+1)^{\text{th}}$ burns encompass the j^{th} coasting arc of table 5.1.

Table 5.3: *burnlist* Array

Element	Data Item	Description
(1,j)	$t_{\text{burn},j}$	time of j^{th} burn (sec since epoch)
(2-4,j)	ΔV_j	j^{th} delta-V vector in inertial coordinates (km/sec)

5.3.4 DSST Software Interface

Every call to the orbit propagator must invoke the interface routine *sat_prop_mod*. The software structure of the DSST interface is illustrated in figure 5.9.

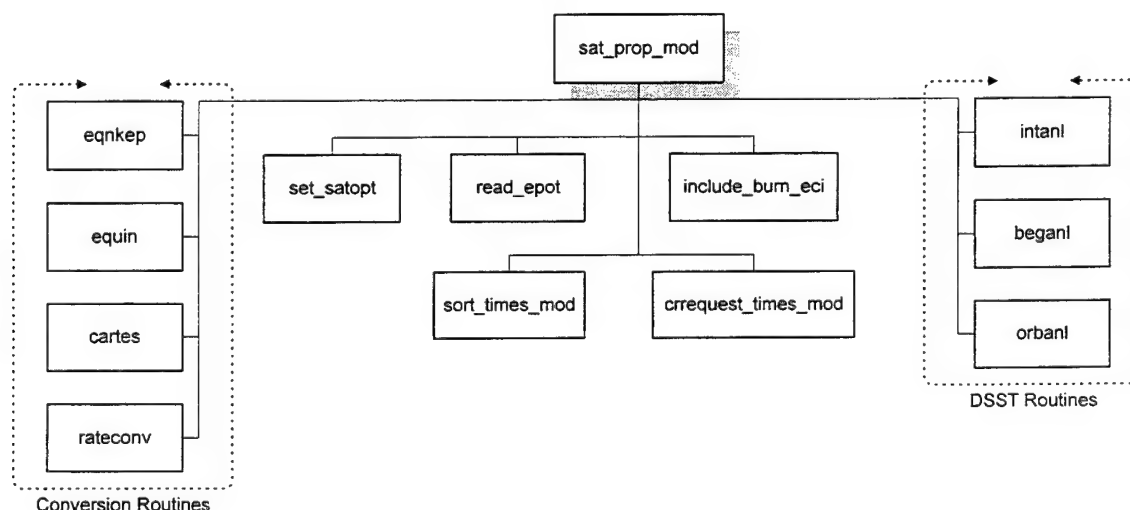


Figure 5.9: DSST Interface Software Structure

For the input epoch state, *sat_prop_mod* is capable of accepting mean Keplerian elements, mean equinoctial elements, or their equivalent Cartesian position and velocity vectors. Routines *eqnkep* and *equin* are used to convert the Keplerian elements and the position / velocity vectors, respectively, to the equinoctial elements for use by the orbit propagator. The interface can output the orbit state, state rates, and the J_2 state transition matrix at each request time.

The epoch time, epoch state vector, and satellite physical properties are input with the *satopt_dbl* array. All the elements of this array are double precision real variables. The format of the *satopt_dbl* array is described in table 5.4.

Table 5.4: *satopt_dbl* Array

Element	Data Item	Description
1	$t_{\text{epoch,date}}$	date of epoch state (YYYYMMDD.0)
2	$t_{\text{epoch,time}}$	time of epoch state (HHMMSS.SSSS)
3	a^*	semi-major axis* (km)
4	e^*	eccentricity*
5	i^*	inclination* (deg)
6	Ω^*	ascending node* (deg)
7	ω^*	argument of perigee* (deg)
8	M^*	mean anomaly* (deg)
9	CD	coefficient of drag
10	ρ_l	atmospheric density correction factor
11	m_{sc}	mass of spacecraft (kg)
12	A_{sc}	area of spacecraft perpendicular to direction of motion (km ²)
13	Δt_s	step size for averaged orbit integrator (sec)

*elements can be equinoctial or position/velocity as well

The orbit propagator also needs to know the perturbations to use in the propagation. This is accomplished with the *satopt_int* array. All of its elements are integers.

Table 5.5: *satopt_int* Array

Element	Data Item	Description
1	Retro	retrograde factor: 1 = direct equinoctial elements -1 = retrograde equinoctial elements
2	Atmos Mdl	atmospheric model: 1 = Jacchia-Roberts
3	Potent Mdl	potential model for spherical harmonics: 4 = JGM2
4	Nmax	maximum degree of central body spherical harmonics
5	Mmax	maximum order of central body spherical harmonics
6	Izonal	zonal harmonic averaging option: 1 = analytical averaging 2 = numerical averaging 3 = off
7	IJ2J2	first order J_2^2 effect: 1 = On 2 = Off
8	Nmaxrs	maximum resonant degree
9	Mmaxrs	maximum resonant order
10	Ithird	solar/lunar third body effects: 1 = analytical averaging 2 = numerical averaging 3 = off
11	Ind Drg	atmospheric drag effects: 1 = On 2 = Off
12	Iszak	J_2 height correction for atmospheric drag: 1 = On 2 = Off
13	Ind Sol	solar radiation pressure effects: 1 = On 2 = Off
14	Nstate	output state transition matrix? 0 = No 6 = Yes

Note that the 14th element of *satopt_int*, Nstate, is the switch for producing the J_2 state transition matrix.

Rather than passing through an exhaustive list of the request times for the orbit propagator, *sat_prop_mod* uses the *intervals* array. Only the initial request time, final request time and time step are needed. The format of the *intervals* array is shown in table 5.6. Routine *crrequest_times_mod* produces the actual list of request times from the *intervals* array. Routine *sort_times_mod* takes these request times and the burn times defined in the *burnlist* array and sorts them to produce the integrator times. Each integrator time is tagged with a logical variable which indicates whether it is an output request time or a burn time.

Table 5.6: *intervals* Array

Element	Data Item	Description
1	$t_{\text{start,date}}$	date of beginning of request interval (YYYYMMDD.0)
2	$t_{\text{start,time}}$	time of beginning of request interval (HHMMSS.SSSS)
3	$t_{\text{end,date}}$	date of end of request interval (YYYYMMDD.0)
4	$t_{\text{end,time}}$	time of end of request interval (HHMMSS.SSSS)
5	Δt	time step (sec)

All interaction with the DSST orbit propagator code is accomplished through three DSST routines. Routine *intanl* transforms the mean elements at epoch from the input coordinate system into the integrator coordinate system and initializes the generator force models. Routine *beganl* starts the semi-analytic orbit generator. It must be told which direction the propagation is to follow. Routine *orbanl* integrates the equations of motion to the current request time and produces the requested output.

The state and state rate output of *sat_prop_mod* is placed into array *satdata*. Its format is described in table 5.7.

Table 5.7: *satdata* Array

Element	Data Item	Description
(1,k)	$t_{\text{date},k}$	output date of k^{th} request time (YYYYMMDD.0)
(2,k)	$t_{\text{time},k}$	output time of k^{th} request time (HHMMSS.SSSS)
(3,k)	a^*	semi-major axis* (km)
(4,k)	e^*	eccentricity*
(5,k)	i^*	inclination* (deg)
(6,k)	Ω^*	ascending node* (deg)
(7,k)	ω^*	argument of perigee* (deg)
(8,k)	M^*	mean anomaly* (deg)
(3,k)	$[da/dt]^*$	semi-major axis rate* (km/sec)
(4,k)	$[de/dt]^*$	eccentricity rate* (1/sec)
(5,k)	$[di/dt]^*$	inclination rate* (deg/sec)
(6,k)	$[d\Omega/dt]^*$	ascending node rate* (deg/sec)
(7,k)	$[d\omega/dt]^*$	argument of perigee rate* (deg/sec)
(8,k)	$[dM/dt]^*$	mean motion* (deg/sec)

*elements and rates can be equinoctial as well

The default element set is equinoctial. However, if Keplerian elements and rates are requested, routine *rateconv* calculates them from the equinoctial elements and rates. The state transition matrix, when requested, is output as four 3x3 matrices at each request time. The four matrices at each request time are of the form

$$\begin{aligned}\Phi_{11}(t_{\text{req}}, t_o) &= \frac{\partial \mathbf{r}(t_{\text{req}})}{\partial \mathbf{r}(t_o)} \\ \Phi_{12}(t_{\text{req}}, t_o) &= \frac{\partial \mathbf{r}(t_{\text{req}})}{\partial \mathbf{v}(t_o)} \\ \Phi_{21}(t_{\text{req}}, t_o) &= \frac{\partial \mathbf{v}(t_{\text{req}})}{\partial \mathbf{r}(t_o)} \\ \Phi_{22}(t_{\text{req}}, t_o) &= \frac{\partial \mathbf{v}(t_{\text{req}})}{\partial \mathbf{v}(t_o)}\end{aligned}$$

5.4 Input Deck

All information required for an ASKS run is input from one source file, called the input deck. The ground station process *const_keep* reads all the input information and eventually passes out the appropriate data to each satellite process. The first section lists the run information applicable throughout the constellation. The remainder of the deck list planar control parameters and individual satellite epoch information. The format of an input deck for a constellation with m planes of n satellites each is illustrated in figure 5.10.

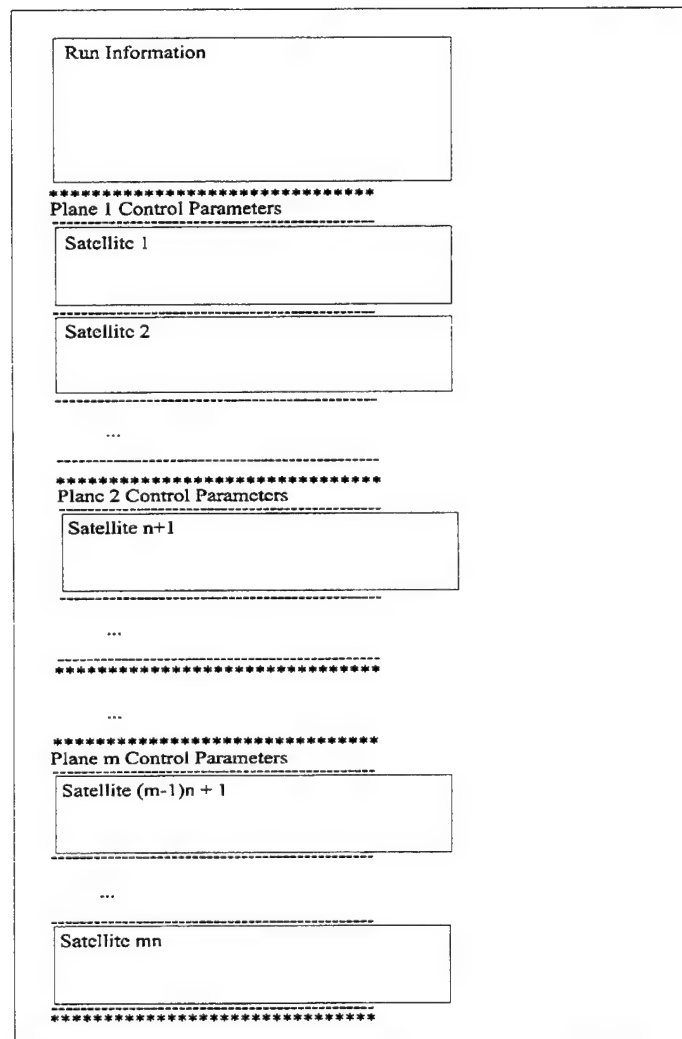


Figure 5.10: Input Deck Format

Note that planes are separated by a row of asterisks and satellite blocks within a plane a separated by a row of hyphens.

The elements of the run information block of the input deck define what type of ASKS run is to be executed. An example run information block is listed below as figure 5.11.

```
Number of Planes      :      3
Stat-Keep Method     :      0  (0=box; 1=formation)

Targeting Method      :      0
Power                 :      1.00
kmax                  :      100
max_burns             :      2

Epoch Date: 19970101.0 Epoch Time:      0.0000
Final Date: 20020101.0 Final Time:      0.0000
Iteration Time Step   :      0.1296000000000000D+07   sec
```

Figure 5.11: Sample Control Parameter Block of Input Deck

The first line simply defines the number of planes in the constellations. The second line defines the type of station-keeping method, box or formation flying, is to be used. These two methods are explained in the following chapter. The third line deals with the targeting method being used. The Power, kmax, and max_burns settings are active inputs for only specific choices of Method. For example, method 0 indicates that no corrections are to be considered. With this setting, the inputs for Power, kmax, and max_burns are ignored, but are still required in the input deck. The remaining lines concern the timing of the run. The dates are in YYYYMMDD.0 format. The times are in HHMMSS.SSSS format. The iteration time step can be any value when no control is implemented, but must be less than one period of the orbit in the constellation with the smallest semi-major axis when a control method is implemented.

The plane control parameters section lists the plane number, the number of satellites in that plane, and the orbital element limits for satellites in that plane. Figure 5.12 lists an example plane control parameter section. The maximum parameter limits are the orbital elements values which are not to be exceeded. The outer limit scale is the percentage of

the maximum limit that defines the real border at which a violation is considered. This safety factor is added to insure that the actual limits are never violated. Note that placing any angular limit above 360° implies that that element is not be controlled. The deadband parameter limits defines the orbital element value below which no corrections is to be made. This option is included to avoid correcting small acceptable deviations from the nominal trajectory. The maximum overshoot limits deal specifically with method 2 and are discussed in the following chapter.

```

Plane          :      1
Sats In This Plane :      5

Maximum Parameter Limits:      1.000000000000000D+00      km      sma
Keplerian Elements:      0.00100000000000000D+00      ecc
      0.7200000000000000D+03      deg      inc
      0.7200000000000000D+03      deg      lan
      0.00100000000000000D+03      deg      ap
      0.7200000000000000D+03      deg      ma

Scale (outer limits) : 0.98
Deadband Parameter Limits:      0.950000000000000D+00      km      sma
Keplerian Elements:      0.00095000000000000D+00      ecc
      0.7200000000000000D+03      deg      inc
      0.7200000000000000D+03      deg      lan
      0.00095000000000000D+03      deg      ap
      0.7200000000000000D+03      deg      ma

Maximum Overshoot Limits :      0.980000000000000D+00      frac      sma
      0.000000000000000D+00      frac      ecc
      0.980000000000000D+00      frac      inc
      0.980000000000000D+00      frac      lan
      0.000000000000000D+00      frac      ap
      0.980000000000000D+00      frac      ma

```

Figure 5.12: Sample Plane Control Parameter Section of Input Deck

A satellite block contains all the information needed for the nominal and actual trajectories. A sample satellite block is listed below as figure 5.13. After initially identifying the satellite number, the block is split up into two parts, the actual satellite and the reference satellite. For the input deck, 'reference' is synonymous with 'nominal'. The format and units for the input of the element set and physical characteristics of the satellite are the same as identified in table 5.4. The format for the force models and the perturbation list is the same as identified in table 5.5. Note that the nominal (reference) section has an option of whether to use DSST or the method of fixed rates is to propagate

the nominal trajectory. If fixed rates is chosen, then the force model and perturbation list is ignored for the nominal satellite trajectory.

```

-----
Satellite Number      :      7

Actual State:
  Keplerian Elements:      0.1047220000000000D+05      km      sma
                           0.3266200000000000D+00      ecc
                           0.1168395808400000D+03      deg      inc
                           0.0994212449500000D+03      deg      lan
                           0.2700524204900000D+03      deg      ap
                           0.0720000000000000D+03      deg      ma

CD:      2.20000000      Rho One:      0.00000000
S/C Mass:      700.00000000      S/C Area:      0.00002500
Integrator Step: 43200.00000000

Retro:      1      Atmos Mdl:      1      Potent Mdl:      4
Nmax:      21      Mmax:      21      Izonal:      1      IJ2J2:      1
Nmaxrs:      21      Mmaxrs:      21      Ithird:      1
Ind Drg:      1      Iszak:      2      Ind Sol:      1

Reference State:
  Keplerian Elements:      0.1047220000000000D+05      km      sma
                           0.3266200000000000D+00      ecc
                           0.1168395808400000D+03      deg      inc
                           0.0994212449500000D+03      deg      lan
                           0.2700524204900000D+03      deg      ap
                           0.0720000000000000D+03      deg      ma

Reference Switch      :      0      ! (0=DSST, 1=Fixed Rates)
Reference State Rates:
  Keplerian Rates:      0.0000000000000000D+00      km/sec      sma
                           0.0000000000000000D+00      1/sec      ecc
                           0.0000000000000000D+00      deg/sec      inc
                           1.1407711610000000D-05      deg/sec      lan
                           0.0000000000000000D+00      deg/sec      ap
                           3.3338114140000000D-02      deg/sec      ma

CD:      2.20000000      Rho One:      0.00000000
S/C Mass:      700.00000000      S/C Area:      0.00002500
Integrator Step: 43200.00000000

Retro:      1      Atmos Mdl:      1      Potent Mdl:      4
Nmax:      21      Mmax:      0      Izonal:      1      IJ2J2:      1
Nmaxrs:      2      Mmaxrs:      2      Ithird:      1
Ind Drg:      2      Iszak:      2      Ind Sol:      2
-----

```

Figure 5.13: Sample Satellite Data Block of Input Deck

5.5 Network Environment

For this thesis project, the ASKS simulator was executed on a network of three UNIX Sun workstations. The machines, *taz*, *porky*, and *petunia*, form the Software Process Improvement (SPI) cluster. All three machines are Sun SPARCstation 20 MPs with two processors each. *taz* and *porky* have 64 MB RAM while *petunia* has 80 MB RAM. The

SPI cluster uses the Sun OS Ver. 5.4 / UNIX System V 4.0 operating system. A central storage device (file server), named *toaster*, serves as a common high density disk. *toaster* is composed of an array of seven 4 GB storage units. Since one of the units serves as an error check and backup, the total storage capacity of the system is 24 GB. The local network environment is displayed in figure 5.14. The computers of the SPI Network used to be part of the ACME lab network that was used by Wallace in his study of parallel orbit propagation [58]. While many of the names remain the same, the processors, available software, network connections, physical locations, and administration have changed.

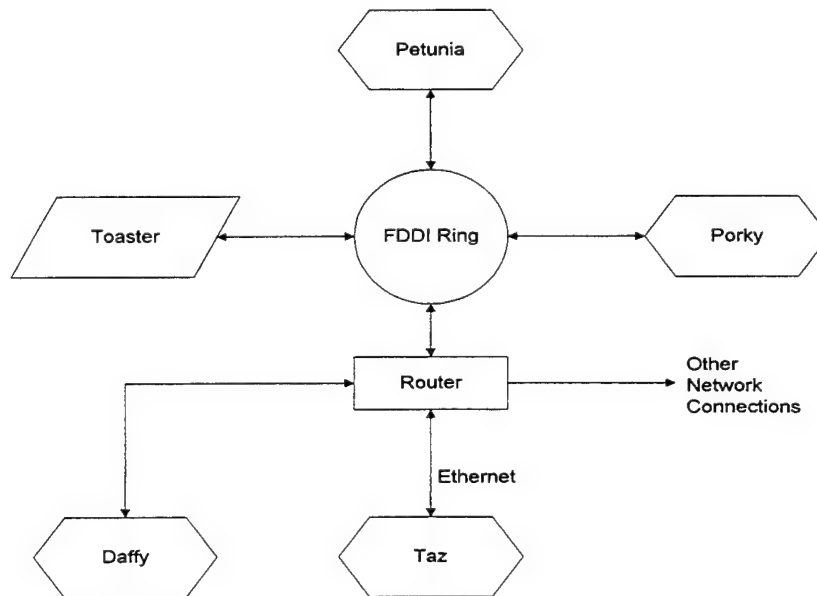


Figure 5.14: SPI Network Environment

toaster, *petunia*, and *porky* are connected by a FDDI fiber optic network interface that allows communication between the three to occur at 100 Mbits/sec. *taz* is connected to the remainder of the system through an Ethernet network interface which allows communication at 10 Mbits/sec. *daffy* is a Pentium 100 MHz desktop PC which was used as the platform for remote logins to the SPI network machines. Its processor was not

involved in any of the simulation executions. Common practice was to use *taz* as the host when initiating any large ASKS run.

5.6 ASKS Source Code Location

The source code for the ASKS is located under the home directory of the author on the SPI cluster's common file server. The highest level directory is

/home/nqs2145/thesis

The location of each of the source code files is listed in figure 5.15.

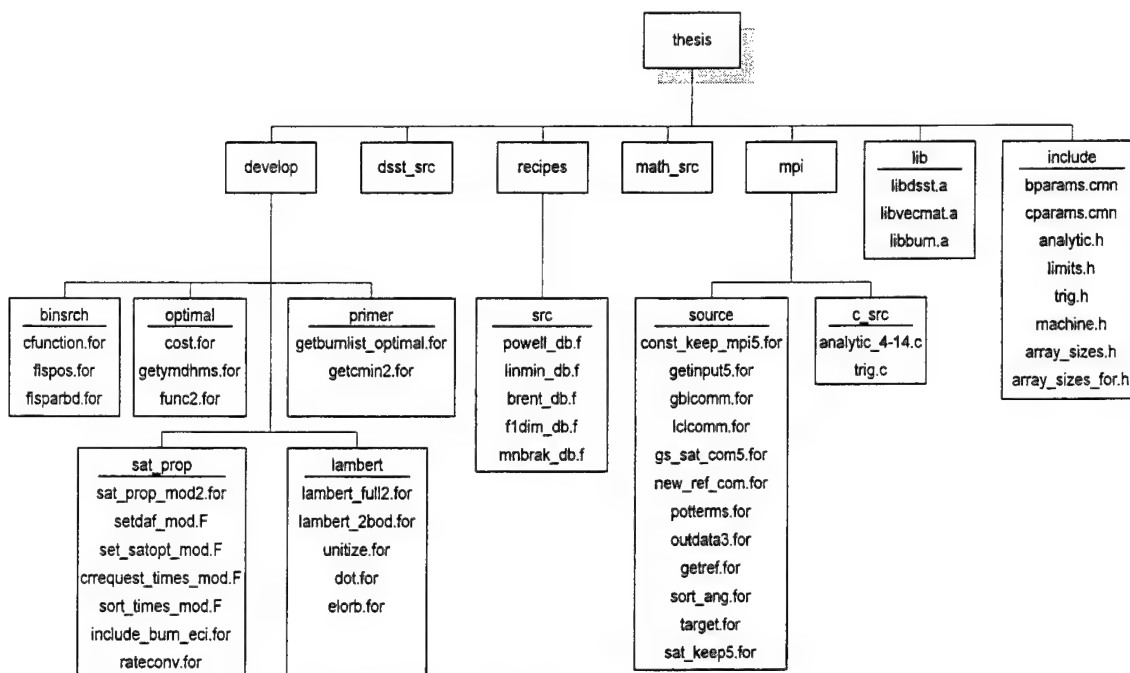


Figure 5.15: ASKS Source Code Location

Directory *dsst_src* contains all the source code for the DSST Standalone Orbit Propagator. Directory *math_src* contains the source code for several vector and matrix manipulation subroutines used throughout the ASKS. *libdsst.a* is the library file

containing the object code for the DSST Standalone. *libvecmat.a* is the library file containing the object code for the vector and matrix manipulation subroutines. *libburn.a* is the library file containing object code for the DSST Standalone propagator plus all the ASKS code under the *develop* and *recipes* directories.

The UNIX makefile which creates the *libburn.a* library file is located in directory *develop*. The UNIX/MPI makefile which creates the ASKS executable is located in directory *mpi*. The command to make the Ellipso ASKS executable is

```
make const_keep_ellip
```

Directory *mpi* is also the location where the ASKS runs are executed. The input deck and all the DSST binary data files must be located in this directory during execution. The command to execute an ASKS run on the full 17 satellite Ellipso constellation is

```
mpirun -np 18 const_keep_ellip
```

After starting one ground station process and 17 satellite processes, the program will query the user for the name of the file containing the input deck. Upon entering the input deck file name, the program begins full execution in parallel.

Three different simulations, each with multiple runs, were executed for this thesis. All information related to these simulations is stored on the Pentium PC computer *daffy*. The top level data directory is

```
c:\naresh\thesis\data\ellipso\
```

Each run directory includes its associated input decks, output files, and Microsoft Powerpoint presentation slides containing the plots of the coverage and element difference histories. The location of each run directory is outlined in figure 5.16.

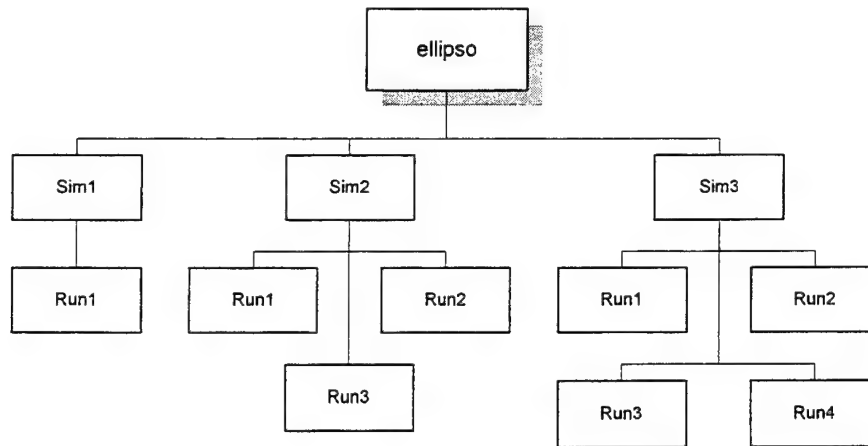


Figure 5.16: Location of Input Decks, Output Files, and Plot Files

5.7 Future Improvements

Some areas for future improvements to the ASKS are

- removal of reinitialization requirement in DSST orbit propagator for consecutive executions using the same epoch state and time
- removal of DSST requirement to re-read all binary data files for every call of *sat_prop_mod*
- enabling output in the true-of-date frame, and.
- inclusion of Lyapunov based control methods.

Chapter 6

Targeting Methods

A targeting method determines a 6 orbital element target state for the next iteration time step when the station-keeping controller in the satellite process determines that a correction needs to be made to one or more of the orbital elements. Therefore, each targeting method, coupled with the criteria for determining when a correction needs to occur and which elements need to be targeted, forms a pseudo-control law. This chapter outlines the correction determination, the criteria used for choosing which elements need to be targeted, and each of the three targeting methods developed in this project.

6.1 Implementing Corrections

The decision on whether to implement a correction is based on the difference between the actual state and nominal state at the current iteration time, called the *state difference*. The difference between the actual state rate and nominal state rate at an iteration time is called the *state difference rate*. The state difference and state difference rate are analyzed with respect to prescribed orbital element boundary limits. The *maximum limit* in each orbital element is the largest amount that an element can vary from its nominal value before mission capability begins to degrade. For communication satellites, this usually means the amount past which the coverage specifications can no longer be guaranteed. The maximum limits for the satellites of the sub-constellations of Ellipso are listed in table

6.1 and table 6.2. To insure that the maximum limit is never reached, a safety zone is created with the establishment of a new boundary, called the *outer limit*. It is the maximum operationally acceptable deviation in the orbital element. ASKS sets this value as a common percentage of each of the individual maximum limits.

Table 6.1: Borealis Maximum Orbital Element Limits [17]

Element	Max Limits
a	1.0 km
e	0.001
i	0.05°
ω	1.0°
Ω	0.2°
M	0.05°

Table 6.2: Concordia Maximum Orbital Element Limits [17]

Element	Max Limits
a	0.1 km
e	0.0003
i	0.05°
ω	NA
$\Omega + M$	0.02°

The *deadband limit* in each orbital element is the amount below which element difference corrections are not required. The deadband limit must be less than or equal to the outer limit. The concept of a deadband was added to stop the controller from correcting small, acceptable deviations from the nominal trajectory. In practice, the deadband limit in each element should be set at a value such that any element difference less than it is operationally acceptable.

The determination of whether a correction is required at an iteration time is simple. If any of the six elements is greater than its respective outer limit, then a correction must occur and a target state must be formed for the next iteration time. A correction should not occur under any other circumstance. Once one of the elements has approached its outer limit, ASKS allows for the possibility of correcting multiple elements by including them in the target state for the next iteration time. This feature was incorporated to take advantage of any fuel savings that may exist when a near-optimal transfer is calculated for multiple elements together rather than separate transfers for each element individually.

6.2 Element Targeting Criteria

The criteria for choosing which elements are to be targeted can be condensed into four statements

- if an element is at its outer limit, it is targeted
- if an element is within the deadband limit of its nominal value, it is not targeted
- if an element is moving toward its nominal value (the element difference between actual and nominal is decreasing), it is not targeted
- if an element is between its deadband and outer limit, and it is moving away from its nominal value (the element difference is growing), then it is targeted

From these four criteria, we note that if the deadband limit is the same as the maximum limit, then only one element will be targeted at each iteration time step.

If an element is targeted, then the target state value of that element is determined by the targeting method. If an element is not targeted, then the target value of that element is the value it would have assumed had the current state been propagated freely to the next iteration time.

6.3 Method 0

Method 0 is not a real targeting method by the definition provided above. It is only used as a switch setting for executing ASKS runs where no corrections are desired. Since an optimal transfer trajectory is never calculated, the constraint on the iteration step size of one orbital period, imposed by the Primer Vector code, does not apply. Therefore, for ASKS runs that only analyze the uncontrolled decay of a constellation's orbits, the iteration step size can be set to any value. This significantly reduces the time it takes to execute these runs.

6.4 Method 1: Shooting the Nominal

Targeting Method 1 sets the value of a targeted element equal to its nominal value at the next iteration time. This is equivalent to bringing the difference between the actual and nominal state in that element to zero at the next iteration time. For example, if the inclination of the actual state had deviated to its outer limit while the remainder of the elements remained within their respective deadband limits, then the target state, using Method 1, would include the nominal value of the inclination while maintaining the deviation in the other elements. This method can also be described as "shooting" for the nominal.

Figure 6.1 displays some Method 1 targeting scenarios. Note that the axes, z_1 and z_2 , represent the state differences in the first and second elements. Therefore, the origin of the plot is the nominal state. Note that a true satellite scenario would include differences in six dimensions, one corresponding to each orbital element. The solid exterior box represents the maximum limits in two dimensions while the dashed line represents the outer limits. The light gray area signifies the state space region where one element is within its deadband limit while the other element is not. The dark gray area signifies the state space region where both elements are within their respective deadband limits. The empty circles represent the actual state at the current iteration time and the solid circles represent the target state at the next iteration time.

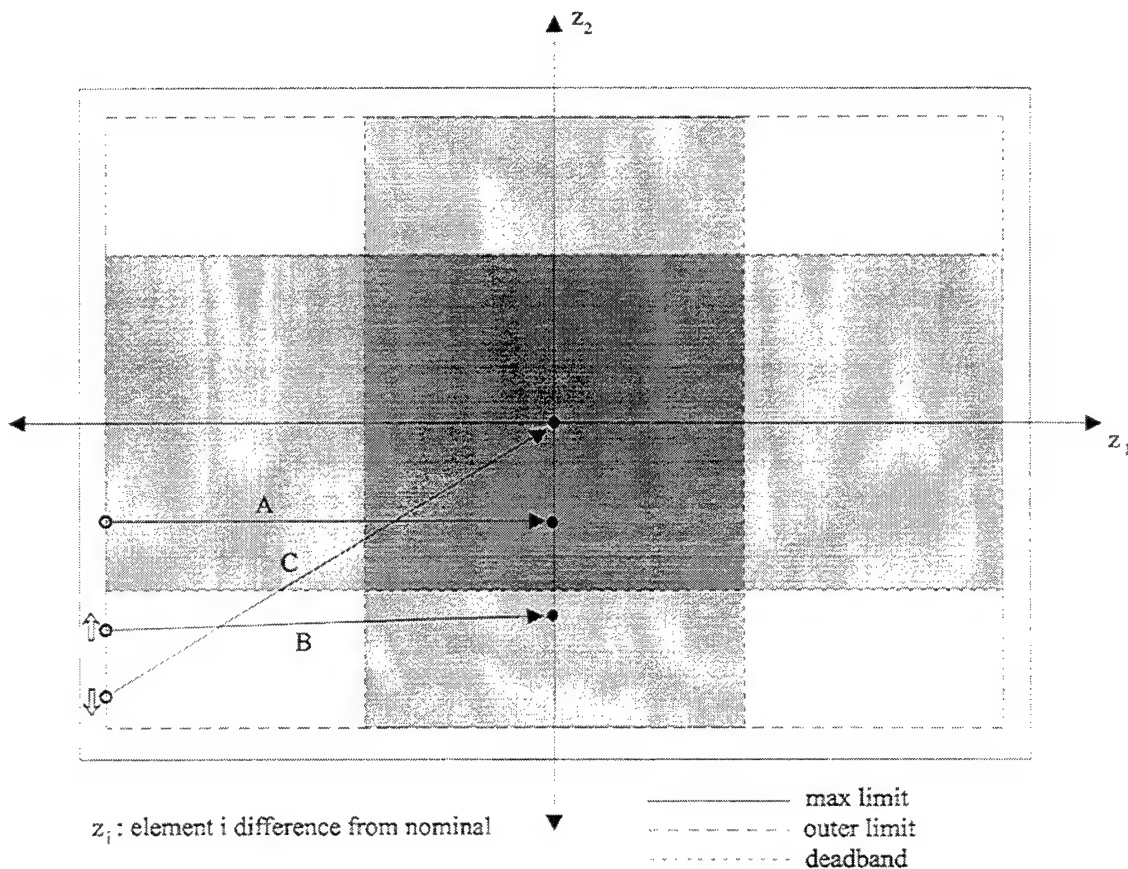


Figure 6.1: Targeting Method 1

If the actual state of a system is not at the outer limit for any of the elements, no correction is made. In scenario A, the actual state is at the outer limit of element 1, but within the deadband limit of element 2. Thus, element 1 is targeted and brought to its nominal value at the next iteration time step, while element 2 is not targeted. Scenarios B and C are similar to each other in that, for both cases, element 1 is at its outer limit and element 2 is between its deadband and outer limit. In this situation, the control system queries the state rate difference for element 2, signified by the arrows. In scenario B, element 2 is moving towards its nominal value, and so it is not targeted. In scenario C, element 2 is moving away from its nominal, and therefore is targeted. Note that when all elements are targeted, the actual and nominal states at the next iteration time are equal.

In Method 1, corrections bring the elements back to their nominal values. This is the logical decision when information about the motion of the elements within the state space region defined by the maximum limits is not available. However, the possibility exists that there is a state space point such that if the actual state were moved there, it would move towards the nominal state over time. From the scenarios of figure 6.1, we see that such a point may exist in the quadrant diagonally opposed to the one from which the outer limit violations occur. Targeting Method 2 attempts to take advantage of this possibility.

6.5 Method 2: Overshooting the Nominal

Targeting Method 2 sets a targeted element equal to a value beyond its nominal value on the state space difference plane. This procedure can be perceived as “overshooting” the nominal. An overcorrection is made with the expectation that the element by element motion of the actual state with respect to the nominal state will remain essentially the

same throughout the state space region within the maximum limits. This is analogous to assuming that the second order effects on the state difference are slowly varying in the state space region bounded by the maximum element limits.

As an example, consider the affect of atmospheric drag on the semi-major axis of a satellite. A controller using targeting Method 1 would constantly correct for a low semi-major axis by bringing its value back up to the nominal value. A Method 2 controller, however, can reduce the frequency of burns, and possibly save station-keeping fuel, by correcting the semi-major axis to a value greater than its nominal, but not greater than its outer limit on the positive difference end. Note that the assumption about the disturbing influence being the same everywhere in the small element region about the nominal is correct for the drag / semi-major axis case, but may not be correct for other disturbing force / orbital element combinations. If an overcorrection is made and a new disturbing force pushes the targeted state away from the nominal, then more harm has been done than good. This situation could lead to repeated corrections back and forth across the nominal value.

Figure 6.2 contains the same scenarios as considered with Method 1 earlier, but with the corresponding Method 2 corrections displayed. In scenarios A and B, where only the violating element is targeted, note that the overcorrections never reach the outer limit on the opposing side of the state space difference domain. This is because each element i ($i = 1, 2, \dots, 6$) has a *maximum overshoot limit* (σ_i) associated with it. The maximum overshoot limit for each element is specified by the user in the input file. σ_i defines the percentage of the distance from the nominal value to the outer limit of the element that the targeted value of the i^{th} element should be at. Note that setting σ_i equal to zero causes the i^{th} element to revert to a Method 1 control scheme. Therefore, targeting Method 1 is a special case of targeting Method 2, where $\sigma_i = 0$ for all elements i .

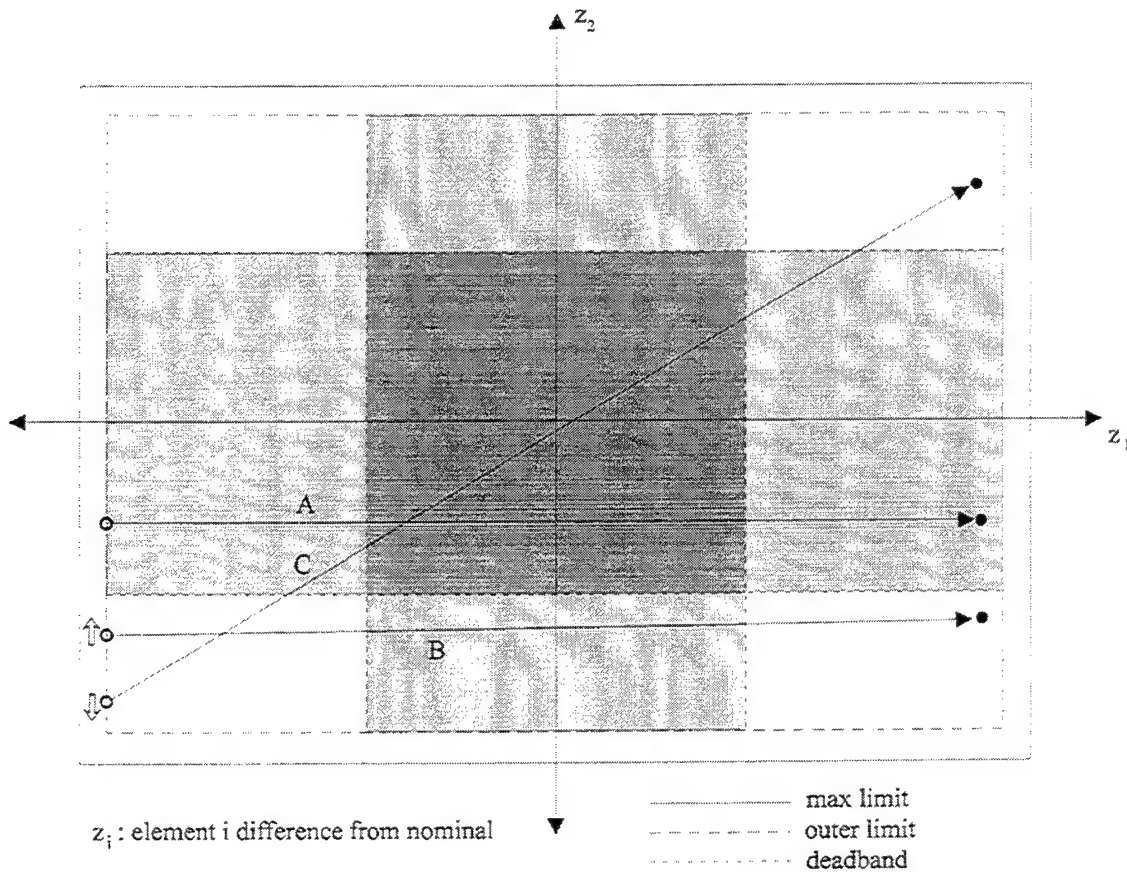


Figure 6.2: Targeting Method 2

When more than one element is targeted using targeting Method 2, not all the elements are overcorrected to their respective σ_i defined values. This feature of the ASKS controller is called *scaled corrections*. In general, an element which violates its outer limits, is likely to be the element with the largest element rate difference between actual and nominal. Because of this, the violating element is always overcorrected fully to its σ_i value. All other accompanying targeted elements are not critical because they have not violated their respective outer limits. To save on station-keeping fuel, these elements are only fractionally brought to their σ_i values. Therefore, for scenario C, element 1 is brought all the way to its σ_i value while element 2 is brought only part way to its σ_i value. The amount secondary targeted elements are corrected depends on how far from their nominal value they are when they were chosen for targeting, and on a user defined

variable called *power*. If $z_i(t_{curr})$ is the current difference of the i^{th} element and $z_i(t_{next})$ is the difference of the i^{th} element associated with the targeted state at the next time step, then the target state is chosen such that

$$z_i(t_{next}) = -\sigma_i z_i(t_{curr}) \left| \frac{z_i(t_{curr})}{\delta r_{i,out}} \right|^{power} \quad (6.1)$$

where $\delta r_{i,out}$ is the outer limit of the i^{th} element.

6.4 Method 3: Directed Corrections

In methods 1 and 2, due to the iteration time step restriction imposed by the Primer Vector code, all target element differences are corrected within the time span of one orbital period. This approach yields reasonable transfer delta-V's for semi-major axis, eccentricity, and inclination corrections. These three elements are traditionally corrected with one or more burns within one orbital period. However, correcting the longitude of the ascending node Ω , the argument of perigee ω , or the mean anomaly M , within a one orbital period time span is not advisable. This is because the transfer trajectories for these corrections contain large delta-V maneuvers.

Consider the example of a mean anomaly difference. A full correction within one orbital period would require a transfer orbit with a significantly different semi-major axis. However, if the semi-major axis were changed only slightly and the transfer orbit maintained for multiple revolutions, then the same mean anomaly difference could be resolved with significantly less fuel expenditure. In addition, the transfer orbit requiring the smaller semi-major axis burns is much less likely to violate the semi-major axis

element limits. Similar multi-orbit transfer trajectories exist for the ascending node and argument of perigee.

To determine how to correct for Ω , ω , and M deviations without targeting them directly, consider the following element plots of a satellite in the Ellipso Borealis Node at Dawn orbit plane for an 8:1 repeat ground track. The three plots were generated by an ASKS run using a Method 2 controller for a , e , and i only. Ω , ω , and M were allowed to vary freely, and were never targeted. Figure 6.3 shows the motion of the semi-major axis and mean anomaly differences from nominal. Figure 6.4 shows the motion of the eccentricity, inclination, and ascending node differences from nominal. And figure 6.5 shows the motion of the inclination and the argument of perigee differences from nominal.

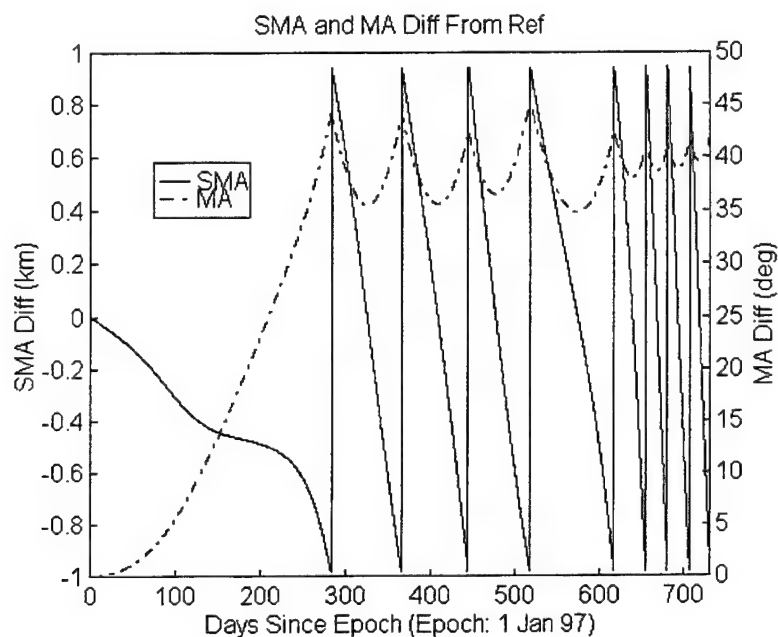


Figure 6.3: Controlled SMA and Floating MA Differences from Nominal

In figure 6.3, we see that a Method 2 correction to the semi-major axis across its nominal value, which is depicted as an instantaneous change upon reaching its limit of 1 km, also changes the mean anomaly difference rate to the negative of its original value. Therefore,

targeting the semi-major axis across its nominal value when the mean anomaly violates its limits is an option for a mean anomaly controller. In effect, the semi-major axis is changed just enough to reverse the phasing bias between the actual and nominal trajectories. This approach only works if the semi-major axis difference is negative when the mean anomaly difference is at its positive limit; and vice-versa. In addition, if the mean anomaly is at its negative outer limit while the semi-major axis rate is negative, then no correction should be made even if this means violating the negative MA outer limit. This is because the negative semi-major axis rate will eventually reduce the semi-major axis enough for the mean anomaly to return within its outer limit. This approach is implemented to avoid implementing corrections which lower the energy of an orbit, since atmospheric drag accomplishes this result anyway.

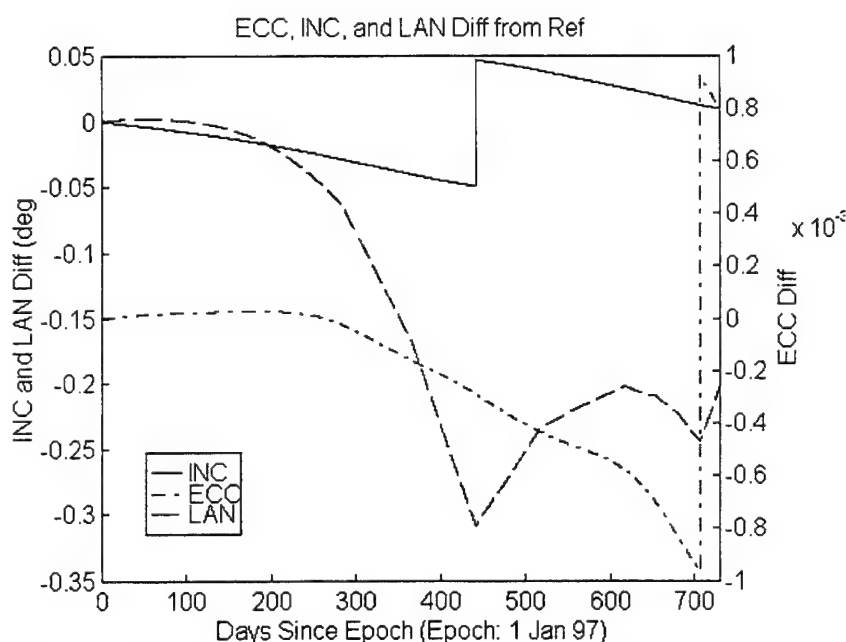


Figure 6.4: Controlled ECC and INC, and Floating LAN Differences from Nominal

Figure 6.4 illustrates that changes in both the eccentricity and the inclination affect the ascending node difference rate. Of the two, eccentricity corrections are generally far cheaper in terms of transfer delta-V's. However, eccentricity corrections will not be

effective if a significant eccentricity change (ie across the nominal value, as in figure 6.4) is not possible at the time of a Ω outer limit violation. In this situation, the inclination must be targeted instead. Therefore, the eccentricity is targeted to its outer limit on the other side of its nominal value, scaled by its maximum overshoot percentage. If the ascending node difference is at its negative difference limit when the eccentricity difference is positive and the inclination difference is negative, or vice-versa, then the inclination is targeted to its opposite outer limit, scaled by the ascending node maximum overshoot value. If a situation develops where both the eccentricity and inclination differences are the opposite sign of the ascending node difference at the time of a Ω outer limit violation, then the ascending node is allowed to violate until either the eccentricity or inclination differences change signs. In practice, this situation rarely develops because the frozen orbit design of Ellipso ties the motion of the inclination and ascending node.

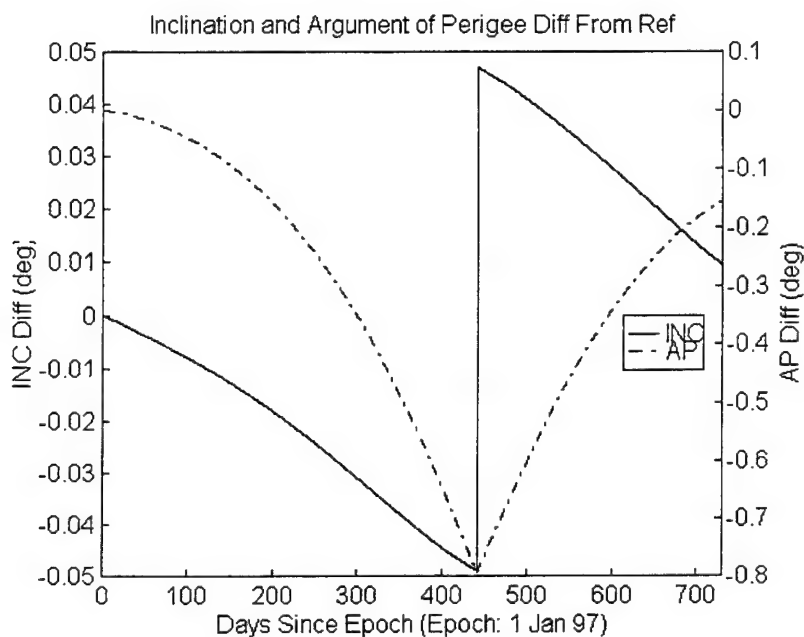


Figure 6.5: Controlled INC and Floating AP Differences from Nominal

Figure 6.5 demonstrates that only an inclination change affects the argument of perigee difference rate. The inclination difference must be negative when the argument of

perigee difference is at its negative limit for this type of correction to work. Once again, the relationship between the inclination and argument of perigee almost always assures this situation for Ellipso Borealis satellites. As with the ascending node case, the inclination is corrected to its opposite outer limit value, scaled by the argument of perigee maximum overshoot percentage.

Therefore, targeting Method 3 treats the semi-major axis, eccentricity, and inclination the same as targeting method 2. However, it targets a combination of eccentricity and inclination to correct ascending node deviations, the inclination to correct the argument of perigee, and the semi-major axis to correct mean anomaly differences. Since corrections to Ω , ω , and M are directed at different orbital elements, this method is called the method of *directed corrections*. It is important to note that while targeting Methods 1 and 2 are applicable to any satellite constellation, targeting Method 3 was designed specifically for the Ellipso Borealis 8:1 repeat ground track subconstellations.

[This page intentionally left blank.]

Chapter 7

Simulations

The ASKS simulations described in this thesis are done to meet three main objectives.

These objectives are:

1. Validate the ΔV statistics calculated by the Automated Station-Keeping Simulator for maintaining the orbits of a satellite constellation.
2. Investigate the advantage of controlling a constellation as a whole as opposed to controlling each satellite individually.
3. Demonstrate that the ASKS can be used to analyze new constellation orbit designs.

One series of simulation runs is executed for each objective. Variations of the Ellipso Mobile Satellite System constellation are used for the sample constellation orbits. The first simulation attempts to validate the ASKS ΔV generator by comparing its results to a study conducted by Chris Sabol [51] for a previous design of the Ellipso Borealis sub-constellation. The second compares the two year coverage histories and ΔV budgets for the absolute and relative mean anomaly station-keeping methods on the current Ellipso design. Targeting method 3 is used for both station-keeping options. And finally, the third simulation compares four different Ellipso orbit designs using coverage histories from uncontrolled ASKS runs. Before any of the simulations, however, a brief description is provided of the different Ellipso orbital designs proposed to date.

7.1 Ellipso Variations

Several different versions of the Ellipso constellation orbit design are used in the following simulations. The differences involve only the Borealis sub-constellation. While there are multiple options for the Concordia sub-constellation as well, only the circular orbit, whose mean orbital elements are listed in table 7.1, is used. The Mean of 1950 elements are provided because they are used in the ASKS input decks. Note that the conversion from the true of date frame to the Mean of 1950 frame changes the inclination by the rotation discussed in section 3.3.4. This same rotation shifts most of the argument of perigee to ascending node because of the near-circular nature of the orbit.

Table 7.1: Concordia Sub-Constellation Orbital Elements [53]

Element	True of Date	Mean of 1950
a	14440.137 km	14440.137 km
e	0.00001	0.00001
i	0.00001°	0.26180°
ω	90°	0.29389°
Ω	0.0°	89.10379°
M	0°, 51.43°, 102.86°, 154.29°, 205.71°, 257.14°, and 308.57°	0°, 51.43°, 102.86°, 154.29°, 205.71°, 257.14°, and 308.57°

The variations in the Borealis sub-constellation consist of nodal placement, repeat ground track, number of satellites, and argument of perigee placement. Each of the variations, however, maintains the Sun synchronous frozen line of apsides (SSFLA) characteristic of Borealis.

Nodal Placement

There are two designs for the placement of the ascending nodes of the Borealis planes. The first places the nodes at the dawn and dusk positions on the Earth's equator. Because the orbits are Sun synchronous, they will remain oriented so that their line of nodes is always perpendicular to the vector from the geocenter to the sun. This is the orientation studied by Chris Sabol in his master's thesis refinement of the original Borealis element sets. The 8:1 repeat ground track node at dawn and dusk mean element sets for the epoch at 0000 hours on 1 Jan 1997, refined in the presence of the zonal harmonics through degree 21, solar/lunar point masses, and solar radiation pressure, are listed in Table 7.2.

Table 7.2: Borealis 8:1 Mean Element Sets for Node at Dawn/Dusk [51]

Element	Node at Dawn Plane True of Date	Node at Dawn Plane Mean of 1950	Node at Dusk Plane True of Date	Node at Dusk Plane Mean of 1950
a	10559.257 km	10559.257 km	10559.2604 km	10559.2604 km
e	0.3453	0.3453	0.34587	0.34587
i	116.5747°	116.6212°	116.5538°	116.5067°
ω	270°	269.7119°	270°	270.2878°
Ω	10°	9.2687°	190°	189.5262°
M	0°, 72°, 144°, 216°, and 288°	0°, 72°, 144°, 216°, and 288°	0°, 72°, 144°, 216°, and 288°	0°, 72°, 144°, 216°, and 288°
Epoch	Midnight, Jan 1 1997	Midnight, Jan 1 1997	Midnight, Jan 1 1997	Midnight, Jan 1 1997

The orbit refinement process implies that the element sets in table 7.2 will maintain their SSFLA characteristics, to negligible errors over five years, if they are propagated only in the presence of the zonal harmonics through degree 21, solar/lunar point masses, and solar radiation pressure [51].

The second design places the ascending nodes of the Borealis planes at the noon and midnight positions on the Earth's equator. These planes remain oriented so that their angular momentum vectors are always perpendicular to the vector from the geocenter to the Sun. The 8:1 repeat ground track, with ascending nodes at noon and midnight, is the current design for the Borealis planes. The epoch mean element sets for this design, refined in the presence of the zonal harmonics through degree 21 and solar/lunar point masses, are listed in table 7.3. The effects of solar radiation pressure on satellites of the node at noon and midnight orientation of Borealis are too great to incorporate into the refinement process.

Table 7.3: Borealis 8:1 Mean Element Sets for Node at Noon/Midnight [52]

Element	Node at Noon Plane True of Date	Node at Noon Plane Mean of 1950	Node at Midnight True of Date	Node at Midnight Mean of 1950
a	10559.271 km	10559.271 km	10559.270 km	10559.270 km
e	0.345705	0.345705	0.345675	0.345675
i	116.565°	116.3074°	116.565°	116.8226°
ω	270°	269.9478°	270°	270.0524°
Ω	280°	279.3744°	100°	99.4212°
M	0°, 72°, 144°, 216°, and 288°	0°, 72°, 144°, 216°, and 288°	0°, 72°, 144°, 216°, and 288°	0°, 72°, 144°, 216°, and 288°
Epoch	Midnight, Jan 1 1997	Midnight, Jan 1 1997	Midnight, Jan 1 1997	Midnight, Jan 1 1997

Repeat Ground Track

Following the analysis done in his thesis, Sabol, with the assistance of Cefola and Draim [52] discovered that a slight change in the frozen orbit geometry of Borealis could result in significant savings in station-keeping fuel. This change involved extending the repeat

ground track cycle from 8:1 to 81:10, or 81 revolutions every 10 days. Doing so moves the orbit from deep resonance to shallow resonance. The epoch mean element sets for the 81:10 repeat ground track node at noon and midnight Borealis orbits, refined in the presence of zonal harmonics through degree 21 and solar/lunar third body effects, are listed in table 7.4. As with the 8:1 node at noon/midnight elements, the effects of solar radiation pressure are too large to include in the orbit refinement.

Table 7.4: Borealis 81:10 Mean Element Sets for Node at Noon/Midnight [52]

Element	Node at Noon Plane True of Date	Node at Noon Plane Mean of 1950	Node at Midnight True of Date	Node at Midnight Mean of 1950
a	10472.201 km	10472.201 km	10472.200 km	10472.200 km
e	0.32652	0.32652	0.32662	0.32662
i	116.583°	116.3254°	116.582°	116.8396°
ω	270°	269.9478°	270°	270.0524°
Ω	280°	279.3744°	100°	99.4212°
M	0°, 72°, 144°, 216°, and 288°	0°, 72°, 144°, 216°, and 288°	0°, 72°, 144°, 216°, and 288°	0°, 72°, 144°, 216°, and 288°
Epoch	Midnight, Jan 1 1997	Midnight, Jan 1 1997	Midnight, Jan 1 1997	Midnight, Jan 1 1997

The 81:10 Borealis orbits have a lower semi-major axis than their 8:1 counterparts. Despite this, Sabol's analysis shows that coverage and minimum elevation angles are not affected significantly [52].

Number of Satellites

To meet the coverage requirements described in section 1.2.2, the Ellipso constellation needs only four satellites in each of the Borealis planes and six satellites in the Concordia

plane. The operational plan for Ellipso, however, calls for the placement of one on-orbit spare in each of the three planes. Each spare is to function just like the remaining satellites in the plane. Because of this, the element sets of tables 7.2, 7.3, and 7.4 include five mean anomaly positions and table 7.1 includes seven mean anomaly positions. In the event of a satellite failure, the functioning satellites in the plane are required to reposition themselves, over time, to provide uniform spacing in mean anomaly. Therefore, the worst case scenario of a 4-4-6 component satellite constellation is also studied.

Argument of Perigee Placement

One of the options available to the node at noon / midnight Borealis orientation is biasing of coverage to the daylight hours. Because of its SSFLA design, reducing the argument of perigee of the node at noon plane, and increasing the argument of perigee of the node at midnight plane, tilts the planes so that the apogees are always in sunlight. This implies that, on average, each satellite will spend more time over the sunlit Earth. This option is important because it offers Ellipso the chance to bias its coverage to daytime market demand. In studying this special case, the argument of perigee is set to 260° for the node at noon plane and 280° for the node at midnight plane.

The Ellipso constellation is different from other constellations in that the mean anomaly is the only candidate element for relative station-keeping across satellites. In constellations such as Iridium and Globalstar, there are no real restrictions against controlling the relative ascending node between planes, and allowing the nominal semi-

major axis of all the satellites in a plane to reduce together while their relative mean anomaly is maintained. For Ellipso, however, the SSFLA characteristics of the Borealis planes restrict most of the elements to a small locus of points. Since the required sun synchronous nodal rate is caused by maintaining the critical inclination, both the inclination and the ascending node are removed as candidates for relative control across the planes. In addition, the semi-major axis, eccentricity and argument of perigee must remain fixed values to maintain the frozen orbit. Because of this, the mean anomaly is the only option for relative station-keeping. Relative mean anomaly station-keeping is implemented by resetting the nominal mean anomaly value of each satellite in the plane to the value that results in the lowest sum of the squares of the mean anomaly differences at each iteration time step. Using this approach allows the entire plane to have a common mean anomaly motion, and yet not require any corrections. If absolute mean anomaly station-keeping is implemented, then the nominal mean anomaly for each satellite is determined by the propagation of its nominal elements.

7.2 Simulation 1: Validation of ASKS

The purpose of Simulation 1 is to produce a station-keeping ΔV budget for the satellites of the 8:1 node at dawn/dusk Borealis planes. Comparing these results to the estimated ΔV budget analytically obtained by Sabol [51] serves as an important step in validating the ASKS ΔV generator. If the ASKS generated ΔV history produces results similar to Sabol's, then an argument can be made for the suitability of the Primer Vector optimal transfer theory to the station-keeping problem, and the general implementation of the control methods used in this thesis.

The objective of Sabol's thesis was to investigate the stability and station-keeping costs of the Borealis SSFLA orbits, and to refine the original orbit design to incorporate several perturbations. His product was a set of elements for the Borealis node at dawn and dusk planes that maintain SSFLA characteristics, for the five year projected life span of Ellipso satellites, in the presence of zonal harmonics through degree 21, solar/lunar point masses, and solar radiation pressure, without requiring any maneuvers. These refined element sets are listed in table 7.2. Sabol predicted that station-keeping maneuvers would only be required to counteract the effects of drag and tesseral resonance. He determined that three different types of maneuvers - drag, eccentricity, and inclination control - would maintain the Borealis satellites within the limits defined in table 6.1. Sabol's estimates of the 5 year ΔV and fuel mass requirements for the three control maneuvers for the worst case satellite are listed in table 7.5.

Table 7.5: 5 Year Predicted ΔV and Fuel Budget for Worst Case Borealis 8:1 Node at Dawn / Dusk Satellite [51]

Mission Lifetime: 5 yrs	ΔV (m/s)	m_f (kg)
Drag Control	34.673	8.531
Eccentricity Control	0.655	0.161
Inclination Control	26.897	6.618
Total	62.225	15.31

To test the ΔV generator, the ASKS execution for Simulation 1 must resemble Sabol's test conditions as accurately as possible. Therefore, targeting method 2 is used with absolute station-keeping for the node at dawn and dusk satellites defined by the element sets listed in table 7.2. The run will execute semi-major axis corrections to simulate drag control, and eccentricity and inclination corrections to simulate their respective controls.

Note that the ascending node, argument of perigee, and mean anomaly are not controlled directly. Sabol predicted that the three control maneuvers seen in table 7.5 would maintain all the elements either directly or indirectly.

The refined Borealis orbit elements are correctly applied only if the nominal trajectory experiences the same perturbations over which the element sets are refined. To simulate this, the zonal harmonics through degree 21, solar/lunar point masses, and solar radiation pressure are all turned on for the nominal (reference) trajectory. The actual satellite trajectory contains the perturbations of the nominal trajectory plus tesseral resonance and atmospheric drag. Therefore, the corrective maneuvers will be based on the state differences caused by only the tesseral resonance and atmospheric drag. The assumption that the refined elements maintain the SSFLA characteristics is supported by analysis provided in Sabol's thesis [51].

To insure that the drag effects in the ASKS run are calculated the same way as in Sabol's estimation, the satellite characteristics must be set the same. Sabol's study uses a 700 kg satellite with a cross-sectional area of 35 m², a drag coefficient of 2.0 and a reflectivity coefficient of 1.2 [51]. The only difference in the ASKS run is that the area is set to 25 m². This is a revised value determined by MCHI after Sabol's thesis [52]. Rather than executing the ASKS run with the older area value, Sabol's drag make-up control output will be scaled by 25/35 in the comparison. This approach allows future work on the Borealis satellites to use the results of this work without rescaling. In addition to the satellite characteristics, the ASKS run also applies the same Jacchia-Roberts atmospheric density model, with Schatten's "hot" solar flux predictions, as used by Sabol.

The input deck for the ASKS run and the resulting orbital element difference plots for the satellites of both planes are provided in Appendix B. Note that these plots are for a two

year duration, and not the five year time span considered by Sabol. For the satellites of both planes, the Method 2 a, e, and i controller executes corrections for violations of the outer limits in these elements. All corrections cause the violating elements to target a value on the opposite side of its nominal. While no corrections are made to Ω , ω , and M directly, their rates are altered by corrections to a, e, and i. These directed corrections, which form the basis of the Method 3 controller discussed in section 6.4, are noticeable and fairly effective in containing the Ω and ω variations. In general, a, e, and i corrections keep the Ω , ω , and M differences from increasing without bounds. The argument of perigee ω is not violated in the node at dawn plane, and is only violated by the 1st (initial $M=0^\circ$) and 5th (initial $M=288^\circ$) satellites in the node at dusk plane. The ascending node Ω is kept within 0.5° for satellites in both planes. The mean anomaly M , however, is not maintained well at all. The maximum M deviation is 40° in the node at dawn plane and 25° in the node at dusk plane.

The 2 year plots in Appendix B show that while the drag, eccentricity, and inclination controls proposed by Sabol maintain a, e, and i within the prescribed limits, they are not sufficient for the full control of the satellites in the Borealis sub-constellation. This is not an entirely unexpected result. Sabol's analysis was based only on the deviations observed in the elements. Correcting these deviations along the trajectory has significant effects on the element difference rates. These rates in turn affect the future motion of the elements for the duration of the trajectory following the correction. The motion caused by the changed rates cannot be observed if the elements themselves are not changed. The orbit propagation tool used by Sabol was not able to analyze the orbits in this manner. Since, the ASKS was specifically designed for this purpose, it is better able to track the motion of repeatedly corrected element trajectories.

The comparison of ΔV statistics between the ASKS run and Sabol's calculated values must take many factors into account. The first is the change in the cross sectional area of the satellite, as discussed above. To account for this, Sabol's drag control ΔV estimates are to be scaled by a factor of 25/35. Another factor is the duration and time span considered. Since the solar flux activity varies over time, simply scaling up the ΔV budget of a shorter duration run is not acceptable. To avoid executing a full 5 year controlled execution of the ASKS, however, we take advantage of the fact that the Schatten solar flux maximum occurs at the center of the Jan 1997 to Jan 2002 time span considered in Sabol's analysis, and that it is essentially symmetric about the maximum value. This implies that the semi-major axis and eccentricity controls can be assumed to be the same in the first half and second half of the Jan 1997 to Jan 2002 five year time span. From the inclination plots (figures B.2 and B.9) we see that the inclination rates remain steady throughout the 2 year run. Therefore, we can take half the magnitude of the five year ΔV statistics estimated by Sabol and compare them to the ΔV statistics produced by a $2\frac{1}{2}$ year run of the ASKS from Jan 1997 to July 1999 without losing accuracy. The ΔV statistics for each of the 10 Borealis satellites for this $2\frac{1}{2}$ year ASKS run, and their percent differences from the Sabol's twice scaled ΔV estimate of 25.159 m/s, are listed in table 7.6.

The ASKS ΔV budgets for each satellite are systematically greater than the worst case ΔV budget predicted by Sabol. The differences range from 10.47% to 114.91%, with the largest occurring for the node at dusk satellite which starts at $M=72^\circ$. This discrepancy is partly due to the fact that some small eccentricity and semi-major axis perturbations were neglected in Sabol's study [51]. The main reason, though, is because of the differences in approaches used to determine the ΔV history.

Table 7.6: 2¹/₂ Year ASKS / Sabol ΔV Comparison For Node At Dawn / Dusk Borealis Satellites

Satellite	Node At	Initial M	ΔV (m/s)	% Diff from Sabol
1	Dawn	0°	31.587	+ 20.75%
2	Dawn	72°	35.142	+ 34.34%
3	Dawn	144°	27.793	+ 10.47%
4	Dawn	216°	36.129	+ 43.60%
5	Dawn	288°	34.122	+ 35.63%
6	Dusk	0°	39.575	+ 57.30%
7	Dusk	72°	54.068	+ 114.91%
8	Dusk	144°	38.418	+ 52.70%
9	Dusk	216°	48.442	+ 92.54%
10	Dusk	288°	31.666	+ 25.86%

Sabol analyzed the maximum deviations in each element for the entire time span, and then estimated ΔV corrections using the equations resulting from the integration of Gauss' form of the variational equations [51]. In doing so, the effect of the corrections on the element rates were not considered. For example, it was noticed that the difference between the actual and nominal inclination rate at epoch stays constant if the semi-major axis and eccentricity are maintained within their maximum limits. This implies that continually correcting a and e repeatedly drives the inclination difference to violate its limits. If the semi-major axis and eccentricity are allowed to vary, as in Sabol's analysis, then the inclination rate difference begins to oscillate, causing the inclination difference to taper off before reaching the maximum limit boundary. Therefore, not incorporating the effects of the corrections on the element rates results in fewer than the actually required number of impulses being included in the ΔV history. The ASKS actually simulates every correction with an orbital transfer. This approach preserves the effects of

the corrections on the element rates, and produces a much more accurate representation of the element difference history and ΔV history.

Because the ASKS approach is better able to model corrected trajectories, we can state that its ΔV budgets represent a more accurate, yet conservative, upper bound on the actual ΔV required for station-keeping the Borealis node at dawn and dusk satellites, if only semi-major axis, eccentricity, and inclination are to be controlled to their table 6.1 limits. Maintaining the argument of perigee, ascending node, and mean anomaly to their table 6.1 limits, however, will require additional corrections, and consequently, a larger ΔV budget.

7.3 Simulation 2: Absolute vs. Relative Mean Anomaly Control

The purpose of Simulation 2 is to produce orbital element difference histories, coverage histories, and ΔV budgets for the control of the Ellipso constellation. The Ellipso constellation used includes the 8:1 node at noon/midnight Borealis planes with 5 satellites each and the Concordia plane with 7 satellites. This simulation consists of three different runs. The first is a Method 0 uncontrolled 2 year execution of ASKS. This run provides a general understanding of the element variations and the baseline coverage characteristics of the Ellipso constellation. The second run is a two year Method 3 ASKS execution using absolute station-keeping for all the elements. The third run is a two year Method 3 ASKS execution using relative station-keeping for the mean anomaly. Comparison of the coverage histories from Run 2 and Run 3 to Run 1 will reveal whether the Method 3 controller is able to meet the Ellipso coverage requirements. Comparison of the Run 2 and Run 3 ΔV budgets will reveal whether there is a fuel cost incentive for

the Ellipso satellites in a plane to be controlled using relative mean anomaly station-keeping.

The element sets for the Borealis satellites in all three runs are those refined by Sabol, Draim, and Cefola [52]. They are listed in table 7.3. Since these element sets are refined in the presence of zonal harmonics through degree 21 and solar/lunar point masses, those are the two perturbations activated for the nominal (reference) trajectories. The actual satellite trajectories will experience these perturbations plus solar radiation pressure, tesseral resonance and atmospheric drag. The element sets used for the Concordia satellites are listed in table 7.1.

Run1

The input deck, one to four-way coverage plots, and element difference plots for Run 1 are located in section C.1 of Appendix C. Note that coverage is calculated for the entire northern hemisphere and for the southern hemisphere above 55°S latitude. The northern hemispheric coverage assumes a 25° minimum elevation angle. The southern hemispheric coverage assumes a 10° minimum elevation angle. This same type of coverage calculation is used for all three runs. These coverage specifications are defined by MCHI [12].

The maximum northern and southern hemispheric coverages occur at the epoch as expected. Note that the epoch southern hemispheric coverage from 0°-55°S latitude is not 100%, as it is for the northern hemisphere, but approximately 97.7%. This is supported by the minimum elevation requirement plot of figure 1.2. It suggests that to obtain 100% coverage from 0°-55°S latitude using a 7 satellite Concordia plane, the

minimum elevation angle requirement must be reduce to 5° from the current 10° , or the southernmost latitude line for 10° minimum elevation angle must be raised to 50°S from 55°S .

For the northern hemisphere, the one-way coverage degrades from 100% to a minimum of 92% after 475 days (~ 16 months) before recovering to 99% at the end of two years. The two-way coverage begins at 85.3% and degrades to 63% after 325 days (~ 11 months) before recovering to about 75% at the end of two years. This coverage variation is clearly caused by the large deviations of the Borealis satellites from their nominal orbital elements. The uneven drag induced semi-major axis decay for the satellites in both Borealis planes drives the errors in the mean anomaly spacing. The variations in eccentricity and argument of perigee demonstrate that the frozen orbit characteristics are slowly degrading as well. Tesseral resonance, caused by the 8:1 repeat ground track, makes the element variations in each of the elements different for satellites in the same plane. These combined effects leave no choice but to implement a controller for each of the elements of the Borealis satellites.

In sharp contrast, the southern hemispheric one-way and two-way coverage does not degrade at all over the two year span of this run. This is reflected in the small deviations of the elements of the Concordia satellites, which provide coverage to the southern hemisphere. Since the Concordia satellites do not experience tesseral resonance, their element differences are the same irrespective of initial mean anomaly placement. The semi-major axis and inclination variations do not violate the table 6.2 limits. Note that while the eccentricity variation does violate its limit of 0.0003, with a maximum of 0.0012, the deviation is periodic and does not have an impact on the coverage. Because there is no loss of coverage due to element variations from the nominal for the Concordia satellites, the Concordia planes in Runs 2 and 3 will not be controlled.

Runs 2 and 3

The input deck, one to four-way coverage plots, and element difference plots for Run 2 and 3 are located in sections C.2 and C.3, respectively, of Appendix C. As explained above, no attempt is made to control the satellites of the Concordia plane since we have shown that their element variations over two years are not significant enough to affect the southern hemispheric coverage. For the Borealis satellites, the mean anomaly maximum limit of 0.05° was deemed too strict and would require too many directed semi-major corrections. Thus the mean anomaly maximum limit for the Borealis satellites was set to 5° for both runs.

The one and two-way northern hemispheric coverage values remain at their epoch values for both runs. Thus, one-way coverage stays at 100% and two-way coverage maintains an average of 85.3% with a very small standard deviation. The small deviations in the two-way coverage are more likely due to noise in the coverage calculation than to any physical disturbance. These plots demonstrate that the Method 3 controller applied with both the absolute and relative mean anomaly station-keeping is successful at maintaining the optimal coverage of the Ellipso constellation.

The semi-major axis, eccentricity, and inclination variations for the Borealis satellites of both runs are kept within their respective maximum limits by targeting Method 2 control procedures. At many points along the two year trajectory, however, corrections are made to these elements when they are not at their outer limits. These corrections are directed by outer limit violations in the ascending node or mean anomaly, as per the Method 3 controller. Note that the argument of perigee never reaches its outer limit of 0.98° for any Borealis satellite in both runs.

One of the interesting aspects of the element difference plots of Run 2 and Run 3 is with the mean anomaly. The mean anomaly plots are figures C.32 and C.38 for absolute station-keeping, and C.48 and C.54 for the relative station-keeping. Note that the mean anomaly outer limit violations drive the semi-major axis corrections until about 600 days (~20 months) into the 2 year run. At that point, the solar flux induced drag affect on the semi-major axis becomes large enough so that the semi-major axis degrades to its negative outer limit of -1.0 km before its corresponding mean anomaly can reach its positive outer limit of $+5.0^\circ$. The semi-major axis violation induced semi-major axis corrections still have the requisite effect of reversing the motion of the mean anomaly variation. Therefore, after 600 days, the mean anomaly is actually maintained tighter than the 5° specified maximum limit purely by the requirements placed on the semi-major axis. Since the northern hemispheric coverage does not ever stray from a value of 100%, this behavior suggests that the semi-major axis limit for Borealis is too tight for the specified coverage requirement.

Figure C.54, the mean anomaly differences for the node at midnight plane for Run 3 displays an interesting situation that develops with the combination of relative mean anomaly station-keeping with directed semi-major axis corrections (Method 3). Note first that negative mean anomaly outer limit violations are not considered to require semi-major axis directed corrections if the semi-major axis rate difference is negative at the time of the violation. This feature was built into the controller to avoid enacting burns which lower the energy of an orbit. The negative semi-major axis rate difference implies that the negative mean anomaly violation will eventually turn around on its own and cross back into the acceptable region. This approach works for individual mean anomaly station-keeping, as seen for the node at midnight satellites of Run 2 (figure C.38). However, when the nominal mean anomaly value for a satellite is allowed to vary based

upon the mean anomaly motions of the other satellites in the Borealis plane, as with the relative station-keeping method, then the combined tendency of the remaining satellites to move ahead in mean anomaly (due to drag) causes the negative mean anomaly violating satellite to push further into the negative violating region. In figure C.54, we see that satellite 2 (initial $M=72^\circ$) is caught in the negative violating region after having strayed too far into it because of the controller restriction against lowering orbit energy. Since this violation did not affect the northern hemispheric coverage, the restriction against reducing orbit energy was retained. In other constellation cases, though, this particular behavior of relative station-keeping may pose a problem that requires special attention in the control method.

Table 7.7: 2 Year ΔV Budgets For Node At Noon / Midnight Borealis Satellites Using Method 3 Controller With Absolute and Relative Mean Anomaly Station-Keeping

Satellite	Node At	Initial M	Absolute SK ΔV (m/s)	Relative SK ΔV (m/s)	Difference ΔV (m/s)
1	Noon	0°	39.001	31.412	- 7.589
2	Noon	72°	43.742	37.433	- 6.309
3	Noon	144°	31.113	35.698	4.585
4	Noon	216°	37.928	41.732	3.804
5	Noon	288°	35.864	38.891	3.027
6	Midnight	0°	24.043	25.031	0.988
7	Midnight	72°	38.018	37.348	-0.670
8	Midnight	144°	23.143	15.535	-7.608
9	Midnight	216°	36.667	33.524	-3.143
10	Midnight	288°	27.875	31.007	3.132

The 2 year ΔV budgets for the Borealis satellites using the Method 3 controller with absolute and relative station-keeping are listed in table 7.7. The maximum satellite ΔV

requirement is 43.742 m/s with absolute station-keeping and 41.732 m/s with relative mean anomaly station-keeping. On average, the per satellite reduction in ΔV using relative mean anomaly station-keeping is only 0.978 m/s, or 2.90%. Once an engineering safety factor is added to the ΔV budgets, this small improvement essentially disappears. Therefore, there is no significant fuel reduction caused by implementing relative station-keeping for the 8:1 Borealis orbit satellites.

7.4 Simulation 3: 81:10 Ellipso Coverage Analysis

The refined 8:1 repeat ground track orbits are the currently accepted design for Borealis. Recently, however, MCHI has begun considering the adoption of a modified design with an 81:10 repeat ground track cycle. Sabol, Draim, and Cefola showed that this new design moves the Borealis from deep resonance to shallow resonance without having a significant impact on the minimum elevation angle specifications [52]. By their calculations, satellites in the 81:10 orbits, which don't experience the uneven tesseral resonance disturbances, require only 5.2 kg of station-keeping fuel for a 5 year mission as opposed to 14.8 kg for the current design [52]. This new design presents an opportunity to demonstrate that the ASKS can be used to analyze new constellation designs even without implementing controlled runs.

The purpose of this simulation, then, is to study the coverage and element difference histories of four possible versions of the Ellipso constellation with 81:10 Borealis orbits. All the runs are Method 0 uncontrolled and last for 5 years. Run 1 is on the standard 5-5-7 satellite 81:10 Ellipso constellation. The epoch element sets for this run are listed in table 7.4. Run 2 is on the 4-4-6 satellite configuration. This means that each Borealis plane will have 4 satellites, and the Concordia plane will have 6 satellites. Runs 3 and 4

will be the same as Runs 1 and 2, but with the arguments of perigee of the two Borealis planes rotated to bias coverage to daylight hours. These runs use the same element sets as Runs 1 and 2, but with a 260° node at noon argument of perigee and a 280° node at midnight argument of perigee. Note that all four runs use relative mean anomaly station-keeping. Since no control method is applied, this is done only to clarify mean anomaly difference plots.

The input deck, one to four-way coverage plots, and element difference plots for Run 1 are located in section D.1 of Appendix D. Since the Concordia satellites have not been modified, they display the same element motion seen in Simulation 2. The element difference plots for the Borealis satellites, however, are strikingly different from their Simulation 2 counterparts. All the satellites in a Borealis plane now have a common semi-major axis, eccentricity, inclination, and ascending node differences over the five years. The argument of perigee differences diverge somewhat, but not significantly with respect to its maximum limits. Since the nominal mean anomaly is adjusted at each time step to allow for relative station-keeping in this element, the mean anomaly differences do diverge, but only to 5.5° over the 5 year time span. While the semi-major axis decays 8 km for the node noon satellites and almost 35 km for the node at midnight satellites, the one-way northern hemispheric coverage remains at 100% for the entire 5 year span with the exception on one small duration deviation. The two-way northern hemispheric coverage displays a gradual secular decrease from an epoch value of 83.2% to about 82.5% at the 2 year point. The southern hemispheric one-way coverage remains steady at 97.9% throughout the time span of the run. The southern hemispheric two-way coverage average is steady at 82.3%, but experiences a higher standard deviation. As a whole, these plots reveal that station-keeping expenditure is not required to maintain one-way

coverage for the 5-5-7 81:10 Ellipso constellation, but is required to maintain two-way coverage.

The one to four-way coverage plots and element difference plots for Run 2 are located in section D.2. Since tesseral resonance is not as predominant as in the 8:1 case, the four satellites of Run 2 Borealis planes exhibit the same element difference motion as the five satellites of the Run 1 Borealis planes. Initial satellite mean anomaly location is not a significant factor in the presence of shallow resonance. For the northern hemisphere, the one-way coverage begins to deviate more often from 100% than with Run 1. The two-way coverage begins at 66% and degrades to 65% in two years. Notice that this is significantly less than the approximately 82% two-way coverage exhibited by the 5-5-7 constellation. In the southern hemisphere, the one-way coverage remains steady at 97.2% while the two-way coverage averages to 65% but ranges from a low of 64.4% to a high of 67.5%. Both the one-way and two way coverage values are lower than their 5-5-7 counterparts. From these coverage plots, we see that the 4-4-6 81:10 Ellipso constellation needs control to maintain both one-way and two-way coverage, and that two-way coverage is more sensitive than one-way coverage to the on-orbit failures of Ellipso satellites.

The one to four-way coverage plots and element difference plots for Run 3 are located in section D.3. The element difference plots for the Run 3 Borealis planes, with rotated 10° argument of perigee, are essentially the same as the Run 1 plots. None of the element variations are significantly affected by the change in perigee locations. In terms of coverage, the largest change is in the two-way coverage values. For the northern hemisphere, the two-way coverage starts at 82.1% and increases slightly to 82.3% in 2 years. In Run 1, this coverage was approximately 83% and decreasing. For the southern hemisphere, the two-way coverage is slightly higher at 82.6% than its Run 1 value. This

behavior is explained by the fact that rotating the planes toward sunlight brings the edge of the Borealis coverage pattern further into the equatorial region where Concordia's coverage pattern is dominant.

The one to four-way coverage plots and element difference plots for Run 4 are located in section D.4. As with Run 3, the element difference plots of Run 4 are not changed by the 10° rotations in argument of perigee. For the northern hemisphere, the one-way coverage deviates even more frequently than in Run 2 (4-4-6 with standard ω) from 100%, but only for short durations and a maximum drop of 0.1%. For the southern hemisphere, the one-way coverage is steady at 97.2%, the same value as with Run 2. The two-way coverage exhibits the same shift as in Run 3. The two-way northern coverage is smaller at 64.5% while the two-way southern coverage is higher at 65.7%.

These four runs reveal some preliminary information about the nature of the proposed 81:10 Ellipso constellation. They verify Sabol, Draim, and Cefola's results about the elimination of the 8:1 deep resonance effects. In addition, they provide the initial coverage analysis for each of the configurations. For a more in-depth analysis, however, coverage histories which distinguish between sun-lit and shadow times are needed to ascertain the true coverage advantage of rotating the Borealis planes. While this capability does not exist in the current coverage utility used by the ASKS, it is an area for future development of the system. In addition, further analysis of the 81:10 Ellipso using controlled ASKS executions is required. These runs can help provide the upper bounds on the station-keeping ΔV budgets for the 81:10 satellites.

Chapter 8

Conclusions and Future Work

This work develops and tests a system for the automated station-keeping of satellite constellations. The system treats constellation station-keeping as an integrated trajectory tracking problem. It simultaneously maintains all satellites of a constellation within the defined orbital element limits of their nominal trajectories. The system can take advantage of the distributed nature of constellations by controlling satellites and planes relative to their each other rather than independently. The control law consists of three components: correction implementation criteria, a function which chooses which orbital elements to correct, and a targeting method which determines a future target state. The system is flexible in that it allows for different targeting methods. The targeted state is achieved with the use a multi-impulse near-optimal orbital transfer calculated using Primer Vector theory.

The Automated Station-Keeping Simulator (ASKS) is the software product created for this project. It is a flexible scaleable computer program which simulates the station-keeping of an entire constellation. There are no restrictions on the type of orbits, plane configurations, or number of satellites that can be considered. The ASKS uses the DSST Standalone Orbit Propagator for its orbit calculations. DSST is an efficient and accurate tool which uses semi-analytic satellite theory to predict state and state rate information. It is capable of incorporating impulsive transfers and accurately modeling several perturbations, including spherical harmonics, tesseral resonance, solar radiation pressure,

solar/lunar point mass disturbances, and atmospheric drag. The ASKS software also uses the Message Passing Interface (MPI). This allows the simulation to operate in parallel on a distributed network of workstations.

Three different targeting methods are developed in this thesis. The ASKS is designed so that additional methods can quickly and easily be added in the future. The first targeting method simply brings elements that are identified for correction back to their nominal element values. The second targeting method attempts to correct the elements beyond the nominal values in an attempt to reduce the frequency of orbital corrections. The third targeting method, called direct corrections, directs changes in the ascending node, argument of perigee, and mean anomaly element rates with corrections to the semi-major axis, eccentricity, and inclination. In addition to these three conventional methods, three detailed Lyapunov non-linear control strategies are proposed.

Finally, three simulations were conducted to analyze the control and coverage characteristics for the Ellipso constellation. In the first simulation, the ΔV generator was validated with a comparison to an Ellipso study conducted by Sabol [51]. The second simulation investigated the advantage of controlling the Ellipso planes as a whole rather than as separate satellites. The third simulation analyzed the coverage characteristics of different orientations of the proposed 81:10 Ellipso constellation orbits.

The remainder of this chapter lists some specific conclusions and identifies some areas of future work related to the ASKS and automated constellation station-keeping methodology.

8.1 Conclusions

Primer Vector Theory

There are two conclusions related to using Primer Vector Theory for the problem of station-keeping.

First, the method for determining the optimal magnitude of an interior burn, without invoking first order assumptions, is to use a binary search scheme to solve for the root of the following equation

$$\frac{\partial dJ}{\partial c} = \frac{(2cq_f + p_f)r_f}{2\sqrt{c^2 q_f + c p_f + 1}} + \frac{(2cq_o + p_o)r_o}{2\sqrt{c^2 q_o + c p_o + 1}} + 1 = 0$$

This equation is the partial derivative of the cost increment dJ with respect to the magnitude of the interior impulse c . The definitions of p , q , and r are listed in equation 2.37 in Chapter 2. The graph of this equation is characterized by alternating steep rises and plateaus. Despite its complicated nature, there is always one solution for the magnitude of the interior impulse.

Second, Powell's method can be used to optimize the time of the interior impulse. This replaces the gradient search on the interior burn time and position displacement used by Jezewski and Rozendaal [34]. This approach greatly simplifies the search for the minimum characteristic velocity, but the resulting burnlist can only be considered to be near-optimal.

The following conclusions are related to the ASKS simulations run on variations of the Ellipso constellation.

The $2\frac{1}{2}$ year ΔV budgets calculated by the ASKS for the 8:1 Borealis satellites in the node at dawn and dusk configuration are listed in table 8.1. Only the semi-major axis, eccentricity, and inclination are controlled with targeting Method 2.

Table 8.1: Average and Maximum $2\frac{1}{2}$ Year ΔV Budgets for Borealis Node at Dawn / Dusk Satellites

	avg ΔV (m/s)	max ΔV (m/s)
Node at Dawn	32.955	36.129
Node at Dusk	42.434	54.068

On average, these ASKS ΔV budgets are 28.96% greater for the node at dawn plane and 68.66% greater for the node at dusk plane than the equivalent maximum ΔV budget estimated by Sabol in his study of these orbits [51]. Since the ASKS simulates every correction and determines its effects on each of the elements, rather than analytically estimating corrections from uncontrolled element histories, these ΔV budgets represent a more accurate, yet conservative, upper bound on the actual ΔV budgets of the Borealis node at dawn and dusk satellites, if only semi-major axis, eccentricity, and inclination are to be controlled. The ascending node, argument of perigee, and mean anomaly violate their orbital element limits. Therefore, additional fuel is required for the control of all the elements.

The 2 year ΔV budgets for the 8:1 Ellipso satellites in the node at noon and midnight planes are listed in table 8.2. No control expenditure is required in the Concordia plane to

maintain coverage. The ASKS runs associated with this simulation use targeting Method 3 with a modified 5° maximum limit on the mean anomaly. For the time span from Jan 1997 to Jan 1999, the worst case ΔV budget for the 8:1 Borealis node at noon/midnight satellites is 43.742 m/s. On average, the per satellite reduction in ΔV using relative mean anomaly station-keeping is only 0.978 m/s, or 2.90%. Once an engineering safety factor is added to the ΔV budgets, this small improvement essentially disappears. Therefore, there is no significant fuel reduction caused by implementing relative mean anomaly station-keeping for the 8:1 Borealis orbit satellites.

Table 8.2: 2 Year ΔV Budgets for Borealis Node at Noon / Midnight Satellites Using Absolute and Relative Mean Anomaly Station-Keeping

	Absolute SK avg ΔV (m/s)	Absolute SK max ΔV (m/s)	Relative SK avg ΔV (m/s)	Relative SK max ΔV (m/s)
Node at Noon	37.530	43.742	37.003	41.732
Node at Midnight	29.949	38.018	28.489	37.348

Some other conclusions can be drawn from this 8:1 Ellipso analysis as well. First, targeting Method 3 is able to maintain all the orbits of the constellation, and the epoch one-way and two-way coverage, without any unexpected violations of the element limits. The negative mean anomaly limit is violated briefly by some satellites in order to avoid burns which reduce orbit energy. Second, if coverage is the only determining factor, the current 1 km semi-major axis limitation for the 8:1 Ellipso should be increased. Finally, the use of targeting Method 3 with relative mean anomaly station-keeping can result in an anomalous situation where one satellite's mean anomaly is forced to remain outside the maximum limits for an extended duration.

The coverage analysis of the 4-4-6 and 5-5-7 satellite 81:10 Ellipso constellations, with and without adjustment of the argument of perigee for biasing towards daylight coverage, yields multiple conclusions. First one-way coverage for the standard 5-5-7 satellite Ellipso constellation can be maintained for 5 years without any station-keeping. Maintenance of two-way coverage, however, requires station-keeping. Second, a 10° rotation in argument of perigee for the 81:10 Borealis planes does not have a significant impact on the coverage characteristics. Finally, the element difference plots for all the configurations verify Sabol, Draim, and Cefola's results about the elimination of the 8:1 deep resonance effects.

8.2 Future Work

ASKS

Some areas of future work that relate to the expansion of the functionality in the Automated Station-Keeping Simulator are

- expansion of the ASKS to include station-keeping via electric propulsion and finite burn models
- incorporation of a genetic algorithms (GA) package for the purpose of optimizing orbital element limits and control parameter settings
- development and integration of Lyapunov control targeting methods; to include exploration of the use of the shaping matrix \mathbf{M} and the scalar functions K and L
- removal of the one orbit period constraint on the iteration time step of the controlling loop

- incorporation of a sectoral coverage analysis capability into the global coverage package
- development of a revised Method 3 targeting strategy that allows the restriction against burns that lower orbit energy when using relative mean anomaly station-keeping
- derivation of a new equation for the cost increment dJ which does not rely on first order assumptions
- application of control algorithms developed in this thesis to the problem of automatically rephasing the operational satellites in a plane following an on-orbit failure
- modification of the communications architecture between ASKS processes to allow crosslink between satellites rather than routing all communication through the ground station

DSST

Certain improvements to the operation of the orbit propagator will allow the ASKS to incorporate control strategies that require accurate positioning with respect to the Earth. Other improvements promise significant reductions in the run time of ASKS executions. These improvements are

- enabling of true-of-date state and state rate output
- removal of orbit integrator re-initialization requirement for consecutive executions using the same epoch state
- removal of DSST requirement to re-read all binary data files for every call of *sat_prop_mod*

- incorporation of 50 x 50 potential field model and J2000 inertial reference frame for precise mean element propagation

Test Cases

There are also several areas of study open to investigation with the ASKS. Some of these are

- the study of larger constellations such as the 66 satellite Iridium using more workstation platforms or computers with large scale symmetric multi-processing capability
- the study of relative station-keeping with the semi-major axis and ascending nodes, as well as mean anomaly
- determination of ΔV budgets for the different configurations of the 81:10 Ellipso constellation

The study of station-keeping presented in this thesis is one part of a larger initiative being pursued by the Astrodynamics Applications business area at the Charles Stark Draper Laboratory. Building upon a solid foundation of satellite flight dynamics research, software tools, and operational systems, the goal of the initiative is establish a knowledge base and develop innovative concepts for constellation flight dynamics. This expansion of scope from individual satellite level to constellation level is spurred by the ongoing development of constellations for global personal communications. Other areas of study in the initiative include distributed processing for flight dynamics software and orbit determination based on GPS and crosslink ranging navigation concepts.

Appendix A

Mean of 1950 / True of Date Output Comparison

This appendix contains all the plots related to the test case executed to show that the orbital element differences, between the actual and nominal states, are the same in the Mean of 1950 and the instantaneous true of date frames. It involves two runs of the GTDS/SST propagator. In both runs, the nominal trajectory is propagated with a 21×0 geopotential force model (zonals only) while the actual trajectory includes a full 21×21 force model, tesseral resonance, solar radiation pressure, atmospheric drag, and solar/lunar third body point masses. Each run is 5 years long from Jan 1997 to Jan 2002. In Run 1, the output is in the Mean of 1950 reference frame. In Run 2, the output is in the instantaneous true of date frame. The differencing and plotting was done with a Tcl routine developed by Brian Kantsiper [35].

Section A.1 contains the GTDS input deck used for Run 1, and the orbital element differences in the Mean of 1950 reference frame. Section A.2 contains the GTDS input deck for Run 2, and the orbital element differences in the instantaneous true of date reference frame. Note that the two sets of plots are identical. This is supported by the radial, cross-track, and along track differences listed in table 3.4. The conclusion is that the differences in the Mean of 1950 and true of date frames are identical.

A.1 Run 1: Mean of 1950 Element Differences

CONTROL	EPHEM			ELLIPSO	XXXXXX
EPOCH		970101.0	000000.000000		
ELEMENT1	2 6 1	10472.201D0	0.342652D0	116.583	
ELEMENT2		280.0	270.0	0.0	
OUTPUT	1 2 1	1020101.0	000000.D0	864000.	
ORBTYP	5 1 1	86400.	1.0		
OGOPT					
DRAG	1	2.0			
NCBODY	1				
ATMOSDEN		1			
SCPARAM		2.5D-5	700.0D0		
MAXDEGEQ	1	21.			
MAXORDEQ	1	0.			
POTFIELD	1 19				
SOLRAD	1	2.0			
OUTOPT	1	970101000000.	1020101000000.0	86400.	
END					
FIN					
CONTROL	EPHEM			ELLIPSO	XXXXXX
EPOCH		970101.0	000000.000000		
ELEMENT1	2 6 1	10472.201D0	0.342652D0	116.583	
ELEMENT2		280.0	270.0	0.0	
OUTPUT	1 2 1	1020101.0	000000.D0	864000.	
ORBTYP	5 1 1	86400.	1.0		
OGOPT					
DRAG	1	1.0			
NCBODY	1 2 3				
ATMOSDEN		1			
SCPARAM		2.5D-5	700.0D0		
MAXDEGEQ	1	21.			
MAXORDEQ	1	21.			
POTFIELD	1 19				
SOLRAD	1	1.0			
OUTOPT	21	970101000000.	1020101000000.0	86400.	
END					
FIN					

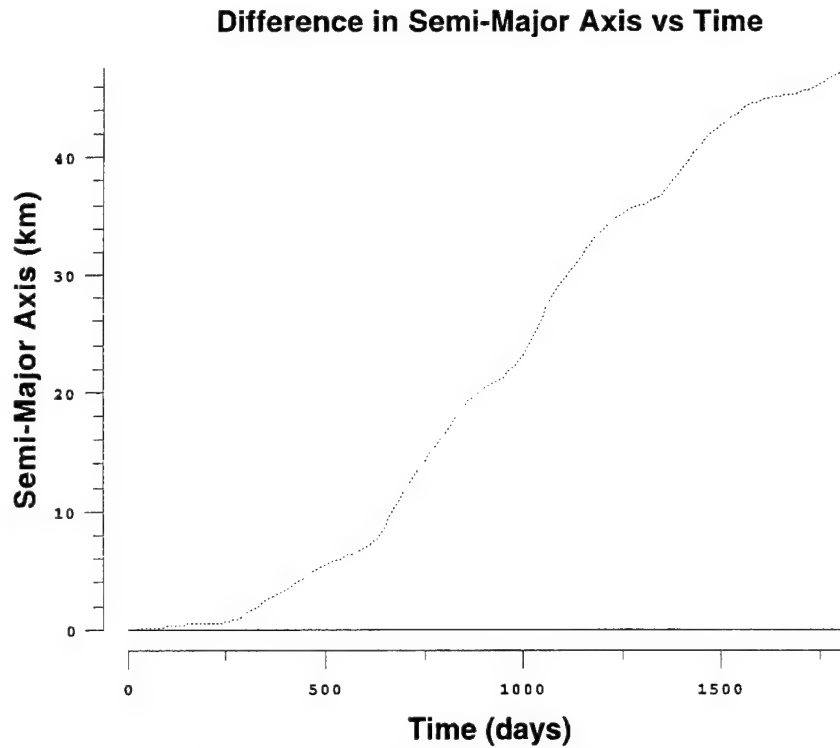


Figure A.1: Semi-major Axis Differences in Mean of 1950 Frame

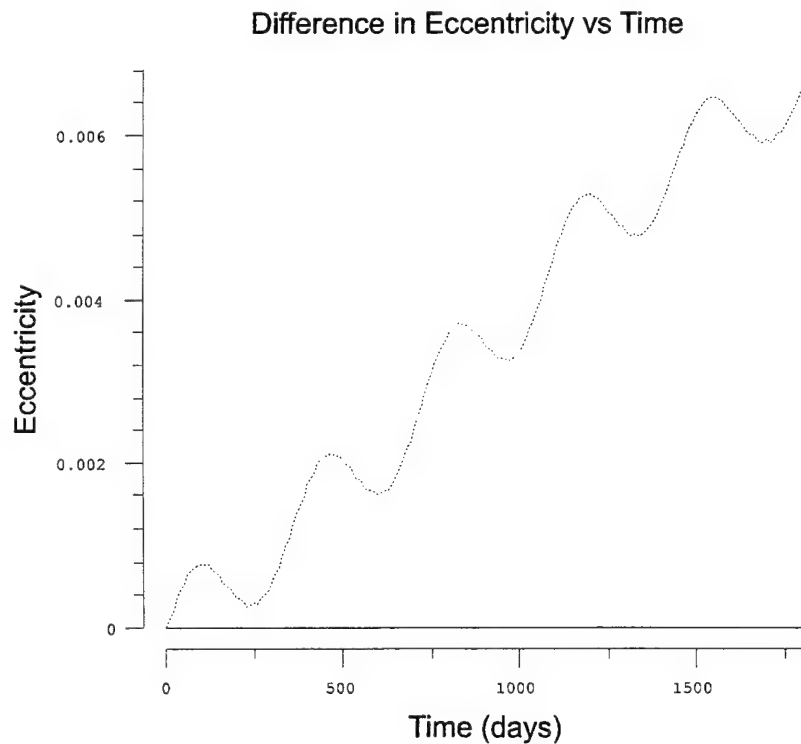


Figure A.2: Eccentricity Differences in Mean of 1950 Frame

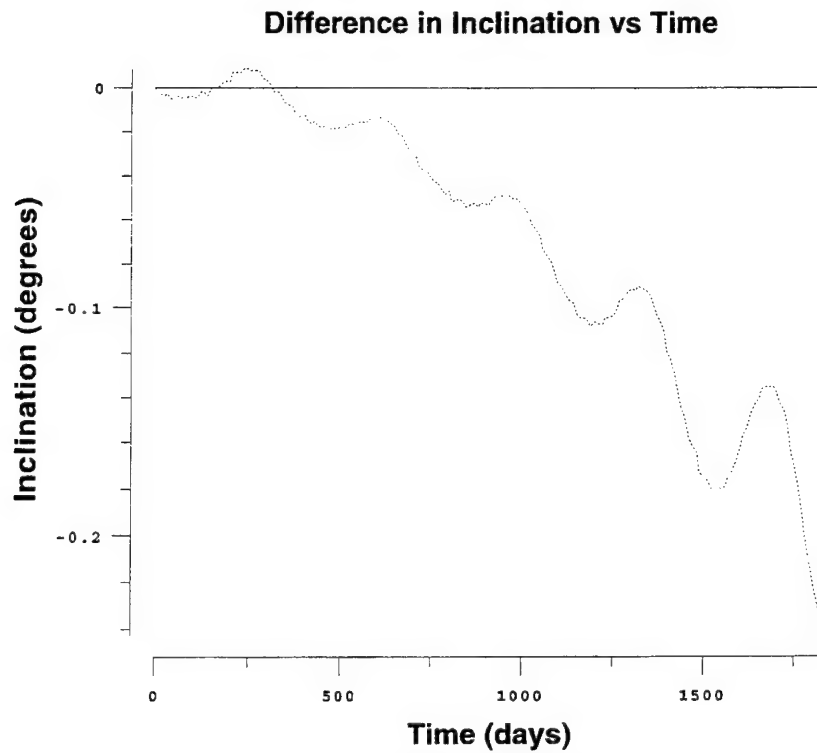


Figure A.3: Inclination Differences in Mean of 1950 Frame

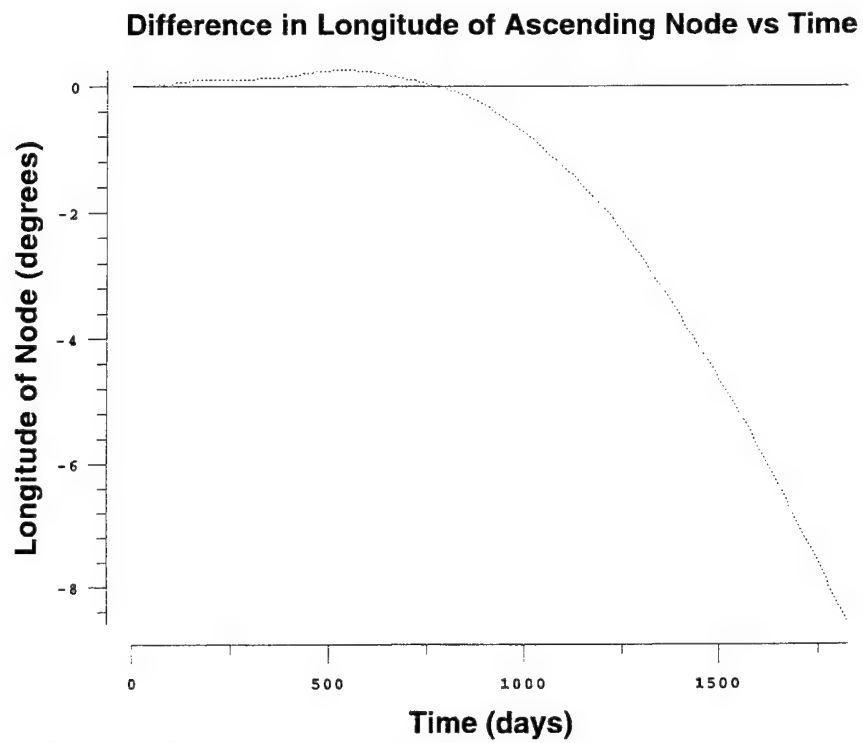


Figure A.4: Ascending Node Differences in Mean of 1950 Frame

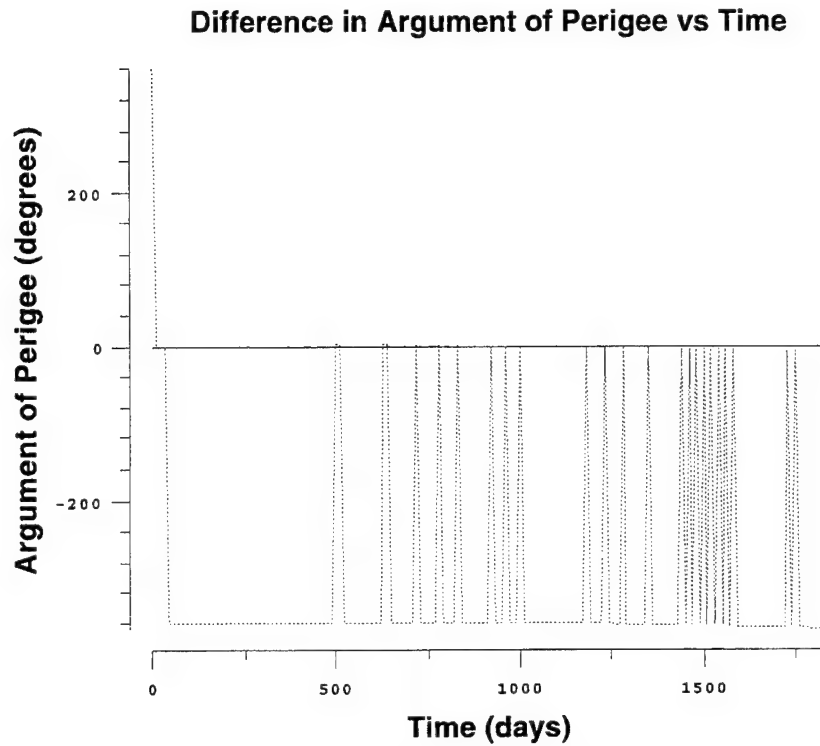


Figure A.5: Argument of Perigee Differences in Mean of 1950 Frame

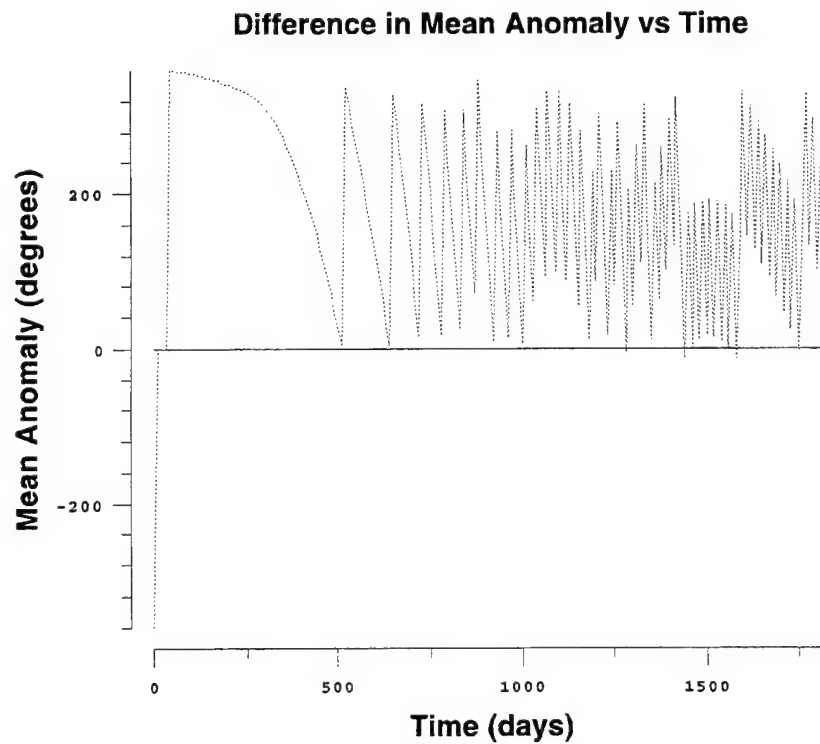


Figure A.6: Mean Anomaly Differences in Mean of 1950 Frame

A.2 Run 2: Instantaneous True of Date Element Differences

CONTROL	EPHEM			ELLIPSO	XXXXXX
EPOCH		970101.0	000000.000000		
ELEMENT1	2 6 1	10472.201D0	0.342652D0	116.583	
ELEMENT2		280.0	270.0	0.0	
OUTPUT	9 2 1	1020101.0	000000.D0	864000.	
ORBTYP	5 1 1	86400.	1.0		
OGOPT					
DRAG	1	2.0			
NCBODY	1				
ATMOSDEN		1			
SCPARAM		2.5D-5	700.0D0		
MAXDEGEQ	1	21.			
MAXORDEQ	1	0.			
POTFIELD	1 19				
SOLRAD	1	2.0			
OUTOPT	1	970101000000.	1020101000000.0	86400.	
END					
FIN					
CONTROL	EPHEM			ELLIPSO	XXXXXX
EPOCH		970101.0	000000.000000		
ELEMENT1	2 6 1	10472.201D0	0.342652D0	116.583	
ELEMENT2		280.0	270.0	0.0	
OUTPUT	9 2 1	1020101.0	000000.D0	864000.	
ORBTYP	5 1 1	86400.	1.0		
OGOPT					
DRAG	1	1.0			
NCBODY	1 2 3				
ATMOSDEN		1			
SCPARAM		2.5D-5	700.0D0		
MAXDEGEQ	1	21.			
MAXORDEQ	1	21.			
POTFIELD	1 19				
SOLRAD	1	1.0			
OUTOPT	21	970101000000.	1020101000000.0	86400.	
END					
FIN					
CONTROL	COMPARE				
COMPOPT					
CMPEPHEM	1102102	970101000000.0	1020101000000.0	1440.	
CMPPLOT	3			2.0	
HISTPLOT	1102102	970101000000.0	1020101000000.0	86400.0	
END					
FIN					

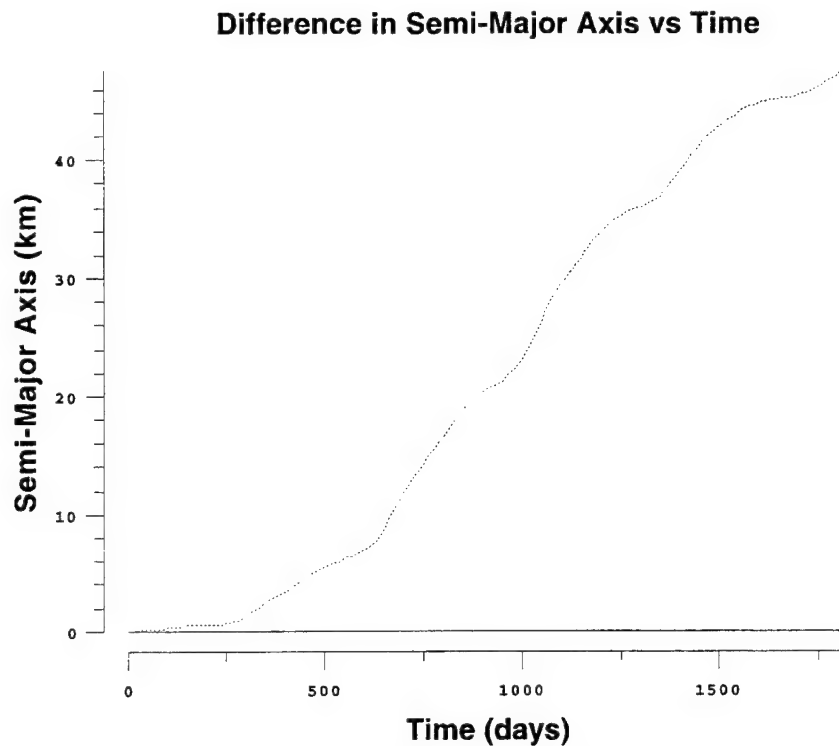


Figure A.7: Semi-major Axis Differences in Instantaneous True of Date Frame

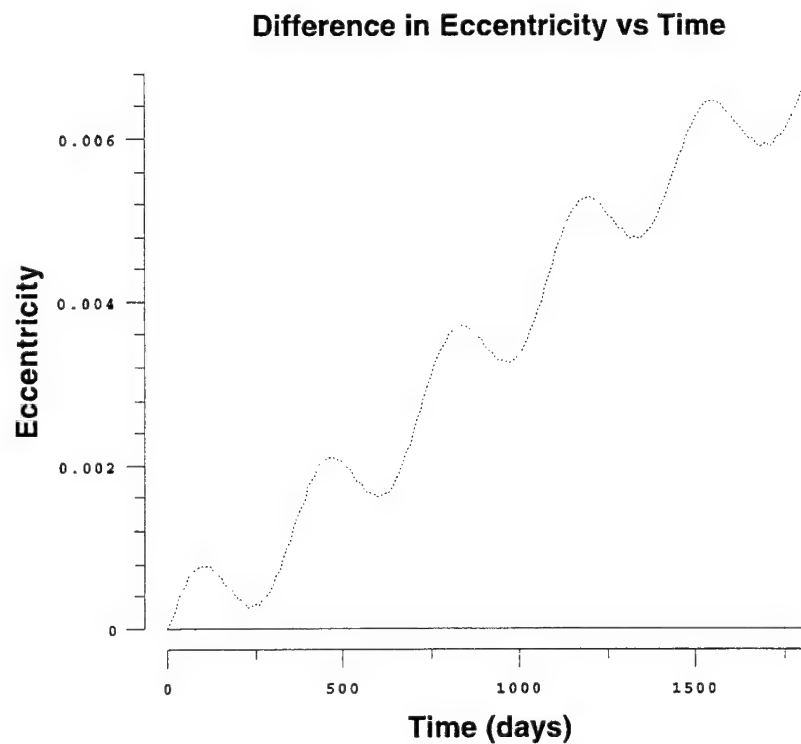


Figure A.8: Eccentricity Differences in Instantaneous True of Date Frame

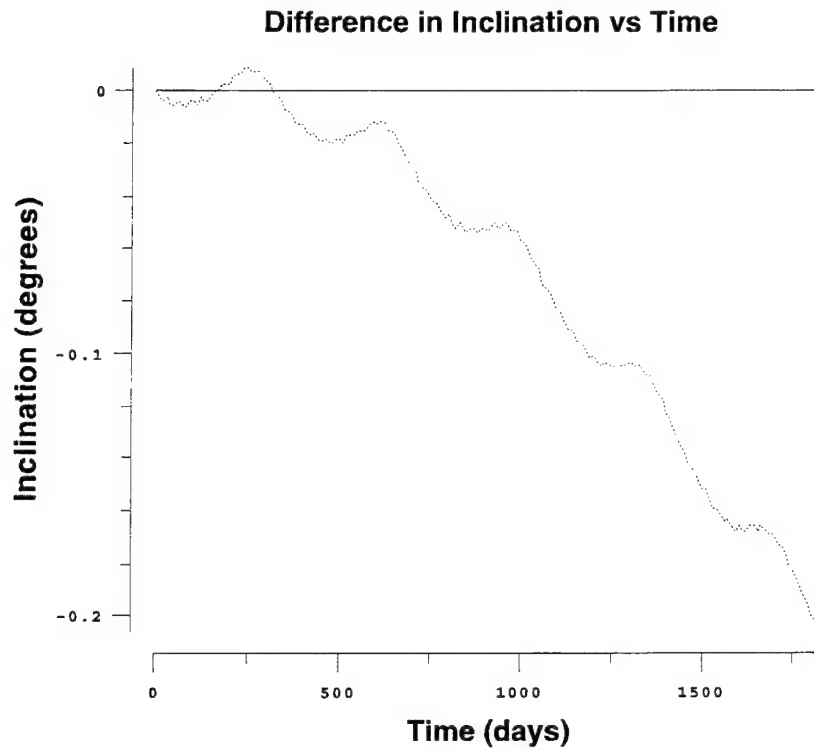


Figure A.9: Inclination Differences in Instantaneous True of Date Frame

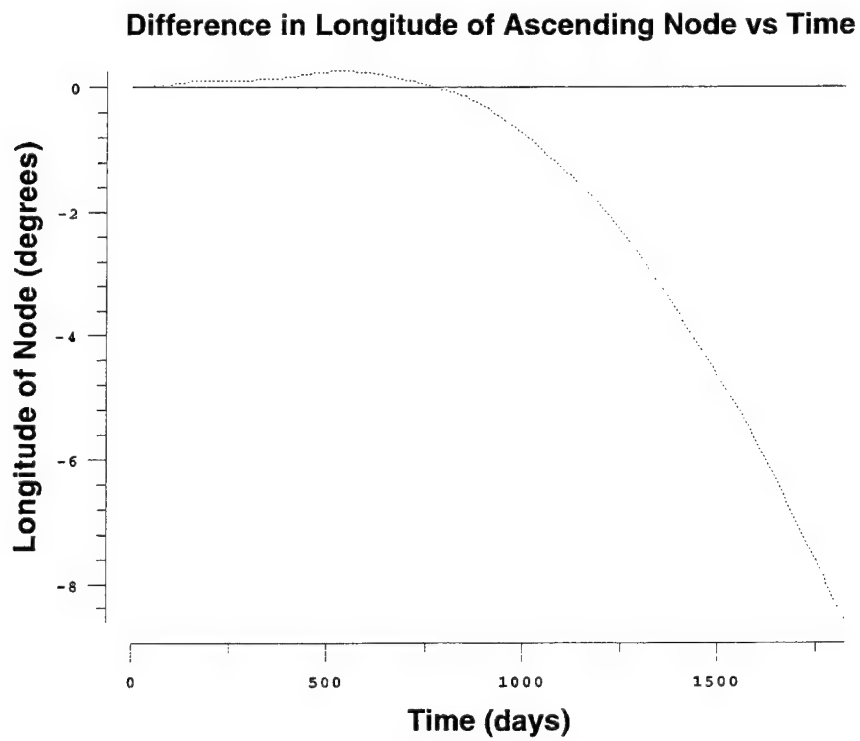


Figure A.10: Ascending Node Differences in Instantaneous True of Date Frame

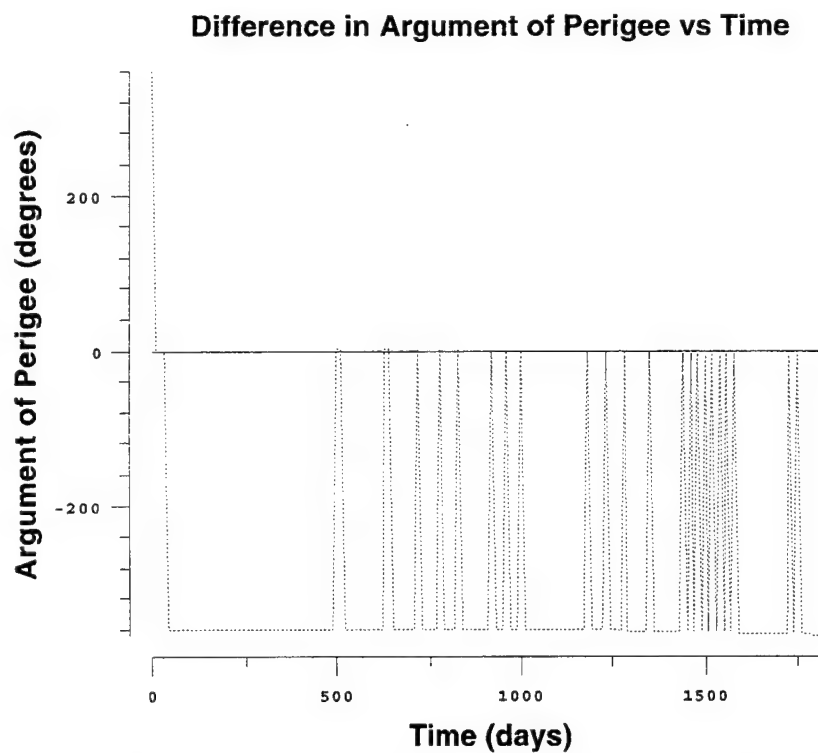


Figure A.11: Ascending Node Differences in Instantaneous True of Date Frame

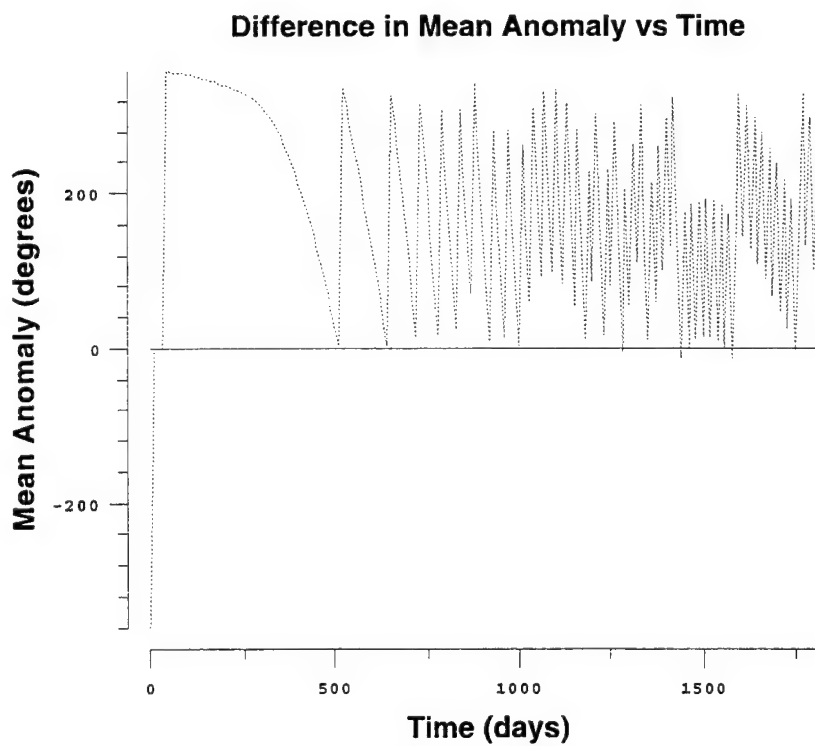


Figure A.12: Mean Anomaly Differences in Instantaneous True of Date Frame

[This page intentionally left blank.]

Appendix B

Simulation 1 Plots

This appendix contains all the plots related to Simulation 1. The purpose of this simulation is to validate the ASKS ΔV generator. This is done by comparing the calculated per satellite ΔV required to maintain the satellites of the dawn/dusk Borealis planes to analytic ΔV values estimated by Sabol for this case [52]. The analysis of the results is located in section 7.2. Simulation 1 includes only one run.

B.1 Sim 1 / Run 1

This run is conducted on the node at dawn/dusk configuration of the Borealis planes. Absolute (box) station-keeping is used with targeting method 2. The maximum parameter limits for the semi-major axis, eccentricity, and inclination are set according to the Ellipso requirements listed in table 6.1. The maximum limits for the remaining element are set to 720° , indicating that no attempt to control them is to be made. The deadband parameter limits are set to between 90% to 95% of the maximum limits. This is done to avoid combined element burns. The maximum overshoot limits for the method 2 controller are set to 98% for the controlled elements.

The epoch orbital elements for this run are listed in table 7.2. The nominal (reference) trajectory is propagated in the presence of zonal harmonics through degree 21, solar/lunar radiation pressure, and solar/lunar point masses. The actual satellite trajectory is

propagated with the perturbations of the nominal trajectory plus tesseral resonance and atmospheric drag.

Section B.1.1 contains the input deck for run1. Sections B.1.2 and B.1.3 contain the orbital element difference plots for the node at dawn and node at dusk planes, respectively.

B.1.1 Input Deck (Sim 1 / Run 1)

The following list is the input deck for run 1 of simulation 1. Only the information for one satellite per plane is depicted for brevity. The satellites in the plane are evenly spaced at epoch.

```

Number of Planes      :      2
Stat-Keep Method      :      0  (0=box; 1=formation)

Targeting Method      :      2
Power                 :      1.00
kmax                  :      50
max_burns             :      4

Epoch Date: 19970101.0 Epoch Time:      0.0000
Final Date: 19990101.0 Final Time:      0.0000
Iteration Time Step   :      0.103000000000000D+05  sec

*****
Plane                  :      1
Sats In This Plane    :      5

Maximum Parameter Limits:      1.00000000000000D+00  km  sma
Keplerian Elements:      0.001000000000000D+00      ecc
                        0.000050000000000D+03  deg  inc
                        0.720000000000000D+03  deg  lan
                        0.720000000000000D+03  deg  ap
                        0.720000000000000D+03  deg  ma

Scale (outer limits) : 0.98
Deadband Parameter Limits:      0.95000000000000D+00  km  sma
Keplerian Elements:      0.000950000000000D+00      ecc
                        0.000045000000000D+03  deg  inc
                        0.720000000000000D+03  deg  lan
                        0.720000000000000D+03  deg  ap
                        0.720000000000000D+03  deg  ma

Maximum Overshoot Limits :      0.98000000000000D+00  frac  sma
                        0.98000000000000D+00  frac  ecc
                        0.98000000000000D+00  frac  inc
                        0.00000000000000D+00  frac  lan
                        0.00000000000000D+00  frac  ap
                        0.00000000000000D+00  frac  ma

```

```

-----
Satellite Number      :      1

Actual State:
  Keplerian Elements:      0.1055925700000000D+05      km      sma
                           0.3453000000000000D+00      ecc
                           0.1166211836800000D+03      deg      inc
                           0.0092686759000000D+03      deg      lan
                           0.2697118636300000D+03      deg      ap
                           0.0000000000000000D+03      deg      ma

CD:                      2.20000000 Rho One:          0.00000000
S/C Mass:                700.00000000 S/C Area:        0.00002500
Integrator Step: 43200.00000000

Retro:      1 Atmos Mdl:  1 Potent Mdl:  4
Nmax:      21 Mmax:      21 Izonal:      1 IJ2J2:  1
Nmaxrs:    21 Mmaxrs:    21 Ithird:     1
Ind Drg:    1 Iszak:      2 Ind Sol:      1

Reference State:
  Keplerian Elements:      0.1055925700000000D+05      km      sma
                           0.3453000000000000D+00      ecc
                           0.1166211836800000D+03      deg      inc
                           0.0092686759000000D+03      deg      lan
                           0.2697118636300000D+03      deg      ap
                           0.0000000000000000D+03      deg      ma

Reference Switch      :      0      ! (0=DSST, 1=Fixed Rates)
Reference State Rates:
  Keplerian Rates:      0.0000000000000000D+00      km/sec sma
                           0.0000000000000000D+00      1/sec  ecc
                           0.0000000000000000D+00      deg/sec inc
                           1.1407711610000000D-05      deg/sec lan
                           0.0000000000000000D+00      deg/sec ap
                           3.3338114140000000D-02      deg/sec ma

CD:                      2.20000000 Rho One:          0.00000000
S/C Mass:                700.00000000 S/C Area:        0.00002500
Integrator Step: 43200.00000000

Retro:      1 Atmos Mdl:  1 Potent Mdl:  4
Nmax:      21 Mmax:      0 Izonal:      1 IJ2J2:  1
Nmaxrs:    2 Mmaxrs:    2 Ithird:     1
Ind Drg:    2 Iszak:      2 Ind Sol:      1
-----
.
.
.
-----
*****
Plane      :      2
Sats In This Plane :      5

Maximum Parameter Limits:
  Keplerian Elements:      1.0000000000000000D+00      km      sma
                           0.0010000000000000D+00      ecc
                           0.0000500000000000D+03      deg      inc
                           0.7200000000000000D+03      deg      lan
                           0.7200000000000000D+03      deg      ap
                           0.7200000000000000D+03      deg      ma

Scale (outer limits) : 0.98
Deadband Parameter Limits:
  Keplerian Elements:      0.9500000000000000D+00      km      sma
                           0.0009500000000000D+00      ecc
                           0.0000450000000000D+03      deg      inc
                           0.7200000000000000D+03      deg      lan
                           0.7200000000000000D+03      deg      ap
                           0.7200000000000000D+03      deg      ma

Maximum Overshoot Limits :
                           0.9800000000000000D+00      frac sma
                           0.9800000000000000D+00      frac ecc
                           0.9800000000000000D+00      frac inc
                           0.0000000000000000D+00      frac lan
                           0.0000000000000000D+00      frac ap
                           0.0000000000000000D+00      frac ma
-----

```

Satellite Number : 6

Actual State:

Keplerian Elements:	0.1055926040000000D+05	km	sma
	0.3458700000000000D+00		ecc
	0.1165067373000000D+03	deg	inc
	0.1895262563400000D+03	deg	lan
	0.2702878487500000D+03	deg	ap
	0.0000000000000000D+03	deg	ma

CD: 2.20000000 Rho One: 0.00000000
S/C Mass: 700.00000000 S/C Area: 0.00002500
Integrator Step: 43200.00000000

Retro:	1 Atmos Mdl:	1	Potent Mdl:	4	
Nmax:	21 Mmax:	21	Izonal:	1	IJ2J2: 1
Nmaxrs:	21 Mmaxrs:	21	Ithird:	1	
Ind Drg:	1 Iszak:	2	Ind Sol:	1	

Reference State:

Keplerian Elements:	0.1055926040000000D+05	km	sma
	0.3458700000000000D+00		ecc
	0.1165067373000000D+03	deg	inc
	0.1895262563400000D+03	deg	lan
	0.2702878487500000D+03	deg	ap
	0.0000000000000000D+03	deg	ma

Reference Switch : 0 ! (0=DSST, 1=Fixed Rates)

Reference State Rates:

Keplerian Rates:	0.0000000000000000D+00	km/sec	sma
	0.0000000000000000D+00	1/sec	ecc
	0.0000000000000000D+00	deg/sec	inc
	1.1407711610000000D-05	deg/sec	lan
	0.0000000000000000D+00	deg/sec	ap
	3.3338114140000000D-02	deg/sec	ma

CD: 2.20000000 Rho One: 0.00000000
S/C Mass: 700.00000000 S/C Area: 0.00002500
Integrator Step: 43200.00000000

Retro:	1 Atmos Mdl:	1	Potent Mdl:	4	
Nmax:	21 Mmax:	0	Izonal:	1	IJ2J2: 1
Nmaxrs:	2 Mmaxrs:	2	Ithird:	1	
Ind Drg:	2 Iszak:	2	Ind Sol:	1	

.
.
.

B.1.2 Method 2 (a,e,i) Borealis 8:1 Node at Dawn Orbital Element Difference Plots

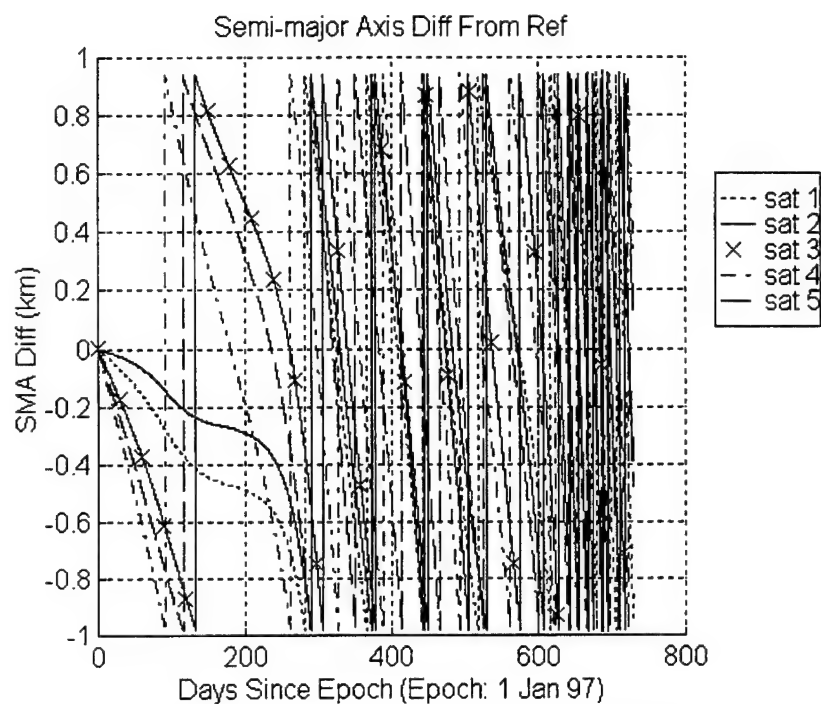


Figure B.1: Semi-major Axis Difference From Nominal Trajectory
(Method 2 (a,e,i) Borealis 8:1 Node at Dawn)

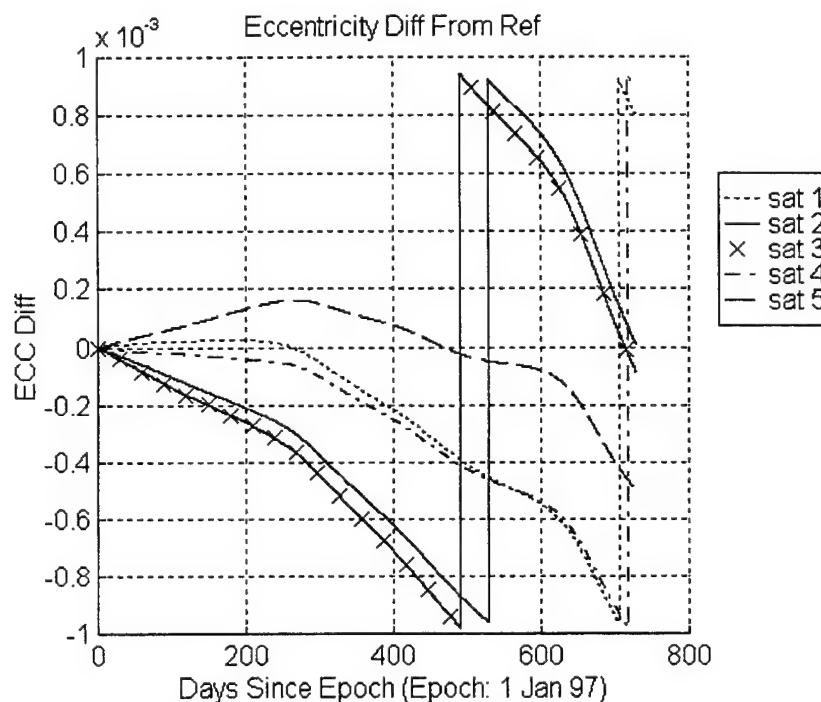


Figure B.2: Eccentricity Difference From Nominal Trajectory
(Method 2 (a,e,i) Borealis 8:1 Node at Dawn)

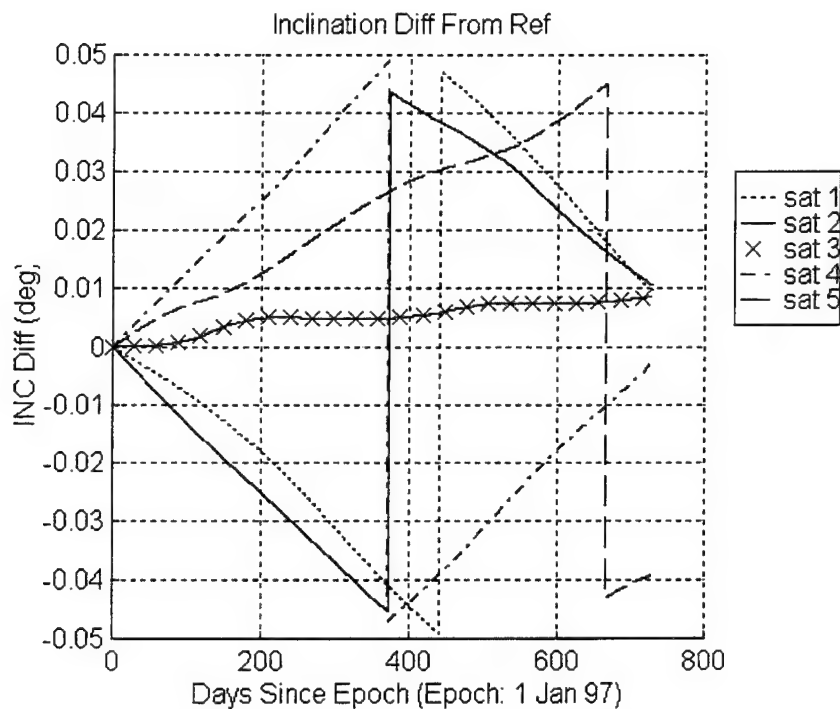


Figure B.3: Inclination Difference From Nominal Trajectory
(Method 2 (a,e,i) Borealis 8:1 Node at Dawn)

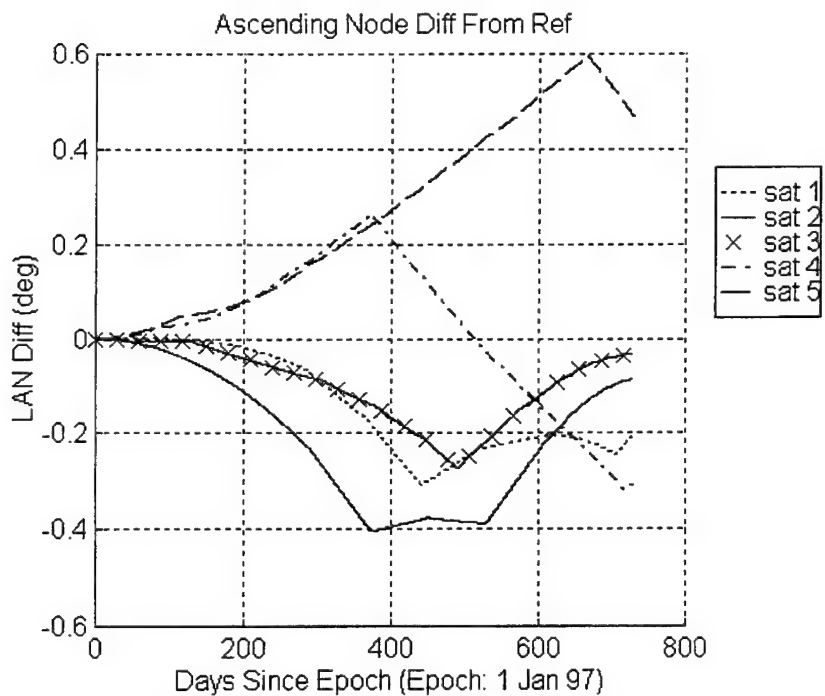


Figure B.4: Ascending Node Difference From Nominal Trajectory
(Method 2 (a,e,i) Borealis 8:1 Node at Dawn)

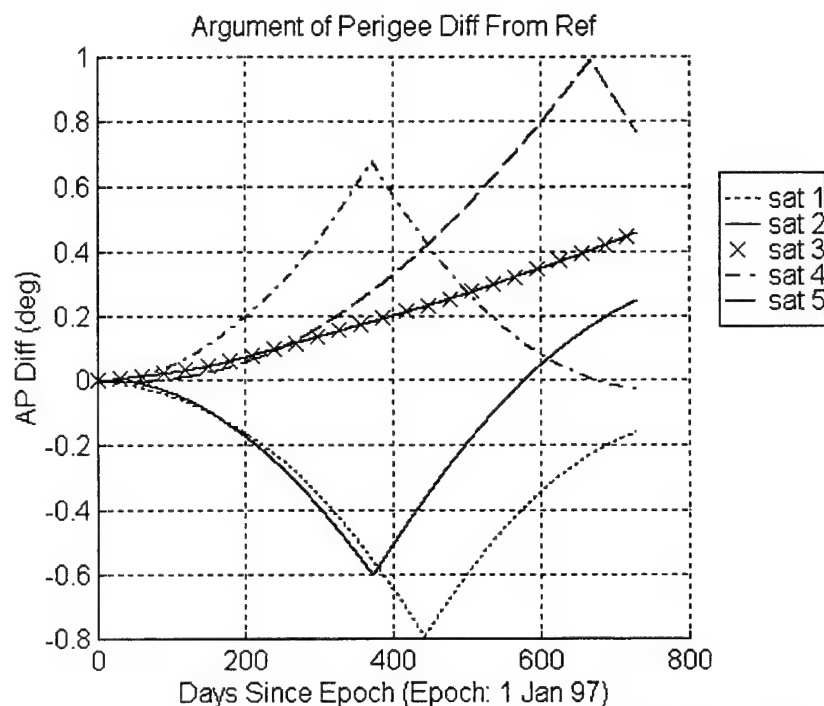


Figure B.5: Argument of Perigee Difference From Nominal Trajectory
(Method 2 (a,e,i) Borealis 8:1 Node at Dawn)

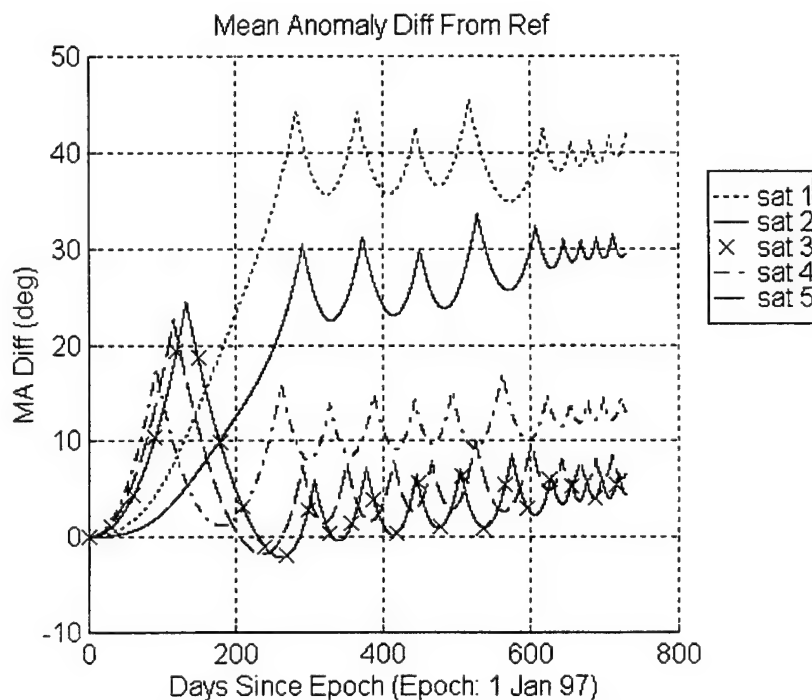


Figure B.6: Mean Anomaly Difference From Nominal Trajectory
(Method 2 (a,e,i) Borealis 8:1 Node at Dawn)

B.1.3 Method 2 (a,e,i) Borealis 8:1 Node at Dusk Orbital Element Difference Plots

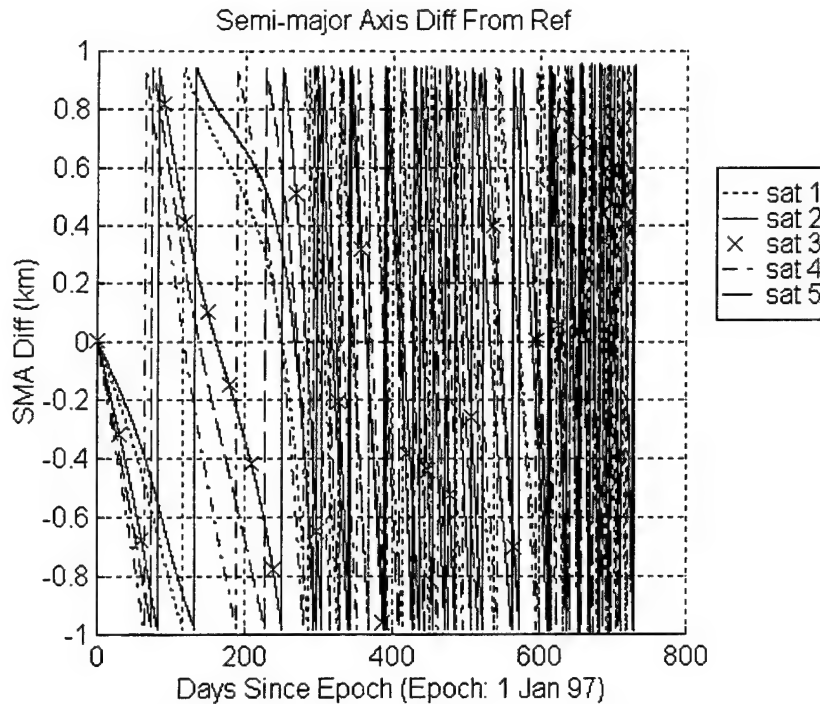


Figure B.7: Semi-major Axis Difference From Nominal Trajectory
(Method 2 (a,e,i) Borealis 8:1 Node at Dusk)

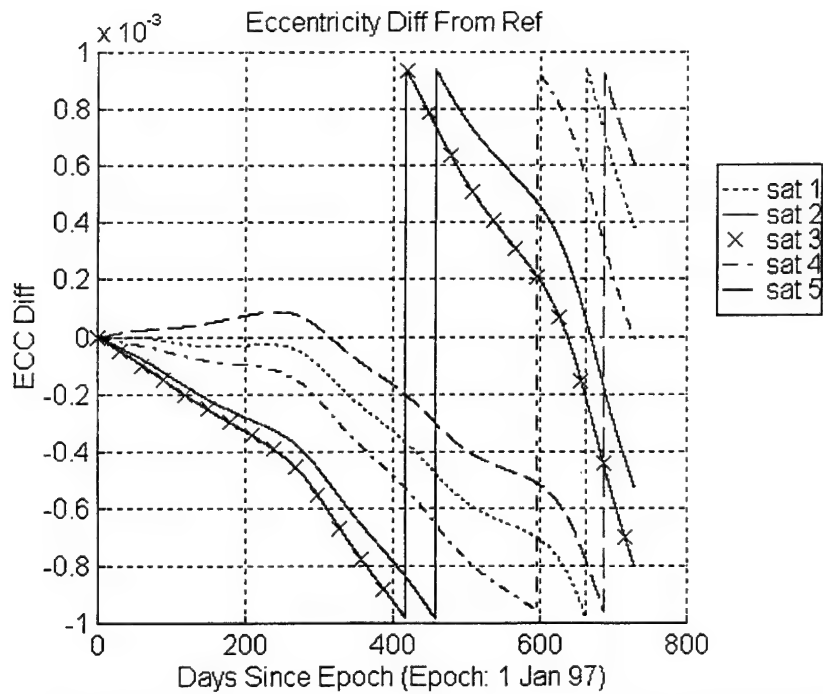


Figure B.8: Eccentricity Difference From Nominal Trajectory
(Method 2 (a,e,i) Borealis 8:1 Node at Dusk)

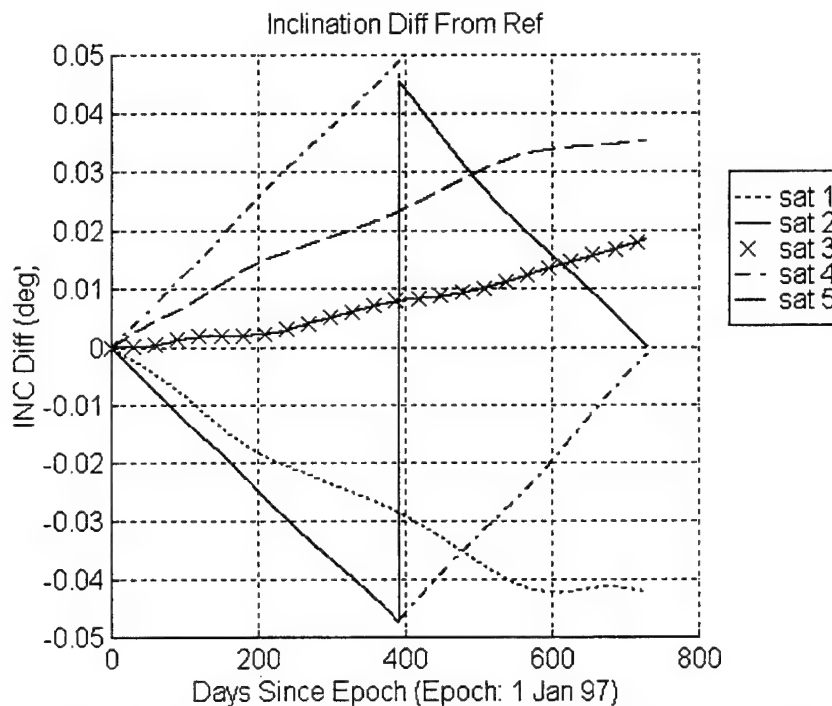


Figure B.9: Inclination Difference From Nominal Trajectory
(Method 2 (a,e,i) Borealis 8:1 Node at Dusk)

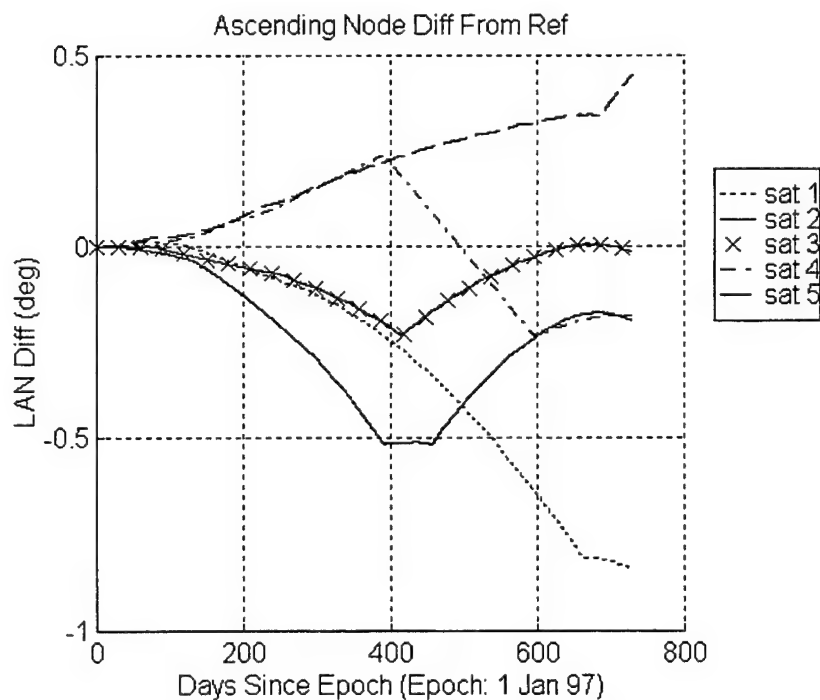


Figure B.10: Ascending Node Difference From Nominal Trajectory
(Method 2 (a,e,i) Borealis 8:1 Node at Dusk)

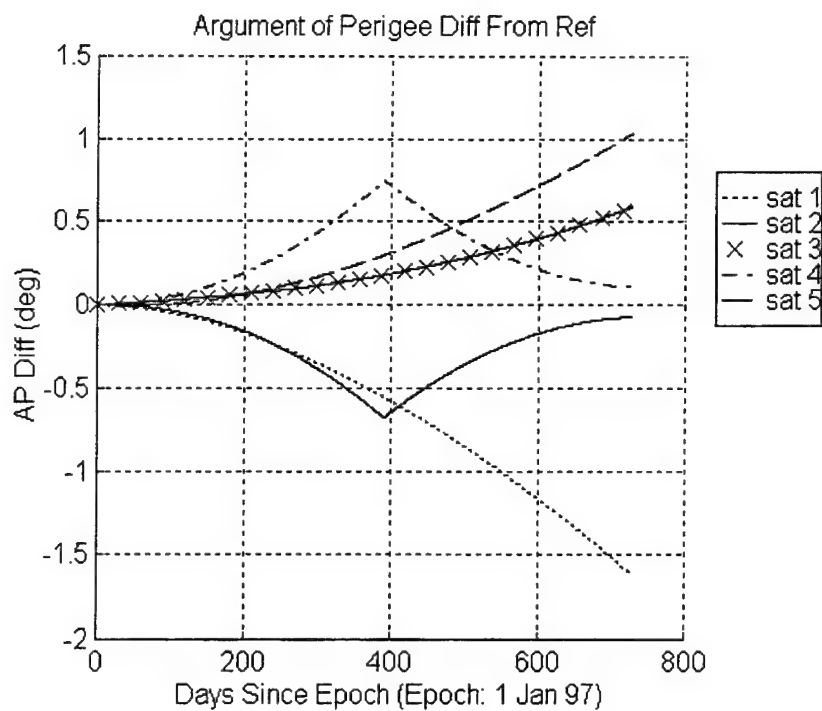


Figure B.11: Argument of Perigee Difference From Nominal Trajectory
(Method 2 (a,e,i) Borealis 8:1 Node at Dusk)

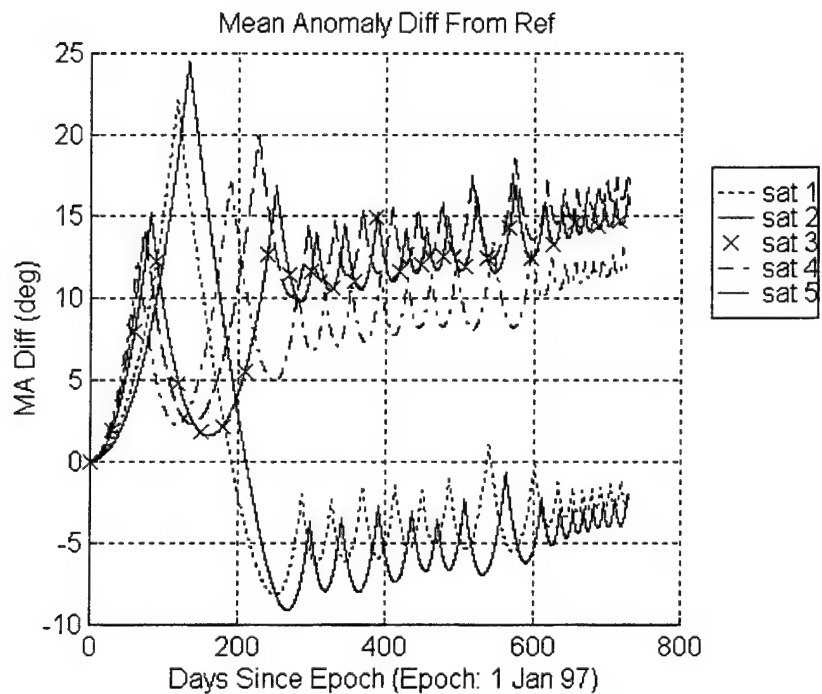


Figure B.12: Mean Anomaly Difference From Nominal Trajectory
(Method 2 (a,e,i) Borealis 8:1 Node at Dusk)

Appendix C

Simulation 2 Plots

This appendix contains all the plots produced in Simulation 2. The purpose of this simulation is to investigate the advantage of controlling a constellation as a whole over controlling each satellite individually. The Ellipso constellation, including the Borealis 8:1 node at noon/midnight planes, is used as the test constellation. All the runs in this simulation assume 5 satellites in each Borealis plane and 7 satellites in the Concordia plane. To provide a basis for comparing the coverage differences, the first run is of an uncontrolled 2yr execution. The second and third runs both use the targeting method 3 controller developed in Chapter 6. The second run treats each satellite separately with absolute station-keeping, while the third run accomplishes relative station-keeping by updating the nominal mean anomaly of each satellite at each time step for even spacing in the plane. The analysis of the results is located in section 7.3.

C.1 Sim 2 / Run 1

This run is an uncontrolled execution of the ASKS on the 8:1 node at noon/midnight configuration of the Borealis planes and the Concordia plane of the Ellipso constellation. Absolute (box) station-keeping is used with targeting method 0. Method 0 indicates that all control related components of the input deck are ignored.

The epoch orbital elements for this run are listed in tables 7.1 and 7.3. The nominal (reference) trajectory is propagated in the presence of zonal harmonics through degree 21, and solar/lunar point masses. The actual satellite trajectory is propagated with the perturbations of the nominal trajectory plus solar radiation pressure, tesseral resonance and atmospheric drag.

Section C.1.1 contains the input deck for run1. Sections C.1.2 contains the one, two, three, and four-way coverage of the constellation over the 2 year time span. Note that coverage is provided for the entire northern hemisphere and for the southern hemisphere above 55°S latitude. The northern hemispheric coverage assumes a 25° minimum elevation angle. The southern hemispheric coverage assumes a 10° minimum elevation angle. Section C.1.3 contains the orbital element difference plots for the Concordia plane. Sections C.1.4 and C.1.5 contain the orbital element difference plots for the node at noon and node at midnight planes, respectively.

C.1.1 Input Deck (Sim 2 / Run 1)

The following list is the input deck for run 1 of simulation 2. Only the information for one satellite per plane is depicted for brevity. The satellites in the plane are evenly spaced at epoch.

```

Number of Planes      :      3
Stat-Keep Method      :      0  (0=box; 1=formation)

Targeting Method      :      0
Power                 :      1.00
kmax                  :      50
max_burns             :      4

Epoch Date: 19970101.0 Epoch Time:      0.0000
Final Date: 19990101.0 Final Time:      0.0000
Iteration Time Step   :      0.1728000000000000D+06  sec

```

Plane : 1
Sats In This Plane : 5

Maximum Parameter Limits: 1.000000000000000D+00 km sma
Keplerian Elements: 0.001000000000000D+00 ecc
0.000050000000000D+03 deg inc
0.000200000000000D+03 deg lan
0.001000000000000D+03 deg ap
0.005000000000000D+03 deg ma

Scale (outer limits) : 0.98

Deadband Parameter Limits: 0.950000000000000D+00 km sma
Keplerian Elements: 0.000950000000000D+00 ecc
0.000045000000000D+03 deg inc
0.000180000000000D+03 deg lan
0.000950000000000D+03 deg ap
0.004700000000000D+03 deg ma

Maximum Overshoot Limits : 0.980000000000000D+00 frac sma
0.980000000000000D+00 frac ecc
0.980000000000000D+00 frac inc
0.650000000000000D+00 frac lan
0.980000000000000D+00 frac ap
1.250000000000000D+00 frac ma

Satellite Number : 1

Actual State:
Keplerian Elements: 0.1055927100000000D+05 km sma
0.345705000000000D+00 ecc
0.1163074000600000D+03 deg inc
0.2793744530100000D+03 deg lan
0.2699478224900000D+03 deg ap
0.000000000000000D+03 deg ma

CD: 2.20000000 Rho One: 0.00000000
S/C Mass: 700.00000000 S/C Area: 0.00002500
Integrator Step: 43200.00000000

Retro: 1 Atmos Mdl: 1 Potent Mdl: 4
Nmax: 21 Mmax: 21 Izonal: 1 IJ2J2: 1
Nmaxrs: 21 Mmaxrs: 21 Ithird: 1
Ind Drg: 1 Iszak: 2 Ind Sol: 1

Reference State:
Keplerian Elements: 0.1055927100000000D+05 km sma
0.345705000000000D+00 ecc
0.1163074000600000D+03 deg inc
0.2793744530100000D+03 deg lan
0.2699478224900000D+03 deg ap
0.000000000000000D+03 deg ma

Reference Switch : 0 ! (0=DSST, 1=Fixed Rates)

Reference State Rates:
Keplerian Rates: 0.000000000000000D+00 km/sec sma
0.000000000000000D+00 1/sec ecc
0.000000000000000D+00 deg/sec inc
1.140771161000000D-05 deg/sec lan
0.000000000000000D+00 deg/sec ap
3.333811414000000D-02 deg/sec ma

CD: 2.20000000 Rho One: 0.00000000
S/C Mass: 700.00000000 S/C Area: 0.00002500
Integrator Step: 43200.00000000

Retro: 1 Atmos Mdl: 1 Potent Mdl: 4
Nmax: 21 Mmax: 0 Izonal: 1 IJ2J2: 1
Nmaxrs: 2 Mmaxrs: 2 Ithird: 1
Ind Drg: 2 Iszak: 2 Ind Sol: 2

.
.
.

Plane : 2

Sats In This Plane : 5

Maximum Parameter Limits: 1.000000000000000D+00 km sma
Keplerian Elements: 0.001000000000000D+00 ecc
0.000050000000000D+03 deg inc
0.000200000000000D+03 deg lan
0.001000000000000D+03 deg ap
0.005000000000000D+03 deg ma

Scale (outer limits) : 0.98

Deadband Parameter Limits: 0.950000000000000D+00 km sma
Keplerian Elements: 0.000950000000000D+00 ecc
0.000045000000000D+03 deg inc
0.000180000000000D+03 deg lan
0.000950000000000D+03 deg ap
0.004700000000000D+03 deg ma

Maximum Overshoot Limits : 0.980000000000000D+00 frac sma
0.980000000000000D+00 frac ecc
0.980000000000000D+00 frac inc
0.650000000000000D+00 frac lan
0.980000000000000D+00 frac ap
1.250000000000000D+00 frac ma

Satellite Number : 6

Actual State:
Keplerian Elements: 0.105592700000000D+05 km sma
0.345675000000000D+00 ecc
0.116822580850000D+03 deg inc
0.099421227530000D+03 deg lan
0.270052412620000D+03 deg ap
0.000000000000000D+03 deg ma

CD: 2.20000000 Rho One: 0.00000000
S/C Mass: 700.00000000 S/C Area: 0.00002500
Integrator Step: 43200.00000000

Retro: 1 Atmos Mdl: 1 Potent Mdl: 4
Nmax: 21 Mmax: 21 Izonal: 1 IJ2J2: 1
Nmaxrs: 21 Mmaxrs: 21 Ithird: 1
Ind Drg: 1 Iszak: 2 Ind Sol: 1

Reference State:
Keplerian Elements: 0.105592700000000D+05 km sma
0.345675000000000D+00 ecc
0.116822580850000D+03 deg inc
0.099421227530000D+03 deg lan
0.270052412620000D+03 deg ap
0.000000000000000D+03 deg ma

Reference Switch : 0 ! (0=DSST, 1=Fixed Rates)

Reference State Rates:
Keplerian Rates: 0.000000000000000D+00 km/sec sma
0.000000000000000D+00 1/sec ecc
0.000000000000000D+00 deg/sec inc
1.140771161000000D-05 deg/sec lan
0.000000000000000D+00 deg/sec ap
3.333811414000000D-02 deg/sec ma

CD: 2.20000000 Rho One: 0.00000000
S/C Mass: 700.00000000 S/C Area: 0.00002500
Integrator Step: 43200.00000000

Retro: 1 Atmos Mdl: 1 Potent Mdl: 4
Nmax: 21 Mmax: 0 Izonal: 1 IJ2J2: 1
Nmaxrs: 2 Mmaxrs: 2 Ithird: 1
Ind Drg: 2 Iszak: 2 Ind Sol: 2

.
.
.

Plane : 3
Sats In This Plane : 7

Maximum Parameter Limits: 0.100000000000000D+00 km sma
 Keplerian Elements: 0.020000000000000D+00 ecc
 0.000060000000000D+03 deg inc
 0.720000000000000D+03 deg lan
 0.720000000000000D+03 deg ap
 0.720000000000000D+03 deg ma

Scale (outer limits) : 0.98

Deadband Parameter Limits: 0.100000000000000D+00 km sma
 Keplerian Elements: 0.020000000000000D+00 ecc
 0.000060000000000D+03 deg inc
 0.720000000000000D+03 deg lan
 0.720000000000000D+03 deg ap
 0.720000000000000D+03 deg ma

Maximum Overshoot Limits : 0.980000000000000D+00 frac sma
 0.980000000000000D+00 frac ecc
 0.980000000000000D+00 frac inc
 0.980000000000000D+00 frac lan
 0.980000000000000D+00 frac ap
 0.980000000000000D+00 frac ma

 Satellite Number : 11

Actual State:
 Keplerian Elements: 0.144401370000000D+05 km sma
 0.000010000000000D+00 ecc
 0.000261802660000D+03 deg inc
 0.089103788040000D+03 deg lan
 0.000293894490000D+03 deg ap
 0.000000000000000D+03 deg ma

CD: 2.20000000 Rho One: 0.00000000
 S/C Mass: 700.00000000 S/C Area: 0.00002500
 Integrator Step: 43200.00000000

Retro: 1 Atmos Mdl: 1 Potent Mdl: 4
 Nmax: 21 Mmax: 21 Izonal: 1 IJ2J2: 1
 Nmaxrs: 21 Mmaxrs: 21 Ithird: 1
 Ind Drg: 1 Iszak: 2 Ind Sol: 1

Reference State:
 Keplerian Elements: 0.144401370000000D+05 km sma
 0.000010000000000D+00 ecc
 0.000261802660000D+03 deg inc
 0.089103788040000D+03 deg lan
 0.000293894490000D+03 deg ap
 0.000000000000000D+03 deg ma

Reference Switch : 0 ! (0=DSST, 1=Fixed Rates)

Reference State Rates:
 Keplerian Rates: 0.000000000000000D+00 km/sec sma
 0.000000000000000D+00 1/sec ecc
 0.000000000000000D+00 deg/sec inc
 1.140771161000000D-05 deg/sec lan
 0.000000000000000D+00 deg/sec ap
 3.333811414000000D-02 deg/sec ma

CD: 2.20000000 Rho One: 0.00000000
 S/C Mass: 700.00000000 S/C Area: 0.00002500
 Integrator Step: 43200.00000000

Retro: 1 Atmos Mdl: 1 Potent Mdl: 4
 Nmax: 21 Mmax: 21 Izonal: 1 IJ2J2: 1
 Nmaxrs: 21 Mmaxrs: 21 Ithird: 3
 Ind Drg: 2 Iszak: 2 Ind Sol: 2

 .
 .
 .

C.1.2 Coverage Plots (Sim 2 / Run 1)

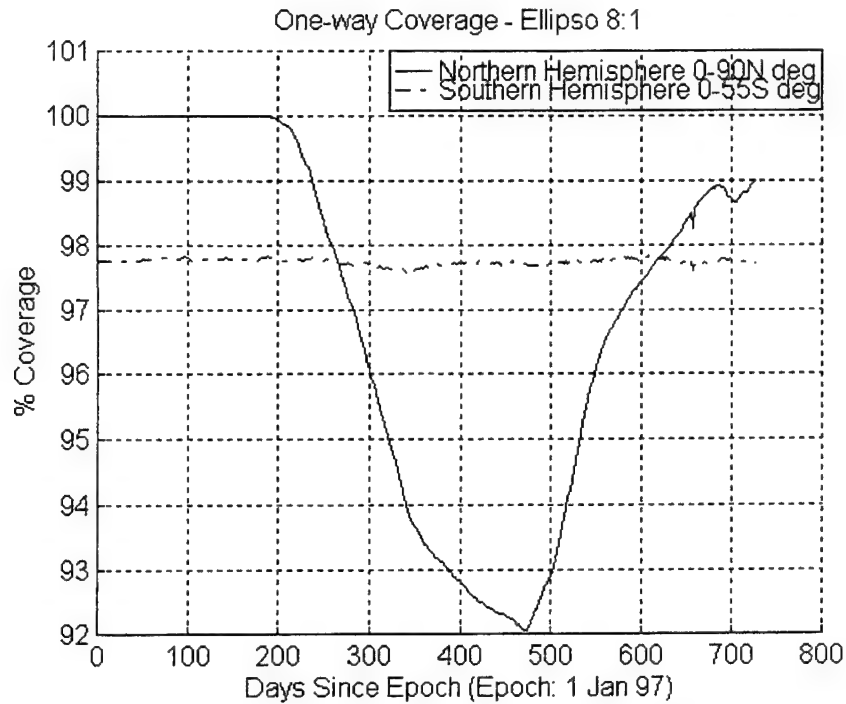


Figure C.1: Ellipso One-Way Coverage
(Uncontrolled Borealis 8:1 Node at Noon/Midnight and Concordia)

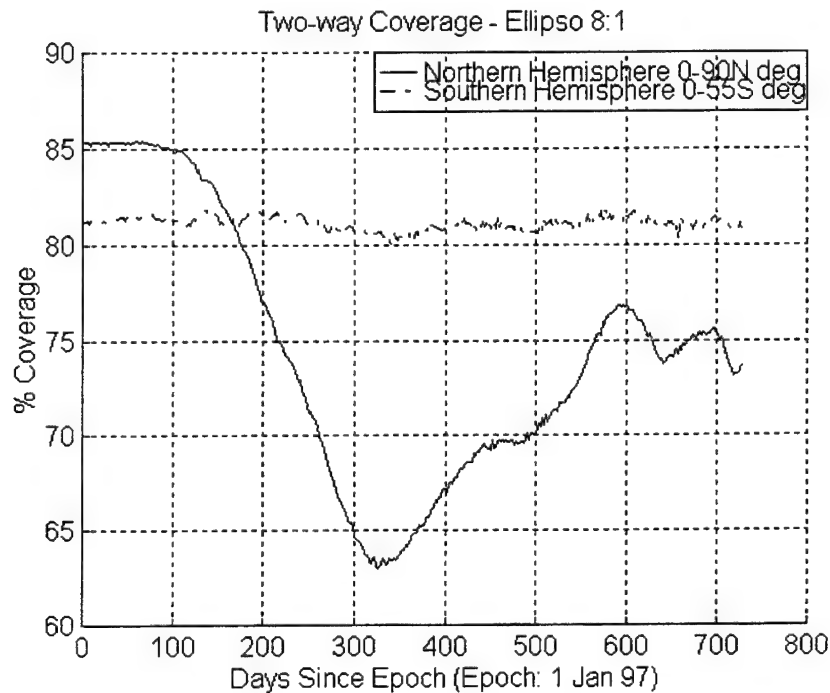


Figure C.2: Ellipso Two-Way Coverage
(Uncontrolled Borealis 8:1 Node at Noon/Midnight and Concordia)

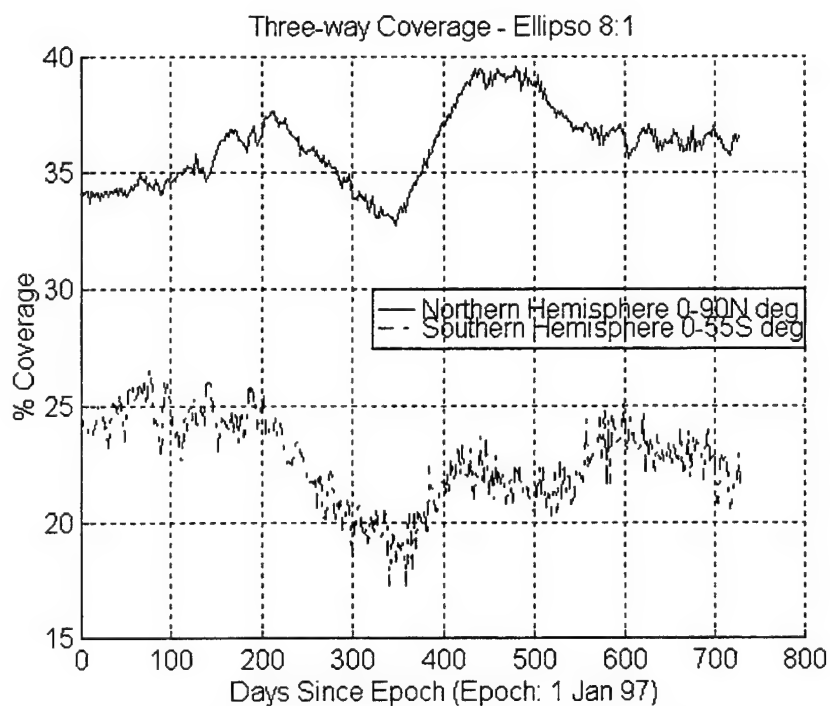


Figure C.3: Ellipso Three-Way Coverage
(Uncontrolled Borealis 8:1 Node at Noon/Midnight and Concordia)

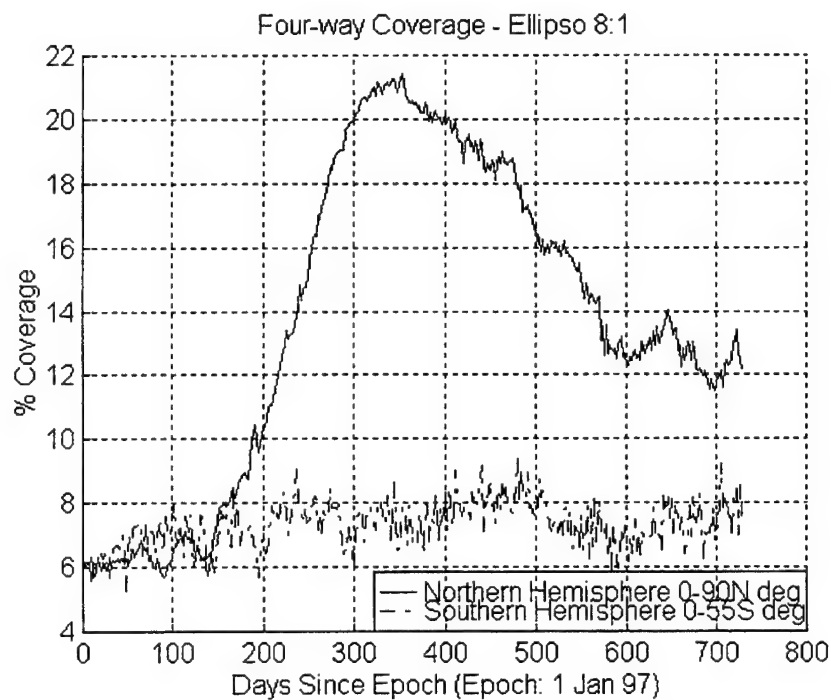


Figure C.4: Ellipso Four-Way Coverage
(Uncontrolled Borealis 8:1 Node at Noon/Midnight and Concordia)

C.1.3 Uncontrolled Concordia Orbital Element Difference Plots

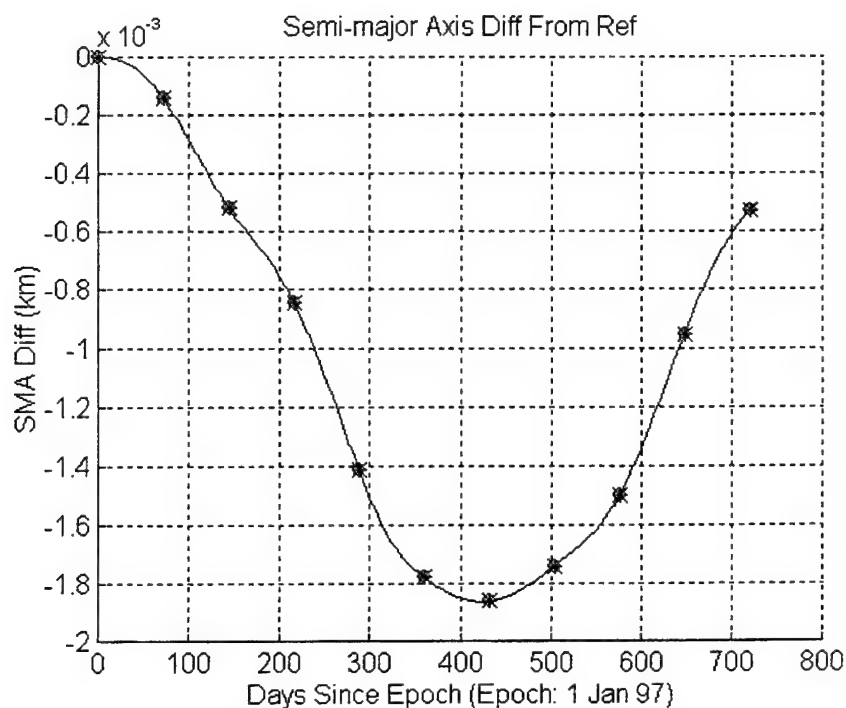


Figure C.5: Semi-major Axis Difference From Nominal Trajectory (Uncontrolled Concordia)

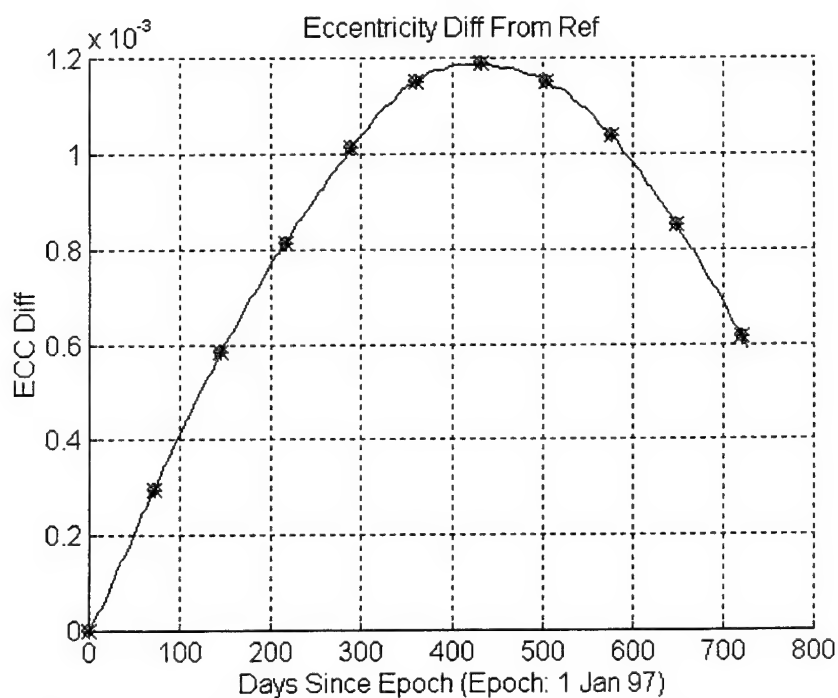


Figure C.6: Eccentricity Difference From Nominal Trajectory (Uncontrolled Concordia)

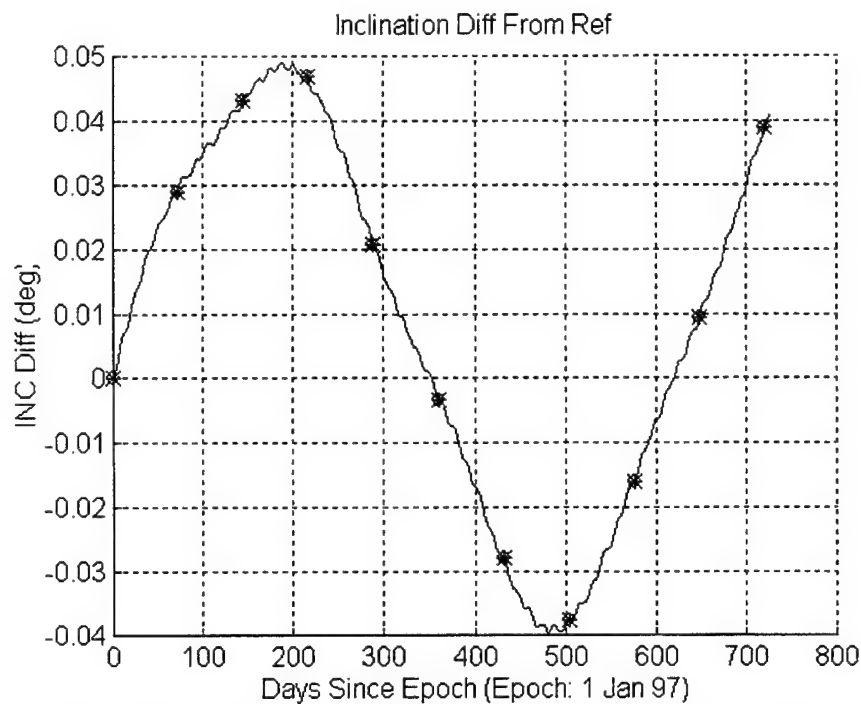


Figure C.7: Inclination Difference From Nominal Trajectory
(Uncontrolled Concordia)

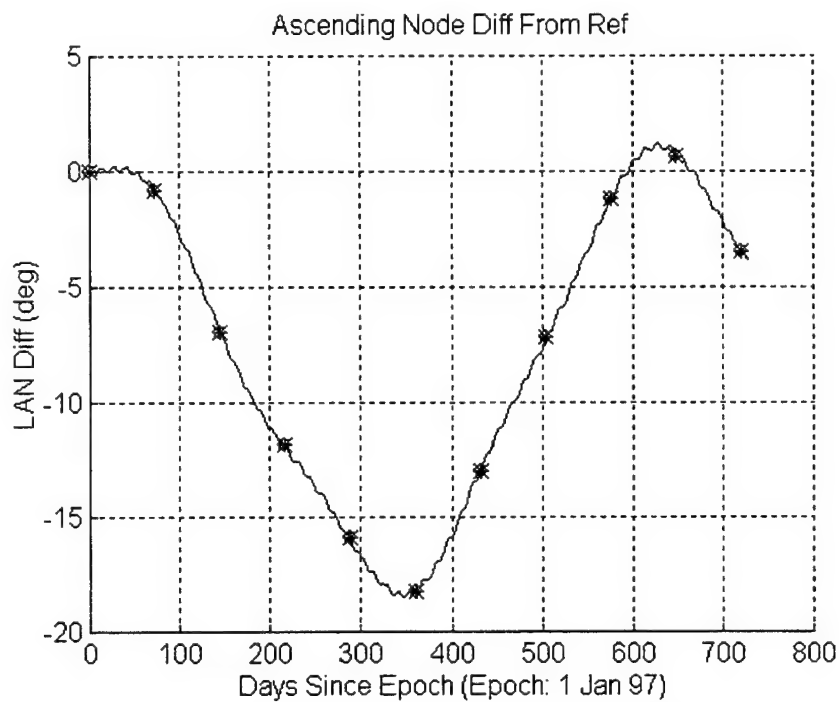


Figure C.8: Ascending Node Difference From Nominal Trajectory
(Uncontrolled Concordia)

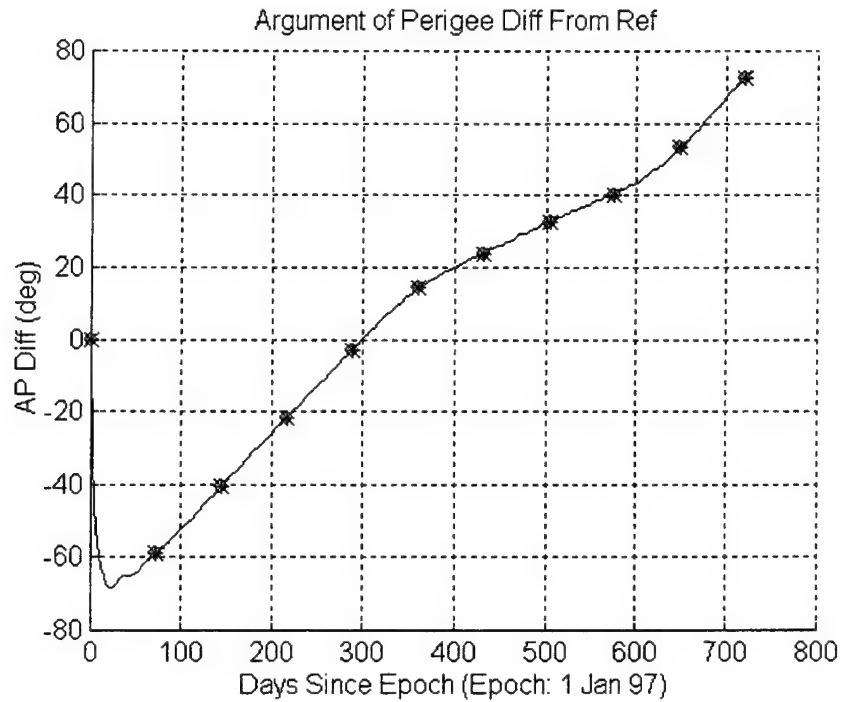


Figure C.9: Argument of Perigee Difference From Nominal Trajectory (Uncontrolled Concordia)

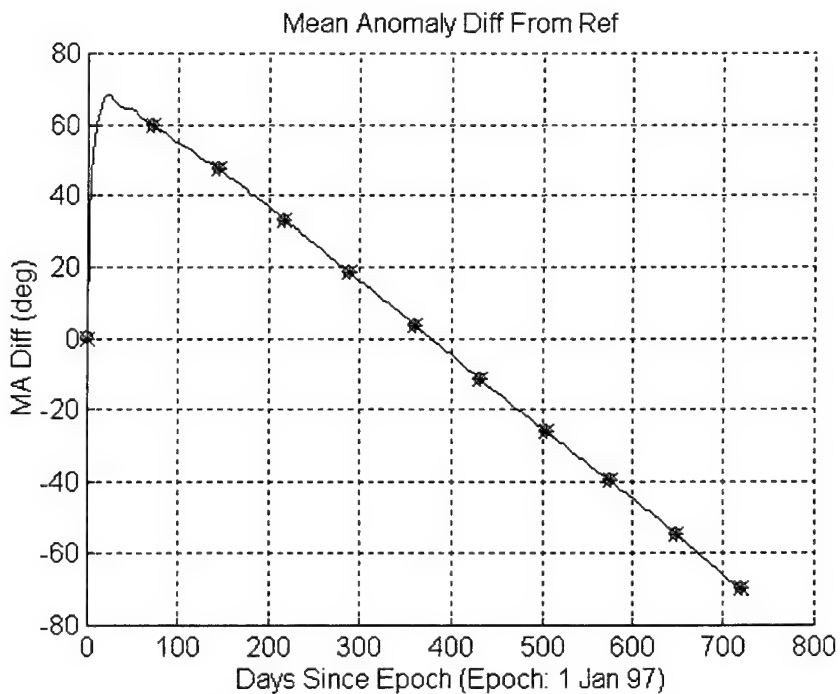


Figure C.10: Mean Anomaly Difference From Nominal Trajectory (Uncontrolled Concordia)

C.1.4 Uncontrolled Borealis 8:1 Node at Noon Orbital Element Difference Plots

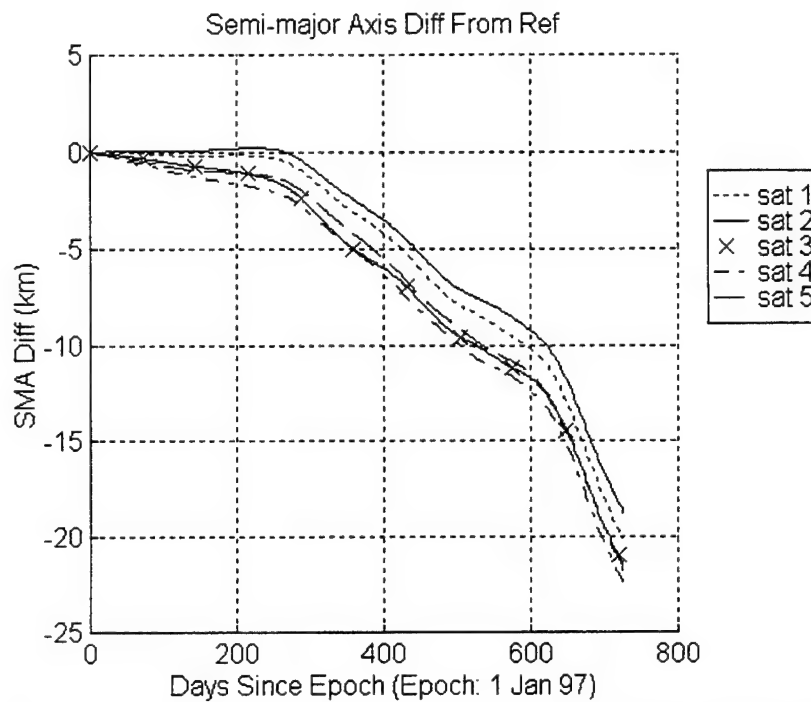


Figure C.11: Semi-major Axis Difference From Nominal Trajectory
(Uncontrolled Borealis 8:1 Node at Noon)

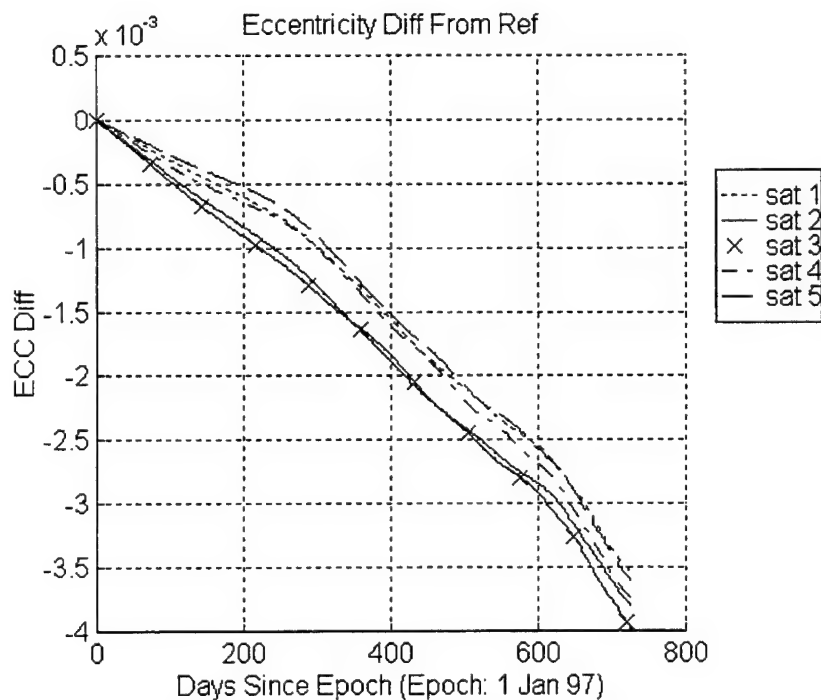


Figure C.12: Eccentricity Difference From Nominal Trajectory
(Uncontrolled Borealis 8:1 Node at Noon)

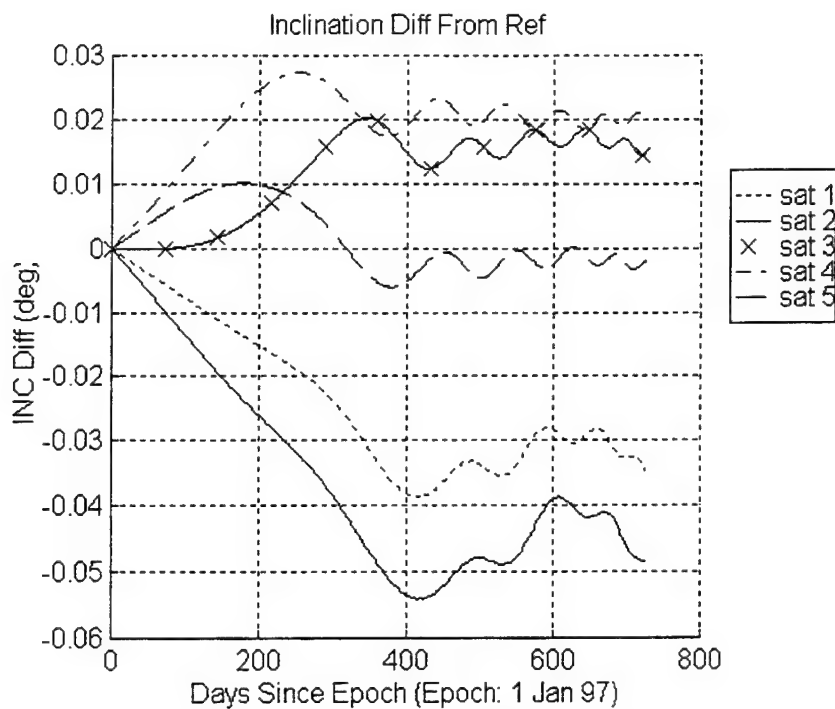


Figure C.13: Inclination Difference From Nominal Trajectory
(Uncontrolled Borealis 8:1 Node at Noon)

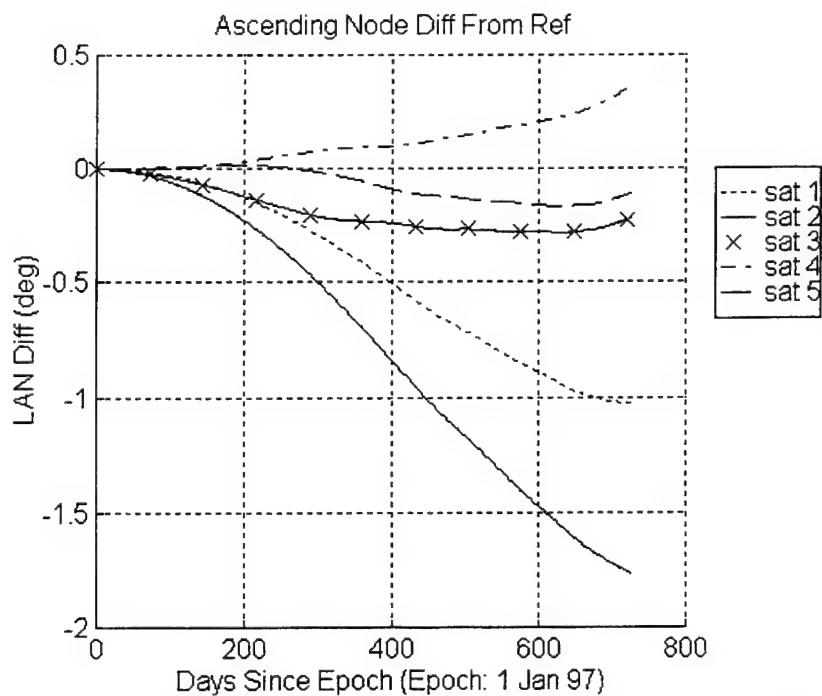


Figure C.14: Ascending Node Difference From Nominal Trajectory
(Uncontrolled Borealis 8:1 Node at Noon)

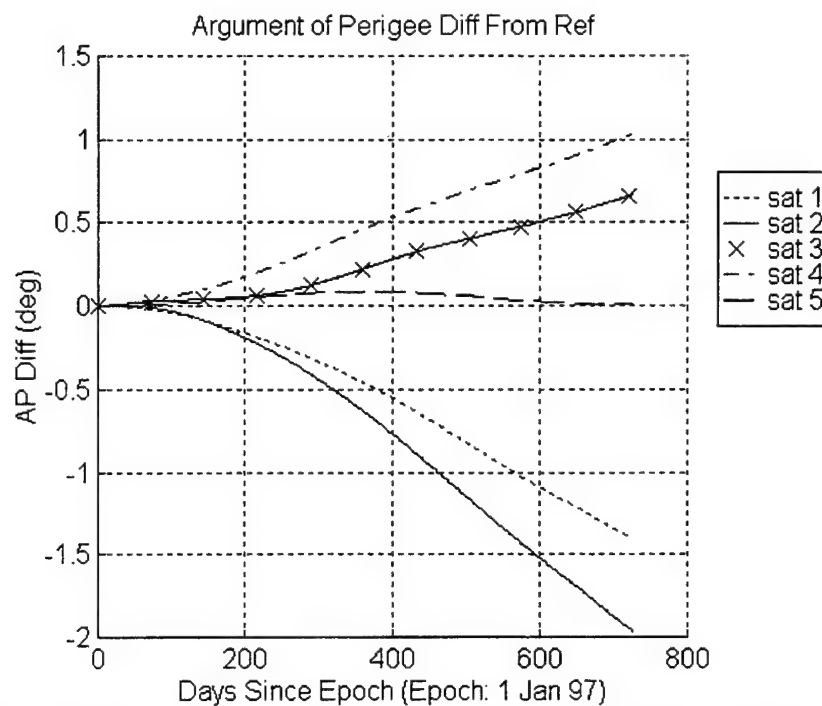


Figure C.15: Argument of Perigee Difference From Nominal Trajectory
(Uncontrolled Borealis 8:1 Node at Noon)

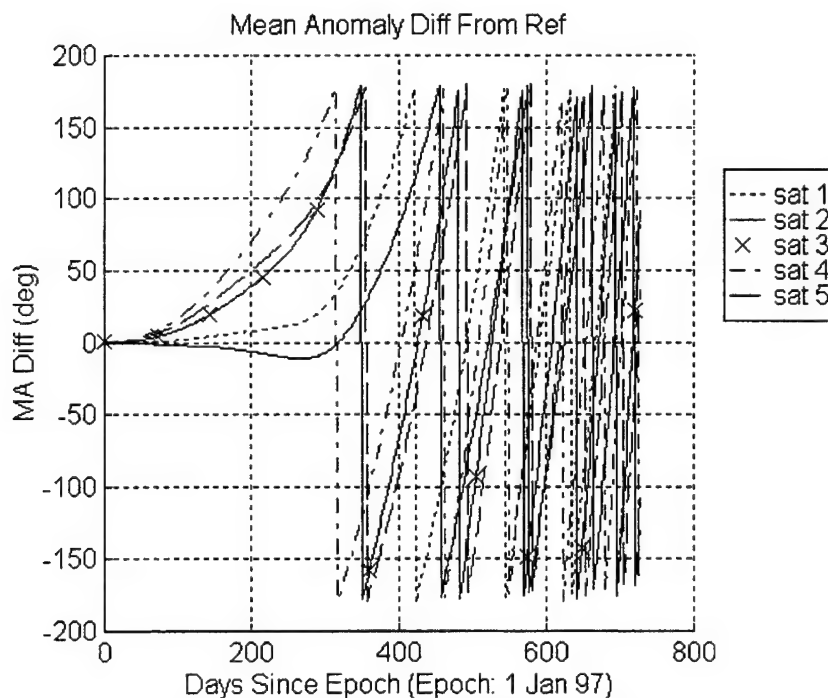


Figure C.16: Mean Anomaly Difference From Nominal Trajectory
(Uncontrolled Borealis 8:1 Node at Noon)

C.1.5 Uncontrolled Borealis 8:1 Node at Midnight Orbital Element Difference Plots

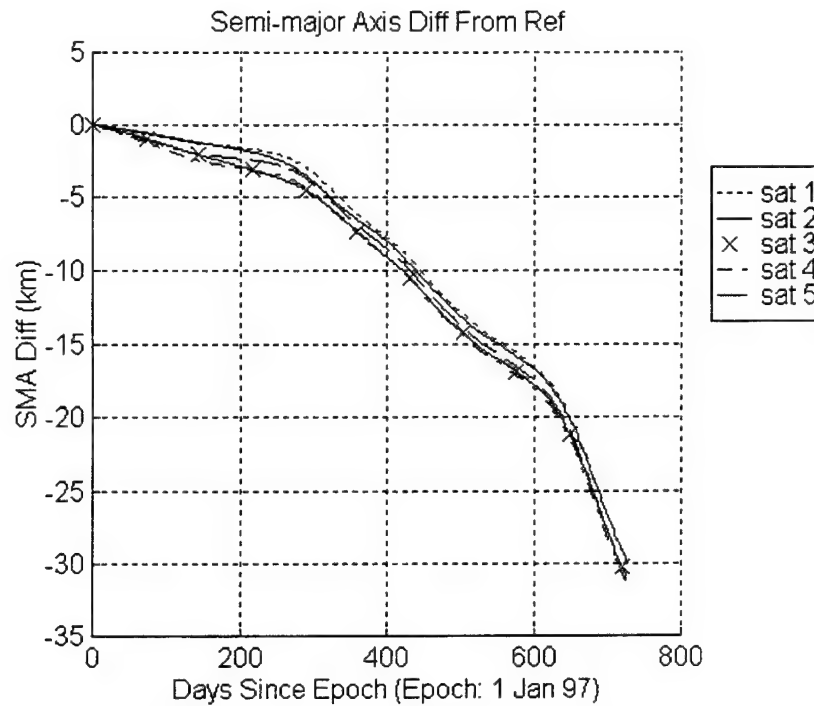


Figure C.17: Semi-major Axis Difference From Nominal Trajectory
(Uncontrolled Borealis 8:1 Node at Midnight)

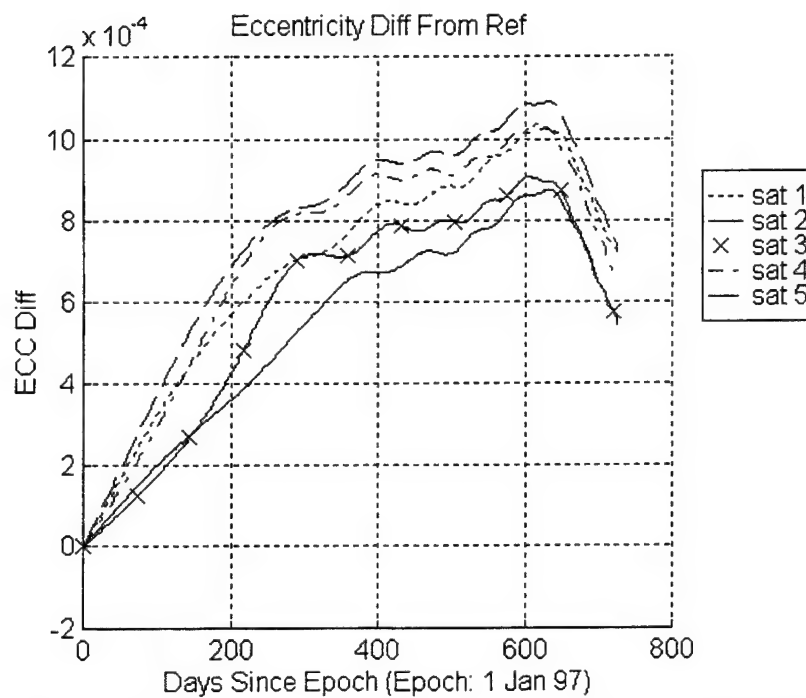


Figure C.18: Eccentricity Difference From Nominal Trajectory
(Uncontrolled Borealis 8:1 Node at Midnight)

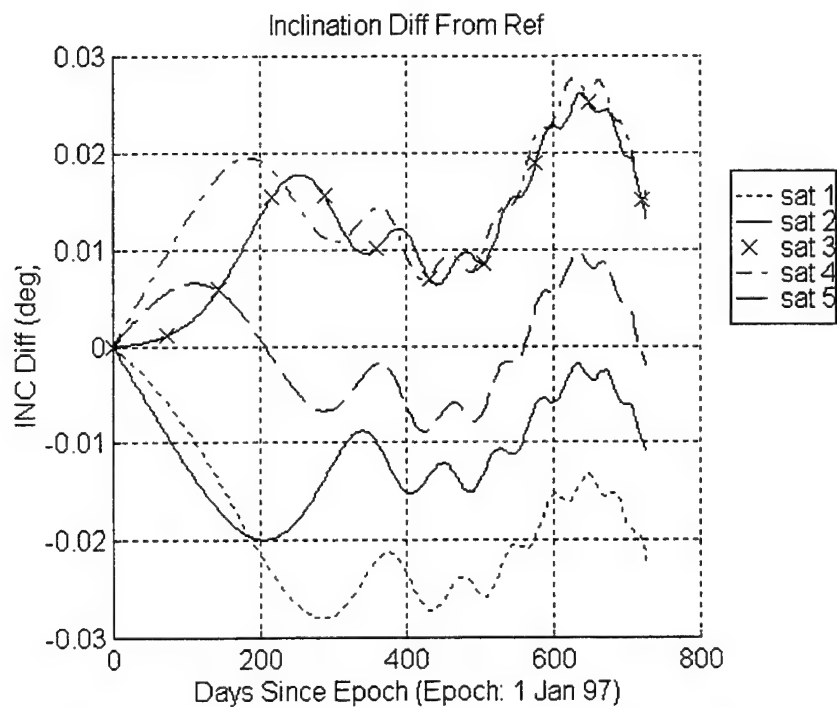


Figure C.19: Inclination Difference From Nominal Trajectory
(Uncontrolled Borealis 8:1 Node at Midnight)

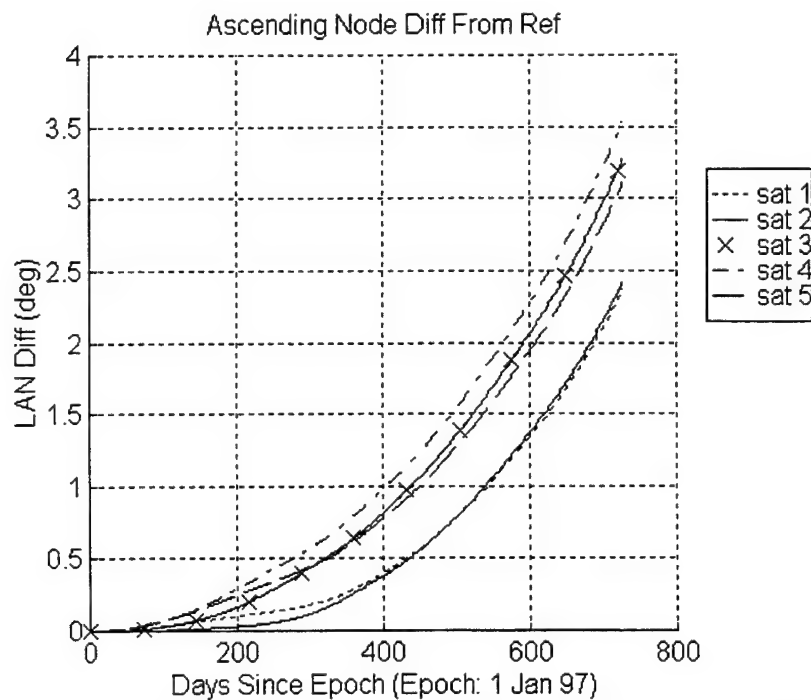


Figure C.20: Ascending Node Difference From Nominal Trajectory
(Uncontrolled Borealis 8:1 Node at Midnight)

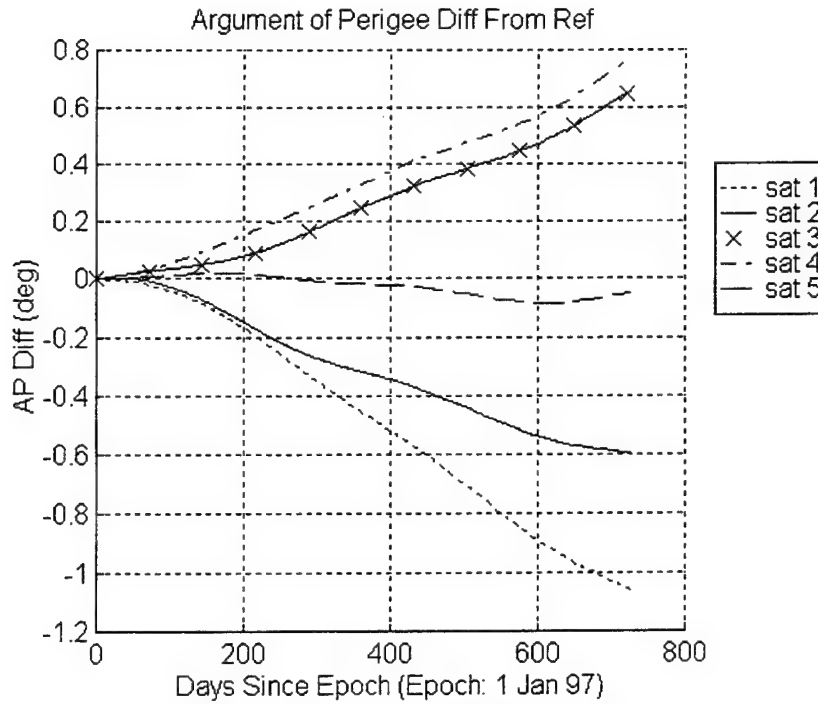


Figure C.21: Argument of Perigee Difference From Nominal Trajectory
(Uncontrolled Borealis 8:1 Node at Midnight)

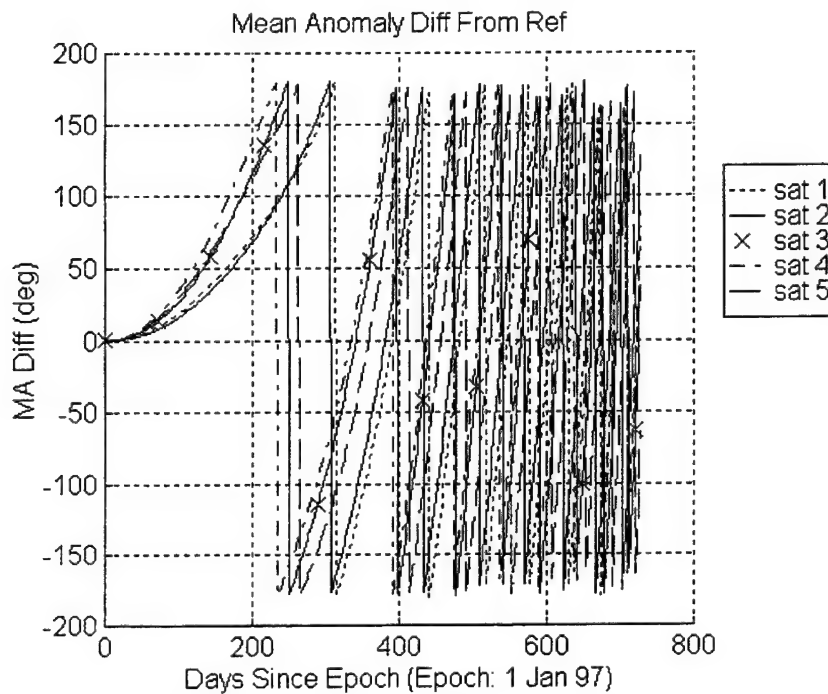


Figure C.22: Mean Anomaly Difference From Nominal Trajectory
(Uncontrolled Borealis 8:1 Node at Midnight)

C.2 Sim 2 / Run 2

This run is an execution of the ASKS on the 8:1 node at noon/midnight configuration of the Borealis planes and the Concordia plane of the Ellipso constellation. Absolute (box) station-keeping is used with targeting method 3. Note that the satellites of the Concordia are left uncontrolled by defining the maximum limits in plane 3 of the input deck higher than the largest values observed in the plots of section C.1.3. The maximum limits for all the elements, except the mean anomaly, for the two Borealis planes are set as listed in table 6.1. The mean anomaly maximum limit is set to 5° . The deadband limits are set just below the maximum limits to avoid multiple element burns.

The epoch orbital elements for this run are listed in tables 7.1 and 7.3. The nominal (reference) trajectory is propagated in the presence of zonal harmonics through degree 21, and solar/lunar point masses. The actual satellite trajectory is propagated with the perturbations of the nominal trajectory plus solar radiation pressure, tesseral resonance and atmospheric drag.

Section C.2.1 contains the input deck for run 2. Sections C.2.2 contains the one, two, three and four-way coverage of the constellation over the 2 year time span. Coverage is provided for the entire northern hemisphere and for the southern hemisphere above 55°S latitude. The northern hemispheric coverage assumes a 25° minimum elevation angle. The southern hemispheric coverage assumes a 10° minimum elevation angle. Since the Concordia plane is not controlled, its orbital element difference plots are the same as in section C.1.3. Sections C.2.3 and C.2.4 contain the orbital element difference plots for the node at noon and node at midnight planes, respectively.

C.2.1 Input Deck (Sim 2 / Run 2)

The following listing is the input deck for run 2 of simulation 2. Only the information for one satellite per plane is depicted for brevity. The satellites in the plane are evenly spaced at epoch.

```
Number of Planes      :      3
Stat-Keep Method      :      0  (0=box; 1=formation)

Targeting Method      :      3
Power                 :      1.00
kmax                  :      50
max_burns             :      4

Epoch Date: 19970101.0 Epoch Time:      0.0000
Final Date: 19990101.0 Final Time:      0.0000
Iteration Time Step   :      0.103000000000000D+05  sec

*****
Plane                 :      1
Sats In This Plane    :      5

Maximum Parameter Limits: 1.000000000000000D+00  km  sma
Keplerian Elements:    0.001000000000000D+00      ecc
                      0.000050000000000D+03      deg  inc
                      0.000200000000000D+03      deg  lan
                      0.001000000000000D+03      deg  ap
                      0.005000000000000D+03      deg  ma

Scale (outer limits) : 0.98
Deadband Parameter Limits: 0.950000000000000D+00  km  sma
Keplerian Elements:    0.000950000000000D+00      ecc
                      0.000045000000000D+03      deg  inc
                      0.000180000000000D+03      deg  lan
                      0.000950000000000D+03      deg  ap
                      0.004700000000000D+03      deg  ma

Maximum Overshoot Limits : 0.980000000000000D+00  frac sma
                          0.980000000000000D+00  frac ecc
                          0.980000000000000D+00  frac inc
                          0.650000000000000D+00  frac lan
                          0.980000000000000D+00  frac ap
                          1.250000000000000D+00  frac ma

-----
Satellite Number      :      1

Actual State:
Keplerian Elements:    0.105592710000000D+05  km  sma
                      0.345705000000000D+00      ecc
                      0.116307400060000D+03      deg  inc
                      0.279374453010000D+03      deg  lan
                      0.269947822490000D+03      deg  ap
                      0.000000000000000D+03      deg  ma

CD:                    2.20000000 Rho One:      0.00000000
S/C Mass:              700.00000000 S/C Area:    0.00002500
Integrator Step: 43200.00000000

Retro:      1 Atmos Mdl: 1 Potent Mdl: 4
Nmax:      21 Mmax:      21 Izonal:      1 IJ2J2: 1
Nmaxrs:     21 Mmaxrs:    21 Ithird:      1
Ind Drg:     1 Iszak:      2 Ind Sol:      1

Reference State:
```

Keplerian Elements: 0.1055927100000000D+05 km sma
0.3457050000000000D+00 ecc
0.1163074000600000D+03 deg inc
0.2793744530100000D+03 deg lan
0.2699478224900000D+03 deg ap
0.0000000000000000D+03 deg ma
Reference Switch : 0 ! (0=DSST, 1=Fixed Rates)
Reference State Rates:
Keplerian Rates: 0.0000000000000000D+00 km/sec sma
0.0000000000000000D+00 1/sec ecc
0.0000000000000000D+00 deg/sec inc
1.1407711610000000D-05 deg/sec lan
0.0000000000000000D+00 deg/sec ap
3.3338114140000000D-02 deg/sec ma

CD: 2.20000000 Rho One: 0.00000000
S/C Mass: 700.00000000 S/C Area: 0.00002500
Integrator Step: 43200.00000000

Retro: 1 Atmos Mdl: 1 Potent Mdl: 4
Nmax: 21 Mmax: 0 Izonal: 1 IJ2J2: 1
Nmaxrs: 2 Mmaxrs: 2 Ithird: 1
Ind Drg: 2 Iszak: 2 Ind Sol: 2

.
.
.

Plane : 2
Sats In This Plane : 5

Maximum Parameter Limits: 1.0000000000000000D+00 km sma
Keplerian Elements: 0.0010000000000000D+00 ecc
0.0000500000000000D+03 deg inc
0.0002000000000000D+03 deg lan
0.0010000000000000D+03 deg ap
0.0050000000000000D+03 deg ma

Scale (outer limits) : 0.98

Deadband Parameter Limits: 0.9500000000000000D+00 km sma
Keplerian Elements: 0.0009500000000000D+00 ecc
0.0000450000000000D+03 deg inc
0.0001800000000000D+03 deg lan
0.0009500000000000D+03 deg ap
0.0047000000000000D+03 deg ma

Maximum Overshoot Limits : 0.9800000000000000D+00 frac sma
0.9800000000000000D+00 frac ecc
0.9800000000000000D+00 frac inc
0.6500000000000000D+00 frac lan
0.9800000000000000D+00 frac ap
1.2500000000000000D+00 frac ma

Satellite Number : 6

Actual State:
Keplerian Elements: 0.1055927000000000D+05 km sma
0.3456750000000000D+00 ecc
0.1168225808500000D+03 deg inc
0.0994212275300000D+03 deg lan
0.2700524126200000D+03 deg ap
0.0000000000000000D+03 deg ma

CD: 2.20000000 Rho One: 0.00000000
S/C Mass: 700.00000000 S/C Area: 0.00002500
Integrator Step: 43200.00000000

Retro: 1 Atmos Mdl: 1 Potent Mdl: 4
Nmax: 21 Mmax: 21 Izonal: 1 IJ2J2: 1
Nmaxrs: 21 Mmaxrs: 21 Ithird: 1
Ind Drg: 1 Iszak: 2 Ind Sol: 1

Reference State:
Keplerian Elements: 0.1055927000000000D+05 km sma
0.3456750000000000D+00 ecc


```

0.1168225808500000D+03 deg inc
0.0994212275300000D+03 deg lan
0.2700524126200000D+03 deg ap
0.0000000000000000D+03 deg ma
Reference Switch : 0 ! (0=DSST, 1=Fixed Rates)
Reference State Rates:
Keplerian Rates: 0.0000000000000000D+00 km/sec sma
0.0000000000000000D+00 1/sec ecc
0.0000000000000000D+00 deg/sec inc
1.1407711610000000D-05 deg/sec lan
0.0000000000000000D+00 deg/sec ap
3.3338114140000000D-02 deg/sec ma

```

```

CD: 2.20000000 Rho One: 0.00000000
S/C Mass: 700.00000000 S/C Area: 0.00002500
Integrator Step: 43200.00000000

```

```

Retro: 1 Atmos Mdl: 1 Potent Mdl: 4
Nmax: 21 Mmax: 0 Izonal: 1 IJ2J2: 1
Nmaxrs: 2 Mmaxrs: 2 Ithird: 1
Ind Drg: 2 Iszak: 2 Ind Sol: 2

```

```

.
.
.

```

```

*****

```

```

Plane : 3
Sats In This Plane : 7

```

```

Maximum Parameter Limits: 0.1000000000000000D+00 km sma
Keplerian Elements: 0.0200000000000000D+00 ecc
0.0000600000000000D+03 deg inc
0.7200000000000000D+03 deg lan
0.7200000000000000D+03 deg ap
0.7200000000000000D+03 deg ma

```

```

Scale (outer limits) : 0.98

```

```

Deadband Parameter Limits: 0.1000000000000000D+00 km sma
Keplerian Elements: 0.0200000000000000D+00 ecc
0.0000600000000000D+03 deg inc
0.7200000000000000D+03 deg lan
0.7200000000000000D+03 deg ap
0.7200000000000000D+03 deg ma

```

```

Maximum Overshoot Limits : 0.9800000000000000D+00 frac sma
0.9800000000000000D+00 frac ecc
0.9800000000000000D+00 frac inc
0.9800000000000000D+00 frac lan
0.9800000000000000D+00 frac ap
0.9800000000000000D+00 frac ma

```

```

-----
Satellite Number : 11

```

```

Actual State:
Keplerian Elements: 0.1444013700000000D+05 km sma
0.0000100000000000D+00 ecc
0.0002618026600000D+03 deg inc
0.0891037880400000D+03 deg lan
0.0002938944900000D+03 deg ap
0.0000000000000000D+03 deg ma

```

```

CD: 2.20000000 Rho One: 0.00000000
S/C Mass: 700.00000000 S/C Area: 0.00002500
Integrator Step: 43200.00000000

```

```

Retro: 1 Atmos Mdl: 1 Potent Mdl: 4
Nmax: 21 Mmax: 21 Izonal: 1 IJ2J2: 1
Nmaxrs: 21 Mmaxrs: 21 Ithird: 1
Ind Drg: 1 Iszak: 2 Ind Sol: 1

```

```

Reference State:
Keplerian Elements: 0.1444013700000000D+05 km sma
0.0000100000000000D+00 ecc
0.0002618026600000D+03 deg inc
0.0891037880400000D+03 deg lan

```

```

0.0002938944900000D+03 deg ap
0.0000000000000000D+03 deg ma
Reference Switch : 0 ! (0=DSST, 1=Fixed Rates)
Reference State Rates:
Keplerian Rates: 0.0000000000000000D+00 km/sec sma
                  0.0000000000000000D+00 1/sec ecc
                  0.0000000000000000D+00 deg/sec inc
                  1.1407711610000000D-05 deg/sec lan
                  0.0000000000000000D+00 deg/sec ap
                  3.3338114140000000D-02 deg/sec ma

```

```

CD: 2.20000000 Rho One: 0.00000000
S/C Mass: 700.0000000 S/C Area: 0.00002500
Integrator Step: 43200.00000000

```

```

Retro: 1 Atmos Mdl: 1 Potent Mdl: 4
Nmax: 21 Mmax: 21 Izonal: 1 IJ2J2: 1
Nmaxrs: 21 Mmaxrs: 21 Ithird: 3
Ind Drg: 2 Iszak: 2 Ind Sol: 2

```

```

-----
.
.
.
-----

```

C.2.2 Coverage Plots (Sim 2 / Run 2)

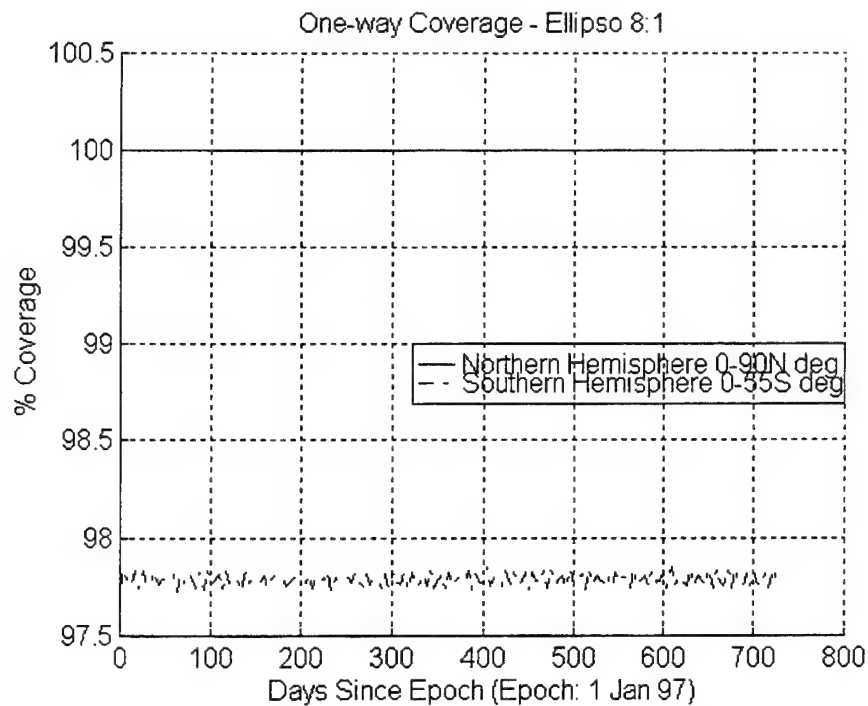


Figure C.23: Ellipso One-Way Coverage
(Method 3 Borealis 8:1 Node at Noon/Midnight and Uncontrolled Concordia)

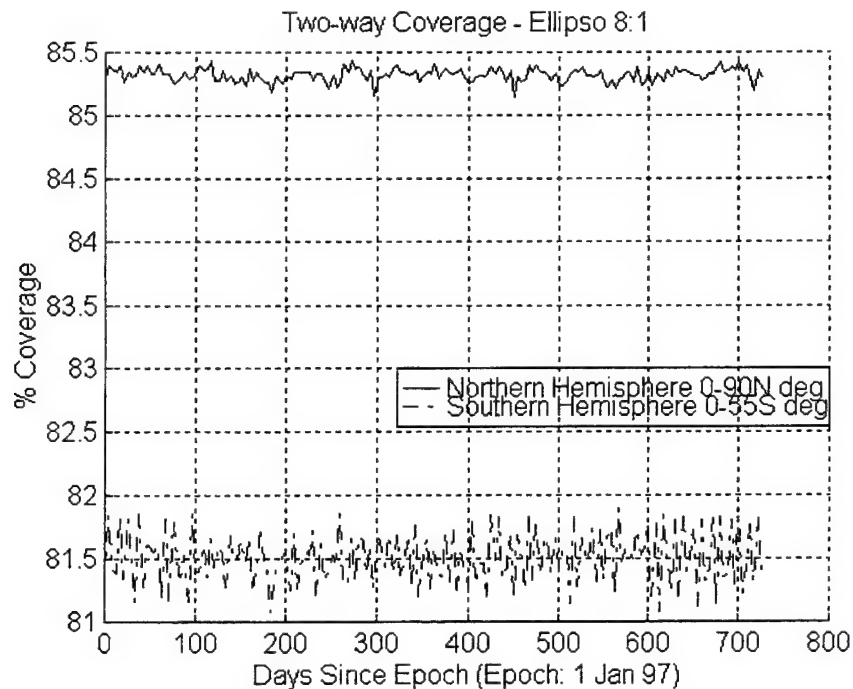


Figure C.24: Ellipso Two-Way Coverage
(Method 3 Borealis 8:1 Node at Noon/Midnight and Uncontrolled Concordia)

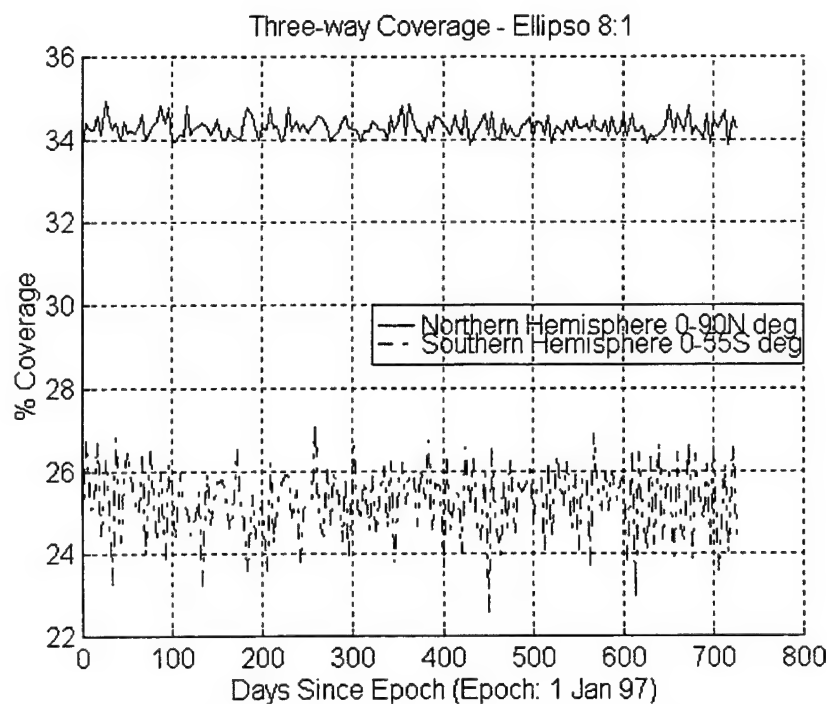


Figure C.25: Ellipso Three-Way Coverage
(Method 3 Borealis 8:1 Node at Noon/Midnight and Uncontrolled Concordia)

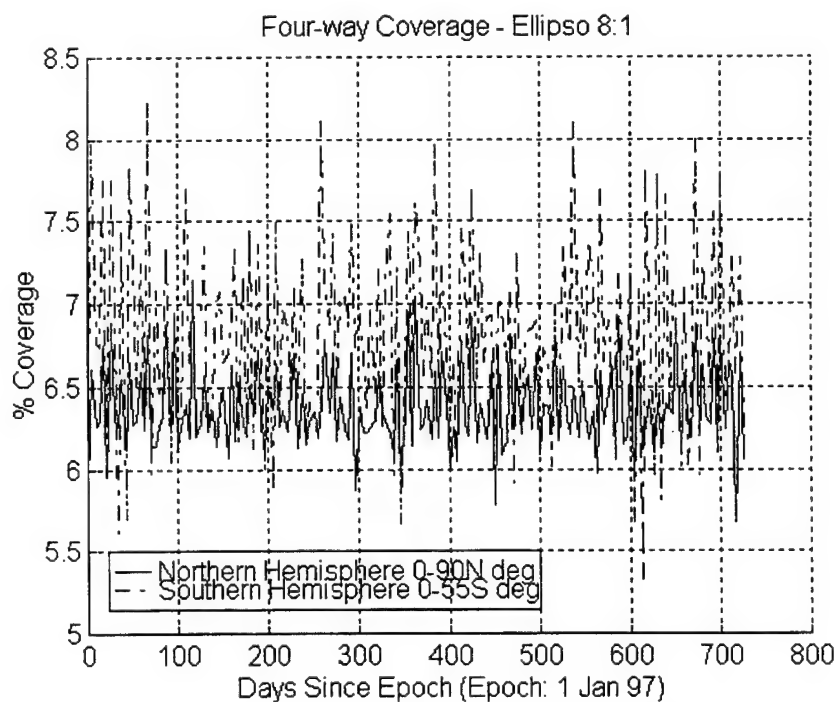


Figure C.26: Ellipso Four-Way Coverage
(Method 3 Borealis 8:1 Node at Noon/Midnight and Uncontrolled Concordia)

C.2.3 Method 3 Borealis 8:1 Node at Noon Orbital Element Difference Plots

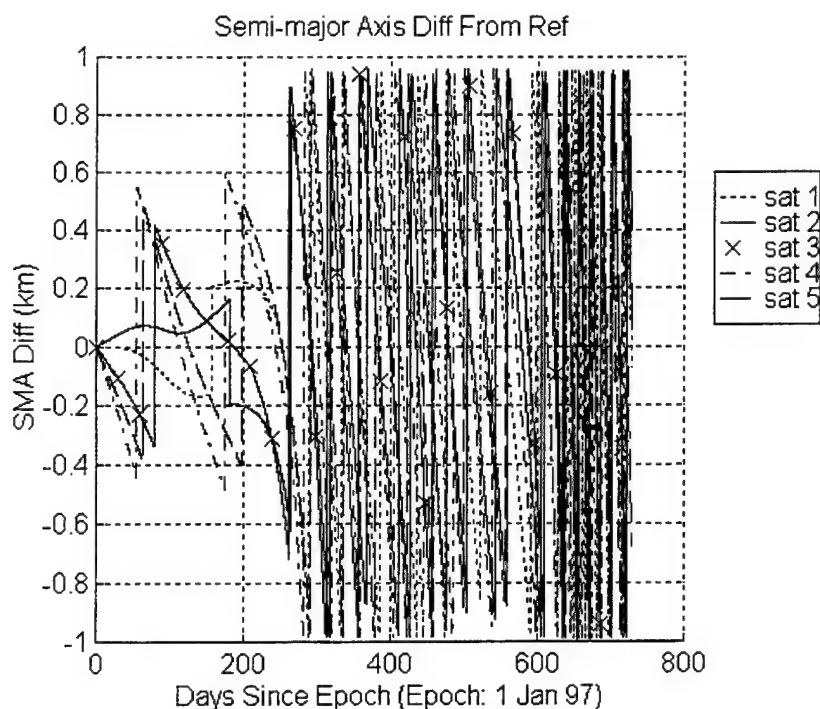


Figure C.27: Semi-major Axis Difference From Nominal Trajectory
(Method 3 Borealis 8:1 Node at Noon)

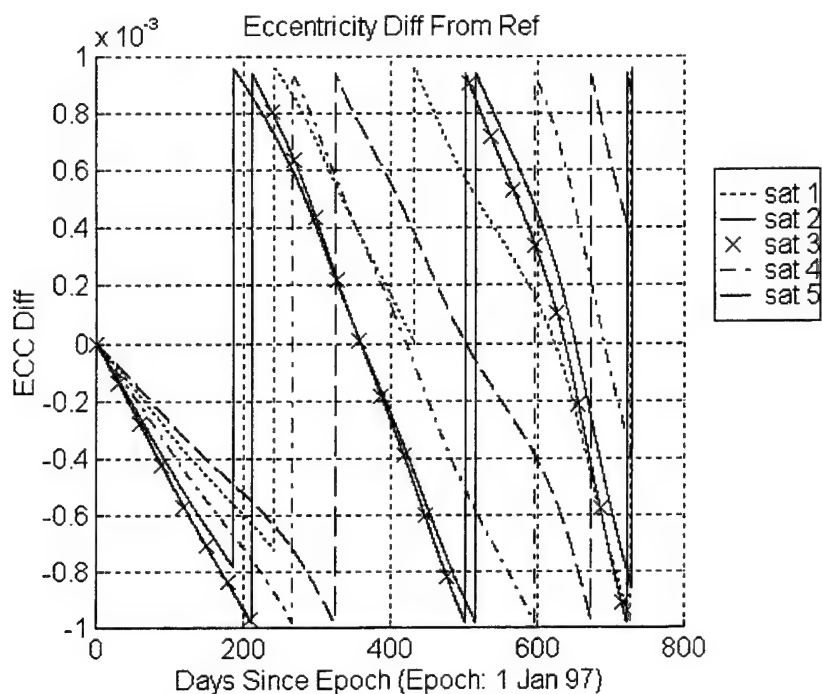


Figure C.28: Eccentricity Difference From Nominal Trajectory
(Method 3 Borealis 8:1 Node at Noon)

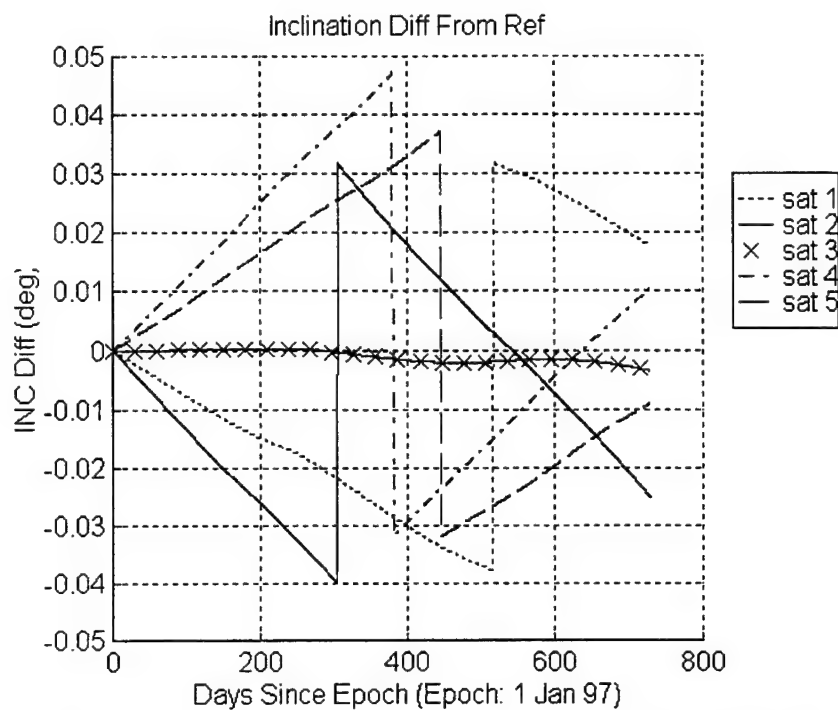


Figure C.29: Inclination Difference From Nominal Trajectory
(Method 3 Borealis 8:1 Node at Noon)

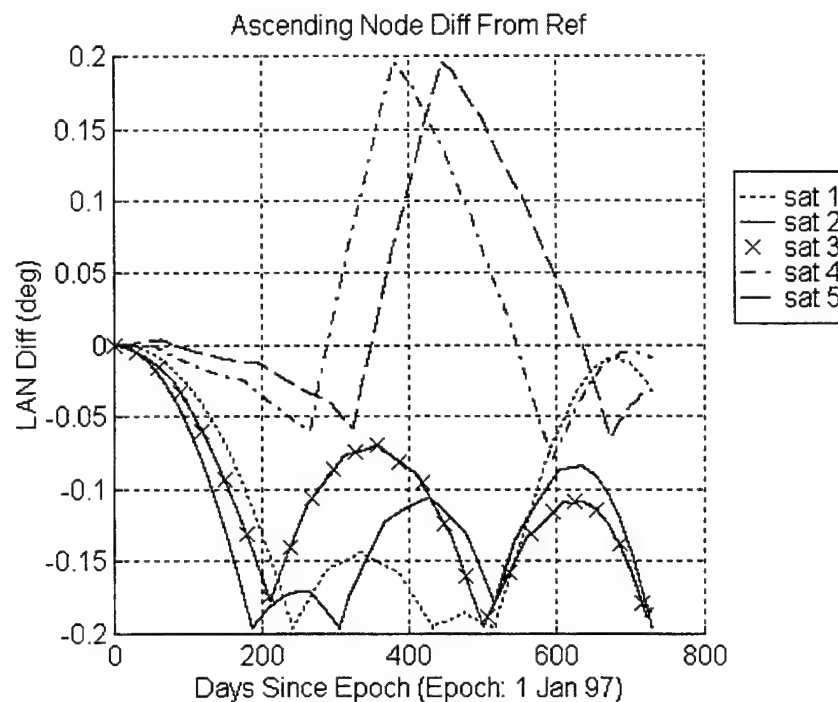


Figure C.30: Ascending Node Difference From Nominal Trajectory
(Method 3 Borealis 8:1 Node at Noon)

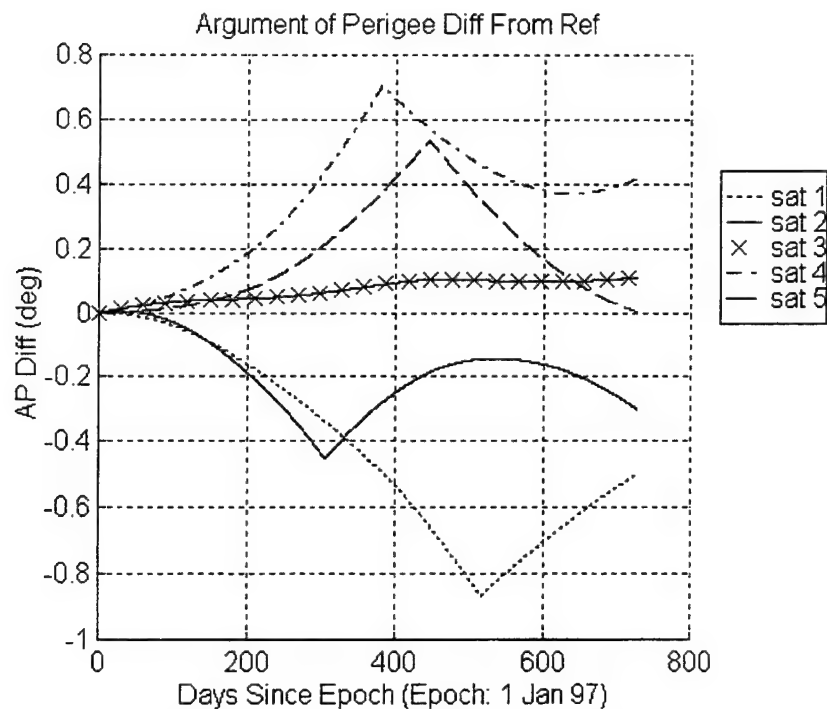


Figure C.31: Argument of Perigee Difference From Nominal Trajectory
(Method 3 Borealis 8:1 Node at Noon)

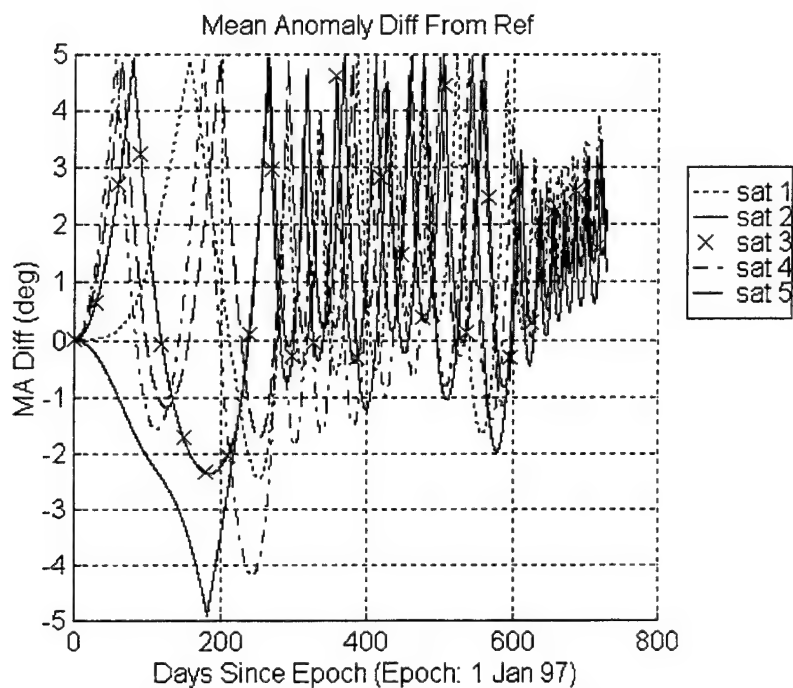


Figure C.32: Mean Anomaly Difference From Nominal Trajectory
(Method 3 Borealis 8:1 Node at Noon)

C.2.4 Method 3 Borealis 8:1 Node at Midnight Orbital Element Difference Plots

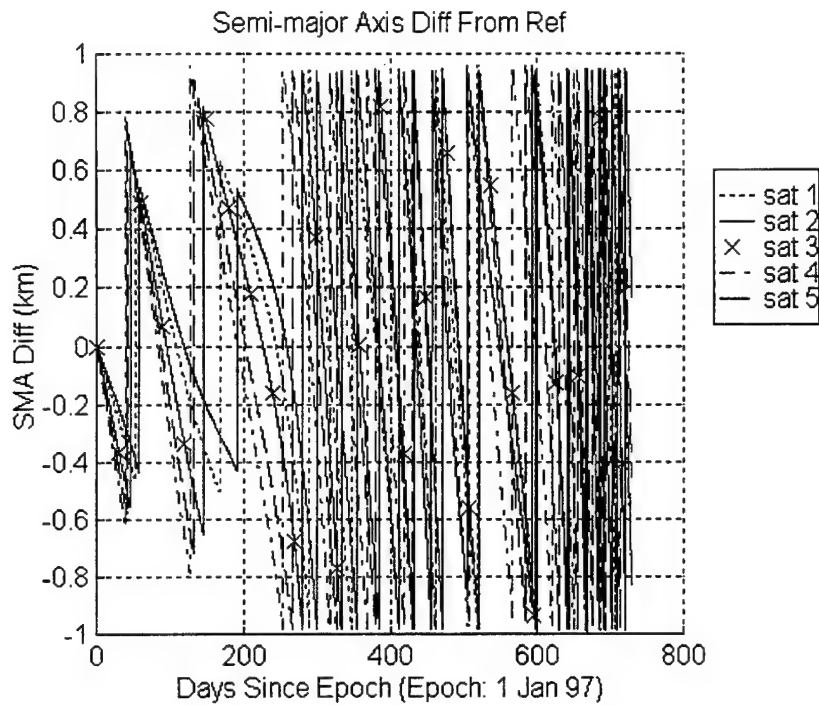


Figure C.33: Semi-major Axis Difference From Nominal Trajectory
(Method 3 Borealis 8:1 Node at Midnight)

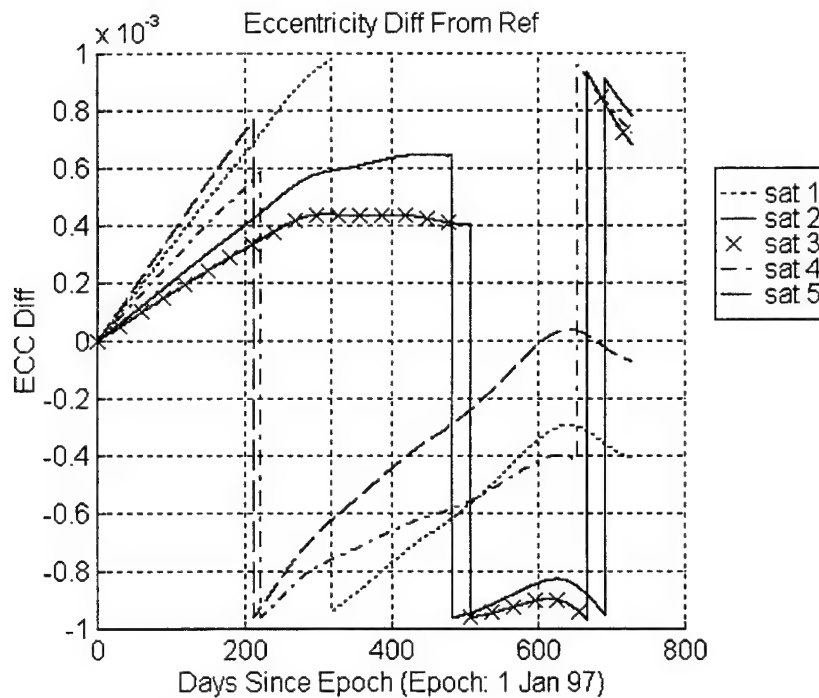


Figure C.34: Eccentricity Difference From Nominal Trajectory
(Method 3 Borealis 8:1 Node at Midnight)

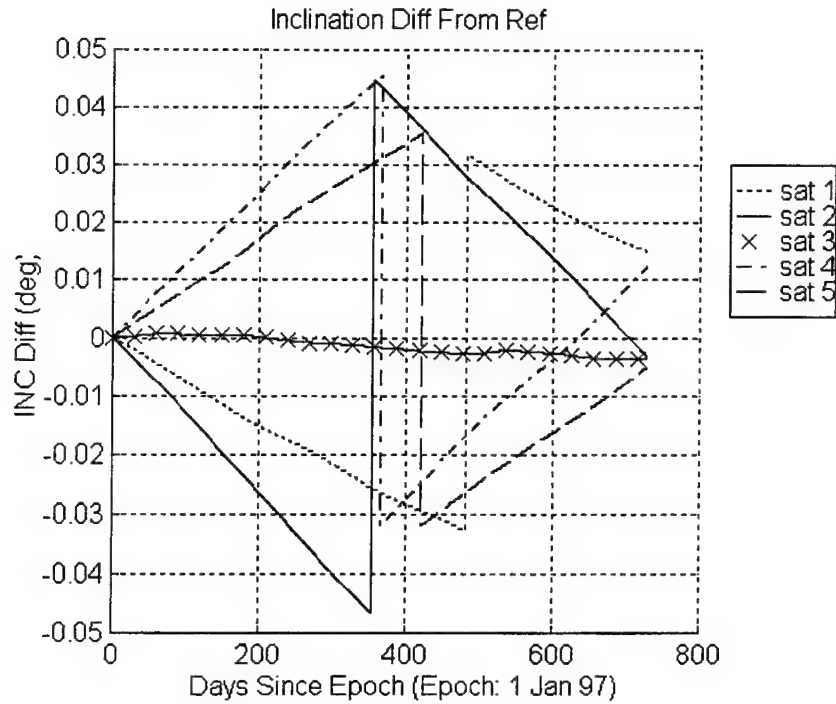


Figure C.35: Inclination Difference From Nominal Trajectory
(Method 3 Borealis 8:1 Node at Midnight)

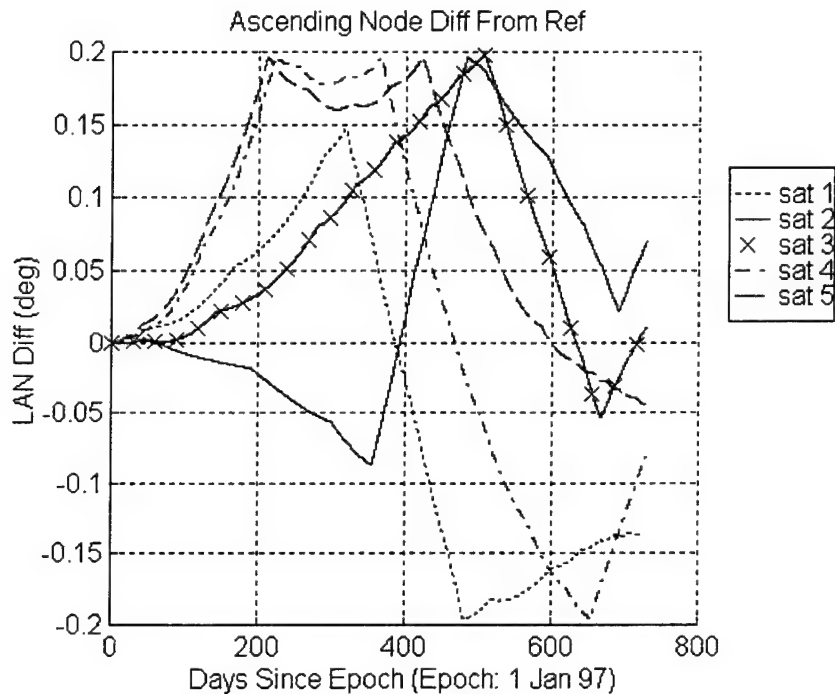


Figure C.36: Ascending Node Difference From Nominal Trajectory
(Method 3 Borealis 8:1 Node at Midnight)

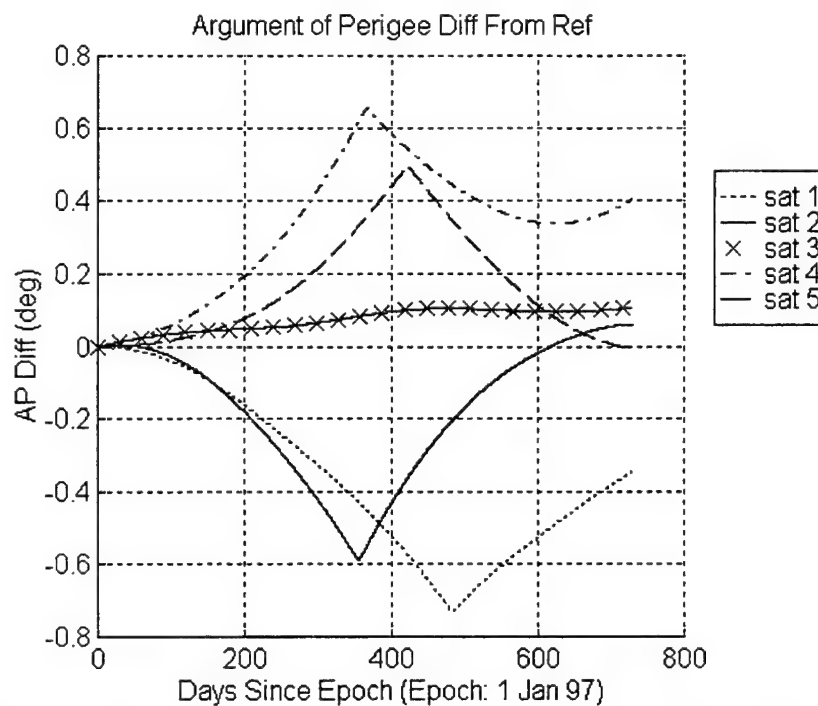


Figure C.37: Argument of Perigee Difference From Nominal Trajectory
(Method 3 Borealis 8:1 Node at Midnight)

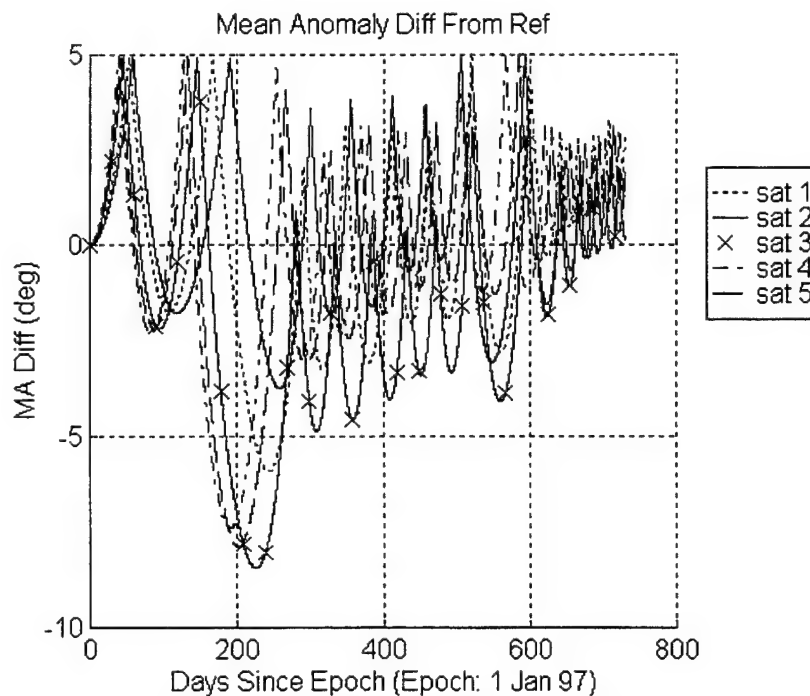


Figure C.38: Mean Anomaly Difference From Nominal Trajectory
(Method 3 Borealis 8:1 Node at Midnight)

C.3 Sim 2 / Run 3

This run is an execution of the ASKS on the 8:1 node at noon/midnight configuration of the Borealis planes and the Concordia plane of the Ellipso constellation. Relative mean anomaly (formation) station-keeping is used with targeting method 3. As with run 2, the satellites of the Concordia are left uncontrolled by defining the maximum limits in plane 3 of the input deck higher than the largest values observed in the plots of section C.1.3. The Borealis limits are also the same as with run 2.

The epoch orbital elements for this run are listed in tables 7.1 and 7.3. The nominal (reference) trajectory is propagated in the presence of zonal harmonics through degree 21, and solar/lunar point masses. The actual satellite trajectory is propagated with the perturbations of the nominal trajectory plus solar radiation pressure, tesseral resonance and atmospheric drag.

Section C.3.1 contains the input deck for run 3. Sections C.3.2 contains the one, two, three and four-way coverage of the constellation over the 2 year time span. Coverage is provided for the entire northern hemisphere and for the southern hemisphere above 55°S latitude. The northern hemispheric coverage assumes a 25° minimum elevation angle. The southern hemispheric coverage assumes a 10° minimum elevation angle. Since the Concordia plane is not controlled, its orbital element difference plots are the same as in section C.1.3. Sections C.3.3 and C.3.4 contain the orbital element difference plots for the node at noon and node at midnight planes, respectively.

C.3.1 Input Deck (Sim 2 / Run 3)

The following listing includes only the run information block of the input deck for run 3 of simulation 2. The remainder of the input deck is the same as for run 2 of simulation 3. The only change is that “formation”, or relative mean anomaly spacing, is set as the station-keeping method instead of “box”, or absolute mean anomaly spacing.

```
Number of Planes      :      3
Stat-Keep Method      :      1  (0=box; 1=formation)

Targeting Method      :      3
Power                 :      1.00
kmax                  :      50
max_burns             :      4

Epoch Date: 19970101.0 Epoch Time:      0.0000
Final Date: 19990101.0 Final Time:      0.0000
Iteration Time Step :      0.1030000000000000D+05  sec
```

C.3.2 Coverage Plots (Sim 2 / Run 3)

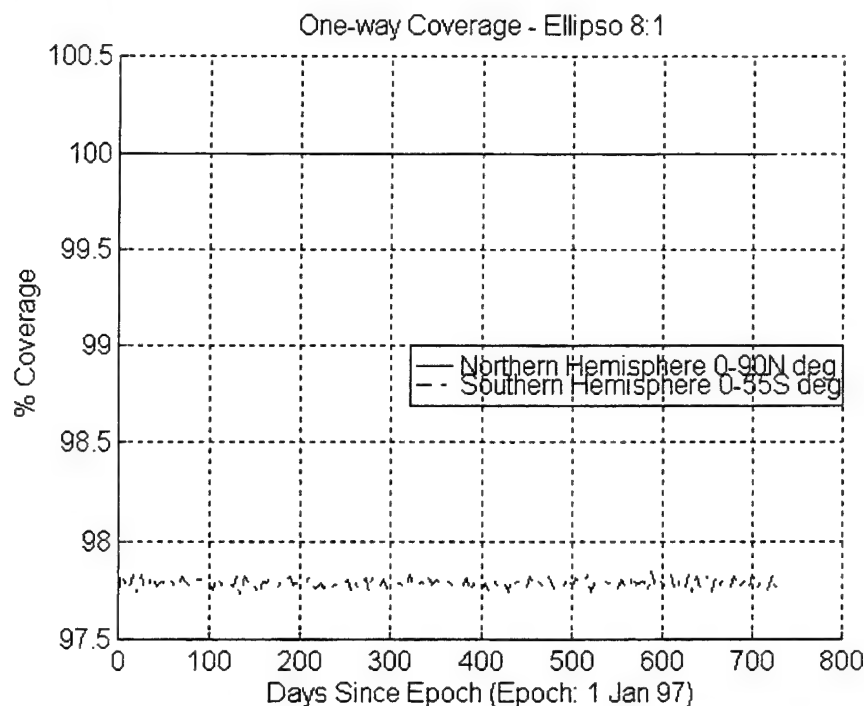


Figure C.39: Ellipso One-Way Coverage
(Method 3 / Relative M Borealis 8:1 Noon/Midnight and Uncontrolled Concordia)

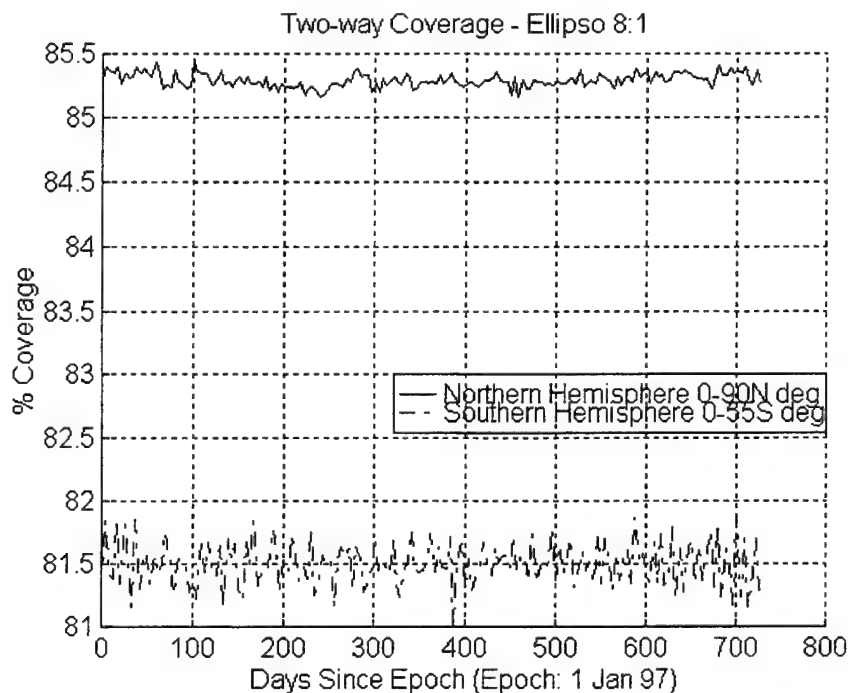


Figure C.40: Ellipso Two-Way Coverage
(Method 3 / Relative M Borealis 8:1 Noon/Midnight and Uncontrolled Concordia)

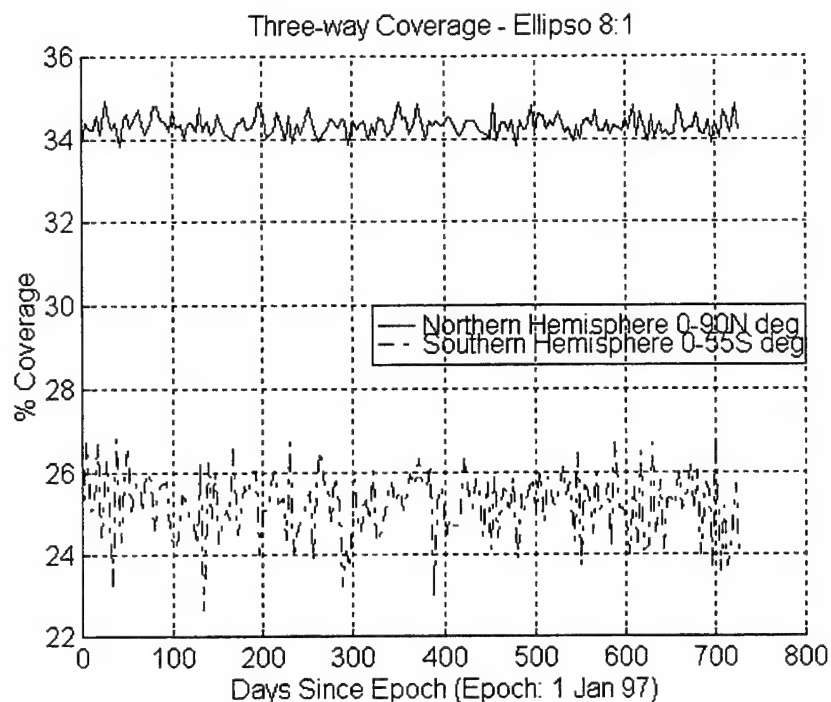


Figure C.41: Ellipso Three-Way Coverage
(Method 3 / Relative M Borealis 8:1 Noon/Midnight and Uncontrolled Concordia)

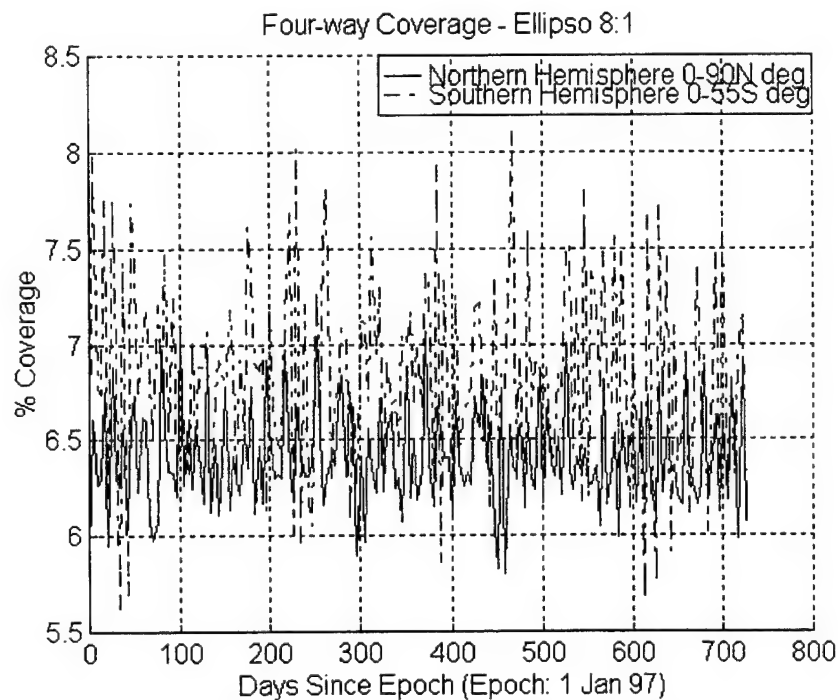


Figure C.42: Ellipso Four-Way Coverage
(Method 3 / Relative M Borealis 8:1 Noon/Midnight and Uncontrolled Concordia)

C.2.3 Method 3 / Relative M Borealis 8:1 Node at Noon Element Difference Plots

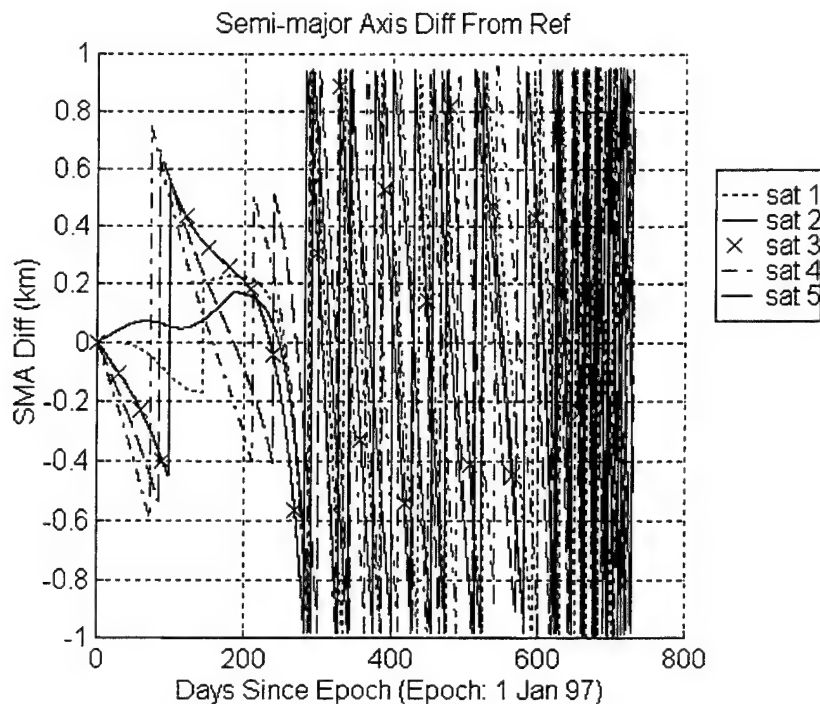


Figure C.43: Semi-major Axis Difference From Nominal Trajectory
(Method 3 / Relative M Borealis 8:1 Node at Noon)

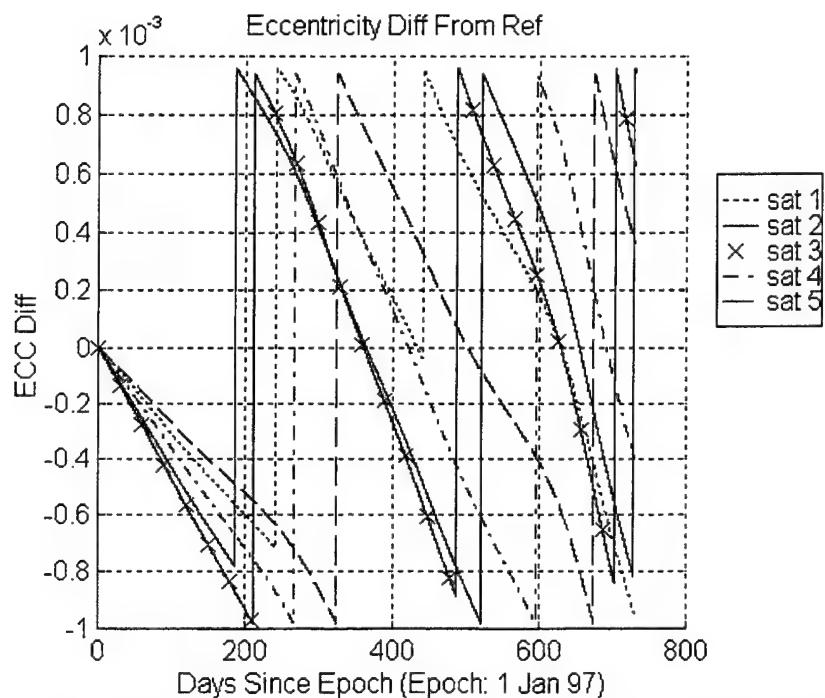


Figure C.44: Eccentricity Difference From Nominal Trajectory
(Method 3 / Relative M Borealis 8:1 Node at Noon)

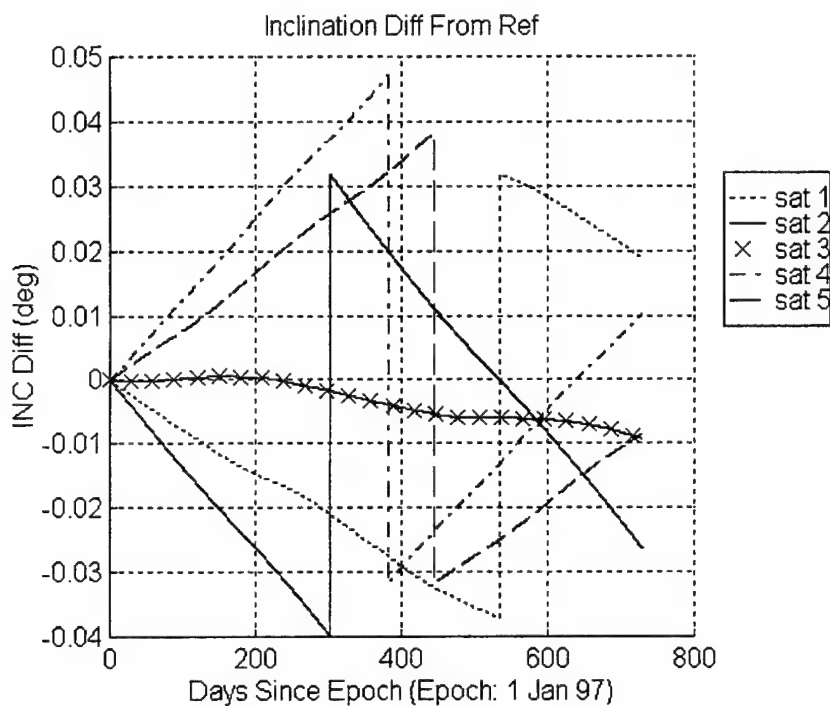


Figure C.45: Inclination Difference From Nominal Trajectory
(Method 3 / Relative M Borealis 8:1 Node at Noon)

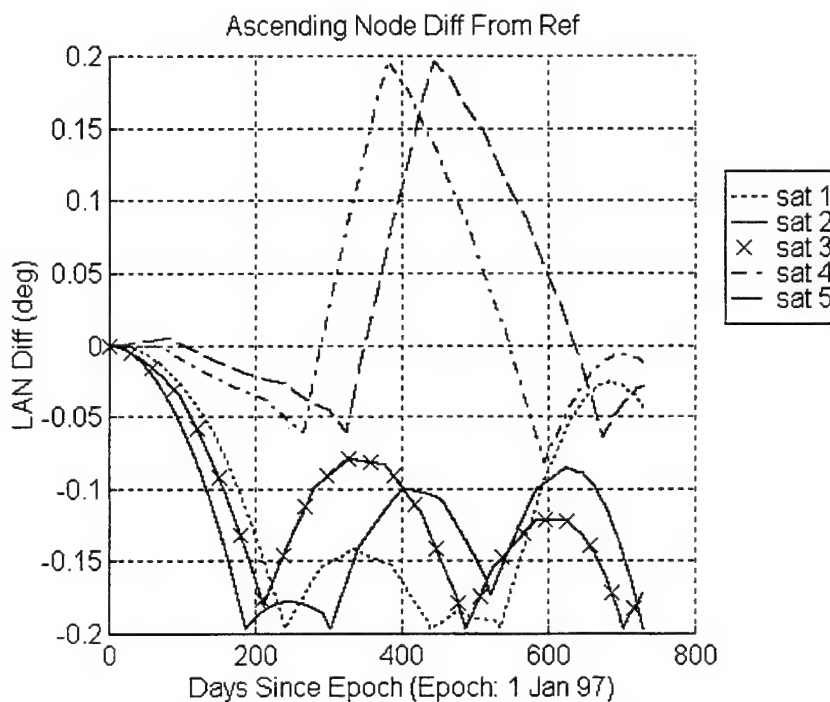


Figure C.46: Ascending Node Difference From Nominal Trajectory
(Method 3 / Relative M Borealis 8:1 Node at Noon)

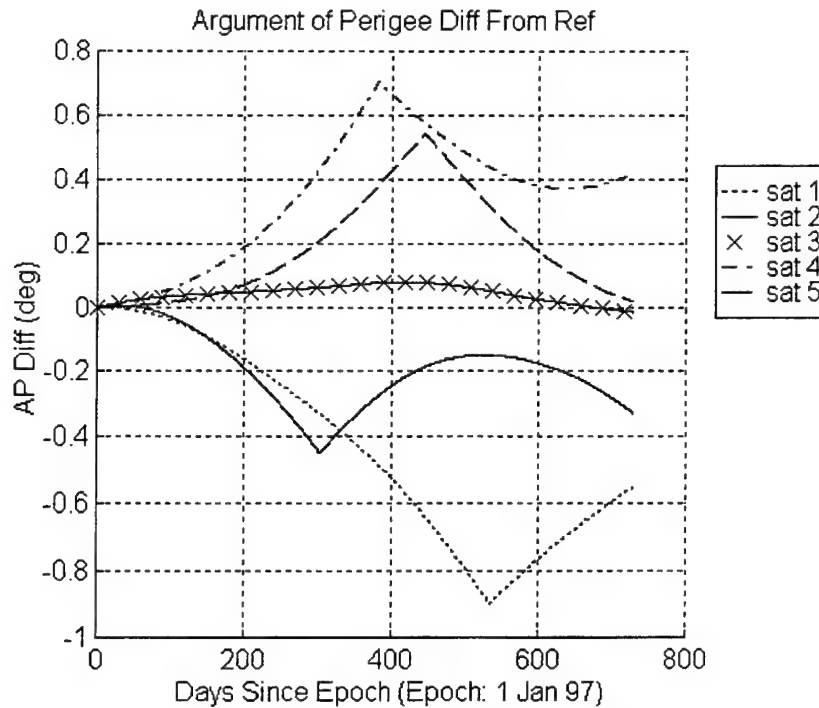


Figure C.47: Argument of Perigee Difference From Nominal Trajectory
(Method 3 / Relative M Borealis 8:1 Node at Noon)

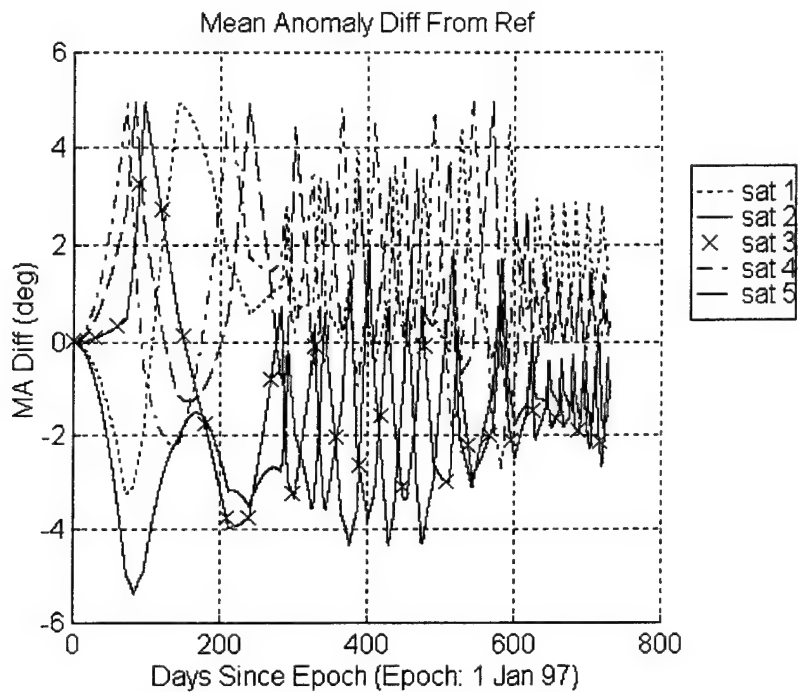


Figure C.48: Mean Anomaly Difference From Nominal Trajectory
(Method 3 / Relative M Borealis 8:1 Node at Noon)

C.2.4 Method 3 / Relative M Borealis 8:1 Node at Midnight Element Difference Plots

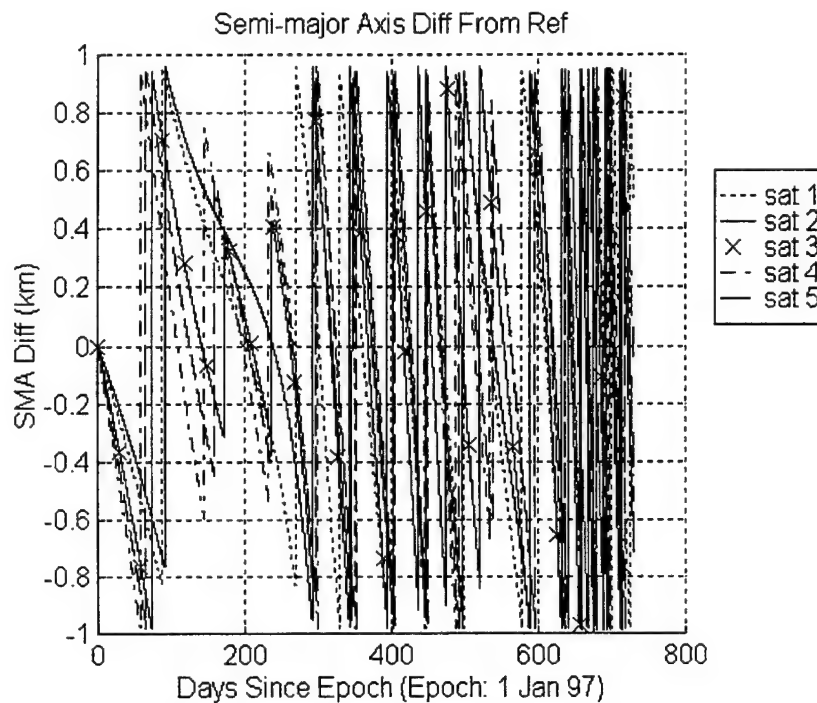


Figure C.49: Semi-major Axis Difference From Nominal Trajectory
(Method 3 / Relative M Borealis 8:1 Node at Midnight)

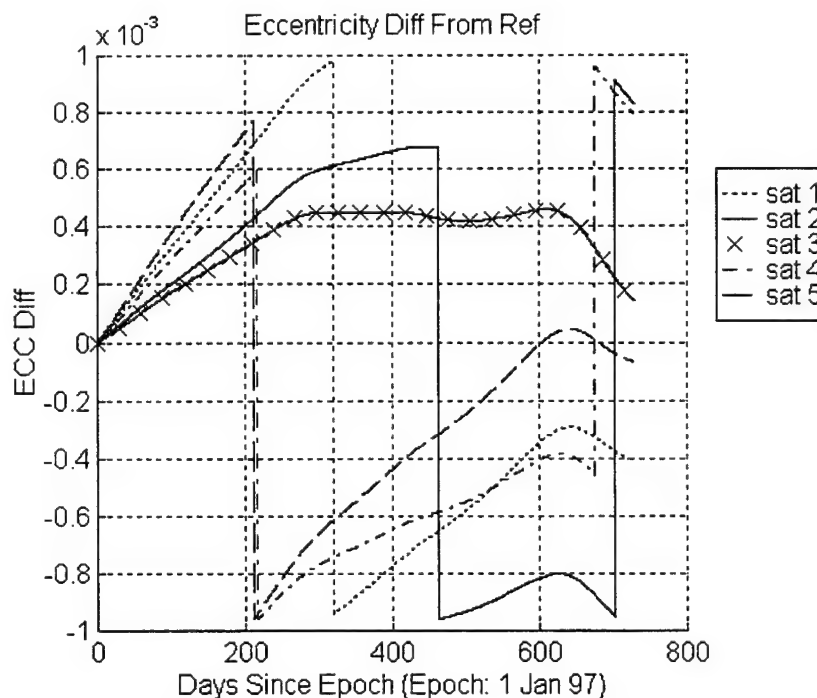


Figure C.50: Eccentricity Difference From Nominal Trajectory
(Method 3 / Relative M Borealis 8:1 Node at Midnight)

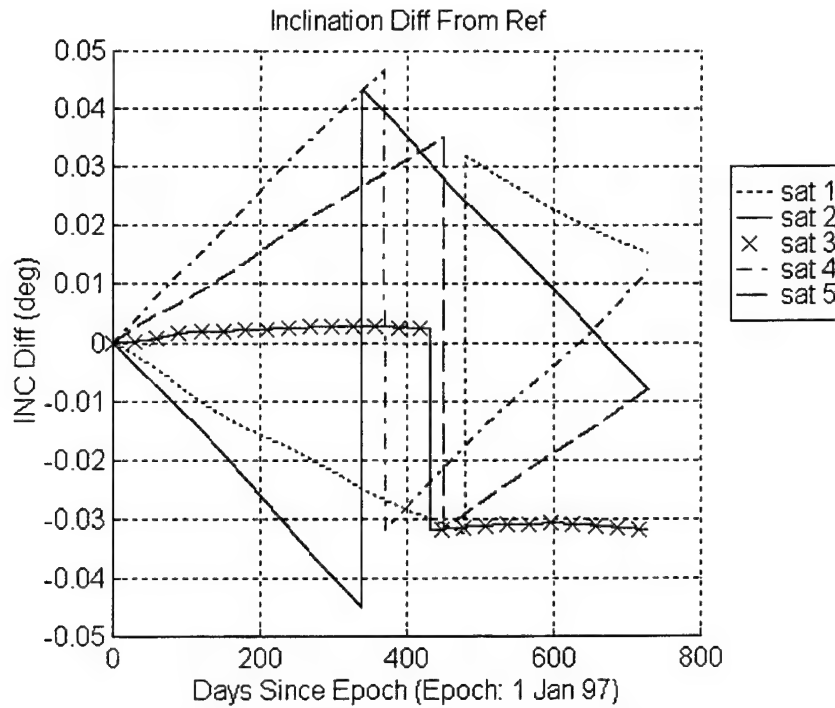


Figure C.51: Inclination Difference From Nominal Trajectory
(Method 3 / Relative M Borealis 8:1 Node at Midnight)

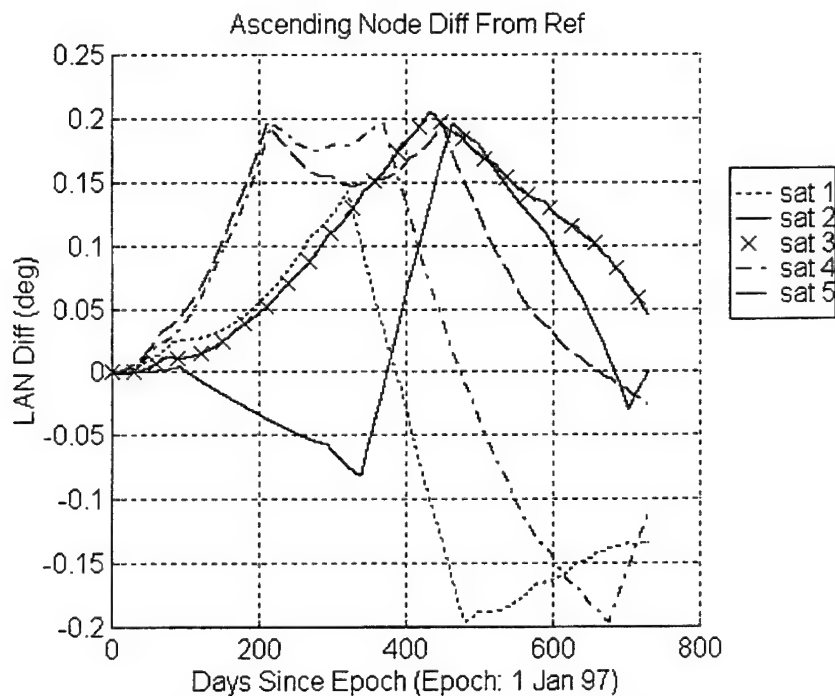


Figure C.52: Ascending Node Difference From Nominal Trajectory
(Method 3 / Relative M Borealis 8:1 Node at Midnight)

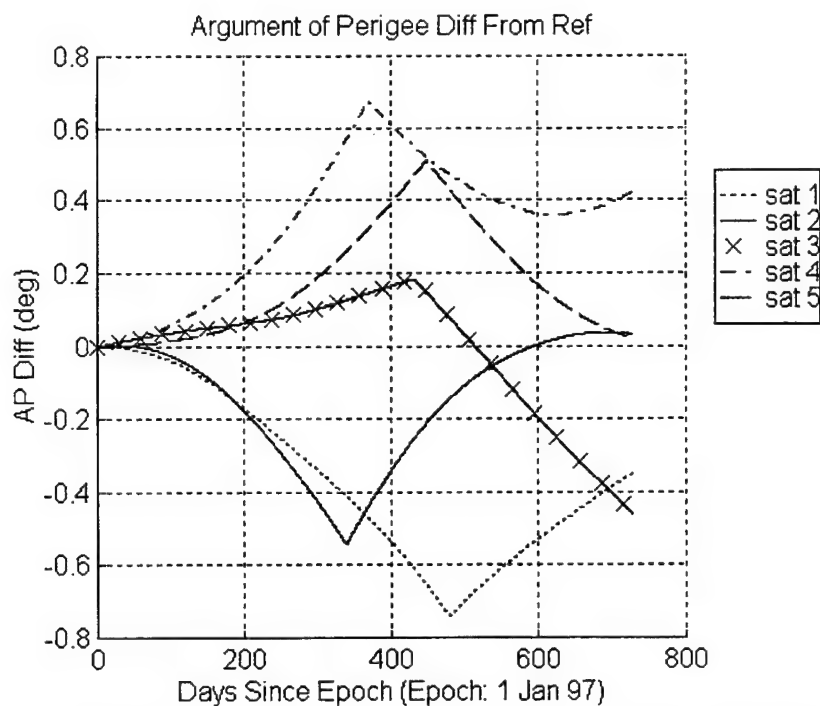


Figure C.53: Argument of Perigee Difference From Nominal Trajectory
(Method 3 / Relative M Borealis 8:1 Node at Midnight)

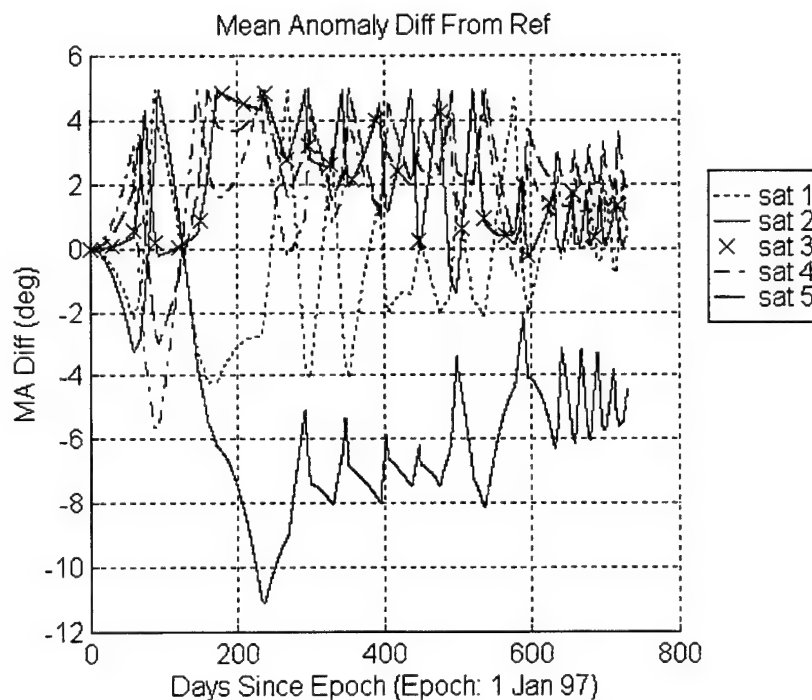


Figure C.54: Mean Anomaly Difference From Nominal Trajectory
(Method 3 / Relative M Borealis 8:1 Node at Midnight)

[This page intentionally left blank.]

Appendix D

Simulation 3 Plots

This appendix contains all the plots produced in Simulation 3. The purpose of this simulation is to demonstrate that the ASKS can be used to compare different constellation orbit designs. The Ellipso constellation, with the Borealis 81:10 node at noon/midnight planes, is used as the test constellation. All the runs in this simulation are Method 0, uncontrolled. They are also all run with relative mean anomaly station-keeping. To provide a basis for comparing the coverage differences, the first run is a 5yr execution of the standard 5-5-7 satellite 81:10 Ellipso configuration. The second run will be the same as the first, except with only a 4-4-6 satellite configuration. The third and fourth runs will be of the 5-5-7 and 4-4-6 configurations, respectively, but with the arguments of perigee of the Borealis planes rotated 10° to bias coverage to daylight hours. The analysis of the results is located in section 7.4.

D.1 Sim 3 / Run 1

This run is a 5 year uncontrolled execution of the ASKS on the 5-5 satellite 81:10 node at noon/midnight configuration of the Borealis planes and the 7 satellite Concordia plane of the Ellipso constellation. There are 5 satellites in each of the Borealis planes and 7 satellites in the Concordia plane. Relative mean anomaly (formation) station-keeping is

used with targeting method 0. Method 0 indicates that all control related components of the input deck are ignored.

The epoch orbital elements for this run are listed in tables 7.1 and 7.4. The nominal (reference) trajectory is propagated in the presence of zonal harmonics through degree 21, and solar/lunar point masses. The actual satellite trajectory is propagated with the perturbations of the nominal trajectory plus solar radiation pressure, tesseral resonance and atmospheric drag.

Section D.1.1 contains the input deck for run1. Sections D.1.2 contains the one, two, three and four-way coverage of the constellation over the 5 year time span. Note that coverage is provided for the entire northern hemisphere and for the southern hemisphere above 55°S latitude. The northern hemispheric coverage assumes a 25° minimum elevation angle. The southern hemispheric coverage assumes a 10° minimum elevation angle. Section D.1.3 contains the orbital element difference plots for the Concordia plane. Sections D.1.4 and D.1.5 contain the orbital element difference plots for node at noon and node at midnight planes, respectively.

D.1.1 Input Deck (Sim 3 / Run 1)

The following list is the equivalent input deck for the current version of the ASKS that will produce the plots for run 1 of simulation 3 shown in the following subsections. This run was originally executed with an older version of the ASKS that used an input deck with data provided in a different order. The numbers in the input deck shown below are the same values as used for the original input deck. Only the information for one satellite per plane is depicted for brevity. The satellites in the plane are evenly spaced at epoch.

```

Number of Planes      :      3
Stat-Keep Method     :      1  (0=box; 1=formation)

Targeting Method      :      0
Power                 :     1.00
kmax                  :      50
max_burns             :      2

Epoch Date: 19970101.0  Epoch Time:      0.0000
Final Date: 20020101.0  Final Time:      0.0000
Iteration Time Step   :      0.129600000000000D+07  sec

```

```

Plane      :      1
Sats In This Plane :      5

```

```

Maximum Parameter Limits:  0.000000000000000D+00  km  sma
Keplerian Elements:       0.000000000000000D+00  ecc
                          0.000000000000000D+03  deg  inc
                          0.000000000000000D+03  deg  lan
                          0.000000000000000D+03  deg  ap
                          0.000000000000000D+03  deg  ma

```

Scale (outer limits) : 0.98

```

Deadband Parameter Limits: 0.000000000000000D+00  km  sma
Keplerian Elements:       0.000000000000000D+00  ecc
                          0.000000000000000D+03  deg  inc
                          0.000000000000000D+03  deg  lan
                          0.000000000000000D+03  deg  ap
                          0.000000000000000D+03  deg  ma

```

```

Maximum Overshoot Limits : 0.980000000000000D+00  frac sma
                          0.980000000000000D+00  frac ecc
                          0.980000000000000D+00  frac inc
                          0.980000000000000D+00  frac lan
                          0.980000000000000D+00  frac ap
                          0.980000000000000D+00  frac ma

```

```

Satellite Number      :      1

```

```

Actual State:
Keplerian Elements:  0.1047220100000000D+05  km  sma
                    0.3265200000000000D+00  ecc
                    0.1163254000500000D+03  deg  inc
                    0.2793744347300000D+03  deg  lan
                    0.2699478143800000D+03  deg  ap
                    0.0000000000000000D+03  deg  ma

```

```

CD:                2.20000000  Rho One:      0.00000000
S/C Mass:          700.00000000  S/C Area:    0.00002500
Integrator Step: 43200.00000000

```

```

Retro:      1 Atmos Mdl:  1  Potent Mdl:  4
Nmax:      21 Mmax:      21  Izonal:      1  IJ2J2:  1
Nmaxrs:     21 Mmaxrs:     21  Ithird:      1
Ind Drg:     1 Iszak:      2  Ind Sol:      1

```

```

Reference State:
Keplerian Elements:  0.1047220100000000D+05  km  sma
                    0.3265200000000000D+00  ecc
                    0.1163254000500000D+03  deg  inc
                    0.2793744347300000D+03  deg  lan
                    0.2699478143800000D+03  deg  ap
                    0.0000000000000000D+03  deg  ma

```

Reference Switch : 0 ! (0=DSST, 1=Fixed Rates)

```

Reference State Rates:
Keplerian Rates:  0.000000000000000D+00  km/sec sma
                  0.000000000000000D+00  1/sec  ecc
                  0.000000000000000D+00  deg/sec inc
                  1.140771161000000D-05  deg/sec lan
                  0.000000000000000D+00  deg/sec ap
                  3.333811414000000D-02  deg/sec ma

```

```

CD:                2.20000000  Rho One:      0.00000000
S/C Mass:          700.00000000  S/C Area:    0.00002500
Integrator Step: 43200.00000000

```



```

Retro:      1 Atmos Mdl:  1 Potent Mdl:  4
Nmax:      21 Mmax:      0 Izonal:      1 IJ2J2:  1
Nmaxrs:    2 Mmaxrs:    2 Ithird:      1
Ind Drg:    2 Iszak:     2 Ind Sol:     2
-----
...
*****
Plane       :      2
Sats In This Plane :    5

Maximum Parameter Limits:      0.000000000000000D+00 km sma
Keplerian Elements:            0.000000000000000D+00 ecc
                                0.000000000000000D+03 deg inc
                                0.000000000000000D+03 deg lan
                                0.000000000000000D+03 deg ap
                                0.000000000000000D+03 deg ma

Scale (outer limits) : 0.98
Deadband Parameter Limits:      0.000000000000000D+00 km sma
Keplerian Elements:            0.000000000000000D+00 ecc
                                0.000000000000000D+03 deg inc
                                0.000000000000000D+03 deg lan
                                0.000000000000000D+03 deg ap
                                0.000000000000000D+03 deg ma

Maximum Overshoot Limits :      0.980000000000000D+00 frac sma
                                0.980000000000000D+00 frac ecc
                                0.980000000000000D+00 frac inc
                                0.980000000000000D+00 frac lan
                                0.980000000000000D+00 frac ap
                                0.980000000000000D+00 frac ma

-----
Satellite Number :      6

Actual State:
Keplerian Elements:            0.104722000000000D+05 km sma
                                0.326620000000000D+00 ecc
                                0.116839580840000D+03 deg inc
                                0.099421244950000D+03 deg lan
                                0.270052420490000D+03 deg ap
                                0.000000000000000D+03 deg ma

CD:      2.20000000 Rho One:      0.00000000
S/C Mass: 700.00000000 S/C Area: 0.00002500
Integrator Step: 43200.00000000

Retro:      1 Atmos Mdl:  1 Potent Mdl:  4
Nmax:      21 Mmax:      21 Izonal:      1 IJ2J2:  1
Nmaxrs:    21 Mmaxrs:    21 Ithird:      1
Ind Drg:    1 Iszak:     2 Ind Sol:     1

Reference State:
Keplerian Elements:            0.104722000000000D+05 km sma
                                0.326620000000000D+00 ecc
                                0.116839580840000D+03 deg inc
                                0.099421244950000D+03 deg lan
                                0.270052420490000D+03 deg ap
                                0.000000000000000D+03 deg ma

Reference Switch :      0 ! (0=DSST, 1=Fixed Rates)
Reference State Rates:
Keplerian Rates:              0.000000000000000D+00 km/sec sma
                                0.000000000000000D+00 1/sec ecc
                                0.000000000000000D+00 deg/sec inc
                                1.140771161000000D-05 deg/sec lan
                                0.000000000000000D+00 deg/sec ap
                                3.333811414000000D-02 deg/sec ma

CD:      2.20000000 Rho One:      0.00000000
S/C Mass: 700.00000000 S/C Area: 0.00002500
Integrator Step: 43200.00000000

Retro:      1 Atmos Mdl:  1 Potent Mdl:  4
Nmax:      21 Mmax:      0 Izonal:      1 IJ2J2:  1
Nmaxrs:    2 Mmaxrs:    2 Ithird:      1

```

```

Ind Drg:      2 Iszak:      2 Ind Sol:      2
-----
...
*****
Plane          :      3
Sats In This Plane :      7

Maximum Parameter Limits:      0.000000000000000D+00      km      sma
Keplerian Elements:      0.000000000000000D+00      ecc
      0.000000000000000D+03      deg      inc
      0.000000000000000D+03      deg      lan
      0.000000000000000D+03      deg      ap
      0.000000000000000D+03      deg      ma

Scale (outer limits) : 0.98
Deadband Parameter Limits:      0.000000000000000D+00      km      sma
Keplerian Elements:      0.000000000000000D+00      ecc
      0.000000000000000D+03      deg      inc
      0.000000000000000D+03      deg      lan
      0.000000000000000D+03      deg      ap
      0.000000000000000D+03      deg      ma

Maximum Overshoot Limits :      0.980000000000000D+00      frac      sma
      0.980000000000000D+00      frac      ecc
      0.980000000000000D+00      frac      inc
      0.980000000000000D+00      frac      lan
      0.980000000000000D+00      frac      ap
      0.980000000000000D+00      frac      ma

-----
Satellite Number      :      11

Actual State:
Keplerian Elements:      0.144401370000000D+05      km      sma
      0.000010000000000D+00      ecc
      0.000261802660000D+03      deg      inc
      0.089103788040000D+03      deg      lan
      0.000293894490000D+03      deg      ap
      0.000000000000000D+03      deg      ma

CD:      2.20000000 Rho One:      0.00000000
S/C Mass:      700.00000000 S/C Area:      0.00002500
Integrator Step: 43200.00000000

Retro:      1 Atmos Mdl:      1 Potent Mdl:      4
Nmax:      21 Mmax:      21 Izonal:      1 IJ2J2:      1
Nmaxrs:      21 Mmaxrs:      21 Ithird:      1
Ind Drg:      1 Iszak:      2 Ind Sol:      1

Reference State:
Keplerian Elements:      0.144401370000000D+05      km      sma
      0.000010000000000D+00      ecc
      0.000261802660000D+03      deg      inc
      0.089103788040000D+03      deg      lan
      0.000293894490000D+03      deg      ap
      0.000000000000000D+03      deg      ma

Reference Switch      :      0      ! (0=DSST, 1=Fixed Rates)
Reference State Rates:
Keplerian Rates:      0.000000000000000D+00      km/sec      sma
      0.000000000000000D+00      1/sec      ecc
      0.000000000000000D+00      deg/sec      inc
      1.140771161000000D-05      deg/sec      lan
      0.000000000000000D+00      deg/sec      ap
      3.333811414000000D-02      deg/sec      ma

CD:      2.20000000 Rho One:      0.00000000
S/C Mass:      700.00000000 S/C Area:      0.00002500
Integrator Step: 43200.00000000

Retro:      1 Atmos Mdl:      1 Potent Mdl:      4
Nmax:      21 Mmax:      21 Izonal:      1 IJ2J2:      1
Nmaxrs:      21 Mmaxrs:      21 Ithird:      3
Ind Drg:      2 Iszak:      2 Ind Sol:      2
-----
...

```

D.1.2 Coverage Plots (Sim 3 / Run 1)

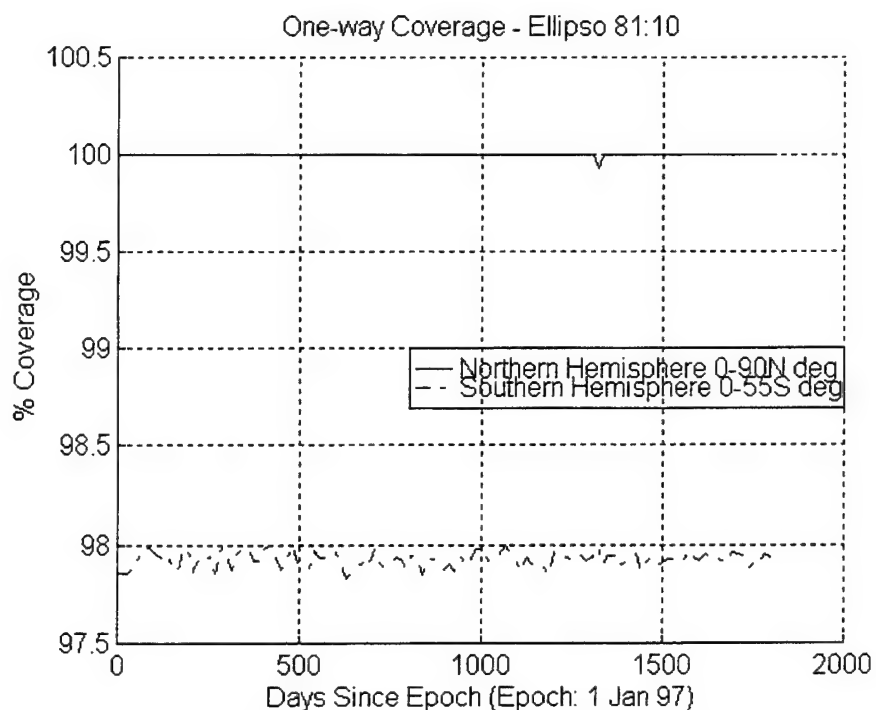


Figure D.1: 5-5-7 Ellipso One-Way Coverage
(Uncontrolled Borealis 81:10 Noon/Midnight and Concordia)

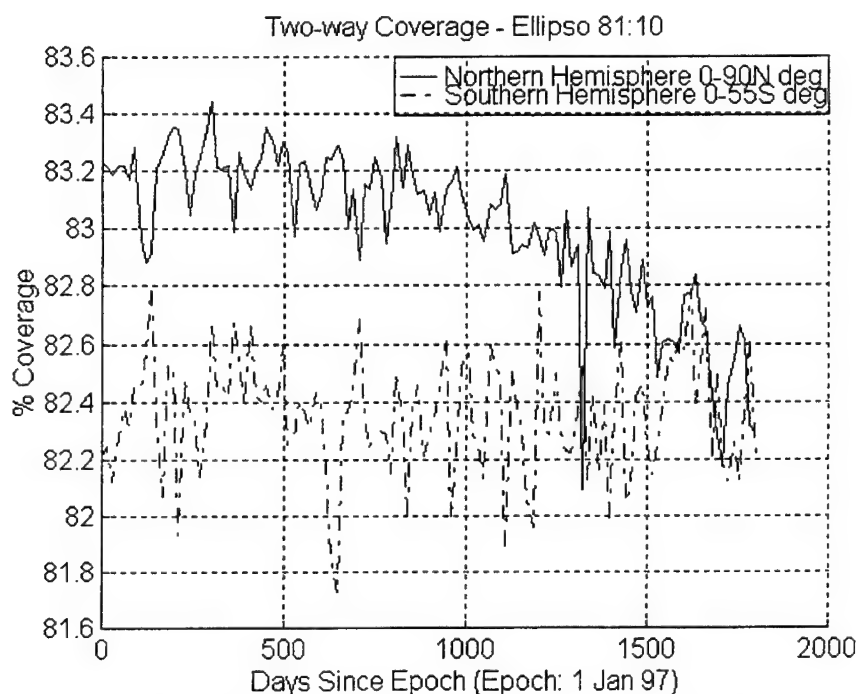


Figure D.2: 5-5-7 Ellipso Two-Way Coverage
(Uncontrolled Borealis 81:10 Noon/Midnight and Concordia)

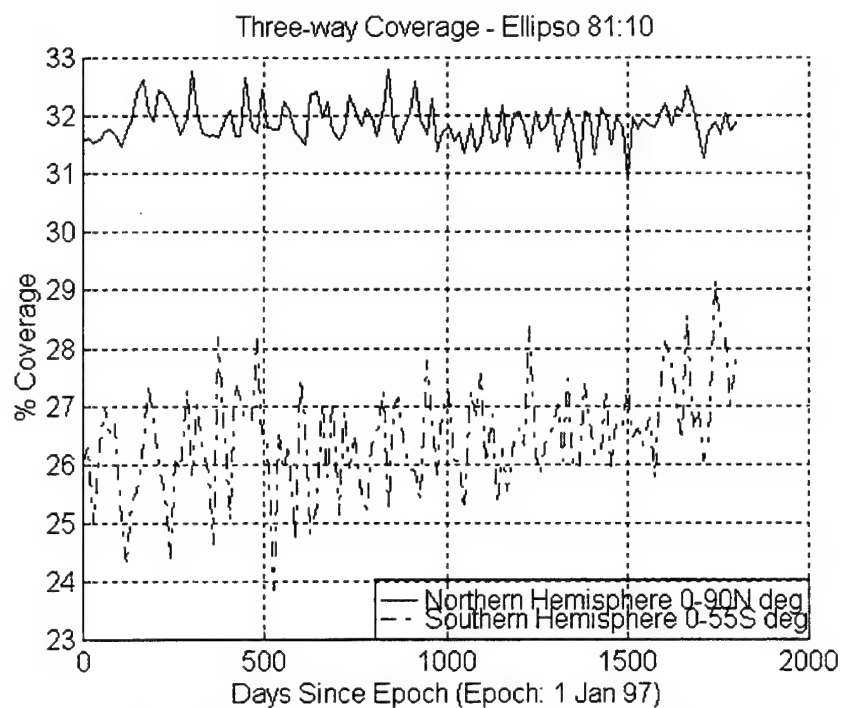


Figure D.3: 5-5-7 Ellipso Three-Way Coverage
(Uncontrolled Borealis 81:10 Noon/Midnight and Concordia)

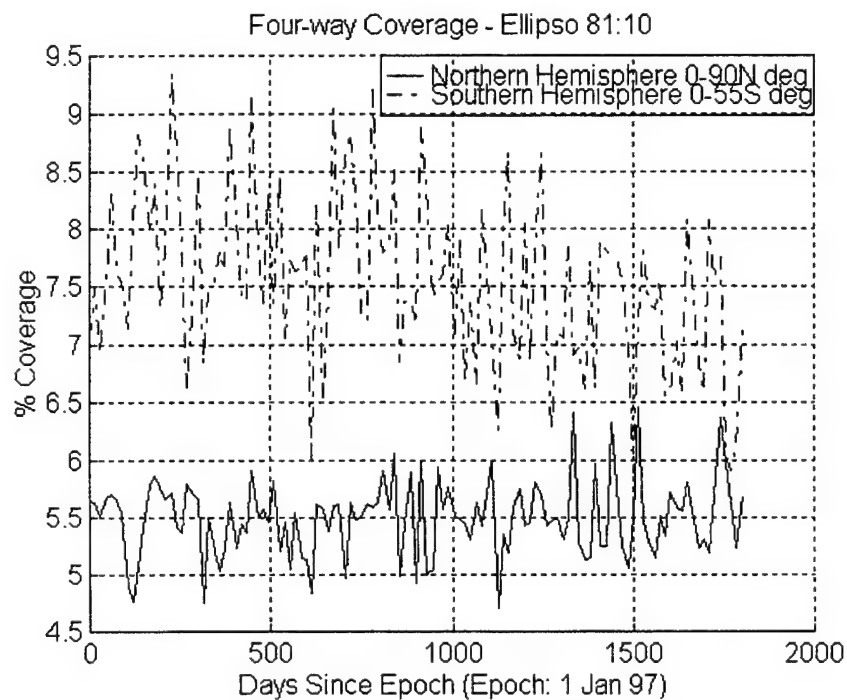


Figure D.4: 5-5-7 Ellipso Four-Way Coverage
(Uncontrolled Borealis 81:10 Noon/Midnight and Concordia)

D.1.3 Uncontrolled Concordia Orbital Element Difference Plots

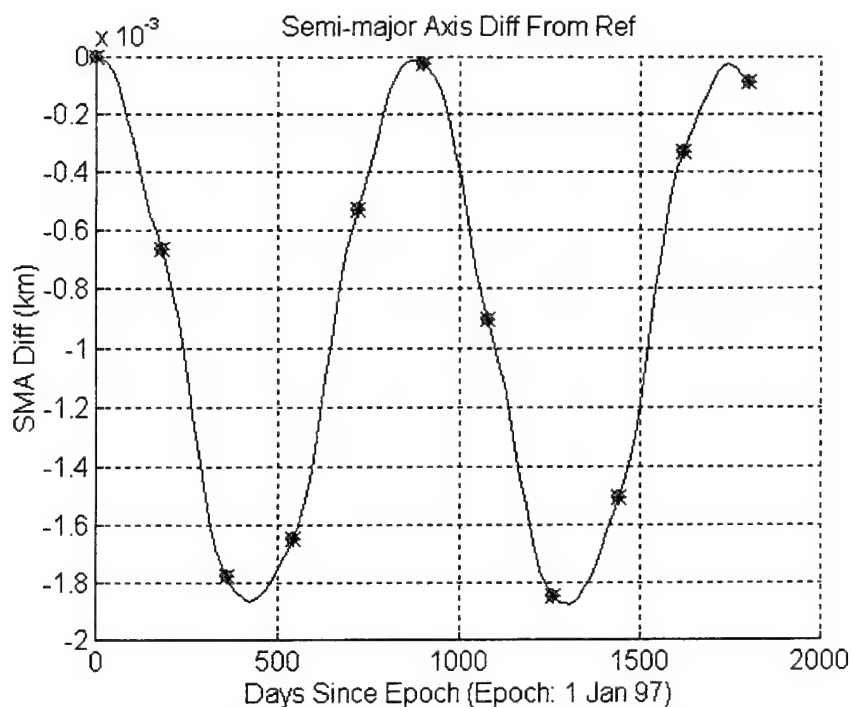


Figure D.5: Semi-major Axis Difference From Nominal Trajectory (Uncontrolled 7 Concordia)

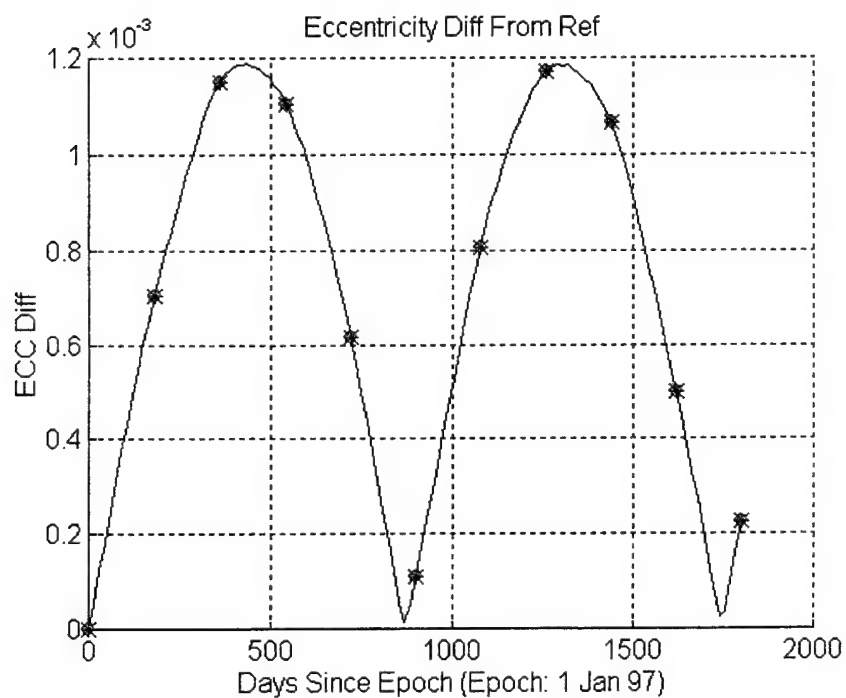


Figure D.6: Eccentricity Difference From Nominal Trajectory (Uncontrolled 7 Concordia)

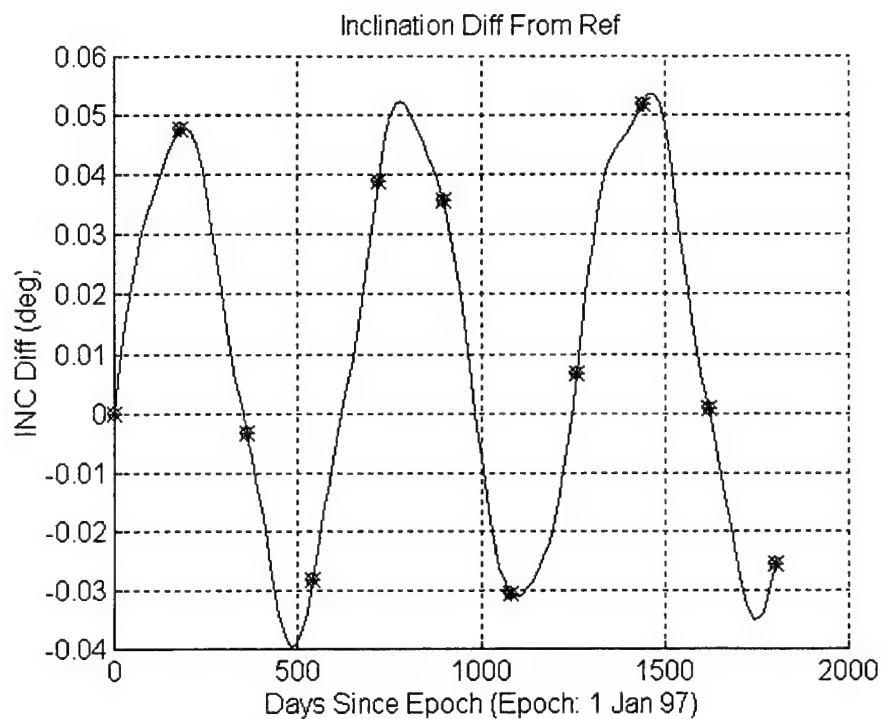


Figure D.7: Inclination Difference From Nominal Trajectory
(Uncontrolled 7 Concordia)

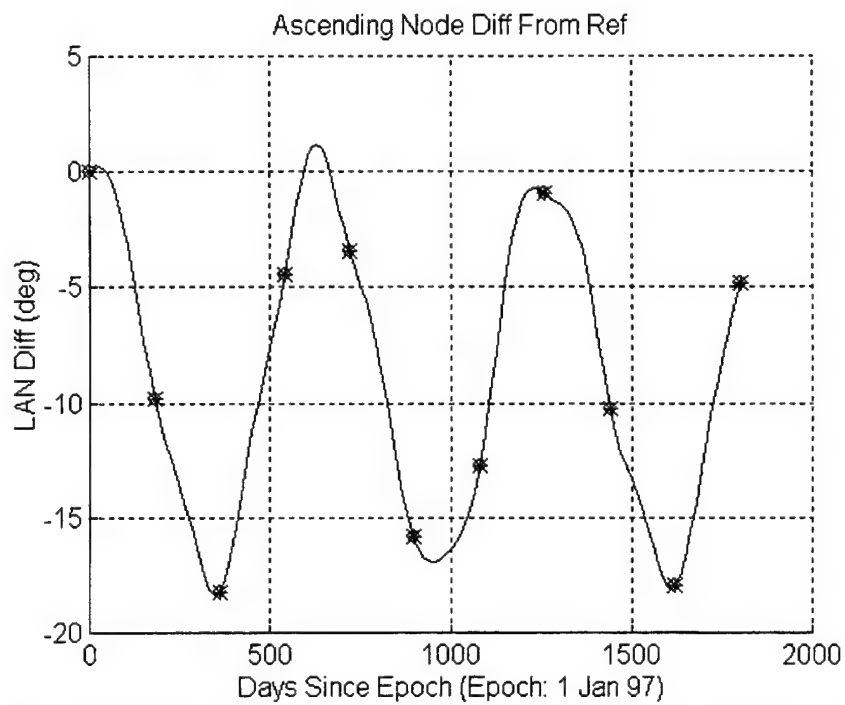


Figure D.8: Ascending Node Difference From Nominal Trajectory
(Uncontrolled 7 Concordia)

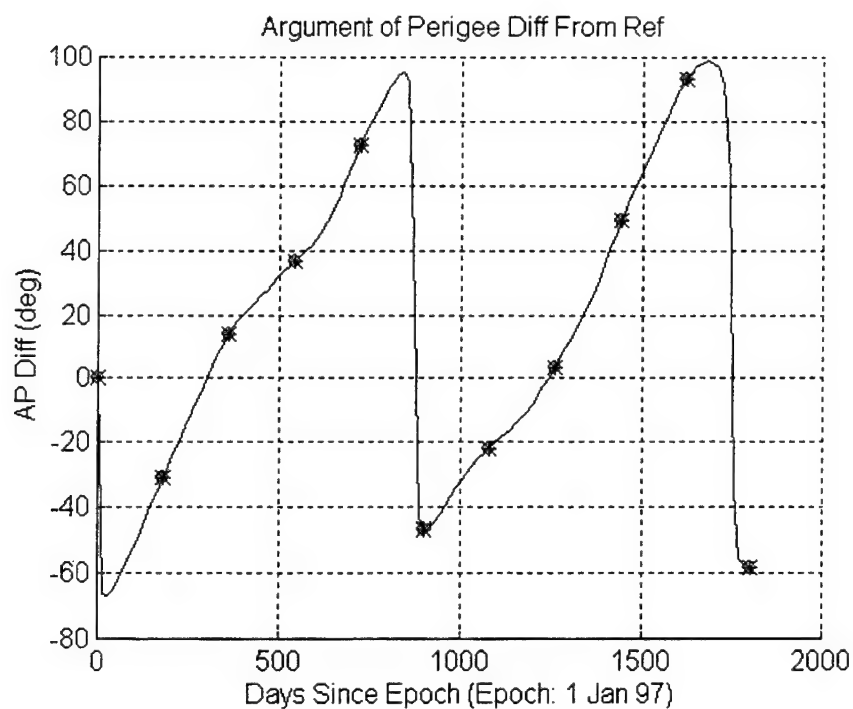


Figure D.9: Argument of Perigee Difference From Nominal Trajectory
(Uncontrolled 7 Concordia)

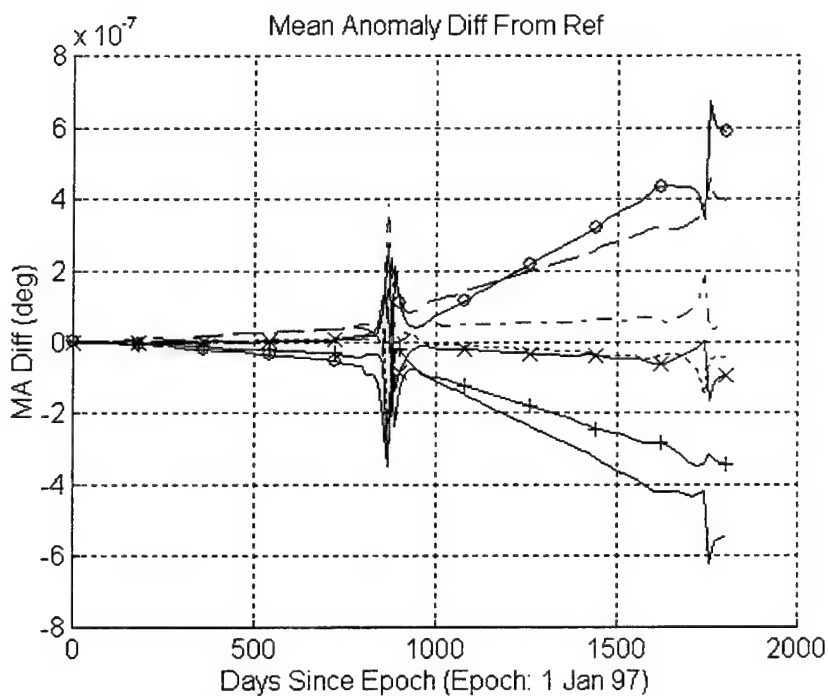


Figure D.10: Mean Anomaly Difference From Nominal Trajectory
(Uncontrolled 7 Concordia)

D.1.4 Uncontrolled Borealis 81:10 Node at Noon Element Difference Plots

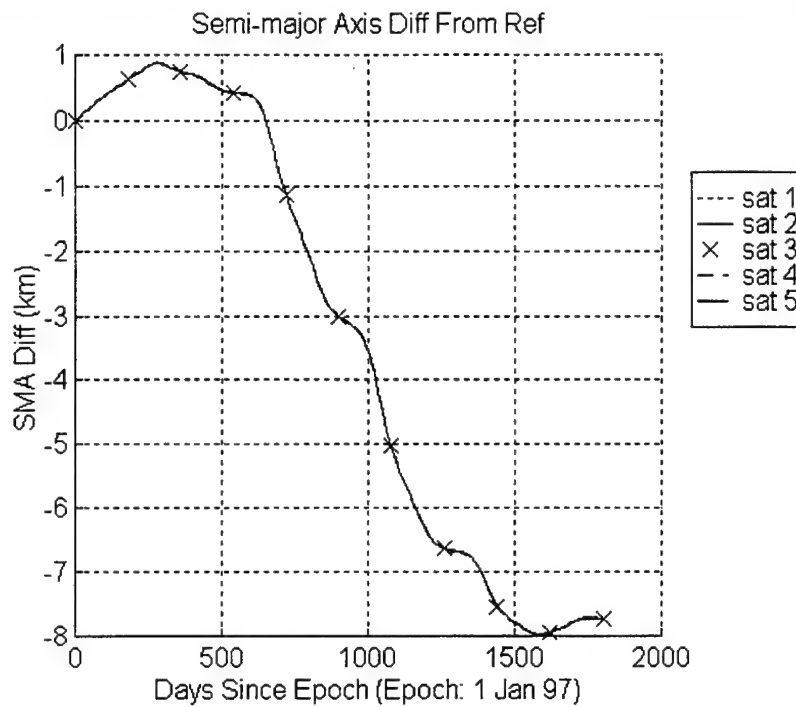


Figure D.11: Semi-major Axis Difference From Nominal Trajectory
(Uncontrolled Borealis 5-5 81:10 Node at Noon)

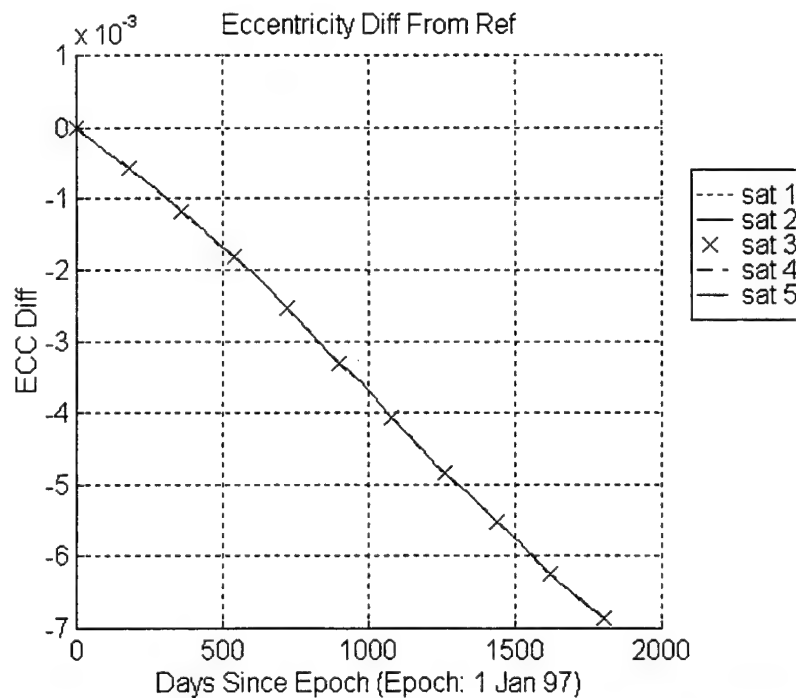


Figure D.12: Eccentricity Difference From Nominal Trajectory
(Uncontrolled Borealis 5-5 81:10 Node at Noon)

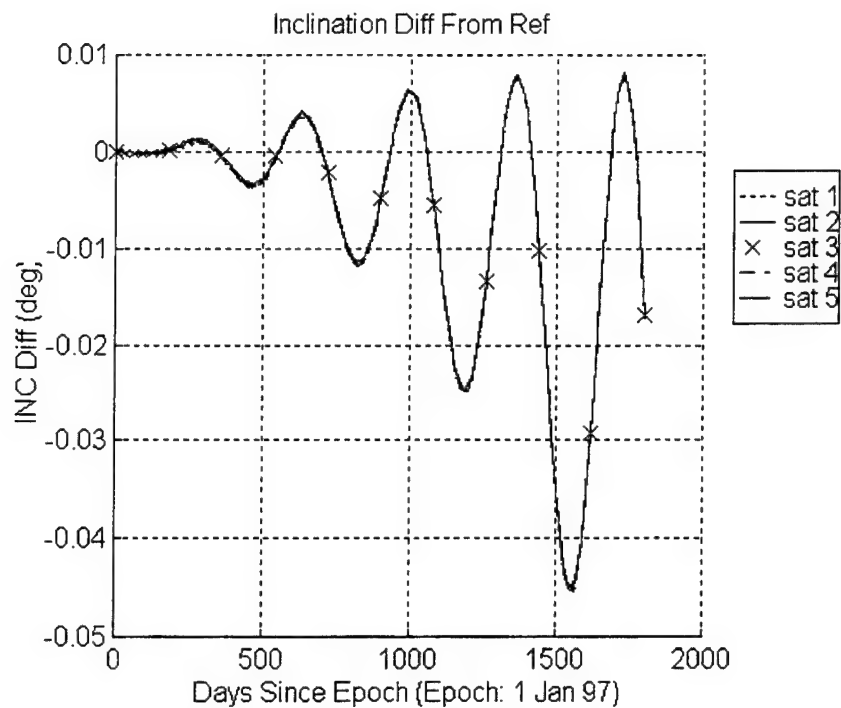


Figure D.13: Inclination Difference From Nominal Trajectory
(Uncontrolled Borealis 5-5 81:10 Node at Noon)

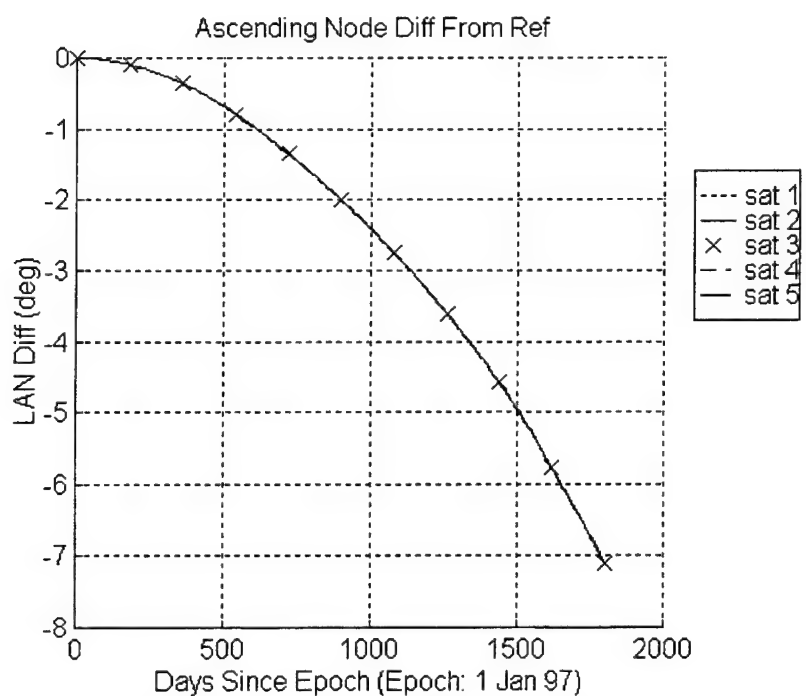


Figure D.14: Ascending Node Difference From Nominal Trajectory
(Uncontrolled Borealis 5-5 81:10 Node at Noon)

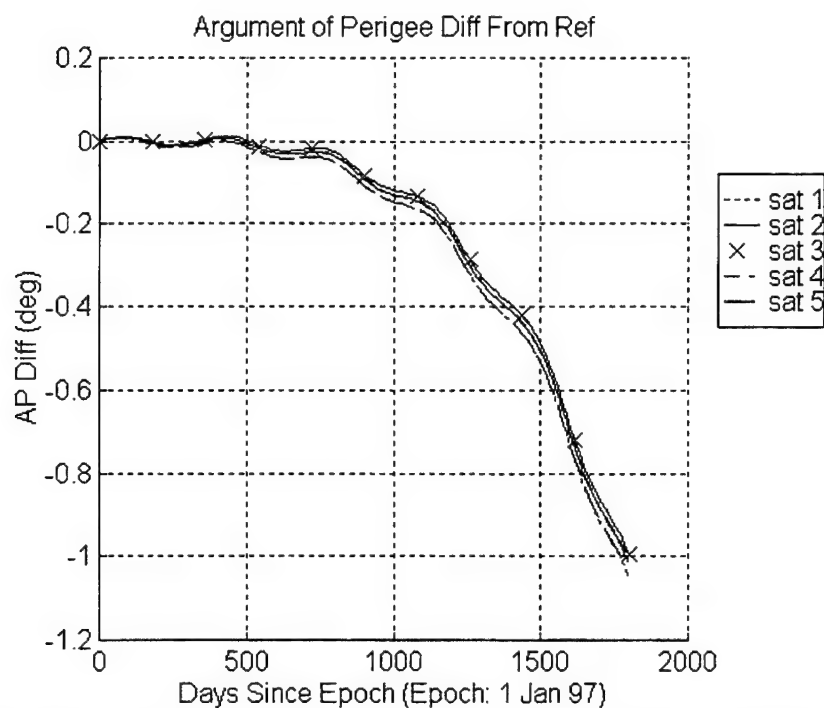


Figure D.15: Argument of Perigee Difference From Nominal Trajectory
(Uncontrolled Borealis 5-5 81:10 Node at Noon)

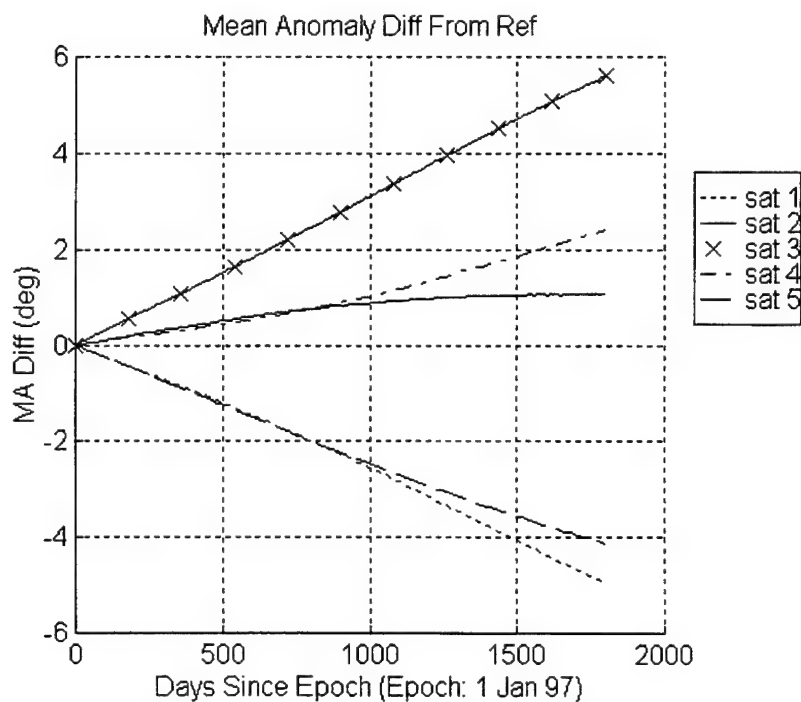


Figure D.16: Mean Anomaly Difference From Nominal Trajectory
(Uncontrolled Borealis 5-5 81:10 Node at Noon)

D.1.5 Uncontrolled Borealis 81:10 Node at Midnight Element Difference Plots

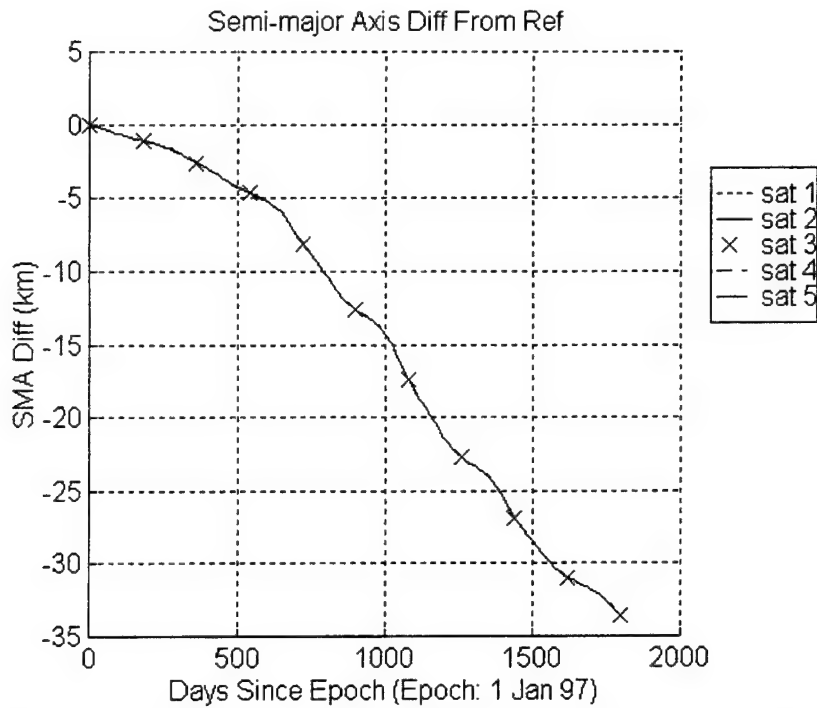


Figure D.17: Semi-major Axis Difference From Nominal Trajectory
(Uncontrolled Borealis 5-5 81:10 Node at Midnight)

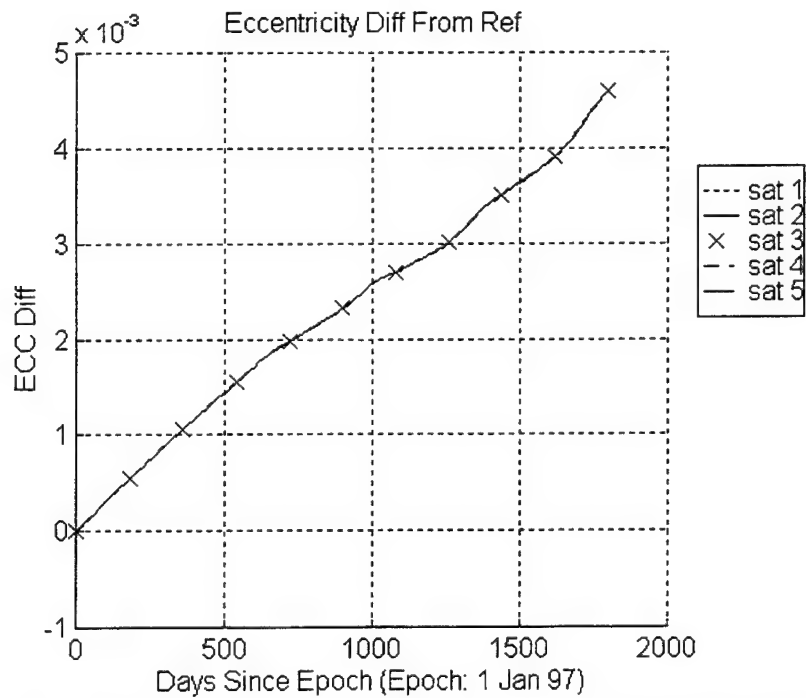


Figure D.18: Eccentricity Difference From Nominal Trajectory
(Uncontrolled Borealis 5-5 81:10 Node at Midnight)

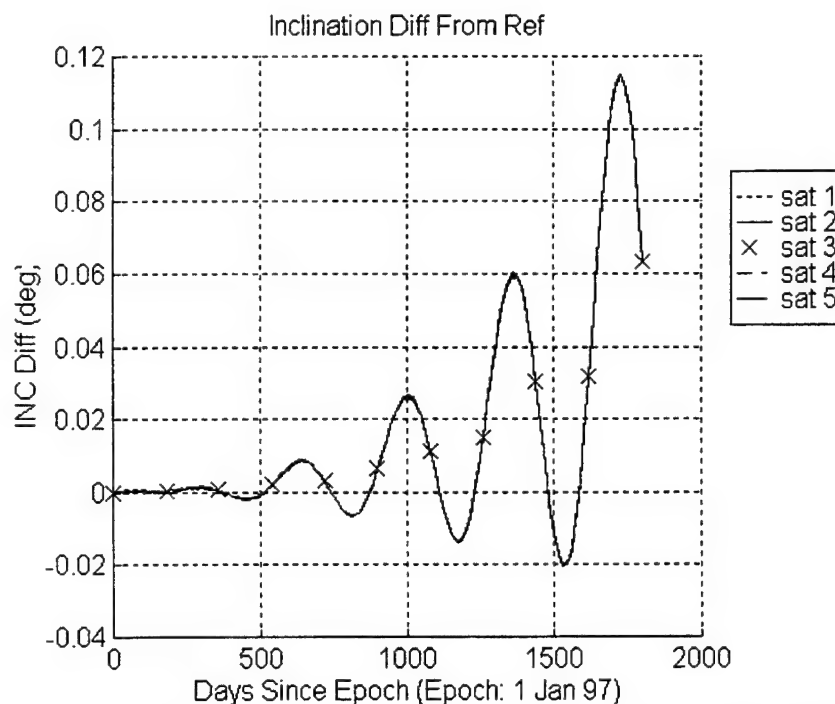


Figure D.19: Inclination Difference From Nominal Trajectory
(Uncontrolled Borealis 5-5 81:10 Node at Midnight)

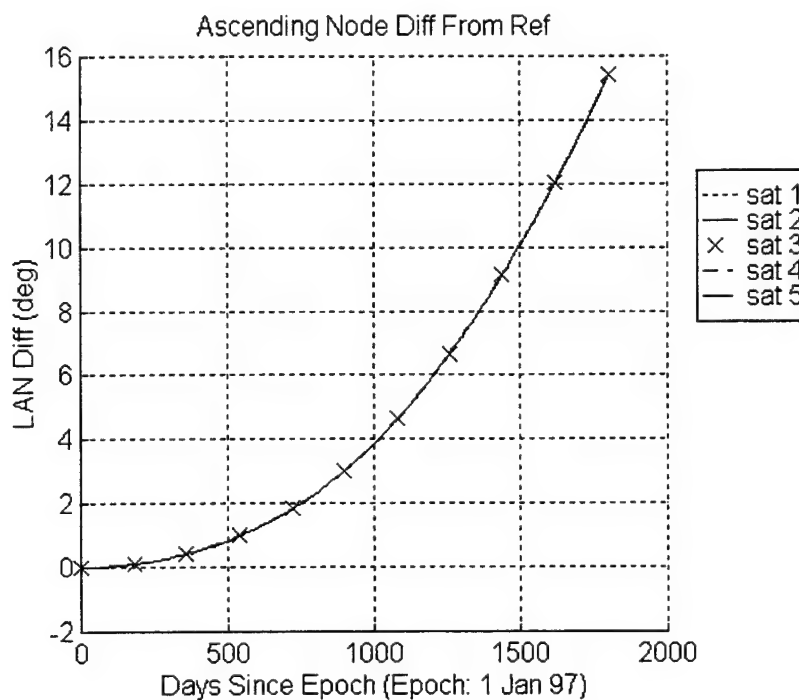


Figure D.20: Ascending Node Difference From Nominal Trajectory
(Uncontrolled Borealis 5-5 81:10 Node at Midnight)

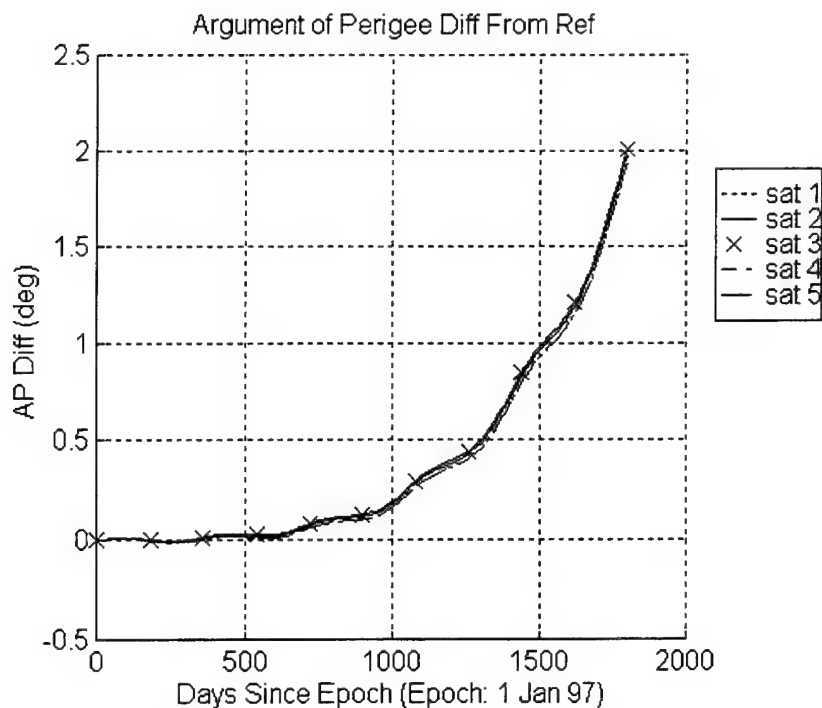


Figure D.21: Argument of Perigee Difference From Nominal Trajectory
(Uncontrolled Borealis 5-5 81:10 Node at Midnight)

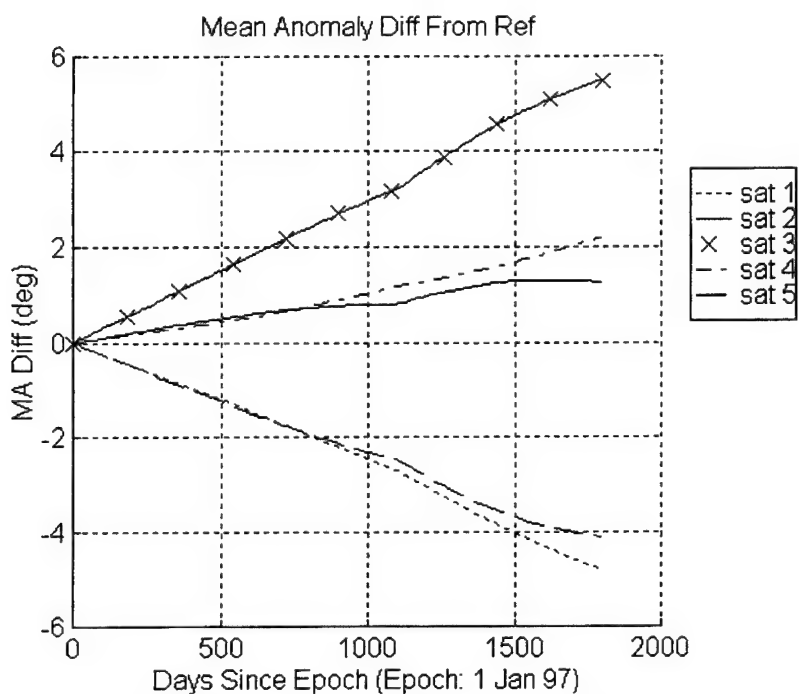


Figure D.22: Mean Anomaly Difference From Nominal Trajectory
(Uncontrolled Borealis 5-5 81:10 Node at Midnight)

D.2 Sim 3 / Run 2

This run is a 5 year uncontrolled execution of the ASKS on the 4-4 satellite 81:10 node at noon/midnight configuration of the Borealis planes and the 6 satellite Concordia plane of the Ellipso constellation. There are 4 satellites in each of the Borealis planes and 6 satellites in the Concordia plane. Relative mean anomaly (formation) station-keeping is used with targeting method 0. Method 0 indicates that all control related components of the input deck are ignored.

The epoch orbital elements for this run are listed in tables 7.1 and 7.4. The nominal (reference) trajectory is propagated in the presence of zonal harmonics through degree 21, and solar/lunar point masses. The actual satellite trajectory is propagated with the perturbations of the nominal trajectory plus solar radiation pressure, tesseral resonance and atmospheric drag.

An input deck is not provided for this run since the only difference between it and the input deck for run 1 seen in section D.1.1 is the number of satellites in the plane, and their initial spacing. Sections D.2.1 contains the one, two, three and four-way coverage of the constellation over the 5 year time span. Note that coverage is provided for the entire northern hemisphere and for the southern hemisphere above 55°S latitude. The northern hemispheric coverage assumes a 25° minimum elevation angle. The southern hemispheric coverage assumes a 10° minimum elevation angle. Since the Concordia plane does not experience tesseral resonance, the 6 satellites in the plane for this configuration have the same orbital element plots as the 7 satellites of the 5-5-7 configuration of section D.1.3, and thus are not repeated. Sections D.2.2 and D.2.3 contain the orbital element difference plots for the node at noon and node at midnight planes, respectively.

D.2.1 Coverage Plots (Sim 3 / Run 2)

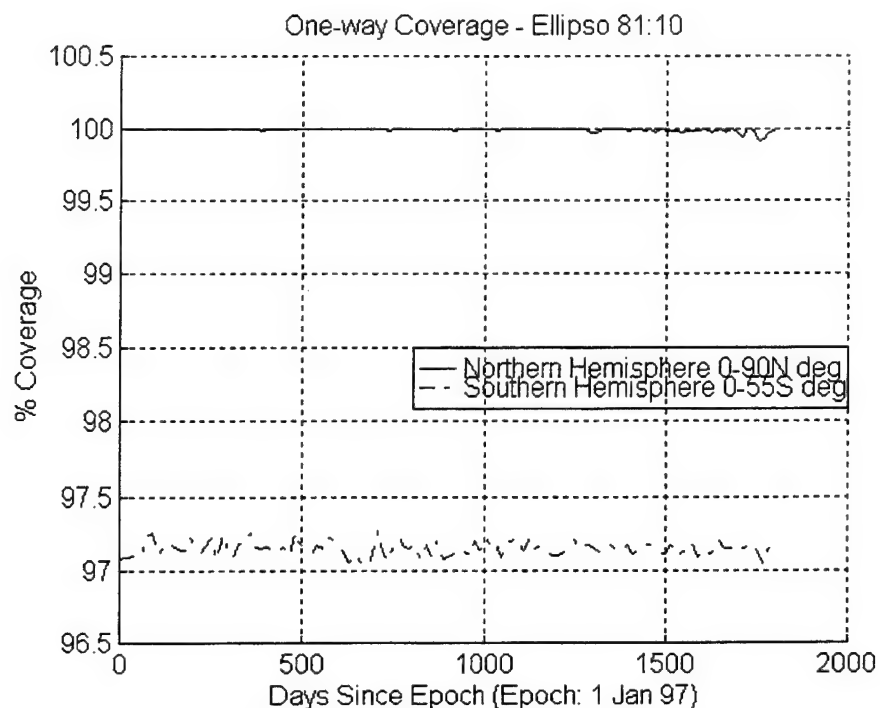


Figure D.23: 4-4-6 Ellipso One-Way Coverage
(Uncontrolled Borealis 81:10 Noon/Midnight and Concordia)

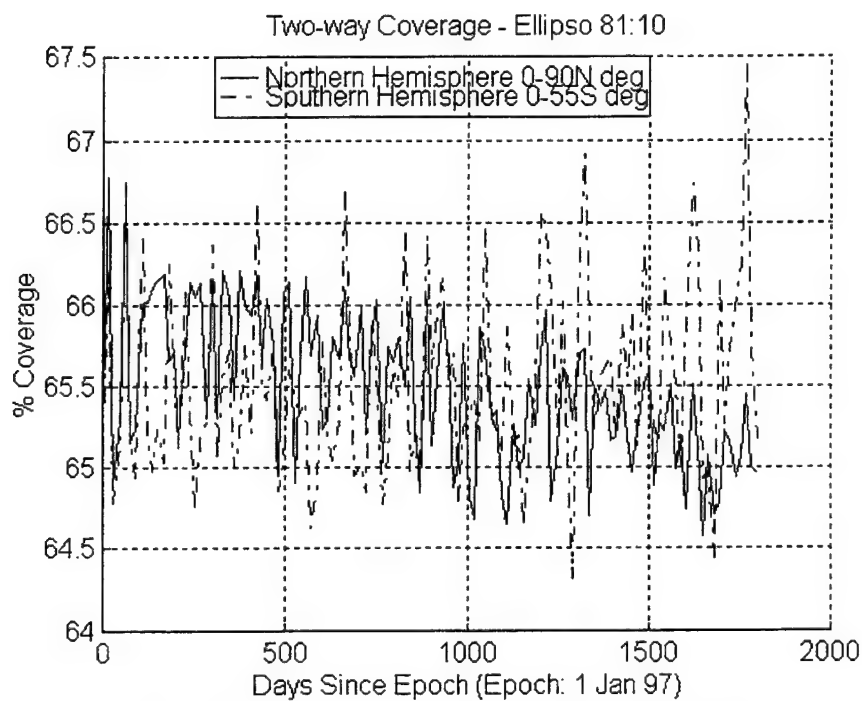


Figure D.24: 4-4-6 Ellipso Two-Way Coverage
(Uncontrolled Borealis 81:10 Noon/Midnight and Concordia)

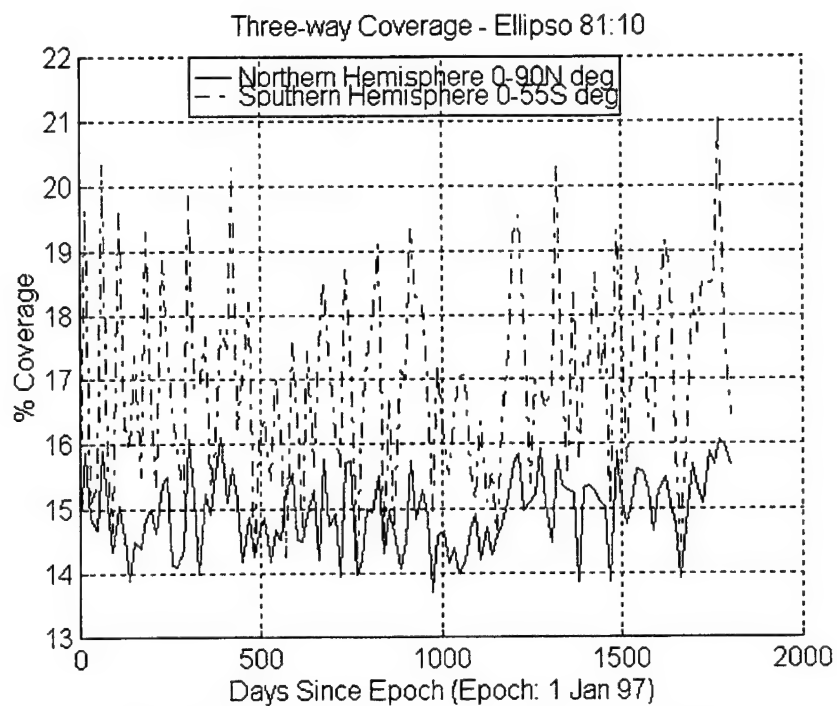


Figure D.25: 4-4-6 Ellipso Three-Way Coverage
(Uncontrolled Borealis 81:10 Noon/Midnight and Concordia)

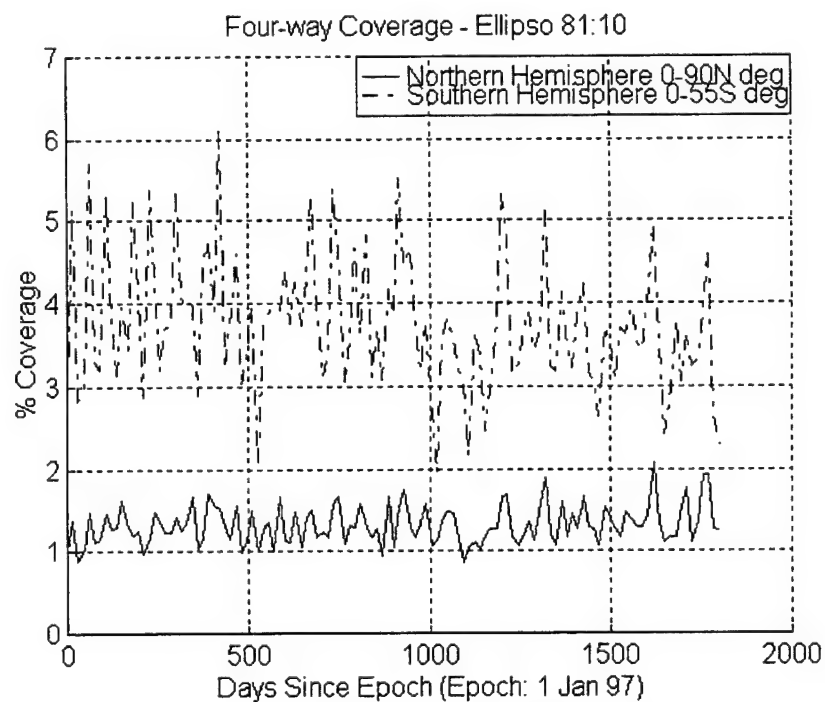


Figure D.26: 4-4-6 Ellipso Four-Way Coverage
(Uncontrolled Borealis 81:10 Noon/Midnight and Concordia)

D.2.2 Uncontrolled Borealis 4-4 81:10 Node at Noon Element Difference Plots

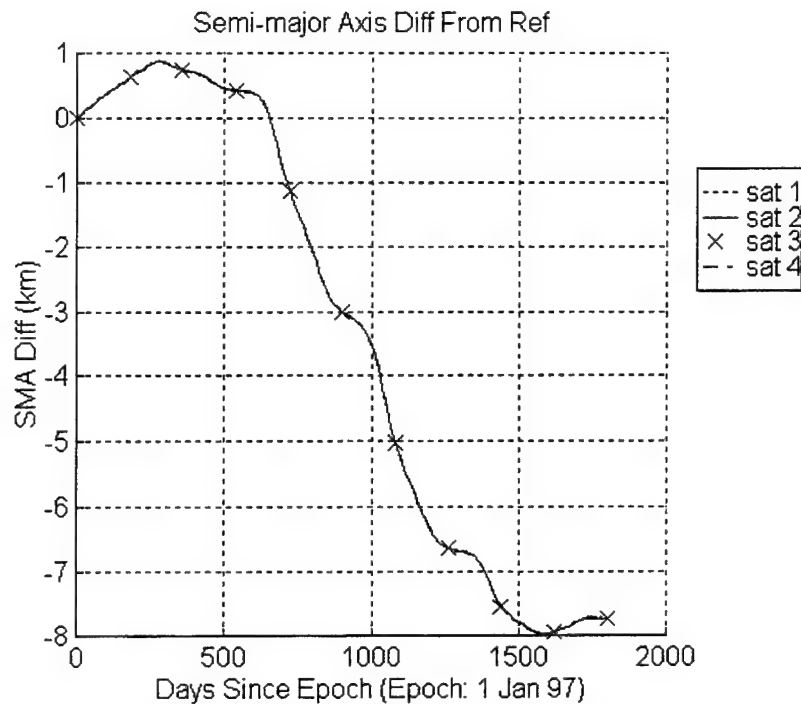


Figure D.27: Semi-major Axis Difference From Nominal Trajectory
(Uncontrolled Borealis 4-4 81:10 Node at Noon)

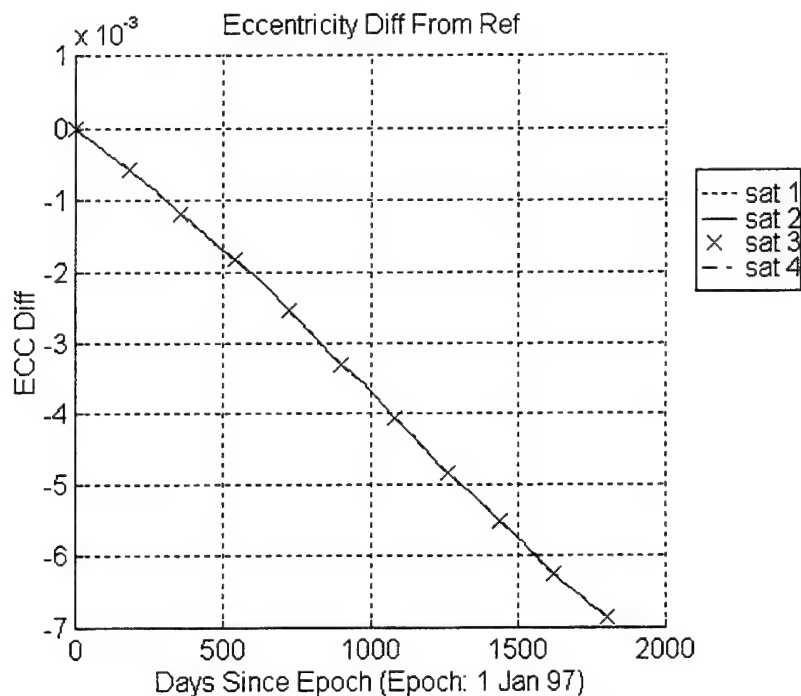


Figure D.28: Eccentricity Difference From Nominal Trajectory
(Uncontrolled Borealis 4-4 81:10 Node at Noon)

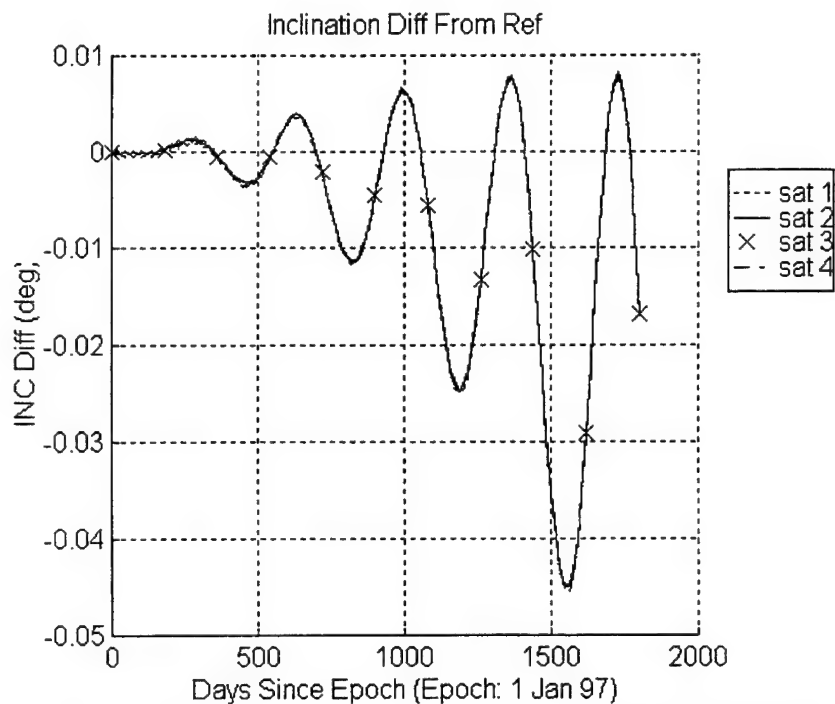


Figure D.29: Inclination Difference From Nominal Trajectory
(Uncontrolled Borealis 4-4 81:10 Node at Noon)

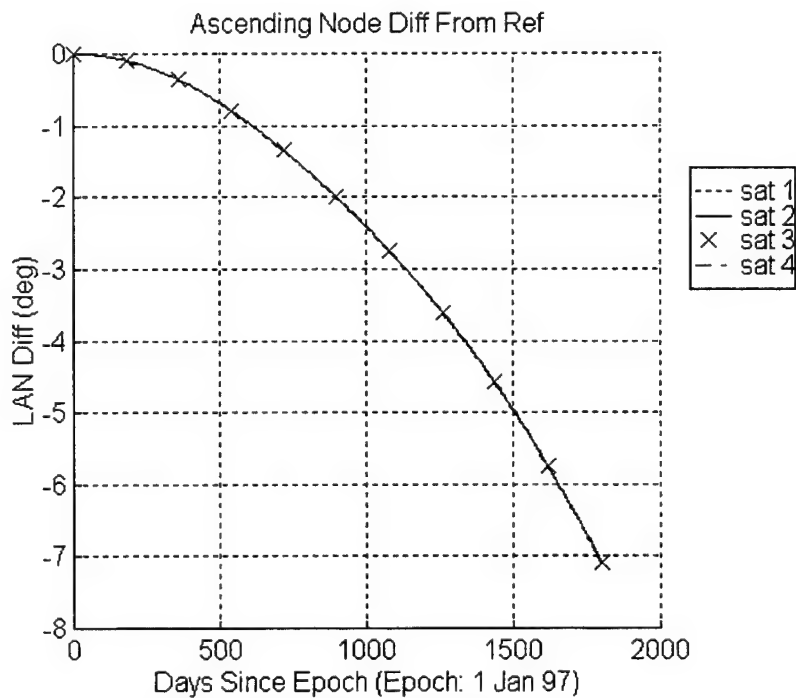


Figure D.30: Ascending Node Difference From Nominal Trajectory
(Uncontrolled Borealis 4-4 81:10 Node at Noon)

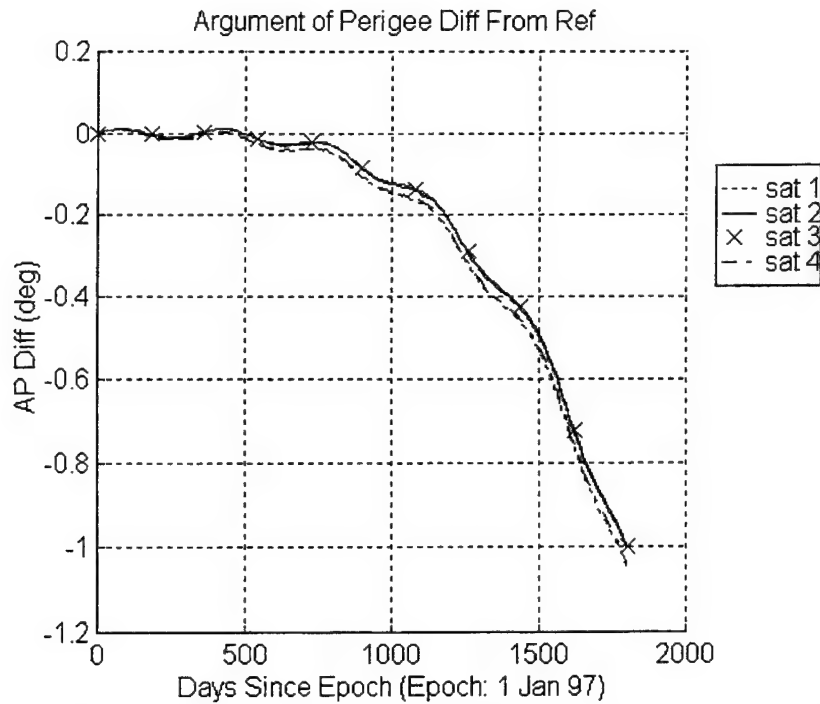


Figure D.31: Argument of Perigee Difference From Nominal Trajectory
(Uncontrolled Borealis 4-4 81:10 Node at Noon)

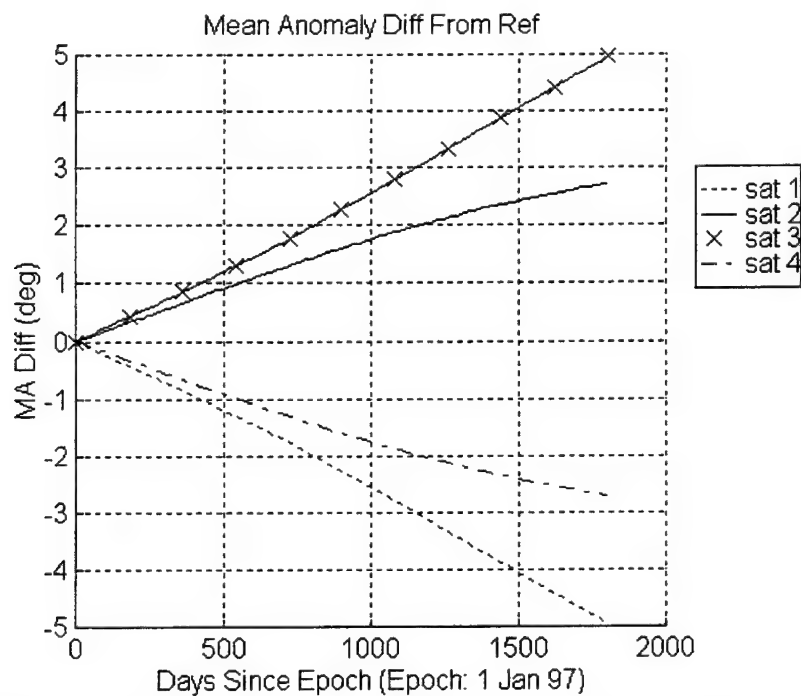


Figure D.32: Mean Anomaly Difference From Nominal Trajectory
(Uncontrolled Borealis 4-4 81:10 Node at Noon)

D.2.3 Uncontrolled Borealis 4-4 81:10 Node at Midnight Element Difference Plots

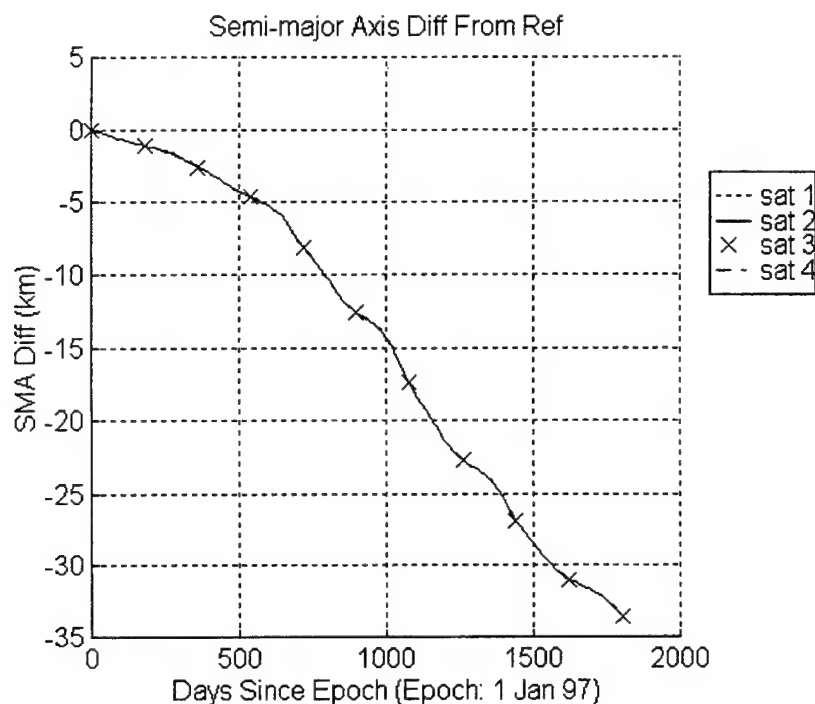


Figure D.33: Semi-major Axis Difference From Nominal Trajectory
(Uncontrolled Borealis 4-4 81:10 Node at Midnight)

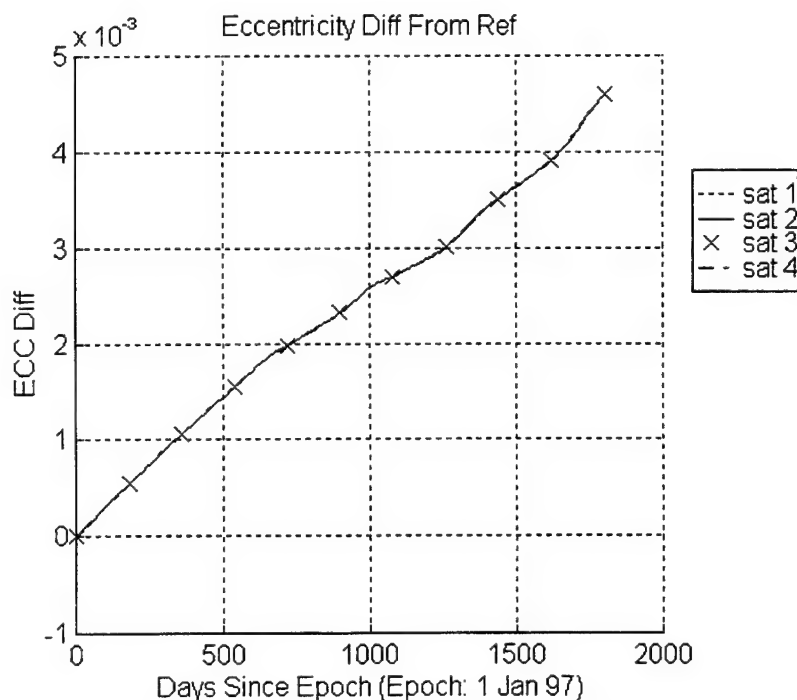


Figure D.34: Eccentricity Difference From Nominal Trajectory
(Uncontrolled Borealis 4-4 81:10 Node at Midnight)

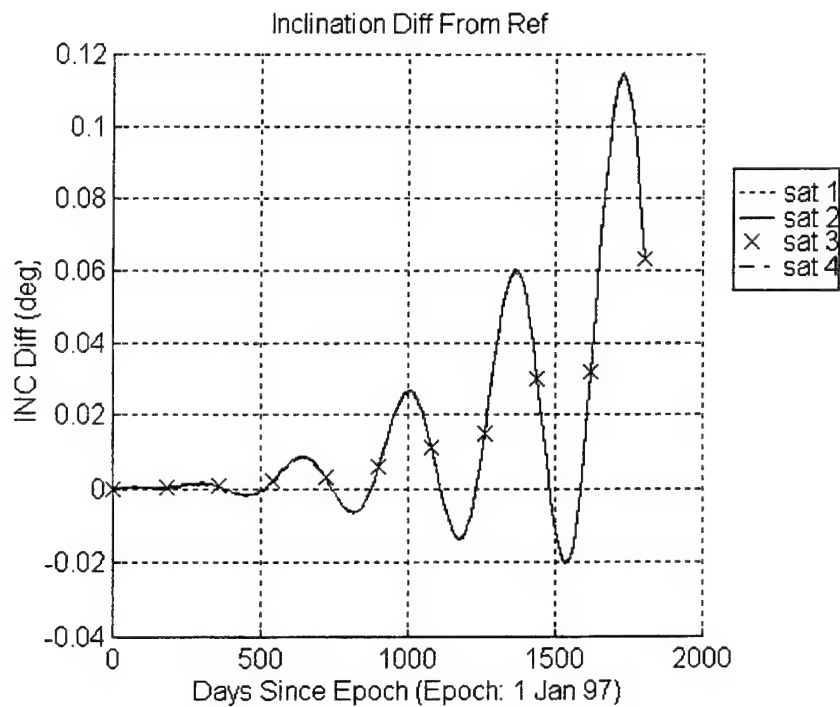


Figure D.35: Inclination Difference From Nominal Trajectory
(Uncontrolled Borealis 4-4 81:10 Node at Midnight)

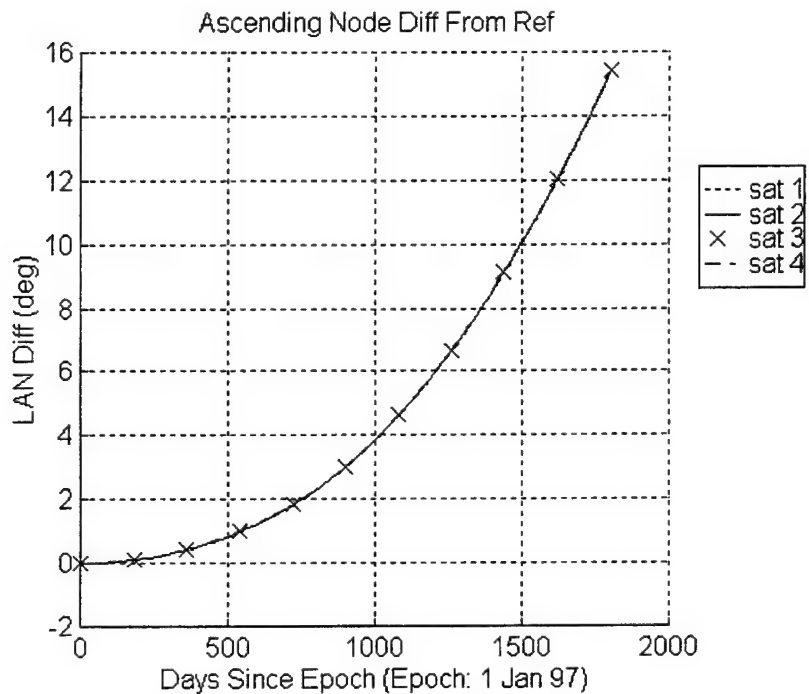


Figure D.36: Ascending Node Difference From Nominal Trajectory
(Uncontrolled Borealis 4-4 81:10 Node at Midnight)

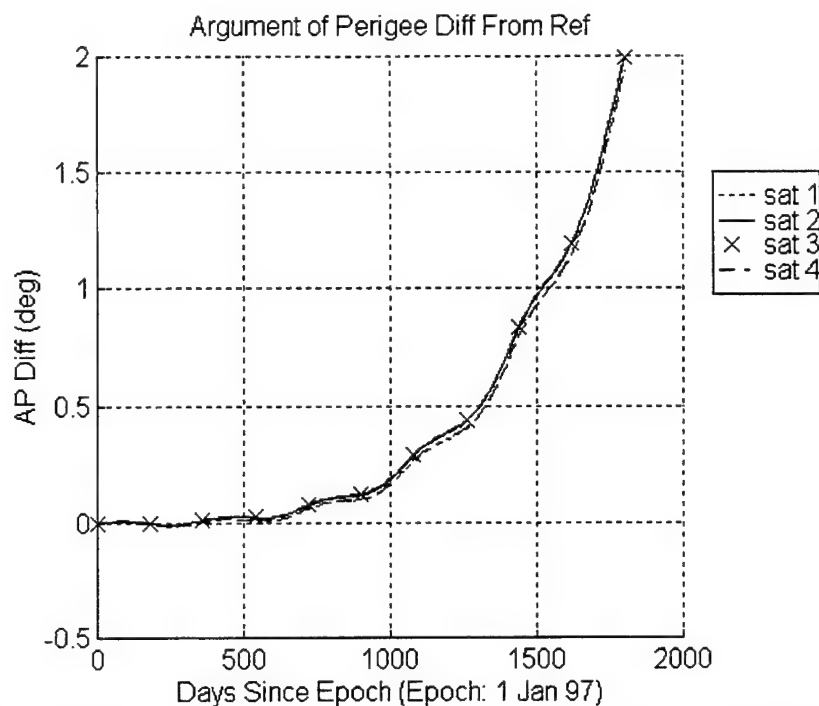


Figure D.37: Argument of Perigee Difference From Nominal Trajectory
(Uncontrolled Borealis 4-4 81:10 Node at Midnight)

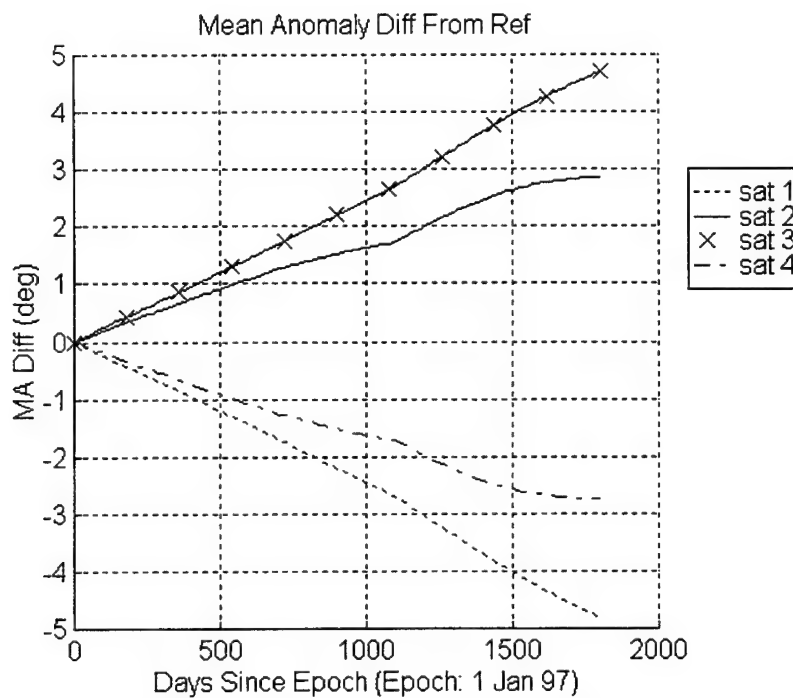


Figure D.38: Mean Anomaly Difference From Nominal Trajectory
(Uncontrolled Borealis 4-4 81:10 Node at Midnight)

D.3 Sim 3 / Run 3

This run is a 5 year uncontrolled execution of the ASKS on the 5-5 satellite 81:10 node at noon/midnight configuration of the Borealis planes, with argument of perigee rotated 10° , and the 7 satellite Concordia plane of the Ellipso constellation. There are 5 satellites in each of the Borealis planes and 7 satellites in the Concordia plane. The argument of perigee is 260° for the Borealis node at noon plane, and 280° for the node at midnight plane. Relative mean anomaly (formation) station-keeping is used with targeting method 0. Method 0 indicates that all control related components of the input deck are ignored.

The epoch orbital elements, with the exception of ω , for this run are listed in tables 7.1 and 7.4. The nominal (reference) trajectory is propagated in the presence of zonal harmonics through degree 21, and solar/lunar point masses. The actual satellite trajectory is propagated with the perturbations of the nominal trajectory plus solar radiation pressure, tesseral resonance and atmospheric drag.

The input deck for this run differs from the one shown in section D.1.1 only in the argument of perigee values of the satellites in the Borealis planes. Sections D.3.1 contains the one, two, three and four-way coverage of the constellation over the 5 year time span. Note that coverage is provided for the entire northern hemisphere and for the southern hemisphere above 55°S latitude. The northern hemispheric coverage assumes a 25° minimum elevation angle. The southern hemispheric coverage assumes a 10° minimum elevation angle. The Concordia element difference plots are the same as shown in section D.1.3. Sections D.3.2 and D.3.3 contain the orbital element difference plots for the node at noon and node at midnight planes, respectively.

D.3.1 Coverage Plots (Sim 3 / Run 3)

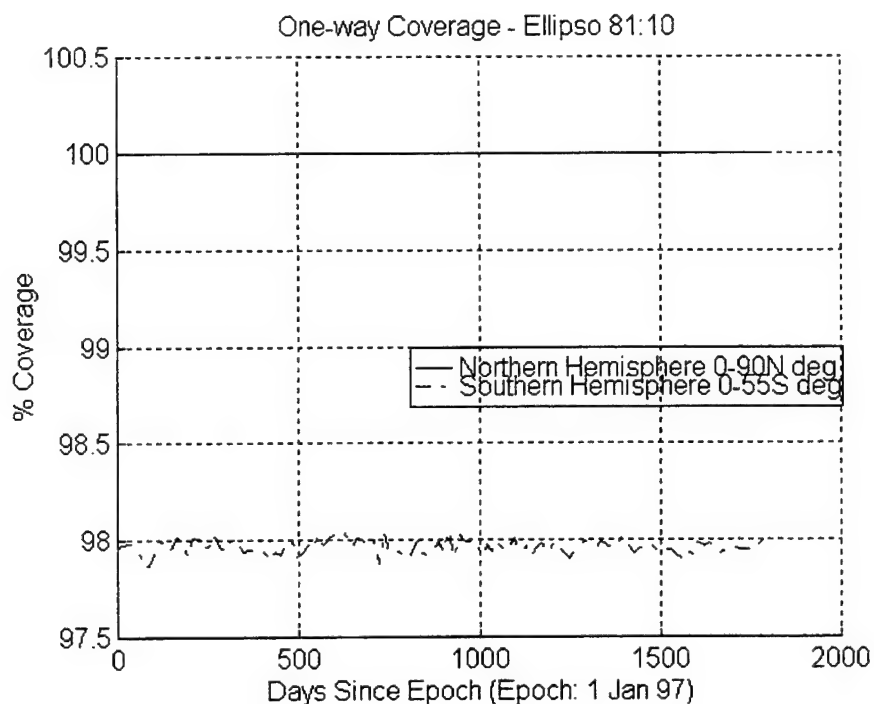


Figure D.39: 5-5-7 10 ω Ellipso One-Way Coverage
(Uncontrolled Borealis 81:10 Noon/Midnight and Concordia)

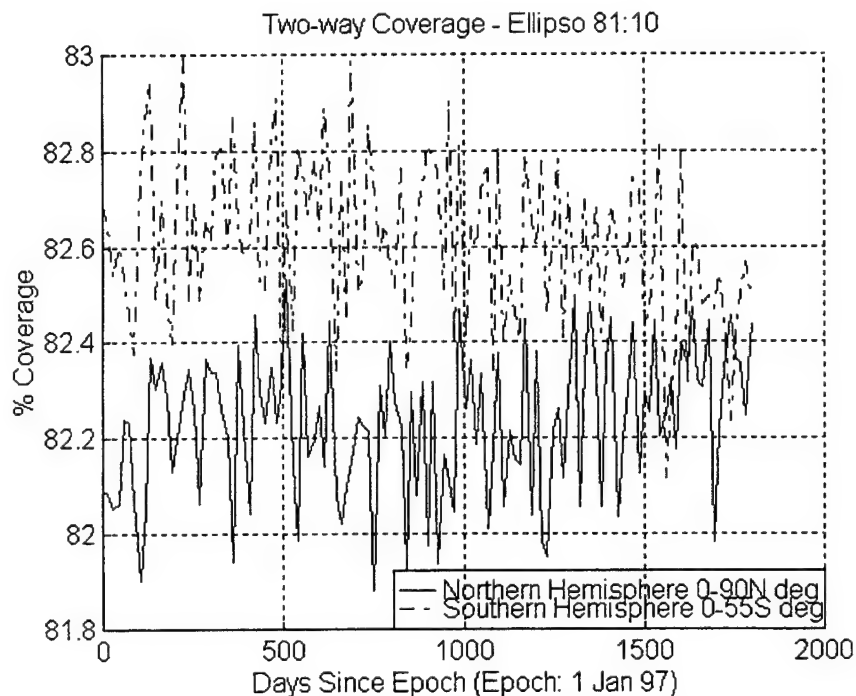


Figure D.40: 5-5-7 10 ω Ellipso Two-Way Coverage
(Uncontrolled Borealis 81:10 Noon/Midnight and Concordia)

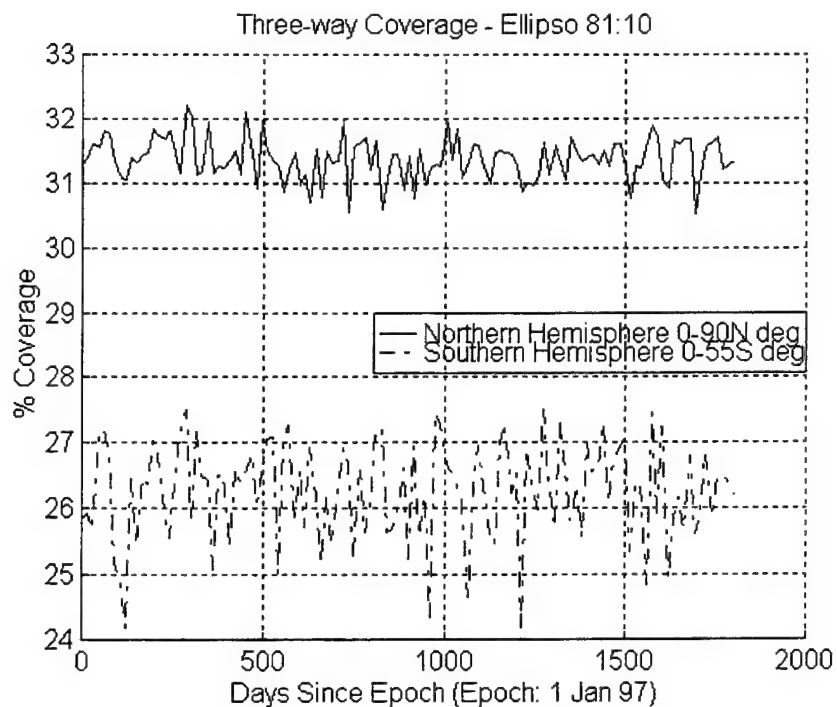


Figure D.41: 5-5-7 10 ω Ellipso Three-Way Coverage
(Uncontrolled Borealis 81:10 Noon/Midnight and Concordia)

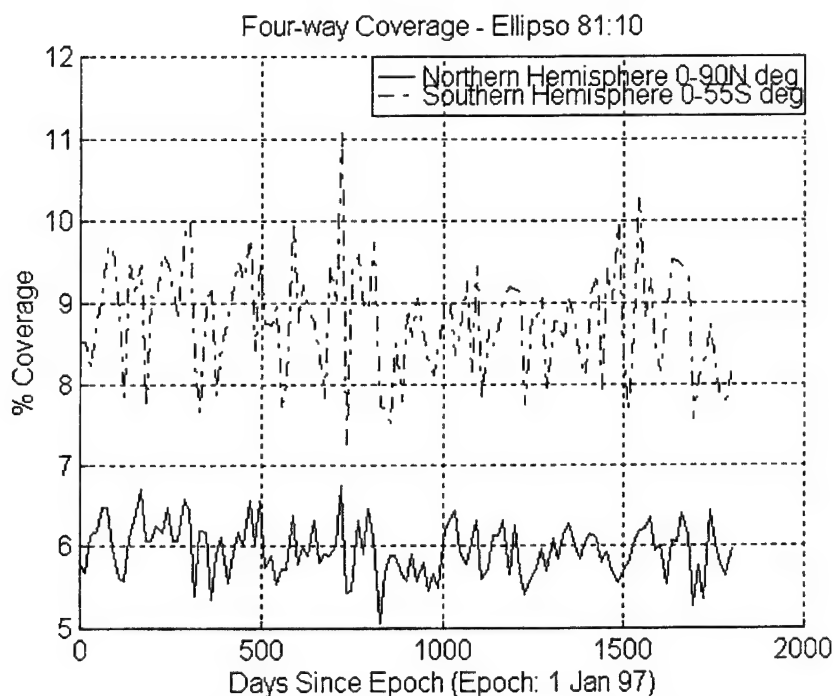


Figure D.42: 5-5-7 10 ω Ellipso Four-Way Coverage
(Uncontrolled Borealis 81:10 Noon/Midnight and Concordia)

D.3.2 Uncontrolled Borealis 5-5 10 ω 81:10 Node at Noon Element Difference Plots

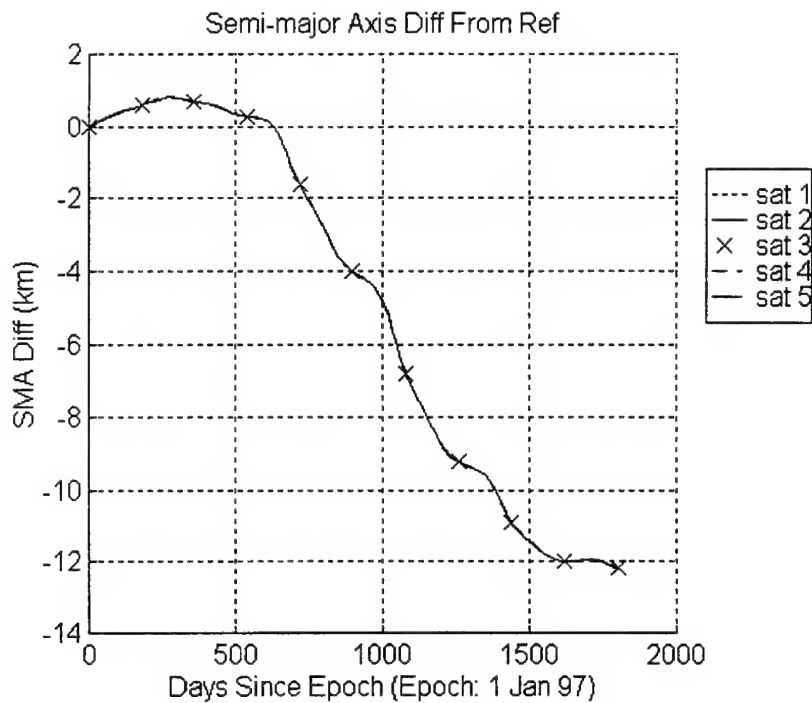


Figure D.43: Semi-major Axis Difference From Nominal Trajectory
(Uncontrolled Borealis 5-5 10 ω 81:10 Node at Noon)

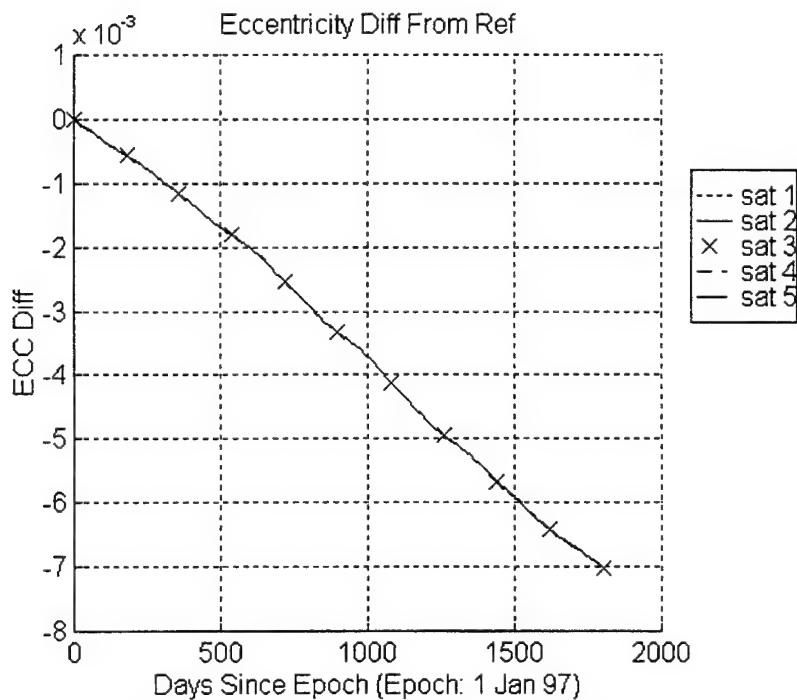


Figure D.44: Eccentricity Difference From Nominal Trajectory
(Uncontrolled Borealis 5-5 10 ω 81:10 Node at Noon)

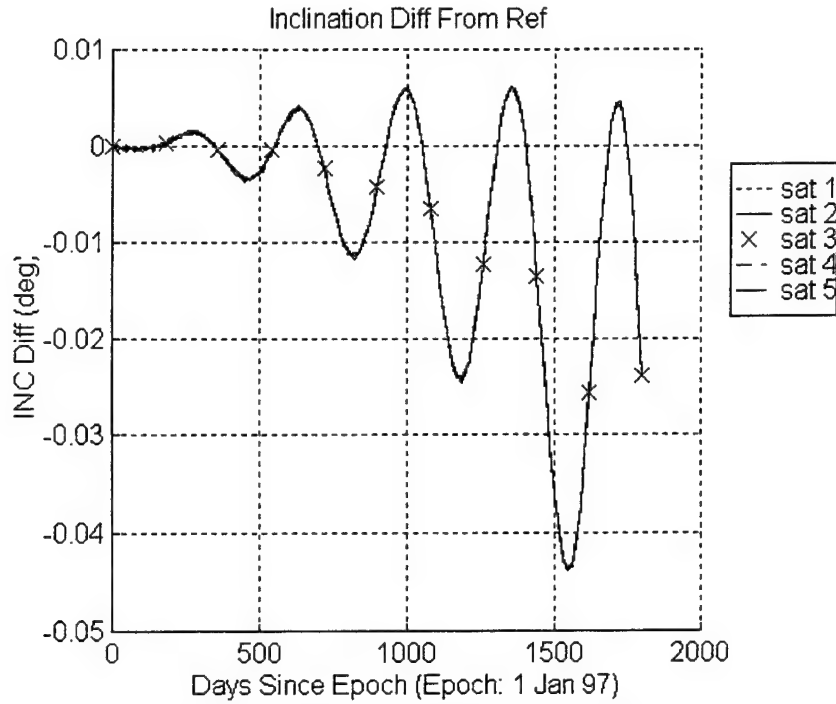


Figure D.45: Inclination Difference From Nominal Trajectory
(Uncontrolled Borealis 5-5 10 ω 81:10 Node at Noon)

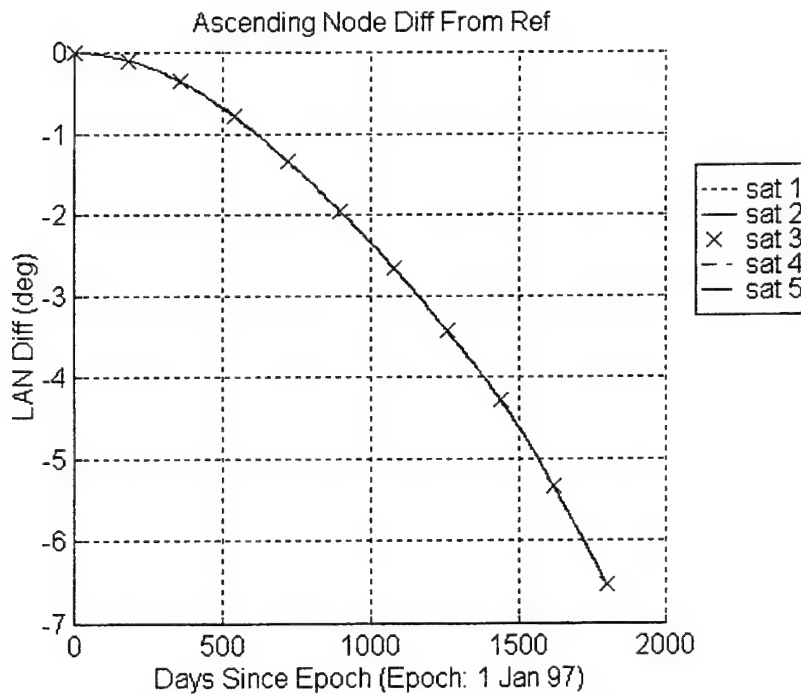


Figure D.46: Ascending Node Difference From Nominal Trajectory
(Uncontrolled Borealis 5-5 10 ω 81:10 Node at Noon)

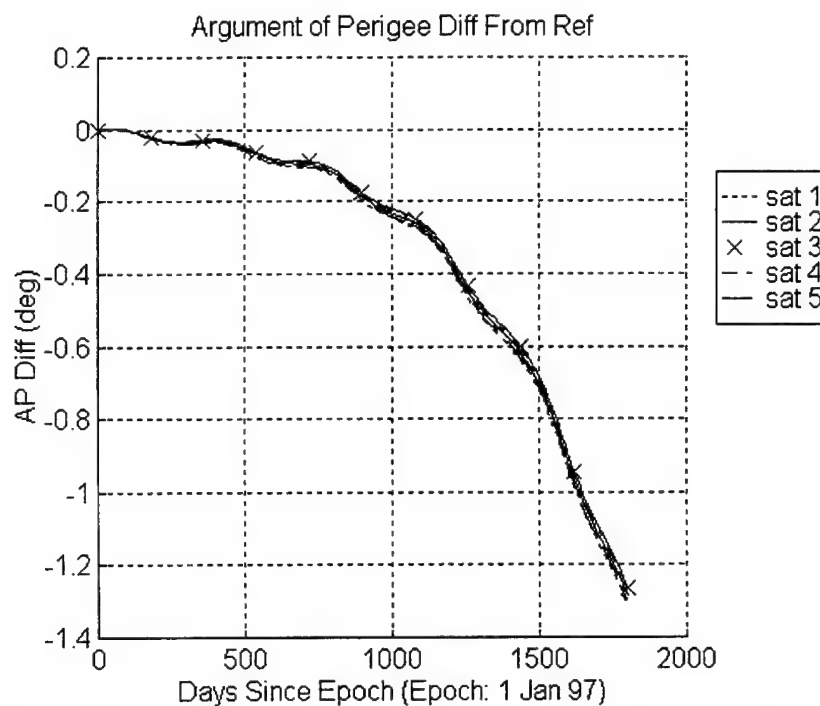


Figure D.47: Argument of Perigee Difference From Nominal Trajectory
(Uncontrolled Borealis 5-5 10ω 81:10 Node at Noon)

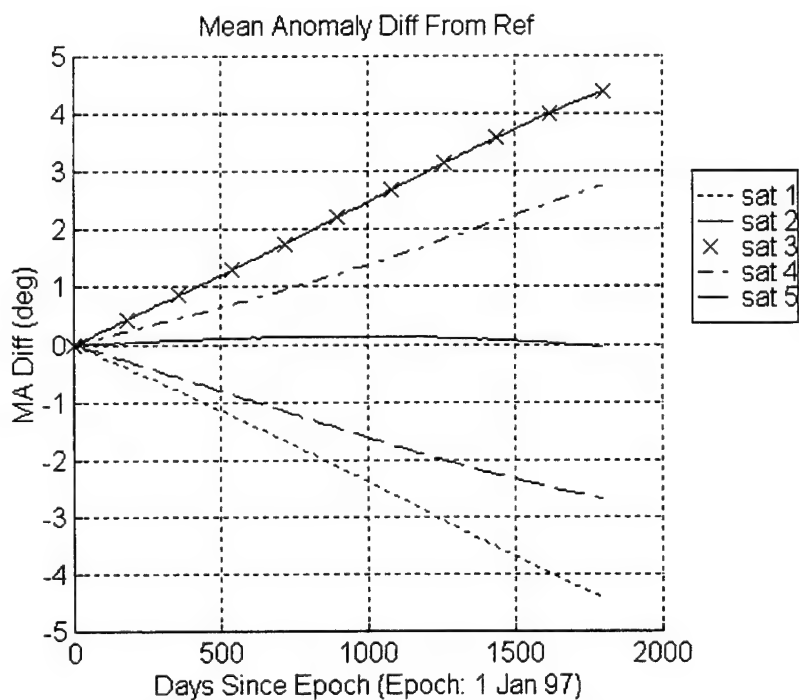


Figure D.48: Mean Anomaly Difference From Nominal Trajectory
(Uncontrolled Borealis 5-5 10ω 81:10 Node at Noon)

D.3.3 Uncontrolled Borealis 5-5 10 ω 81:10 Node at Midnight Element Difference Plots

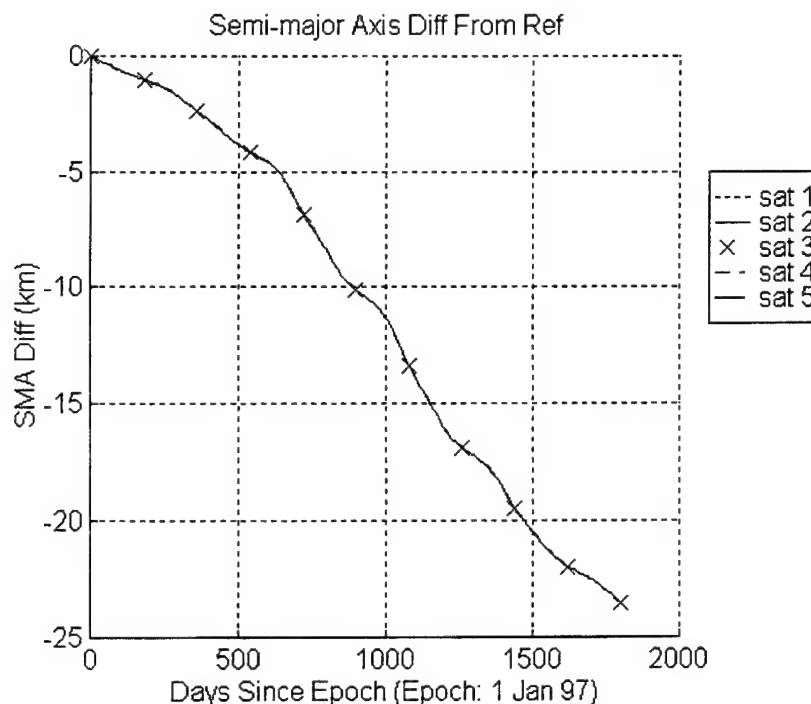


Figure D.49: Semi-major Axis Difference From Nominal Trajectory (Uncontrolled Borealis 5-5 10 ω 81:10 Node at Midnight)

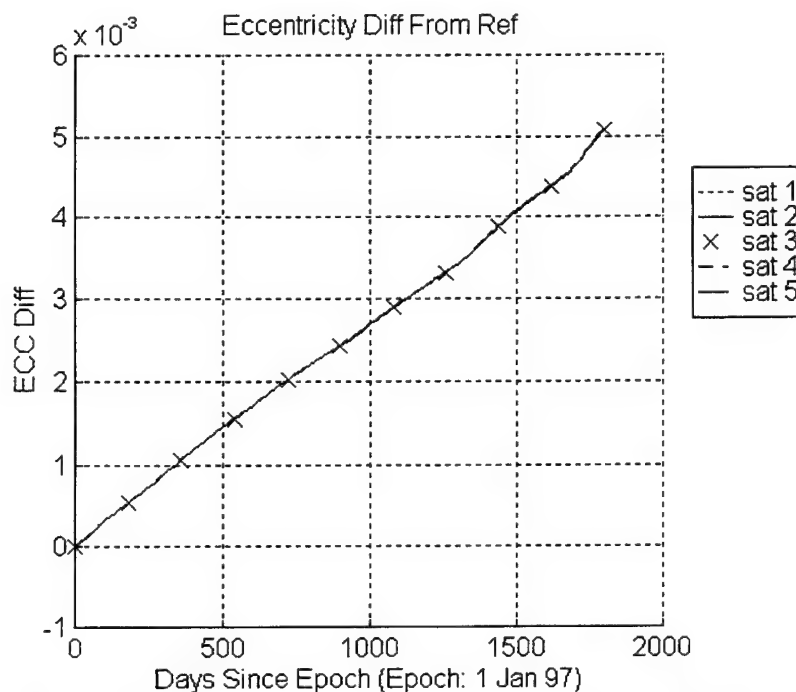


Figure D.50: Eccentricity Difference From Nominal Trajectory (Uncontrolled Borealis 5-5 10 ω 81:10 Node at Midnight)

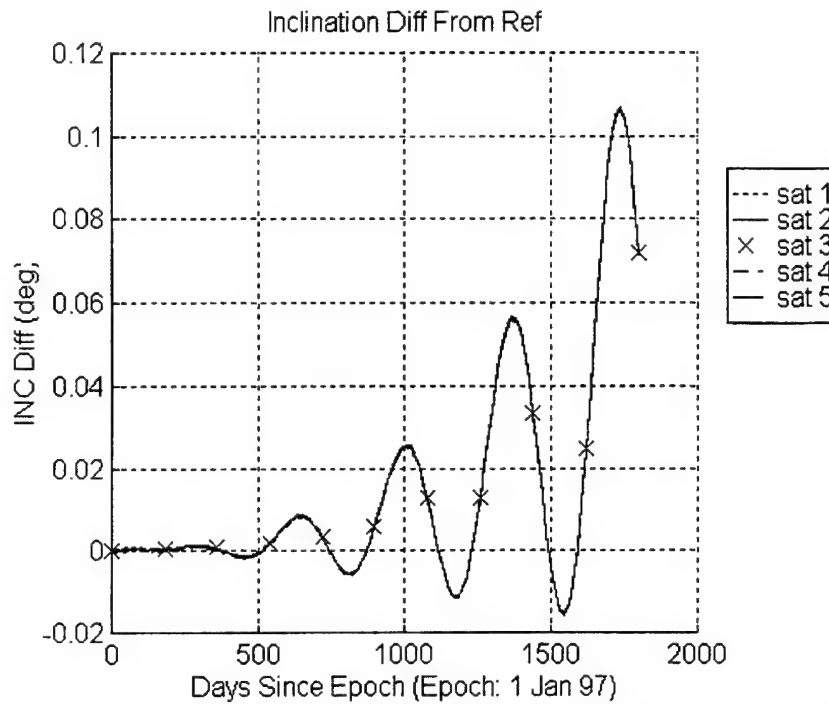


Figure D.51: Inclination Difference From Nominal Trajectory
(Uncontrolled Borealis 5-5 10ω 81:10 Node at Midnight)

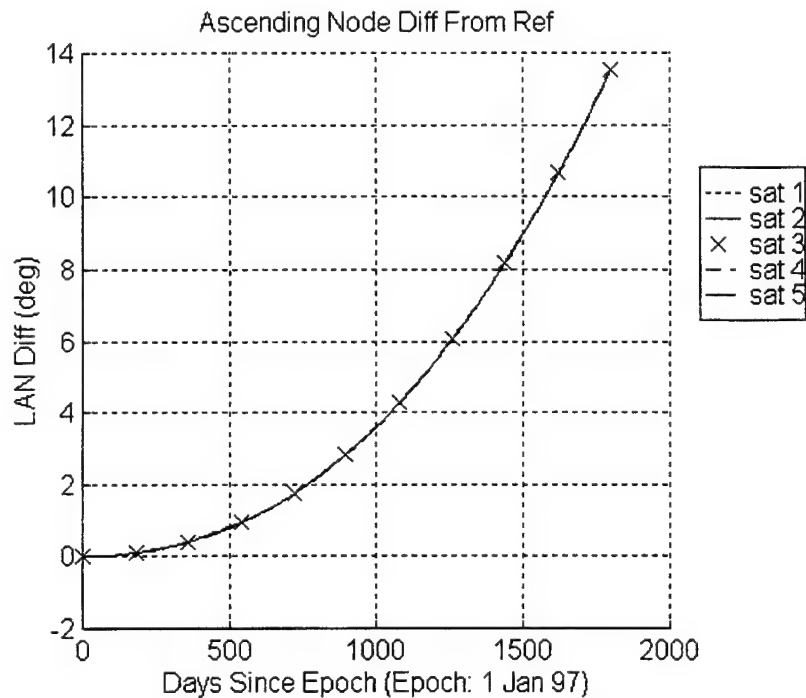


Figure D.52: Ascending Node Difference From Nominal Trajectory
(Uncontrolled Borealis 5-5 10ω 81:10 Node at Midnight)

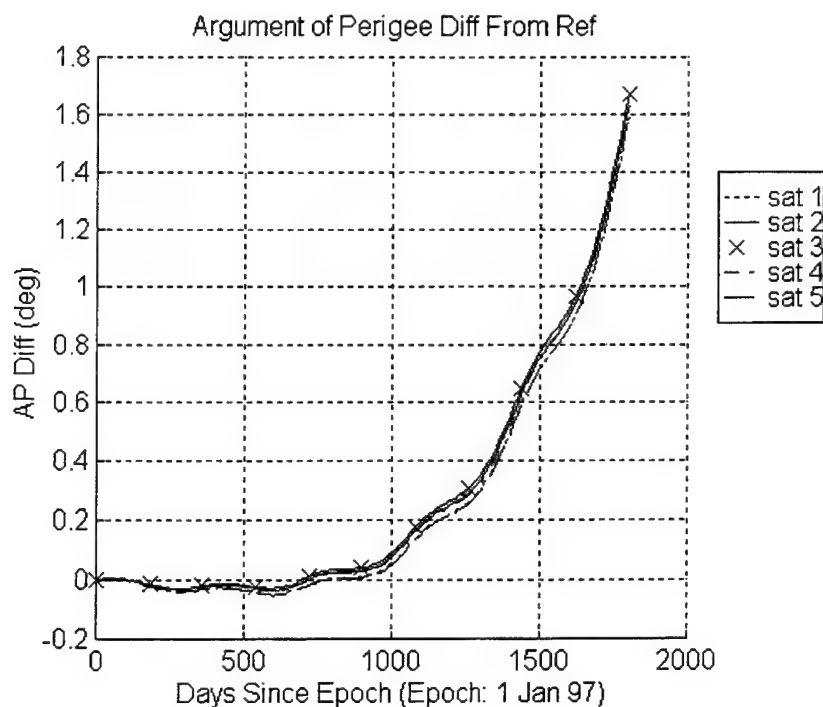


Figure D.53: Argument of Perigee Difference From Nominal Trajectory
(Uncontrolled Borealis 5-5 10ω 81:10 Node at Midnight)

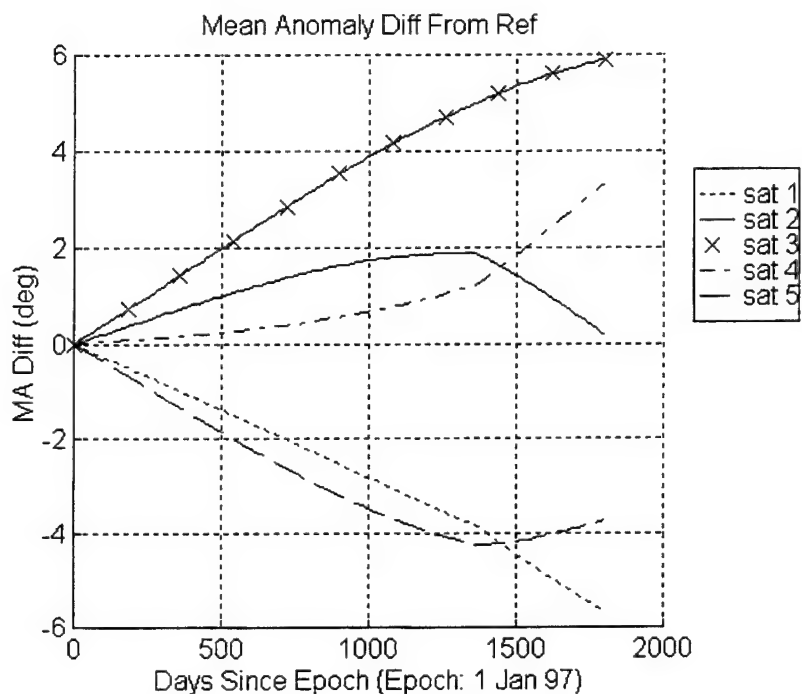


Figure D.54: Mean Anomaly Difference From Nominal Trajectory
(Uncontrolled Borealis 5-5 10ω 81:10 Node at Midnight)

D.4 Sim 3 / Run 4

This run is a 5 year uncontrolled execution of the ASKS on the 4-4 satellite 81:10 node at noon/midnight configuration of the Borealis planes, with argument of perigee rotated 10° , and the 6 satellite Concordia plane of the Ellipso constellation. There are 4 satellites in each of the Borealis planes and 6 satellites in the Concordia plane. The argument of perigee is 260° for the Borealis node at noon plane, and 280° for the node at midnight plane. Relative mean anomaly (formation) station-keeping is used with targeting method 0. Method 0 indicates that all control related components of the input deck are ignored.

The epoch orbital elements, with the exception of ω , for this run are listed in tables 7.1 and 7.4. The nominal (reference) trajectory is propagated in the presence of zonal harmonics through degree 21, and solar/lunar point masses. The actual satellite trajectory is propagated with the perturbations of the nominal trajectory plus solar radiation pressure, tesseral resonance and atmospheric drag.

The input deck for this run differs from the one shown in section D.1.1 only in the argument of perigee values of the satellites in the Borealis planes and the number of satellites in each of the planes. Sections D.4.1 contains the one, two, three and four-way coverage of the constellation over the 5 year time span. Note that coverage is provided for the entire northern hemisphere and for the southern hemisphere above 55°S latitude. The northern hemispheric coverage assumes a 25° minimum elevation angle. The southern hemispheric coverage assumes a 10° minimum elevation angle. The Concordia element difference plots are the same as shown in section D.1.3. Sections D.4.2 and D.4.3 contain the orbital element difference plots for the node at noon and node at midnight planes, respectively.

D.4.1 Coverage Plots (Sim 3 / Run 4)

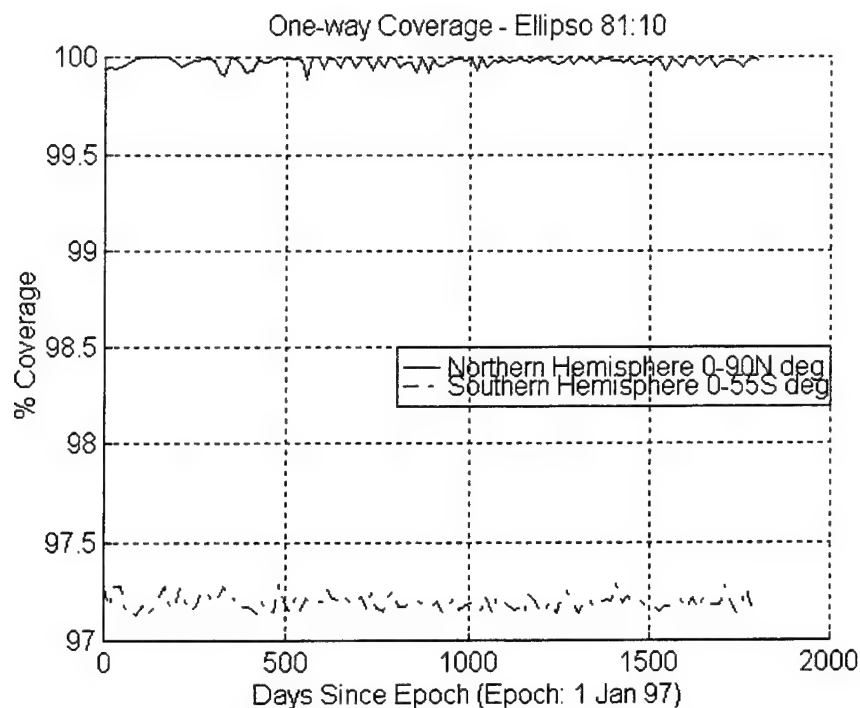


Figure D.55: 4-4-6 10 ω Ellipso One-Way Coverage
(Uncontrolled Borealis 81:10 Noon/Midnight and Concordia)

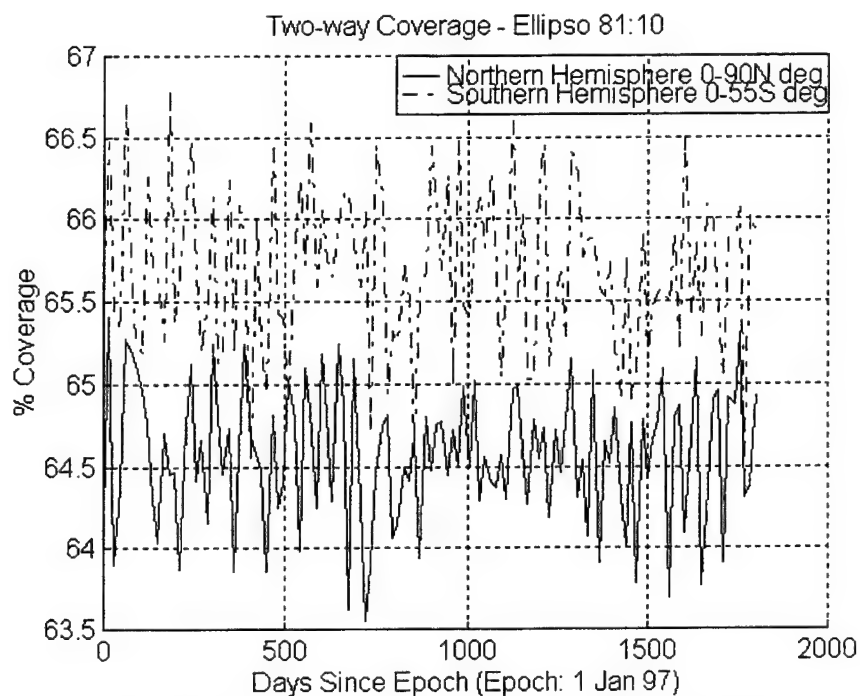


Figure D.56: 4-4-6 10 ω Ellipso Two-Way Coverage
(Uncontrolled Borealis 81:10 Noon/Midnight and Concordia)

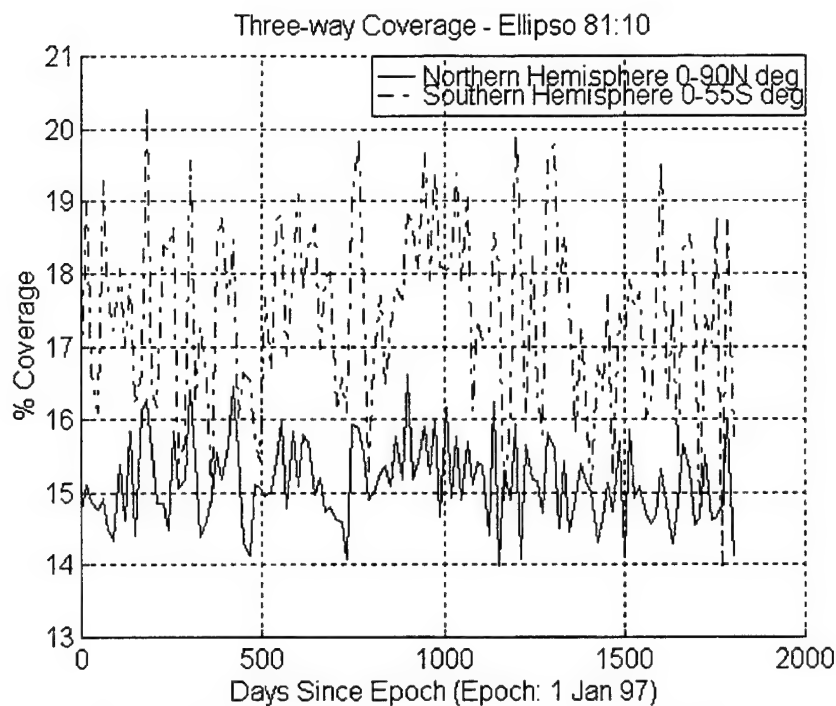


Figure D.57: 4-4-6 10 ω Ellipso Three-Way Coverage
(Uncontrolled Borealis 81:10 Noon/Midnight and Concordia)

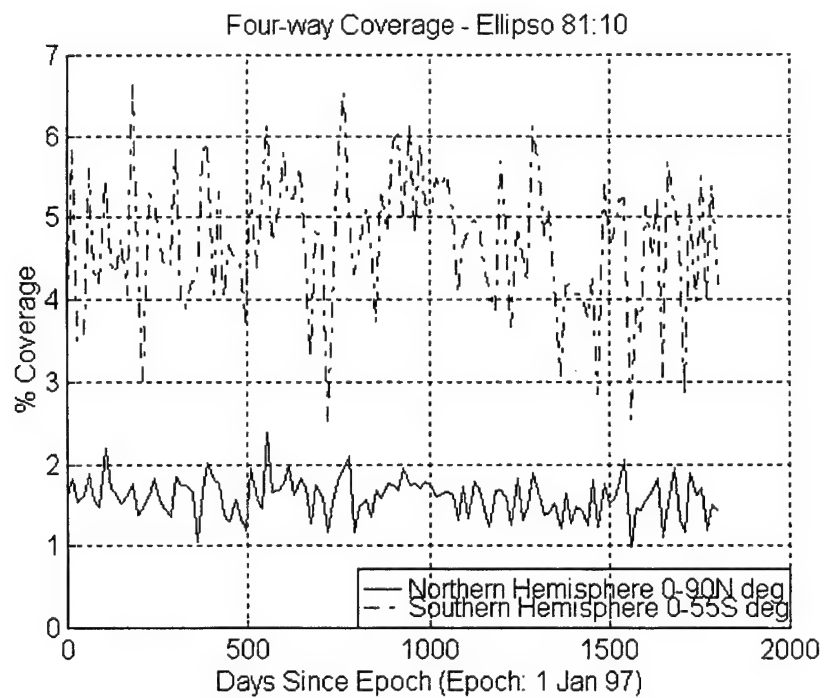


Figure D.58: 4-4-6 10 ω Ellipso Four-Way Coverage
(Uncontrolled Borealis 81:10 Noon/Midnight and Concordia)

D.4.2 Uncontrolled Borealis 4-4 10 ω 81:10 Node at Noon Element Difference Plots

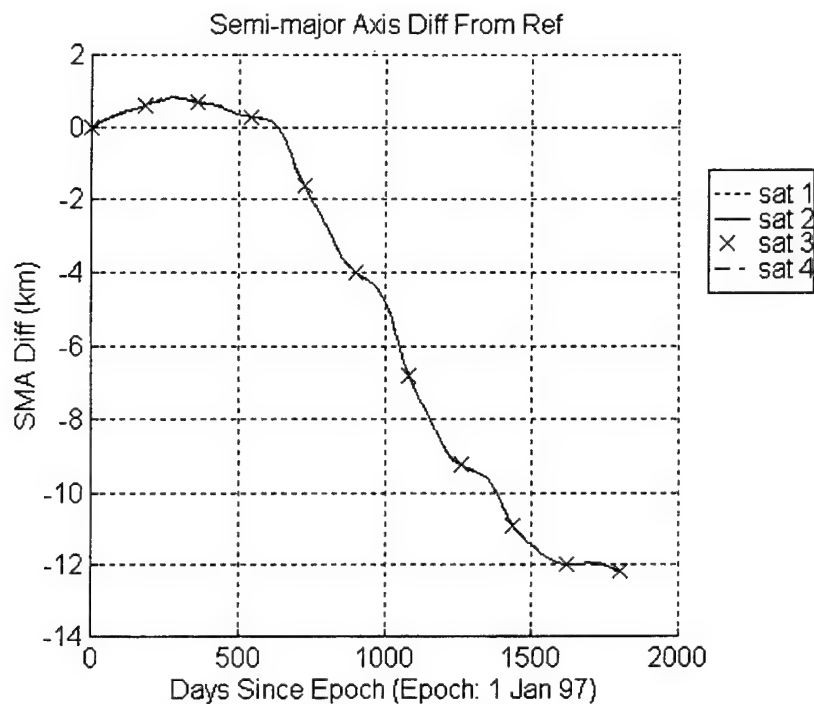


Figure D.59: Semi-major Axis Difference From Nominal Trajectory
(Uncontrolled Borealis 4-4 10 ω 81:10 Node at Noon)

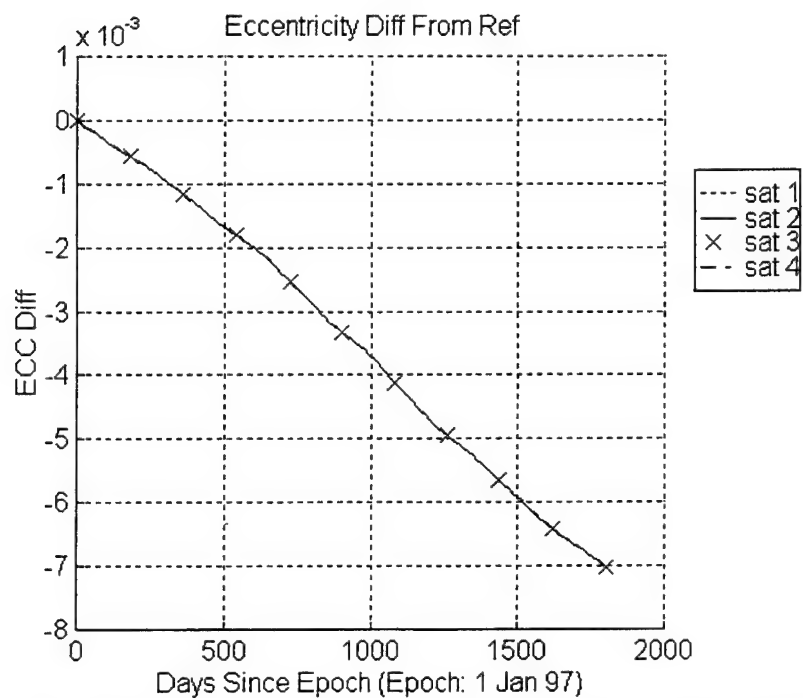


Figure D.60: Eccentricity Difference From Nominal Trajectory
(Uncontrolled Borealis 4-4 10 ω 81:10 Node at Noon)

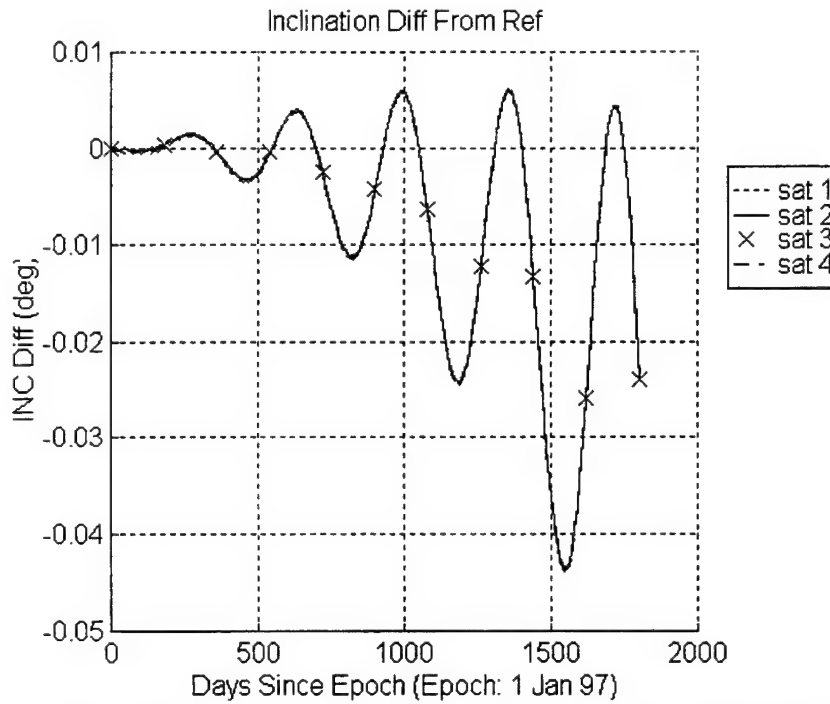


Figure D.61: Inclination Difference From Nominal Trajectory
(Uncontrolled Borealis 4-4 10 ω 81:10 Node at Noon)

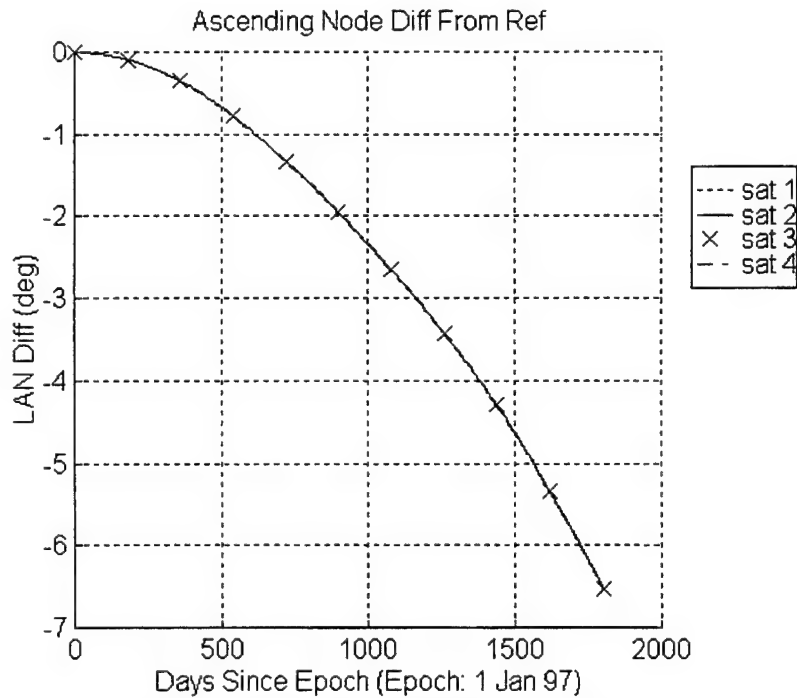


Figure D.62: Ascending Node Difference From Nominal Trajectory
(Uncontrolled Borealis 4-4 10 ω 81:10 Node at Noon)

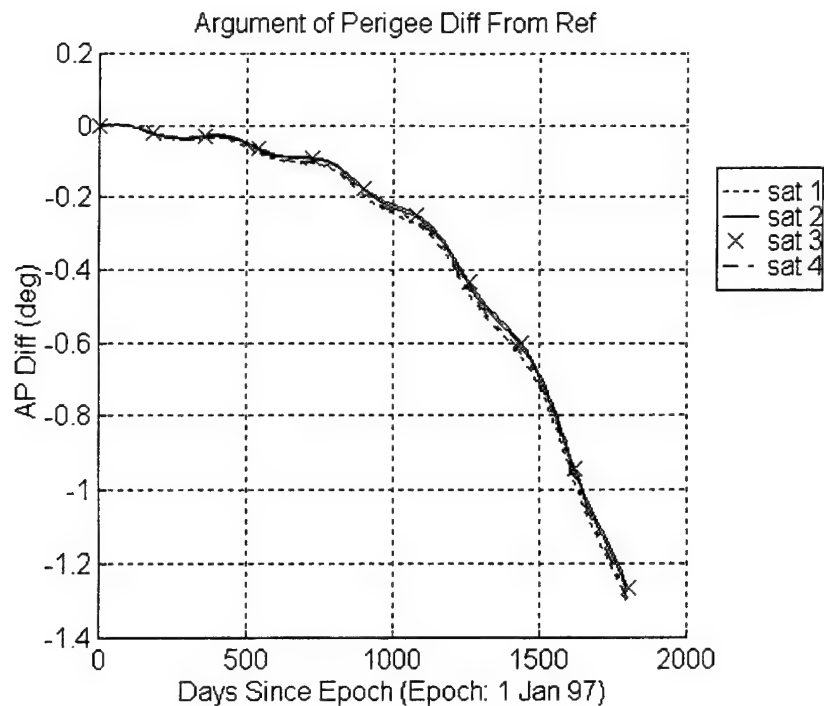


Figure D.63: Argument of Perigee Difference From Nominal Trajectory
(Uncontrolled Borealis 4-4 10 ω 81:10 Node at Noon)

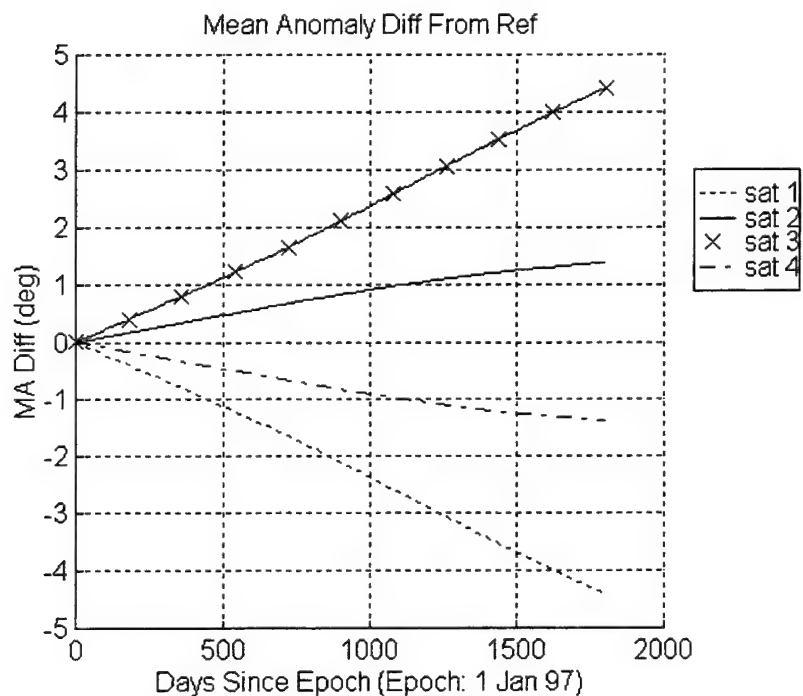


Figure D.64: Mean Anomaly Difference From Nominal Trajectory
(Uncontrolled Borealis 4-4 10 ω 81:10 Node at Noon)

D.4.3 Uncontrolled Borealis 4-4 10 ω 81:10 Node at Midnight Element Difference Plots

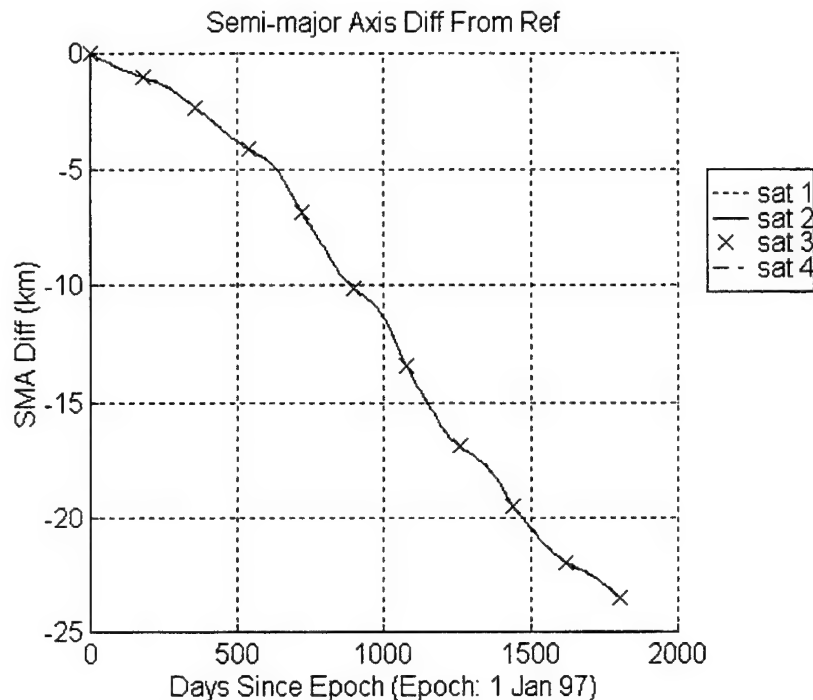


Figure D.65: Semi-major Axis Difference From Nominal Trajectory (Uncontrolled Borealis 4-4 10 ω 81:10 Node at Midnight)

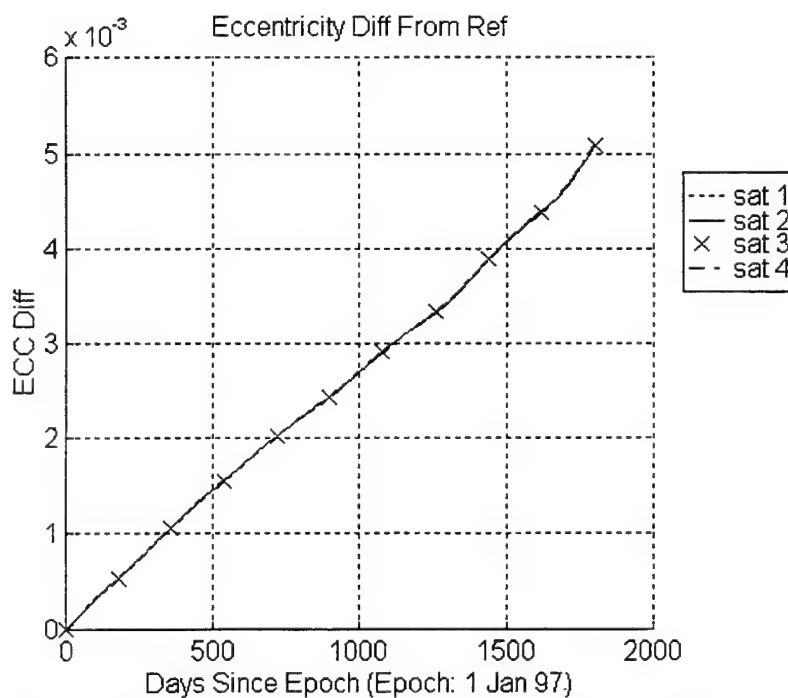


Figure D.66: Eccentricity Difference From Nominal Trajectory (Uncontrolled Borealis 4-4 10 ω 81:10 Node at Midnight)

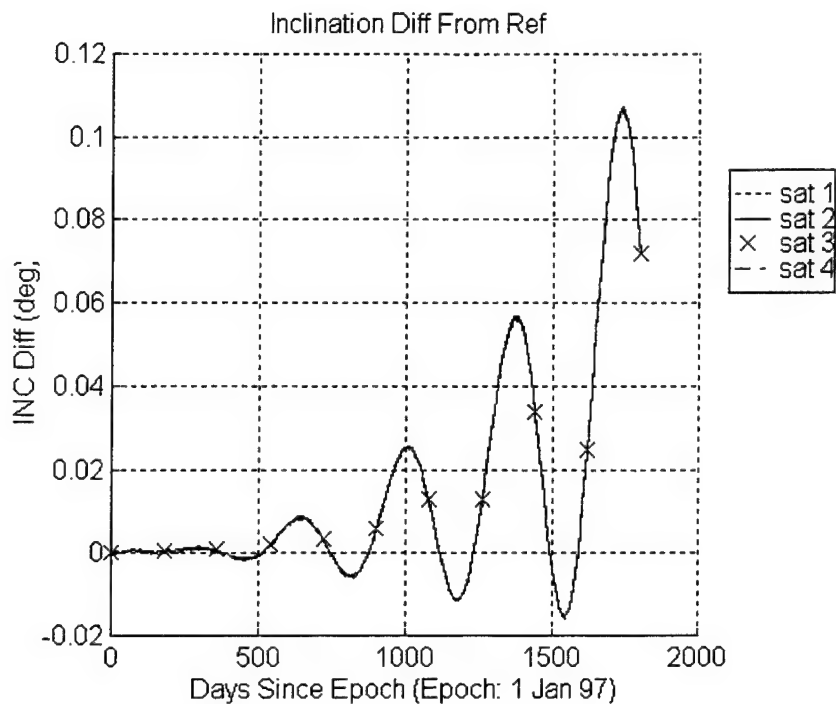


Figure D.67: Inclination Difference From Nominal Trajectory
(Uncontrolled Borealis 4-4 10 ω 81:10 Node at Midnight)

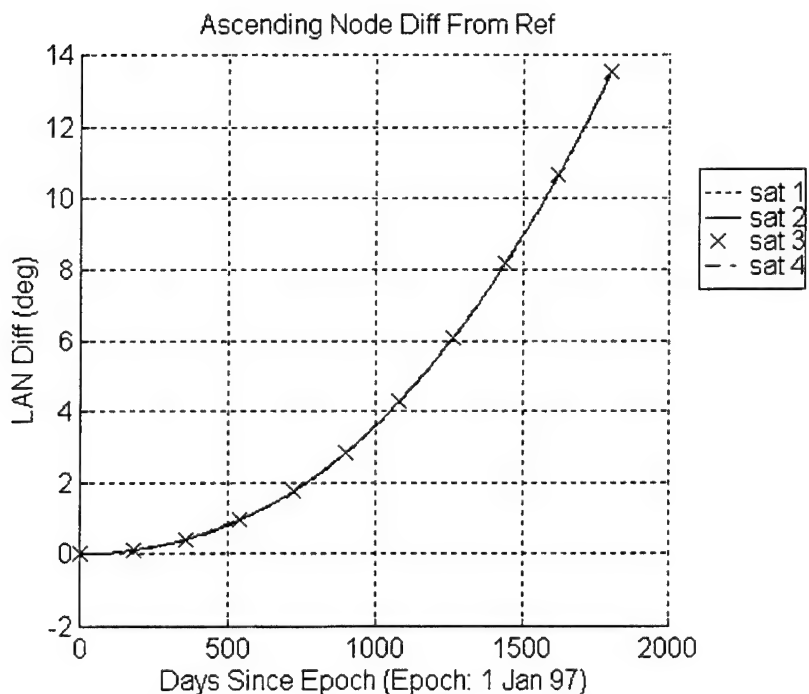


Figure D.68: Ascending Node Difference From Nominal Trajectory
(Uncontrolled Borealis 4-4 10 ω 81:10 Node at Midnight)

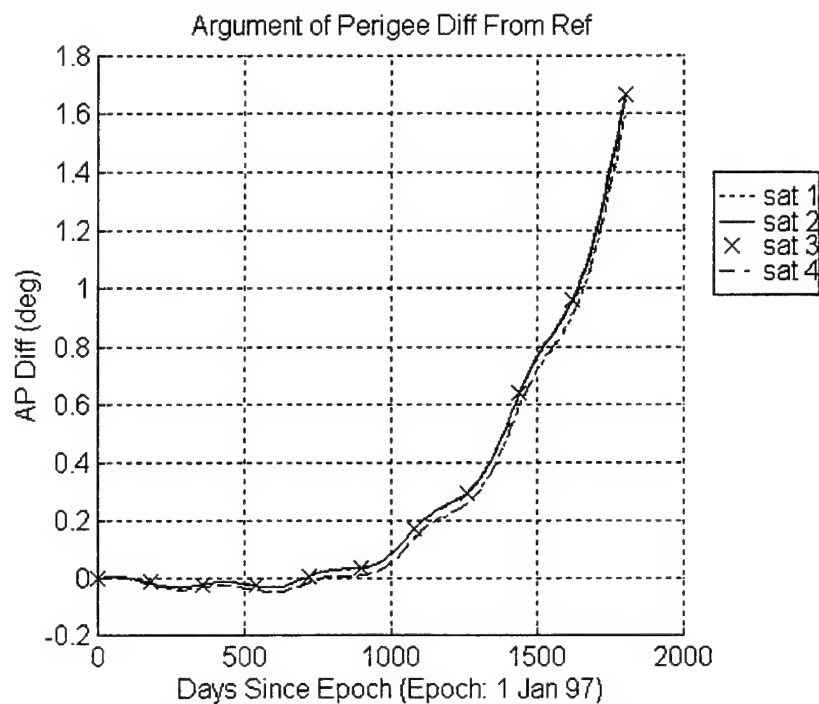


Figure D.69: Argument of Perigee Difference From Nominal Trajectory
(Uncontrolled Borealis 4-4 10 ω 81:10 Node at Midnight)

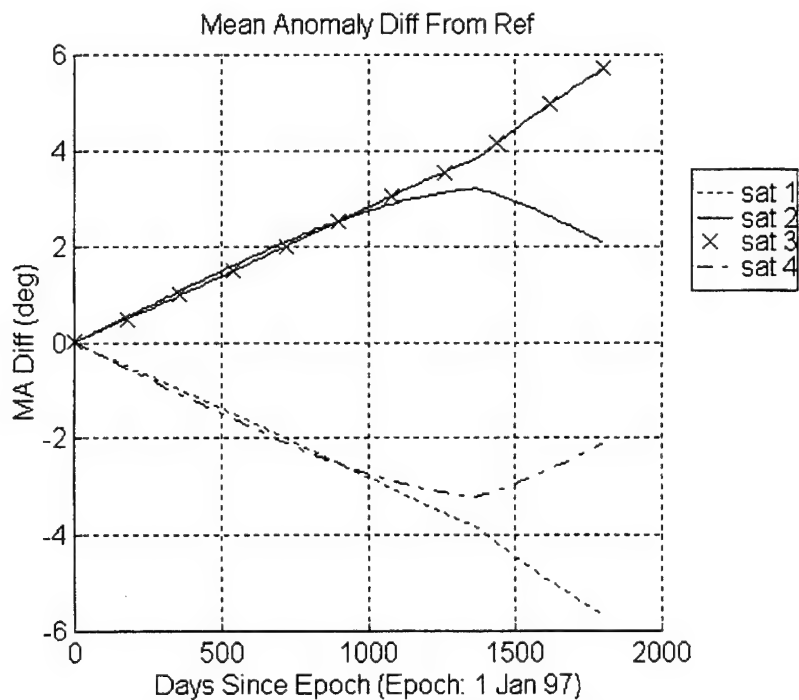


Figure D.70: Mean Anomaly Difference From Nominal Trajectory
(Uncontrolled Borealis 4-4 10 ω 81:10 Node at Midnight)

[This page intentionally left blank.]

References

- [1] Barker, W.N., Casali, S. J., & Wallner, R. N., "The Accuracy of General Perturbation and Semianalytic Satellite Ephemeris Theories," AAS Paper 95-432, AAS/AIAA Astrodynamics Specialist Conference, Halifax, Nova Scotia, August 1995
- [2] Bate, R. R., Mueller, D. D., & White J. E., *Fundamentals of Astrodynamics*, Dover Publications, New York, 1971
- [3] Battin, Richard H., *An Introduction to the Mathematics and Methods of Astrodynamics*, AIAA Education Series, New York, 1987
- [4] Broucke, R. A. & Cefola, P. J., "On The Equinoctial Orbital Elements," *Celestial Mechanics*, Vol 5, 1972, pp. 303-310
- [5] Brouwer, D. & Hori, G., "Theoretical Evaluation of Atmospheric Drag Effects in the Motion of an Artificial Satellite," *Astronomical Journal*, Vol. 66, No. 1290, June 1961
- [6] Cappellari, J. O., Velez, C. E., & Fuchs, A. J., editors, *Mathematical Theory of the Goddard Trajectory Determination System*, Report X-582-76-77, Goddard Space Flight Center, April 1976
- [7] Carter, David, "Jacchia-Roberts Files from Schatten's Data," Draper Intralab Memorandum to Paul Cefola, ESD 94-188, March 24, 1994

- [8] Carter, Scott S., *Precision Orbit Determination From GPS Receiver Navigation Solutions*, MS Thesis, MIT, Cambridge, MA, June 1996
- [9] Carter, T. & Brient, J., "Linear Impulsive Rendezvous Problem," *Journal of Optimization Theory and Applications*, Vol 86, 1995, pp. 553-584
- [10] Castiel, D., Brosius, J. W., & Draim, J. E., "Ellipso™: Coverage Optimization Using Elliptic Orbits," Paper AIAA-94-1098-CP, 15th AIAA International Communications Satellite Systems Conference, 1994
- [11] Castiel, D., Draim, J. E., & Brosius, J. W., "Elliptical Orbit Satellite System and Deployment with Controllable Coverage Characteristics," United States Patent Number 5,582,367, 10 Dec 1996
- [12] Castiel, D. & Draim, J. E., "The Ellipso™ Mobile Satellite System," *Proceedings of the Fourth International Mobile Satellite Conference*, Ottawa, Canada, June 6-8 1995
- [13] Cefola, Paul J., Program Manager, Astrodynamics Applications, Draper Laboratory, Cambridge, MA: personal discussions from 1 Apr to 9 May, 1997
- [14] Cefola, P., "Standalone Semianalytical Orbit Propagator Preliminary User Guide and System Description," CSDL-C-5719, under contract by Aerospace Corporation, P.O. No. 57924-NV
- [15] Cefola, P., Proulx, R., et.al., "The RADARSAT Flight Dynamics System: An Extensible, Portable, Workstation-based Mission Support System," AIAA Paper 94-3726, AIAA/AAS Astrodynamics Conference, 1-3 August 1994, Scottsdale, AZ

- [16] Chobotov, Vladimir A., Ed., *Orbital Mechanics*, AIAA Education Series, Washington D.C., 1991
- [17] "Constellation Maintenance," MCHI presentation by Engineering Staff, Mobile Communications Holdings, Inc., 14 March 1996
- [18] Cox, C. M., Feiertag, R. J., Oza, D. H., & Doll, C. E., "Evaluation of Semiempirical Atmospheric Density Models for Orbit Determination Applications," Proceedings of the Flight Mechanics/Estimation Theory Symposium, Goddard Space Flight Center, 1994, pp. 399-412
- [19] Danielson, D. A., Neta, B., & Early, L. W., *Semianalytic Satellite Theory (SST): Mathematical Algorithms*, Naval Postgraduate School Technical Report NPS-MA-94-001
- [20] Draim, J. E. & Kacena, T. J., "Populating the Abyss - Investigating More Efficient Orbits," 6th Annual AIAA/USU Conference on Small Satellites, Sept. 21-24 1992
- [21] Draim, J. & Castiel, D., "Optimization of the Borealis and Concordia Sub-Constellations of the Ellipso Mobile Communications System," IAF Paper 96-A.1.01, 47th International Astronautical Congress, 7-11 October 1996, Beijing, China
- [22] Early, L. W., "A Portable Orbit Generator Using Semianalytical Satellite Theory," Paper 86-2164-CP, AIAA/AAS Astrodynamics Conference, Williamsburg, Va, August 1986

- [23] Fieger, Martin E., *An Evaluation of Semianalytical Satellite Theory Against Long Arcs of Real Data For Highly Eccentric Orbits*, MS Thesis, MIT, Cambridge, MA, January 1987
- [24] Fischer, Jack, "Inside DSST: An Investigation Into the Draper Semianalytic Satellite Theory," internal C S Draper presentation, available from author 617-258-1559
- [25] Fonte, Daniel J., *Implementing a 50 x 50 Gravity Field Model in an Orbit Determination System*, MS Thesis, MIT, Cambridge, MA, June 1993
- [26] Garrison, T., Ince, M., Pizzicaroli, J., & Swan, P., "IRIDIUM® Constellation Dynamics: The Systems Engineering Trades," Paper IAF-95-U.2.04, 46th International Astronautical Congress, Oslo, Norway, Oct. 2-6 1995
- [27] Gropp, W., Lusk, E., & Skjellum A., *Using MPI: Portable Parallel Programming with the Message-Passing Interface*, MIT Press, Cambridge, MA, 1995
- [28] Gross, L. R. & Prussing, J. E., "Optimal Multiple-Impulse Direct-Ascent Fixed-Time Rendezvous," AIAA Journal, Vol 12, No 7, July 1974, pp. 885-889
- [29] Hoots, F. R. & France, R. G., "An Analytic Satellite Theory Using Gravity and a Dynamic Atmosphere," AIAA Paper 82-1409, AIAA/AAS Astrodynamics Conference, San Diego, CA, 9-11 August 1982
- [30] Hough, Michael E., *Orbits Near Critical Inclination, Including Lunarsolar Perturbations*, PhD Thesis, Stanford University, 1979

- [31] Hulkover, Neal D., "A Reevaluation of Ellipso™, Globalstar, IRIDIUM™/SM and Odyssey™," presentation at Volpe Transportation Center, Cambridge, MA, 18 October 1994, copies available from Jack Fischer 617-258-1559
- [32] Jezewski, D. J., *Primer Vector Theory and Applications*, NASA Technical Report R-454, November 1975
- [33] Jezewski, D. J., Brazzel, J. P., Prust, E. E., Brown, B. G., Mulder T. A., & Wissinger, D. B., "A Survey of Rendezvous Trajectory Planning," AAS Paper 91-505, AAS/AIAA Astrodynamics Specialist Conference, Durango, CO, August 1991
- [34] Jezewski, D. J. & Rozendaal, H. L., "An Efficient Method for Calculating Optimal Free-Space N-Impulse Trajectories," *AIAA Journal*, Vol 6, 1968, pp. 2160-2165
- [35] Kantsiper, Brian, *An Approach to the Control of Satellite Constellations*, tentative title, PhD Thesis, MIT, Cambridge, MA, Sept 1997
- [36] Kirk, Donald E., *Optimal Control Theory*, Prentice Hall, New Jersey, 1970
- [37] Larson, W. J. & Wertz, J. R., Eds., *Space Mission Analysis and Design*, 2nd Edition, Microcosm Inc., 1992
- [38] Lawden, D. F., "Optimal Trajectories for Space Navigation," London, Butterworths, 1963
- [39] Lee, Byoungsoo & Grantham, Walter J., "Aeroassisted Orbital Maneuvering Using Lyapunov Optimal Feedback Control," *Journal of Guidance*, Vol 12, No 2, Mar-Apr 1989, pp. 237-242

- [40] Lion, R. M. & Handelsman, M., "Primer Vector on Fixed-Time Impulsive Trajectories, AIAA Journal, Vol 6, 1968, pp. 127-132
- [41] McInnes, Colin , "Potential Function Methods for Autonomous Spacecraft Guidance and Control," AAS Paper 95-447, AAS/AIAA Astrodynamics Specialist Conference, Halifax, Nova Scotia, August 14-17, 1995
- [42] McInnes, Colin R., "Autonomous Proximity Manoeuvring [sic] Using Artificial Potential Functions," ESA Journal, Vol 17, 1993, pp. 159-169
- [43] McInnes, Colin R., "Autonomous Ring Formation for A Planar Constellation of Satellites," Journal of Guidance, Vol 18, No 5, pp. 1215-1217
- [44] McClain, Wayne D., *A Semianalytic Artificial Satellite Theory, Volume 1: Application of the Generalized Method of Averaging to the Artificial Satellite Problem*, 1992, available from Wayne McLain, Charles Stark Draper Laboratory, 555 Technology Square, Cambridge, MA 02139
- [45] Press, W. H., Teukolsky, S. A., Vetterling, W. T., & Flannery, B. P., *Numerical Recipes in FORTRAN: The Art of Scientific Computing*, 2nd Edition, Cambridge University Press, 1992
- [46] Proulx, Ron, Software Engineering Directorate, Draper Laboratory, Cambridge, MA: personal discussions from 1 Apr to 9 May, 1997
- [47] Prussing, J. E., "Optimal Impulsive Linear Systems: Sufficient Conditions and Maximum Number of Impulses," Journal of Astronautical Sciences, Vol 43, No 2, Apr-Jun 1995, pp.195-206

- [48] Prussing, J. E. & Chiu, J. H., "Optimal Multiple-Impulse Time-Fixed Rendezvous Between Circular Orbits," *Journal of Guidance, Control & Dynamics*, Vol 9, No 1, Jan-Feb 1986, pp. 17-22
- [49] Prussing, J. E. & Conway, B. A., "Optimal Terminal Maneuver for a Cooperative Impulsive Rendezvous," *Journal of Guidance, Control & Dynamics*, Vol 12, No 3, May-Jun 1989, pp. 433-435, also Errata, Vol 12, No 4, Jul-Aug 1989, p. 608
- [50] Roy, A. E., *Orbital Motion*, 3rd Ed., Adam Hilger, Bristol, 1988
- [51] Sabol, Christopher, *Application of Sun-Synchronous Critically Inclined Orbits to Global Personal Communications Systems*, MS Thesis, MIT, Cambridge, MA, November 1994
- [52] Sabol, C., Draim, J., & Cefola, P., "Refinement of a Sun-Synchronous Critically Inclined Orbit for the Ellipso Personal Communication System," AAS Paper 95-340, AAS/AIAA Astrodynamics Specialist Conference, Halifax, Nova Scotia, August 1995, to appear in the *Journal of Astronautical Sciences*
- [53] Shah, Naresh, "Preliminary Perturbation Analysis of ELLIPSO Concordia Orbit," Draper Intralab Memorandum E50-96-155, 11 Apr 1996, available from Dr. Paul Cefola, C S Draper Laboratory, Cambridge, MA
- [54] Slotine, Jean-Jacques E. & Li, Weiping, *Applied Nonlinear Control*, Prentice Hall, New Jersey, 1991
- [55] Smith, R. L. & Lucas, M. J., *Primary Coordinate Systems and Coordinate System Transformations in GTDS*, NASA Goddard Space Flight Center, Contract NAS 5-24300 Task Assignment 757, June 1980

- [56] Snir, M., Otto, S., Huss-Lederman, S., Walker, D., & Dongarra, J., *MPI: The Complete Reference*, MIT Press, Cambridge, MA, 1996
- [57] Taur, D. R., Coverstone-Carroll, V., & Prussing J. E., "Optimal Impulsive Time-Fixed Orbital Rendezvous and Interception with Path Constraints," *Journal of Guidance, Control & Dynamics*, Vol 18, No 1, Jan-Feb 1995, pp. 54-60
- [58] Wallace, Scott T., *Parallel Orbit Propagation and the Analysis of Satellite Constellations*, MS Thesis, MIT, Cambridge, MA, June 1995
- [59] Yurasov, V., "Universal Semianalytic Satellite Motion Propagation Method," US/Russian Space Surveillance Workshop, Poznan, Poland, July 5 1996